Precipitation Pathways of Amorphous Silica

Daniela Brigitte van den Heuvel

Submitted in accordance with the requirements
for the degree of Doctor of Philosophy

The University of Leeds
School of Earth and Environment

May 2016

Declaration

The candidate confirms that the work submitted is her own, except where work which has formed part of jointly authored publications has been included. The contribution of the candidate and the other authors to this work has been explicitly indicated below. The candidate confirms that appropriate credit has been given within the thesis where reference has been made to the work of others.

Chapter 2 is a literature review paper in preparation for *Earth Science Reviews* as

> van den Heuvel, D. B., Tobler D. J., Gunnarsson, I. and Benning, L. G., in prep. Precipitation of amorphous silica (SiO_2) from high enthalpy geothermal fluids – A review.

The review was initiated and outlined by DBH. DBH, DJT and LGB co-wrote the section on silica sinter formation. DBH and IG co-wrote the section on the precipitation of silica in geothermal power plants. The remaining sections were written by DBH with contributions from all co-authors.

Chapter 3 has been published as

> Meier, D. B., Gunnlaugsson, E., Gunnarsson, I., Jamtveit, B., Peacock, C. L. and Benning, L. G., 2014. Microstructural and chemical variation in silica-rich precipitates at the Hellisheiði geothermal power plant. *Mineralogical Magazine* **78**, 1381-1389.

Sampling was carried out by EG and IG, supported by local staff from the Hellisheiði power plant where necessary. The analyses of the precipitates and geothermal waters were done by DBM and EG with support of technical staff at the University of Leeds and Reykjavik Energy. Data interpretation, writing and production of figures was done by DBM with contributions from all co-authors.

Chapter 4 is in preparation for submission to *Geochemica et Cosmochemica Acta* as

> van den Heuvel, D. B., Gunnlaugsson, E., Gunnarsson, I., Stawski, T. M., Peacock, C. L. and Benning, L. G., in prep. Two pathways of amorphous silica precipitation control scaling inside in-use geothermal pipelines.

Sampling was carried out by EG, DBH and LGB supported by local staff from the Hellisheiði power plant. The analyses of the precipitates and geothermal waters were done by DBH and EG with support of technical staff at the University of Leeds, Reykjavik Energy, the GeoForschungsZentrum Potsdam and the University of Bern. Data interpretation, writing and production of figures was completed by DBH with contributions from all co-authors.

Chapter 5 is ready for submission to *Geothermal Transactions* as

> van den Heuvel, D. B., Gunnlaugsson, E. and Benning, L. G., in prep. Surface roughness and composition control silica deposition from geothermal fluids.

Sampling was carried out by EG, DBH and LGB supported by local staff from the Hellisheiði power plant. The analyses of the precipitates and geothermal waters were done by DBH and EG with support of technical staff at the University of Leeds and Reykjavik Energy. Data interpretation, writing and production of figures was completed by DBH with contributions from all co-authors.

Chapter 6 has been published as:

> van den Heuvel, D. B., Gunnlaugsson, E., Peacock, C. L. and Benning, L. G., 2016. *Passivation of metal surfaces against corrosion by silica scaling*. Proceedings, 41st Workshop on Geothermal Reservoir Engineering Stanford University.

Sampling was carried out by EG, DBH and LGB, supported by local staff from the Hellisheiði power plant. The analyses of the precipitates and geothermal waters were done by DBH and EG with support of technical staff at the University of Leeds and Reykjavik Energy. Data interpretation, writing and production of figures was completed by DBH with contributions from all co-authors.

Chapter 7 is accepted with major revisions in *Scientific Reports* as

> van den Heuvel, D. B., Stawski, T. M., Tobler D. J., Wirth, R., Peacock, C. L. and Benning, L. G., in review. Formation of silica-lysozyme composites via co-precipitation and adsorption.

Laboratory synthesis of composites was done by DBH. SAXS experiments were completed by DBH, TMS and Rogier Besselink at PETRA III (DESY) and data evaluation done by TMS. HEXD and conversion to PDF was done by DJT at APS. HR-TEM was done by RW and DBH and evaluated with the help of TMS. Other experimental data was collected and evaluated by DBH. Writing and production of figures was completed by DBH with significant contributions from all co-authors. TMS wrote the supplementary information on SAXS data evaluation

Acknowledgments

Even though it is my name written on the cover of this thesis, I could not have completed it without the invaluable help of a large number of people who I would like to say a special "thank you" to.
My team of amazing supervisors and close collaborators:

Liane G. Benning, for your superhuman and never faltering support during the last 3.5 years. You guided me using the perfect mix of the carrot and the stick, making my PhD a great experience and a success.

Caroline Peacock, for your honesty and support and for coming up with different angles when we could not see the wood for the trees anymore.

Tomasz Stawski, for your patient introduction to the nanoworld and its techniques by being a great researcher and a good friend.

Dominique Tobler, for the fruitful collaborations we had and for always having an open ear when I needed scientific information, advice or a simple rant.

Einar Gunnlaugsson, for going the extra mile to make the field experiments at Hellisheiði a success. Being able to rely on your thoroughness during these experiments took a lot of pressure off me.

Ingvi Gunnarsson, for your scientific input in the perfect moments and your excitement about my work.

I am sincerely grateful to the Marie Skłodowska-Curie actions for sponsoring my PhD as part of the MINSC Initial Training Research network (Project number 290040). I would also like to thank the International Geothermal Association (IGA),

the European Association of Geochemistry (EGA) and the School of Earth and Environments for research and travel grants awarded during my PhD.

I would like to thank the huge number of people who helped me during my laboratory and field experiments and the subsequent analyses, even if some of the data has not ended up in this thesis:

University of Leeds Andy Connelly, Stephen Reid, Fiona Keay, Sam Allshaw, Richard Walshaw, Lesley Neave, Anthony Winross, Stephen Burgess and Harri Williams, Adrian Cunliffe, Susanne Patel, Stuart Micklethwaite, Mike Ward, Juan-Diego Rodriguez Blanco.

Reykjavik Energy: Haldór Bergmann, Einar Örn Thrastarsson, Þorsteinn A. Þorgeirsson and anyone else at Reykjavik Energy and ON power who was involved in the sampling or analyses of my samples.

Elsewhere: Richard Wirth, Anja Schreiber, Sylvia Pinkerneil at GFZ Potsdam, Bob Knight at the University of Hull, staff at the P12 beamline at PETRA III (DESY) and the staff at beamline 11-ID-B at the Advanced Photon Source.

A massive "thank you" also goes to all my science buddies. You were there for me during the last 3.5 years, no matter if I needed scientific advice, a laugh and a drink (and possibly a Karaoke session), someone to complain to or someone to calm me down when things got a bit too much: Pilar Ramirez-Garcia, Edine Pape, Cindy Lockwood, Jörgen Rosenqvist, Jan Prikryl, Diwaker Jha, Gisela Weibel, Andrea Arale Vidal, James Witts, Tim Küsters, Andy Bray, Andy Hobson, Jenny Thompson, Aislinn Boylan, Mark Xiong, Deirdre Clark, Chris Grimm, Giulia Montanari, Fernando Berro Jimenez, Rhian Rees-Owen, Lucy Campbell, Ekbal Hussain, David Bekaert and Romain Guilbaud. I would also like to thank all the PIs who helped out with feedback and advice during my PhD, especially Thomas Müller and Simon Poulton. Äs grosses Merci also to my family and my friends back home for all your understanding and support and all the jokes about British weather and food!

And finally, I would like to thank my husband Dominik. Doing a PhD can be stressful at times but knowing there is someone who has your back at all times makes everything so much easier. Without your support, this thesis would simply not exist.

Abstract

Amorphous silica is one of the most common phases to precipitate from geothermal fluids. It precipitates by self-assembly of monomeric silica (H_4SiO_4) via heterogeneous and homogeneous nucleation and subsequent growth of nuclei by addition of dissolved silica. The mechanism and the factors controlling the individual steps of silica precipitation have been studied in numerous laboratory experiments over the last decades and are, despite their complexity, well understood. However, due to the higher complexity of natural geothermal fluids (e.g high fluid flow rates, microbial activity or complex fluid chemistries), these findings cannot be directly applied to the study of silica scaling inside geothermal power plants and silica sinters around hot springs.

In the first part of this thesis we present the results from the first ever time-resolved study of silica precipitation inside in-use geothermal pipelines. Silica scales formed primarily via heterogeneous nucleation on steel surfaces, resulting in a silica layer rapidly covering these surfaces. This pathway of silica deposition was controlled by surface roughness, total silica concentration and temperature and allowed the deposition of up to 1 g of silica per day and m^2. Homogeneous nucleation also occurred and lead to the formation of silica microspheres which were deposited preferentially into depressions and along edges or were aggregated to fan- and ridge-shaped structures growing towards the flow, depending on the fluid flow regime. While the 3D structures could result in more turbulent flow, decreasing the flow rate, the formation of the silica layer could potentially even be beneficial for the operation of a geothermal power plant as it passivates the surface against corrosion.

For the second part of this thesis, we studied the interaction of a silica solution with a protein (= lysozyme), during which hybrid composites were formed. By investigating these final products in detail, we determined that, depending on the timing of the silica-lysozyme interactions (during or after silica polymerisation) and the ratio of silica-to-protein, the resulting composites showed different structures

and surface properties. This is of interest for biomineralisation as it elucidates how biomolecules interact with dissolved silica and how microorganisms can control this process.

List of Contents

List of Figures

List of Tables

List of Acronyms and Abbreviations

Ads	silica-lysozyme composites prepared by adsorption
AFM	atomic force microscope
APS	Advanced Photon Source
BET	Brunauer–Emmett–Teller
CNT	Classical Nucleation Theory
COA	cryogenic opal A
CoP	silica-lysozyme composites prepared by co-precipitation
DESY	Deutsches Elektronen-Synchrotron
DLCA	diffusion-limited colloid aggregation
DLS	dynamic light scattering
EDL	electric double layer
EDS	energy dispersive spectroscopy
EELS	electron energy loss spectroscopy
EMBL	European Molecular Biology Laboratory
EPS	exopolymeric substances
FIB	focused ion beam
FTIR	Fourier transform infrared spectroscopy
HAADF	high-angle annular dark field
HEXD	high-energy X-ray diffraction
IC	ion chromatography
ICP-OES	inductively coupled plasma optical emission spectroscopy
ICP-MS	inductively coupled plasma mass spectrometry
IEP	isoelectric point
IQR	interquartile range
LCPA	long-chain polyamines
LMIS	liquid metal ion source
LO	lift-out FIB technique

LOI	loss on ignition
mdn	median
MilliQ	ultrapure water (~18.2 MΩ cm)
OPA	non-precious opal
P235GH	high-resistance carbon steel grade
PAR	photosynthetically active radiation
PDB	protein database
PDF	pair distribution function
PHREEQC	geochemical modelling code
RLCA	reaction limited colloid aggregation
RSA	random sequential adsorption
S275	structural carbon steel grade
S316	stainless steel grade
SAXS	small-angle X-ray scattering
SDV	silica deposition vesicle
SI	saturation index
SSA	specific surface area
(FEG/CFE) SEM	(field emission gun/cold field emission) scanning electron microscopy
(HR) TEM	(high resolution) transmission electron microscopy
VG	volcanic glass
XRD	X-ray diffraction
XRF	X-ray fluorescence

Chapter 1

Introduction

This chapter gives a brief introduction to silica precipitation under geothermal conditions and sets out the aims and objectives of the thesis. In addition, the field and laboratory approaches as well as the layout of the thesis are briefly outlined.

1.1 Background

Geothermal systems (Figure 1.1) are defined as freely moving fluids which transport heat from a heat source in the Earth's crust (due to magmatic activity or the normal geothermal gradient of the Earth) to a heat sink, usually the Earth's surface (Dickson and Fanelli, 2013). Geothermal fluids are commonly meteoric waters which penetrate into the subsurface via structural features and are subsequently heated up. The dilute nature of the fluids and the increasing temperature result in interactions between the fluid and the surrounding rock, such as dilution of minerals. This leads to an enrichment of the fluid with dissolved components. As silicates are the dominant mineral group in the Earth's crust, geothermal fluids are commonly rich in dissolved SiO_2. The fluids can be pumped from an impermeable reservoir at depth for energy production or, if permeable structural features are present, they can surface naturally, and emerge as hot springs and geysers. When the geothermal fluids are cooled, the solubility of silica is reduced and the fluids become supersaturated with respect to amorphous silica. This leads to rapid precipitation. Inside geothermal power plants these deposits are called silica scales and around hot springs silica sinters.

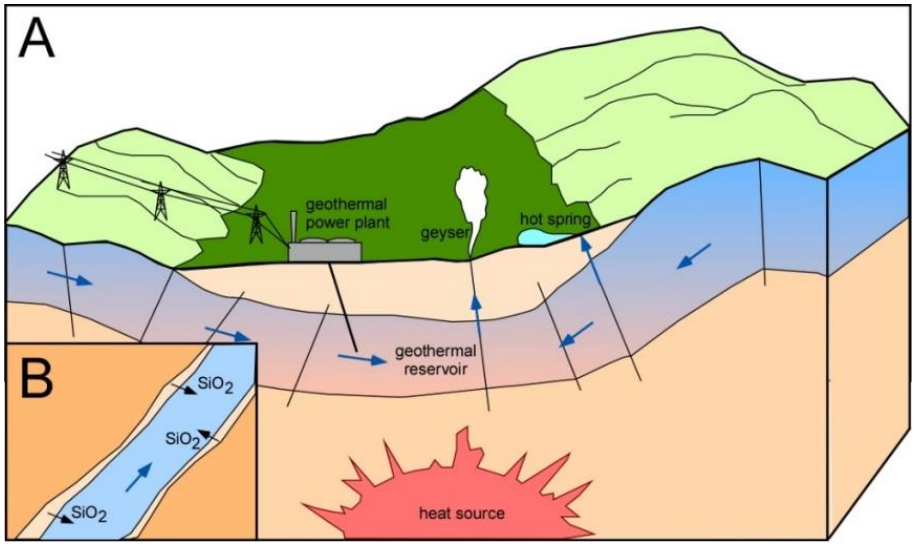

Figure 1.1: *Simplified schematic of a 'standard' geothermal system (modified after Dickson and Fanelli, 2013) showing (A) the heat source, reservoir and geothermal fluid which emerges naturally as hot springs or geysers or is pumped from the reservoir for the production of geothermal energy and (B) mineral dissolution in the reservoir which is responsible for high concentrations of silica (SiO_2) in the fluid.*

The silica precipitation is controlled by the self-assembly of dissolved silica, leading to an amorphous network of SiO_4^{4-} tetrahedra (Iler, 1979). The process can occur via homogeneous nucleation of particles in the fluid and/or heterogeneous nucleation on pre-existing surfaces (Benning and Waychunas, 2007). In either case, once the nuclei have formed they grow by the attachment of more dissolved silica. Silica particles in the fluid will eventually be aggregated and deposited. The thermodynamics and kinetics of the different steps of the silica self-assembly process have been investigated in a large number of laboratory studies over the last decades. A variety of parameters such as temperature, pH, silica concentration and salinity have been identified as factors controlling precipitation (Goto, 1956; Weres et al., 1981; Icopini et al., 2005; Tobler et al., 2009; Tobler and Benning, 2013). While advancing our understanding of how amorphous silica precipitates under specific conditions, the results from these laboratory studies cannot be directly applied to field settings due to the more complex nature of these systems such as the number of parameters controlling precipitation, the large fluid volumes and often high flow rates as well as the more complex fluid compositions (Carroll et al., 1998). Thus, detailed and time resolved experiments that follow the precipitation of silica inside

pipelines of geothermal power plants and in natural hot springs are needed to fill this gap in our knowledge base.

The study of silica scaling inside geothermal power plants is difficult as experiments can only be conducted in a way where they do not disrupt normal operations. This limits access to fluids or solids precipitated. To circumvent these problems, experiments conducted at geothermal power plants generally involve the use of a bypass systems (Rothbaum et al., 1979; Harrar et al., 1982; Carroll et al., 1998). However, the conditions inside the bypass are not identical to those inside of in-use geothermal pipelines due to the lower flow rates and the different hydrodynamic conditions (numerous valves and pipes with a smaller diameter). Depending on the design of the bypass, additional artefacts such as cooling or oxygenation of the fluid can also be introduced (Rothbaum et al., 1979). Thus, the precipitation pathways and/or rates determined from such studies are not necessarily representative of the behaviour of amorphous silica inside the actual geothermal pipelines. Furthermore, analysing fluids extracted from the geothermal pipelines for total silica concentration and silica speciation can be used to infer the polymerisation and precipitation of silica (Gunnarsson et al., 2010). However, the lack of solid materials to be studied limits the informative value of such studies. The ideal study of silica scaling in geothermal systems would be conducted inside the actual geothermal pipelines under conditions of normal operation and allowing access to both, fluid samples and the precipitated solids. However, no such precipitation study has been carried out yet despite the fact that this would be an important step on the way to quantifying the pathways of precipitation of amorphous silica inside geothermal power plants. Advancing our fundamental understanding of the process of silica scale formation is crucial in the development of a universally applicable mitigation approach for silica precipitation. Currently, a wide range of approaches to mitigate amorphous silica scaling, such as pH control, dilution with steam condensate, ageing of the fluid or the use of (in)organic inhibitors are currently in use in various geothermal power plants (Yanagase et al., 1970; Harrar et al., 1982; Henley, 1983; Gallup, 1998; Gallup, 2002; Demadis, 2005). To be able to evaluate how silica precipitation occurs inside geothermal power plants was the big challenge that constituted the main focus of my PhD thesis.

The second place where silica precipitation is important are hot springs emanating at the Earth surface. To study silica precipitation in such settings is generally easier than inside geothermal power plants. However, the often slow precipita-

tion rates and daily to seasonally variable physico-chemical conditions present their own challenges for the design and interpretation of field experiments. In addition, the formation of silica sinters is most often not a purely abiotic process as thermophilic microbes have been shown to strongly affect the precipitation of silica. The presence of microbial surfaces can even lead to sinter formation from fluids undersaturated with respect to amorphous silica (Tobler et al., 2008). While numerous studies have evaluated the nature of the microbial community, as well as the effect of microbes on sinter textures and growth rates and biosilicification (Phoenix et al., 2001; Mountain et al., 2003; Handley et al., 2005; Tobler et al., 2008) there is a lack of data on the molecular level interaction between silica and the functional groups of the bacterial cell walls. In order to study this interaction in more detail, laboratory studies involving silica and biomolecules (proteins, sugars, lipids) are needed. This was the second focus of my thesis.

1.2 Aims and Objectives

Based on the two research gaps identified above, understanding the mechanisms of silica scaling in geothermal power plants as well as the interactions between dissolved silica and biomolecules at the molecular scale, we defined the following aims and objectives for this thesis:

Aim 1: Identify the precipitation pathways of silica inside of in-use pipelines at an operational geothermal power plant (Hellisheiði power plant, Iceland).

> **Objective 1:** Identify if silica scaling is dominated by homogeneous nucleation of particles in the fluid and their subsequent deposition or heterogeneous nucleation on pipeline surfaces and quantify precipitation rates.
>
> **Objective 2:** Identify the physico-chemical parameters of the fluid and pipe surfaces which affect the precipitation mechanisms and rates of silica.
>
> **Objective 3:** Investigate the effect of silica scaling on corrosion and assess the passivation potential of silica deposits.

Aim 2: Determine how the presence of biomolecules enhances the precipitation of silica.

Objective 1: Test the effect of different biomolecules (proteins, sugars, lipids) on silica precipitation pathways and rates at different concentrations and temperatures.

Objective 2: Test how the speciation of silica (monomers vs. colloids) by adding the biomolecules during different steps in the precipitation reaction.

1.3 Experimental Approach

The experimental approach for the work presented in this thesis is briefly described here with the details of the individual methods given in the experimental sections and/or the supplementary information of each manuscript in Chapters 3 to 7. Methods which are not routinely used in the Earth Sciences (e.g., small angle X-ray scattering, pair distribution function analyses, or the determination of ζ-potential) are described in more detail in Appendices A and B.

1.3.1 Field-based approach

In order to address aim 1 ("Identify the precipitation pathways of silica inside an operational geothermal power plant") we devised a set of field experiments together with our collaborators at the Hellisheiði power plant, SW-Iceland (Figure 1.2 A & B). These field experiments involved the preparation and deployment of metal scaling plates inside in-use geothermal pipelines (Figure 1.2 C), in order to investigate silica scaling in the pipelines of the power plant during normal operation. The scaling plates were 2 to 2.5 cm wide, 5 cm long, 0.2 cm thick and made of S316 stainless steel (Figure 1.2 D). These were immersed in the geothermal fluid at several locations within the power plant (Figure 1.2 B). The points of immersion were in all cases after the steam had been separated and the pipelines only contained separated water that was supersaturated with respect to amorphous silica. The individual locations differed with respect to physico-chemical conditions such as temperature, flow rate and fluid composition, allowing us to assess the effect of these parameters on amorphous silica precipitation.

In the early stages of my PhD (summer 2013) we carried out an initial investigation of the silica scaling at Hellisheiði, by studying scaling plates prepared and deployed by the power plant operators Reykjavik Energy for 6-8 weeks. After retrieval, the plates were imaged using field emission gun scanning electron microscopy (FEG-SEM) and analysed using energy dispersive spectroscopy (EDS) and X-ray diffraction (XRD) to obtain information on microstructures and composition of the precipitates. This initial study, published in *Mineralogical Magazine* (Chapter 3), showed that the formation of silica scales at Hellisheiði was likely controlled by several competing factors whose relative importance could not be separated based on these initial data obtained. Thus, we decided to carry out a time-resolved scaling plate study where identical scaling plates were deployed at each location for time periods between 1 day and 10 weeks. As each scaling plate holder could hold two plates, we designed a second type of scaling plates which consisted of a S316 stainless steel scaling plate onto which coupons (2 to 2.5 cm wide, 1.3 cm long, 0.2 cm thick) made of volcanic glass, non-precious opal and S275 carbon steel were glued
(Figure 1-2 D & E). These coupons allowed us to study the effect of surface composition and roughness (polished *vs.* unpolished surfaces) on silica scaling.

The precipitates which accumulated during the deployments were analysed by the same methods used in the initial study (SEM, EDS, XRD). In addition, we investigated the internal structure of the precipitates by both scanning (SEM) and transmission electron microscopy (TEM) using small cross sections prepared by focused ion beam (FIB) sectioning (Appendix A) and profiles obtained by embedding the samples in epoxy resin and cutting them perpendicularly. We also monitored the fluid chemistry more closely, collecting samples at the beginning and the end of each deployment and also analysing filters for precipitates that formed in solution (XRD, SEM). The fluid samples were analysed by inductively coupled plasma optical emission spectroscopy (ICP-OES) for major cations, inductively coupled plasma mass spectrometry (ICP-MS) for minor cations, ion chromatography (IC) for anions and different titration approaches for dissolved gases (Arnórsson et al., 2006). Continuous measurements of temperature and fluid flow rates (reported hourly) were obtained from the power plant operators for the whole duration of our field deployments to assess if changes in power plant operation may have affected our scaling plate precipitation processes.

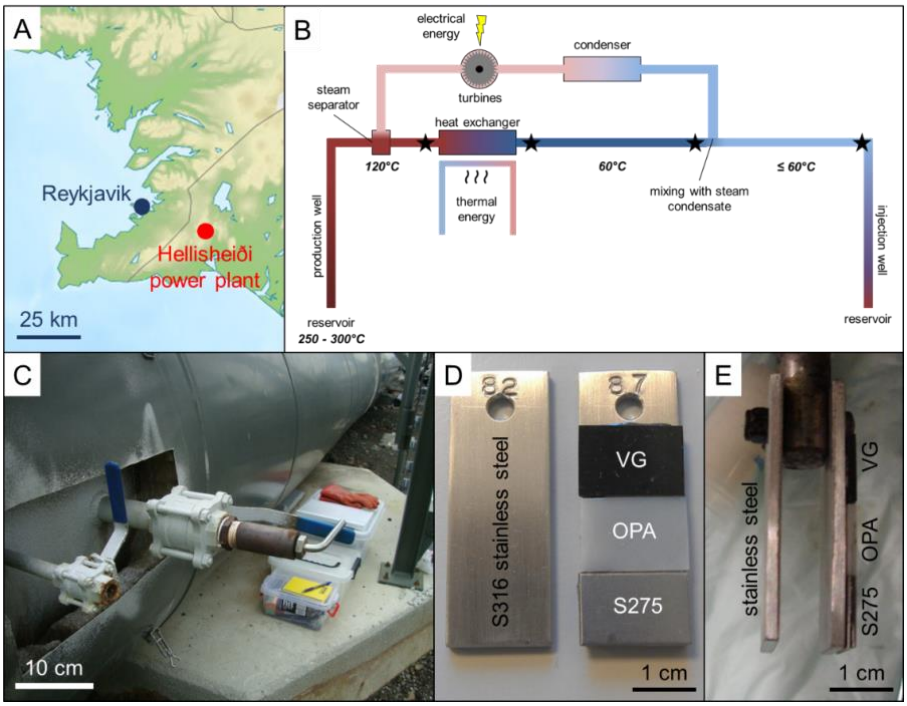

Figure 1.2: *Field studies were conducted at the Hellisheiði power plant. (A) Map of SW-Iceland showing the location of the Hellisheiði power plant, (B) system schematic indicating the points (*) where the scaling plates were immersed, (C) photograph of one of the sampling locations with the sampling rod inside (handle of rod indicated flow direction from left to right), (D) photograph of the two types of scaling plates used (left: stainless steel, right: stainless steel with coupons of volcanic glass, non-precious opal and S275 carbon steel glued on) and (E) photograph of samples attached to sampling rod before deployment.*

1.3.2 Laboratory-based approach

In order to study aim 2 ("Determine how the presence of biomolecules enhances the precipitation of silica") we synthesised and characterised silica-lysozyme composites. We chose the protein lysozyme for our study. Lysozyme is a small prolate ellipsoidal protein (3 x 4.5 nm) with a molecular mass of 14.3 kDa. It consists of 129 amino acids, including 6 lysine and 11 arginine residues exposed at the surface of the molecule (Canfield, 1963; Jollès et al., 1963). This gives the molecule an overall positive surface charge over a large pH range (pH_{IEP} = 11.1, Haynes and Norde, 1994) making electrostatic interactions with negatively charged silica species possible. Lysozyme has been used previously in the study of biomimetic silica composites

(Coradin et al., 2003) as its physicochemical properties are extremely well studied, which makes it an ideal model protein, and due to its overall similarity to silaffins.

Silaffins are a group of small proteins (4 to 17 kDa) characterized by an abundance of basic amino acids such as arginine and lysine. Together with long-chain polyamines (LCPA) and proteins of the cingulin and silicidin groups, they control silica precipitation inside diatoms and are believed to also control the characteristics of the resulting solid cell walls (Perry and Keeling-Tucker, 2000; Kröger and Poulsen, 2008).

Silica-lysozyme composites were produced in batch experiments performed at ambient conditions in the laboratory. A high-pH silica stock solution (1000 ppm) was prepared and precipitation induced by neutralising the solution by adding HCl. Variable amounts of lysozyme stock solution were diluted to obtain solutions ranging from 25 to 1000 ppm lysozyme. These were added to the silica stock solutions (a) immediately after neutralisation (co-precipitation experiments) or (b) after leaving the polymerising solution overnight (adsorption experiments). The final solutions were analysed by small-angle X-ray scattering (SAXS) for particle sizes (Appendix B) and for their surface charge by measuring their ζ-potential (Appendix B). To obtain solid samples, aliquots of the colloidal solution were dried. The atomic structure of the composites was determined using X-ray diffraction (XRD) and synchrotron-based total scattering, which was converted to a pair distribution function (PDF, Appendix B). The composites were analysed for their functional group make up by Fourier transform infrared spectroscopy (FTIR), while total carbon contents (= lysozyme content) were analysed by mass spectrometry. The structure of the composites at the nanoscale was investigated using transmission electron microscopy (TEM) and the location of lysozyme within the composites was identified by electron energy loss spectroscopy (EELS) mapping and energy dispersive spectroscopy (EDS). In addition, the specific surface areas (SSAs) of the composites were determined by nitrogen adsorption.

Initially, we had planned to repeat the synthesis of the silica-lysozyme composites at elevated temperatures using the geothermal simulator developed by Tobler and Benning (2013) in order to mimic conditions in hot springs. In addition, we wanted to also study the effect of a well-studied sugar (e.g., xantham gum) and a lipid (e.g., glycerol) on silica precipitation at ambient conditions and at elevated temperatures. However, after our first visit to Iceland in summer 2013, the focus of the project changed away from the silica-biomolecule interaction as we realised the great opportunities for a detailed field study at Hellisheiði power plant.

1.4 Structure of thesis

This thesis consists of three main sections: front materials, manuscripts and back materials. The front materials (Chapter 1) consist of a background section, the research objectives and a brief description of the experimental approach. This is then followed by the main body of the thesis: five manuscripts published or in preparation for peer-reviewed journals and a published but non-peer-reviewed conference proceeding:

Chapter 2: Precipitation of amorphous silica (SiO_2) from high enthalpy geothermal fluids – A review (in preparation for *Earth Science Reviews*).

> This chapter compiles and discusses the literature available on the precipitation of silica from geothermal systems. It starts by defining the term "amorphous silica" and describing the behaviour of silica in solution, i.e., solubility and speciation. The main body of the review deals with a discussion of the silica precipitation mechanism and rates as derived from laboratory experiments and in comparison with findings from studies in hot springs and geothermal power plants. The review also identifies areas of future research in the field of silica precipitation under geothermal conditions.

Chapter 3: Microstructural and chemical variation in silica-rich precipitates at the Hellisheiði geothermal power plant (published in *Mineralogical Magazine*)

> This paper reports the first ever description of silica scales from the Hellidheiði power plant. Silica was precipitated onto small metal scaling plates inserted into the flowing fluid at different locations within the power plant. The precipitates formed dominantly by homogeneous nucleation of particles in the fluid which then aggregated to form a variety of microtextures depending on the physico-chemical conditions (temperature, composition, flow rate etc.) of the fluid they formed from. However, exactly how and why particular physico-chemical conditions lead to the microstructures observed remained unclear.

Chapter 4: Two pathways of amorphous silica precipitation control scaling inside in-use geothermal pipelines (in preparation for *Geochimica et Cosmochimica Acta*).

> In order to better understand silica scaling at the Hellidheiði power plant, we did a time-resolved scaling plate study, involving more detailed monitoring of the physico-chemical conditions of the fluid. The results showed that silica was precipitated by two independent pathways: (1) heterogeneous nucleation and growth of an uneven, coherent silica layer and (2) homogeneous nucleation leading to the formation of particles, growth and aggregation. We also obtained the first ever silica scaling rates for the Hellidheiði power plant, showing that precipitation slowed down over time.

Chapter 5: Surface roughness and composition control silica deposition from geothermal fluids (ready for submission to *Geochemical Transactions*).

> Scaling plates with a volcanic glass, a non-precious opal and a S275 carbon steel coupons glued on were deployed to study the effect of surface properties on silica scaling. Heterogeneous nucleation was found to strongly depend on surface roughness while subsequent growth was independent of the surface characteristics. Homogeneous nucleation was not affected by the surface properties but particle deposition was enhanced by a high topographic relief.

Chapter 6: Passivation of metal surfaces against corrosion by silica scaling (published as *Proceedings, Workshop on Geothermal Reservoir Engineering Stanford University*).

> Silica scaling and concurrent corrosion of carbon steel by $H_2S_{(aq)}$ were investigated. It was found that corrosion was prevented or at least substantially reduced in locations where silica scaling occurred rapidly. This indicates that, when precise control of silica precipitation in geothermal systems becomes feasible, silica scaling could be used to passivate steel surfaces against corrosion.

Chapter 7: Formation of silica-lysozyme composites via co-precipitation and adsorption (accepted with major revisions in *Scientific Reports*).

> The characteristics of silica-protein (= lysozyme) composites were investigated at the nanometre-scale and the interactions between dissolved and colloidal silica and the lysozyme molecules were inferred. The results showed that the timing of the silica-lysozyme interactions and the ratio between the two components controlled the properties of the resulting composites. This indicates that there is a simple pathway for the synthesis of specific biomimetic silica-lysozyme composites.

The last part of this thesis is the back materials (Chapter 8) containing a synthesis discussion, an outline of work currently in progress and directions for future research of silica precipitation under geothermal conditions.

References

Arnórsson, S., Bjarnason, J.Ö., Giroud, N., Gunnarsson, I., Stefánsson, A., 2006. Sampling and analysis of geothermal fluids. *Geofluids* **6**, 203-216.

Benning, L.G., Waychunas, G.A., 2007. Nucleation, growth, and aggregation of mineral phases: Mechanisms and kinetic controls, *Kinetics of Water-Rock Interaction*. Springer, pp. 259-333.

Canfield, R.E., 1963. The amino acid sequence of egg white lysozyme. *Journal of Biological Chemistry* **238**, 2698-2707.

Carroll, S., Mroczek, E., Alai, M., Ebert, M., 1998. Amorphous silica precipitation (60 to 120 C): Comparison of laboratory and field rates. *Geochimica et Cosmochimica Acta* **62**, 1379-1396.

Coradin, T., Coupé, A., Livage, J., 2003. Interactions of bovine serum albumin and lysozyme with sodium silicate solutions. *Colloids and Surfaces B: Biointerfaces* **29**, 189-196.

Demadis, K.D., 2005. A structure/function study of polyaminoamide dendrimers as silica scale growth inhibitors. *Journal of Chemical Technology and Biotechnology* **80**, 630-640.

Dickson, M.H., Fanelli, M., 2013. *Geothermal energy: utilization and technology*. Routledge, London.

Gallup, D.L., 1998. Aluminum silicate scale formation and inhibition (II): scale solubilities and laboratory and field inhibition tests. *Geothermics* **27**, 485-501.

Gallup, D.L., 2002. Investigations of organic inhibitors for silica scale control in geothermal brines. *Geothermics* **31**, 415-430.

Goto, K., 1956. Precipitation of silica in the presence of aluminum. *Bulletin of the Chemical Society of Japan* **29**, 740-741.

Gunnarsson, I., Ívarsson, G., Sigfússon, B., Thrastarson, E.Ö., Gíslason, G., 2010. *Reducing silica deposition potential in waste waters from Nesjavellir and Hellisheiði Power Plants*, Iceland, Proceedings World Geothermal Congress Bali.

Handley, K., Campbell, K., Mountain, B., Browne, P., 2005. Abiotic–biotic controls on the origin and development of spicular sinter: *in-situ* growth experiments, Champagne Pool, Waiotapu, New Zealand. *Geobiology* **3**, 93-114.

Harrar, J., Locke, F., Otto Jr, C., Lorensen, L., Monaco, S., Frey, W., 1982. Field tests of organic additives for scale control at the Salton Sea geothermal field. *Society of Petroleum Engineers Journal* **22**, 17-27.

Haynes, C.A., Norde, W., 1994. Globular proteins at solid/liquid interfaces. *Colloids and Surfaces B: Biointerfaces* **2**, 517-566.

Henley, R., 1983. pH and silica scaling control in geothermal field development. *Geothermics* **12**, 307-321.

Icopini, G.A., Brantley, S.L., Heaney, P.J., 2005. Kinetics of silica oligomerization and nanocolloid formation as a function of pH and ionic strength at 25 C. *Geochimica et Cosmochimica Acta* **69**, 293-303.

Iler, R.K., 1979. *The chemistry of silica: solubility, polymerization, colloid and surface properties, and biochemistry*. Wiley, London.

Jollès, J., Jauregui-Adell, J., Bernier, I., Jollès, P., 1963. La structure chimique du lysozyme de blanc d'oeuf de poule: étude détaillée. *Biochimica et Biophysica Acta* **78**, 668-689.

Kröger, N., Poulsen, N., 2008. Diatoms-from cell wall biogenesis to nanotechnology. *Annual Review of Genetics* **42**, 83-107.

Mountain, B., Benning, L., Boerema, J., 2003. Experimental studies on New Zealand hot spring sinters: rates of growth and textural development. *Canadian Journal of Earth Sciences* **40**, 1643-1667.

Perry, C.C., Keeling-Tucker, T., 2000. Biosilicification: the role of the organic matrix in structure control. *JBIC Journal of Biological Inorganic Chemistry* **5**, 537-550.

Phoenix, V., Konhauser, K., Adams, D., Bottrell, S., 2001. Role of biomineralization as an ultraviolet shield: Implications for Archean life. *Geology* **29**, 823-826.

Rothbaum, H., Anderton, B., Harrison, R., Rohde, A., Slatter, A., 1979. Effect of silica polymerisation and pH on geothermal scaling. *Geothermics* **8**, 1-20.

Tobler, D.J., Benning, L.G., 2013. *In-situ* and time resolved nucleation and growth of silica nanoparticles forming under simulated geothermal conditions. *Geochimica et Cosmochimica Acta* **114**, 156-168.

Tobler, D.J., Shaw, S., Benning, L.G., 2009. Quantification of initial steps of nucleation and growth of silica nanoparticles: An *in-situ* SAXS and DLS study. *Geochimica et Cosmochimica Acta* **73**, 5377-5393.

Tobler, D.J., Stefansson, A., Benning, L.G., 2008. *In-situ* grown silica sinters in Icelandic geothermal areas. *Geobiology* **6**, 481-502.

Weres, O., Yee, A., Tsao, L., 1981. Kinetics of silica polymerization. *Journal of Colloid and Interface Science* **84**, 379-402.

Yanagase, T., Suginohara, Y., Yanagase, K., 1970. The properties of scales and methods to prevent them. *Geothermics* **2**, 1619-1623.

Chapter 2

Precipitation of amorphous silica (SiO_2) from high enthalpy geothermal fluids – A review

Daniela B. van den Heuvel[1], Dominique J. Tobler[2],
Ingvi Gunnarsson[3], Liane G. Benning[1,4]

[1] *Cohen Geochemistry Group, School of Earth and Environment, University of Leeds, Leeds LS2 9JT, UK*
[2] *Nano –Science Center, Departmernt of Chemistry, University of Copenhagen, Copenhagen 2100, Denmark*
[3] *Reykjavik Energy, Baejarhals 1, 110 Reykjavik, Iceland*
[4] *German Research Center for Geosciences, GFZ, 14473 Potsdam, Germany*

Abstract

Dissolved silica (SiO_2) is one of the most abundant phases in geothermal fluids. Upon rapid cooling at the Earth's surface, the fluids become supersaturated with respect to silica and an amorphous, highly hydrated silica phase is precipitated. Around hot springs these deposits are called silica sinters while inside geothermal power plants they are described as silica scales.

The precipitation process of silica involves polymerisation of monomeric silica (H_4SiO_4) to form dimers and linear and cyclic oligomers. This self-assembly process can occur in the fluid (homogeneous nucleation), resulting in silica particles which eventually aggregate, or on a surface (heterogeneous nucleation), resulting in a dense layer coating the surface. The physico-chemical parameters of the fluid (e.g., total silica concentration, temperature, pH, and hydrodynamics), silica speciation

and the properties of available surfaces (e.g., microbes) are controlling the rate of silica precipitation as shown by laboratory experiments. In addition, many of these physical, chemical or biological factors also affect the precipitation of silica from natural geothermal fluids both in hot spring or power plant settings as identified from a plethora of field studies. However, in natural geothermal fluids all these parameters are in competition with one another and it is thus not possible to apply findings from laboratory studies to field settings directly. Based on this comparison between laboratory- and field-based studies we identified a range of ideally interdisciplinary research needed to help progress the field of amorphous silica precipitation from geothermal fluids in the future.

2.1 Introduction – What is amorphous silica?

Silicon dioxide (SiO_2) is the most common component in the silicate earth, accounting for over 45 wt.% of it. Silicon dioxide is present in almost every environment and can occur as a wide range of polymorphs which are stable under virtually all physico-chemical conditions (Sosman, 1965; Iler, 1979; Heaney, 1994; Swamy et al., 1994). SiO_2 polymorphs span both crystalline and amorphous phases and, together with dissolved SiO_2, are referred to as silica (Iler, 1979). The basic building block of most silica phases is a central silicon atom which is surrounded by four oxygen atoms in tetrahedral coordination (Figure 2.1 A). Each SiO_4^{4-} tetrahedron shares one or several of its oxygens with a neighbouring tetrahedra to form a 3D framework. In crystalline varieties of silica (e.g., quartz), this framework is characterised by a regular packing of SiO_4^{4-} tetrahedra (Figure 2.1 B) according to the crystal structure of the phase. In amorphous silica phases there is no structure to the organisation of the individual SiO_4^{4-} tetrahedra, resulting in a non-periodic and therefore non-crystalline phase (Figure 2.1 C). Due to the random structure, not every oxygen is used as a bridging oxygen so that the individual silicon atoms retain a variable number of hydroxyl groups (Perry and Keeling-Tucker, 2000). In addition, adsorbed or interstitial water is also present. However, water-free amorphous silica also exists. This type of vitreous silica forms if melts are cooled very rapidly, i.e., in volcanic processes or, rarely, from impact melts or melts formed during lightning strikes (Rogers, 1946; Glass, 1984). As these forms of amorphous silica are outside the scope of this review, the term amorphous silica is hereafter used to mean hydrated, amorphous silica that formed from aqueous solutions only.

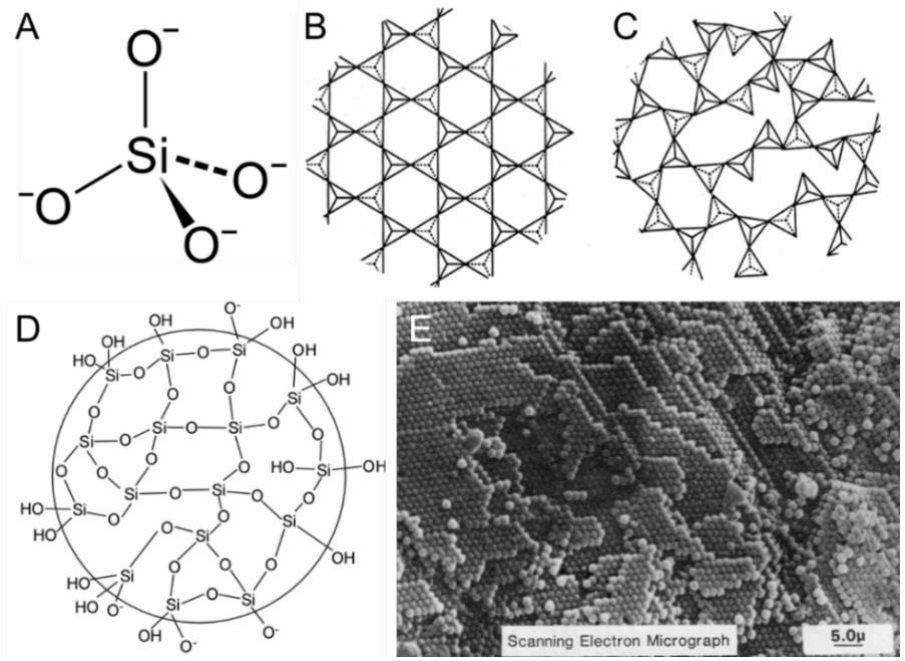

Figure 2.1: *The structure of silica: (A) SiO_4^{4-} tetrahedron, the basic building block of most silica polymorphs, 2D structures of (B) crystalline silica (α-quartz) with regular packing of SiO_4^{4-} tetrahedra and (C) amorphous silica with random packing (modified after Bergna and Roberts, 2005), (D) schematic illustration of an hydrated amorphous silica particle (modified after Perry and Keeling-Tucker, 2000) and (E) regular packing of monodispersed silica spheres in precious opal (from Sanders, 1985).*

Amorphous silica as defined above can precipitate from silica-rich aqueous solutions in a wide variety of natural environments. Once saturation with respect to amorphous silica is reached, polymerization leads to the formation of small spherical particles (Figure 2.1 D). Eventually the particles aggregate to form laterally extensive 3D structures. These aggregates made up of colloidal particles are described as opaline silica (Figure 2.1 E). Two types of amorphous opaline silica are known (Flörke, 1991; Graetsch, 1994): opal A_N (amorphous, network-like) and opal A_G (amorphous, gel-like). Opal A_N exhibits a glassy structure but is hydrated unlike the glasses mentioned previously (interstitial water and silanol groups). This type of opaline silica forms by rapid quenching of silica-rich vapour and/or waters in volcanic fields, resulting in crusts or fillings in vesicles (Flörke et al., 1973). Opal A_G can be described as a gel-like aggregate of spherical silica particles with diameters of 150 to 400 nm (Sanders, 1964). If the spheres are monodisperse and exhibit regular cubic, hexagonal or mixed closest packing (Figure 2.1 E), the structure of the phase gives rise to diffraction of light (yet no diffraction of X-rays), resulting in the magnif-

icent colours that are so well known for precious opal. These SiO_2 phases (sometimes erroneously called 'minerals') contain 3 to 18 wt.% water in the form of H_2O molecules trapped inside the silica network, as interstitial water and internal and surficial silanol groups (Segnit et al., 1965; Langer and Flörke, 1974; Aines and Rossman, 1984; Graetsch, 1994; Herdianita et al., 2000; Jones and Renaut, 2004). The high water content together with the low porosities in precious opals indicate that the individual spheres in turn are made up of densely packed smaller particles around 10 to 20 nm in size (Jones and Segnit, 1969). If the spheres making up the opal A_G are polydisperse and are more randomly oriented, the phase lacks play of colour and is opalescent. This is called potch or common opal. This non-precious opal A_G is by far the most common type of amorphous silica in natural systems. Thus the term "amorphous silica" will be used to exclusively describe this polymorph as defined by Flörke (1991) in the rest of this review.

2.2 Silica in geothermal systems

One of the most common ways of abiotically precipitating amorphous silica is from the cooling of geothermal fluids. Geothermal systems are defined as "convecting water in the upper crust of the Earth, which, in a confined space, transfers heat from a heat source to a heat sink, usually the free surface" (Hochstein, 1990). Thus any 'standard' geothermal system consists of the following three components (Figure 2.2 A): a heat source (owing to magmatic activity or the normal geothermal gradient of the Earth), a volume of permeable host rock acting as a natural heat exchanger (= reservoir) and a fluid which acts as a heat carrier (= geothermal fluid). The fluids are commonly meteoric waters which penetrate into the reservoirs via faults and cracks and are subsequently heated up. The dilute nature of the fluids and the increasing temperature result in interactions between the fluid and the surrounding rock, such as dissolution of minerals, leading to an enrichment of the fluid with dissolved components (Figure 2.2 B). As silicates are the dominant mineral group in the Earth's crust, many geothermal fluids become rich in dissolved silica. The maximum concentration of aqueous silica in a geothermal fluid depends on the reservoir temperature and is controlled by the *in-situ* quartz solubility or, if the temperature is below 110 °C, by the solubility of chalcedony (Fournier and Rowe, 1966; Arnórsson, 1975). As amorphous silica has a higher solubility than all

crystalline silica phases (Figure 2.3 A), the fluid is undersaturated with respect to amorphous silica under reservoir conditions.

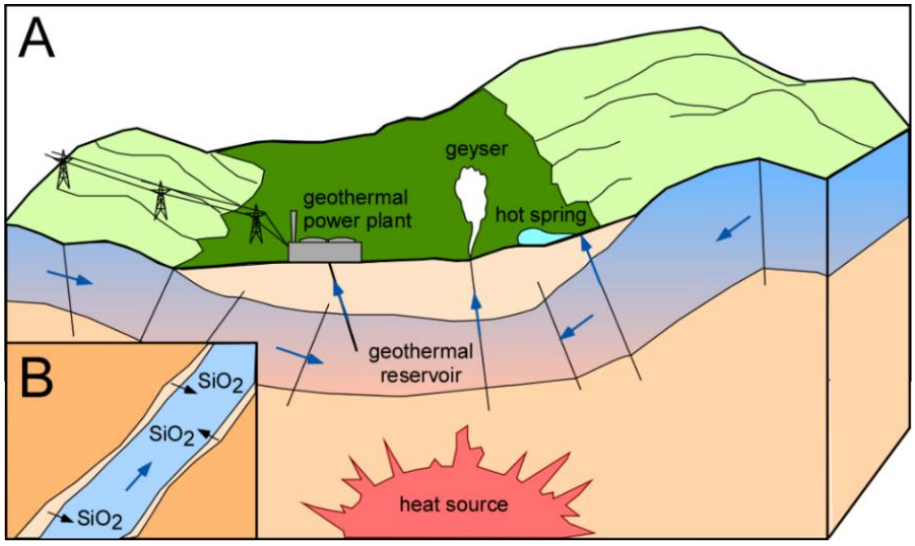

Figure 2.2: *Simplified schematic of a 'standard' geothermal system (modified after Dickson and Fanelli, 2013) showing (A) the heat source, reservoir and geothermal fluid which emerges naturally as hot springs or geysers or is pumped from the reservoir for the production of geothermal energy and (B) mineral dissolution in the reservoir which is responsible for high concentrations of silica (SiO_2) in the fluid.*

Geothermal fluids can reach the surface naturally, i.e., by ascending along fractures, where they emerge as hot springs and geysers or by being pumped from a hot reservoir for the production of geothermal energy (Figure 2.2 A). In both situations, geothermal fluids are cooled during ascent and when reaching the surface (in a hot spring or inside a pipe of a geothermal power plant) they are often supersaturated with respect to quartz and chalcedony. However, due to the slow precipitation kinetics of all crystalline SiO_2 phases (Iler, 1979; Sjöberg, 1996) precipitation of these phases does not occur, and the fluid has to cool further until it becomes supersaturated with respect to amorphous silica which then precipitates rapidly.

2.2.1 Solubility of amorphous silica

The solubility of amorphous silica is controlled by temperature, pressure, pH and the presence of other chemical species. The effect of temperature on silica solubility was studied experimentally by Gunnarsson and Arnórsson (2000), who showed a

non-linear increase of the solubility with increasing temperature from around 100 ppm at ambient temperatures to 1500 ppm or more at 350 °C (Figure 2.3). Furthermore, in acidic to neutral pH, the solubility is low (100 to 200 ppm), while above pH 9 the solubility increases rapidly to more than 1000 ppm due to the formation of the silicate ion $H_3SiO_4^-$ (Figure 2.3) (Alexander, 1954; Goto, 1956; Iler, 1979). Increasing pressure also leads to a slightly higher solubility of silica, yet the effect is small (Willey, 1974; Fournier and Rowe, 1977; Fournier, 1985). In contrast, an increase of ionic strength (e.g., in brines) leads to a decrease in amorphous silica solubility (Weres et al., 1981; Chen and Marshall, 1982; Fournier and Marshall, 1983) due to the "salting out" effect, i.e., a relative increase in concentration of silica due to water molecules being used in the hydration shells of cations. Chen and Marshall (1982) could show that this effect was strongest for iron, aluminium and manganese due to their high hydration numbers.

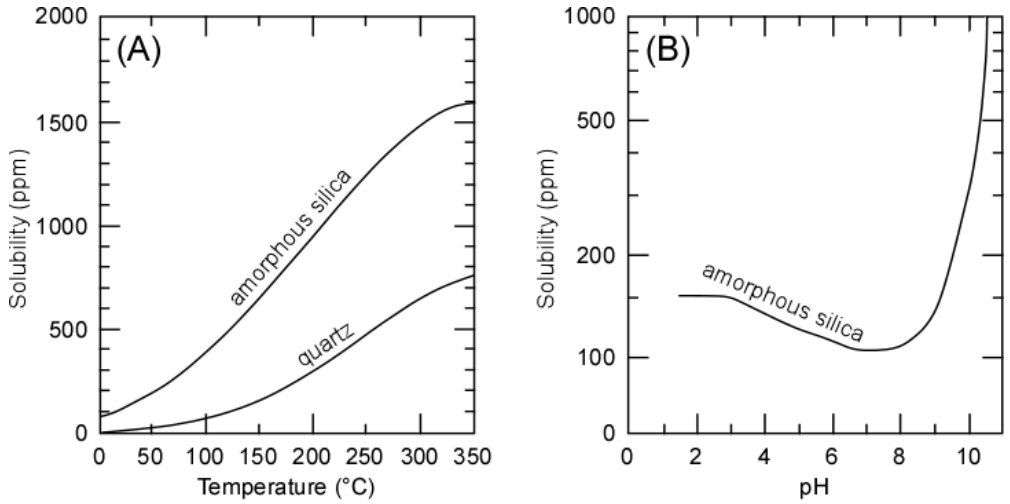

Figure 2.3: *Solubility of silica as a function of (A) temperature (modified after Gunnarsson and Arnórsson, 2000) and (B) pH at 25 °C (modified after Iler, 1979).*

2.2.2 Silica speciation

The total concentration of dissolved silica in geothermal fluids is made up of a range of species. In a fluid undersaturated with respect to amorphous silica, the dominant component is monomeric silica (H_4SiO_4) (Rothbaum and Rohde, 1979; Zotov and Keppler, 2002). Monomeric silica is characterised by a central silicon ion tetrahedrally coordinated by four OH-groups. Each OH-group is surrounded by two water molecules which attach via hydrogen bonding. It is a weak acid with a $K_a = 10^{-9.8}$ at

25 °C which increases to $K_a \sim 10^{-8.8}$ at 120 °C (Fleming and Crerar, 1982). Thus in geothermal systems, which generally show slightly alkaline pH values, deprotonated silica monomers ($H_3SiO_4^-$) are abundant. The term "monomeric silica" is often used to describe silica analysed by one of the molybdosilicate methods (Eaton et al., 2005). The method is based on the ability of silica monomers to form a cage-like silicomolybdic acid in the presence of ammonium heptamolybdate. Thus, in theory, the molybdosilicate methods will only analyse monomeric silica. However, several studies have shown that small oligomers can dissolve during the analyses and are thus also analysed by the molybdosilicate methods (Iler, 1979; Tanakaa and Takahashib, 2001; Coradin et al., 2004). Many studies get around this issue by using the term "molybdate-reactive silica". While correctly describing the results obtained by the molybdosilicate methods, this term groups together different silica species which potentially show different behaviour during polymerisation and deposition (see below), reducing the usefulness of the determination of "molybdate-reactive silica". Nevertheless, this is the usual and preferred method of choice for many industrial or academic analytical laboratories that analyse geothermal fluids.

Besides monomeric silica, small oligomers (dimers, trimers, tetramers, etc.) also occur in geothermal fluids. Rothbaum and Rhode (1979) found that, between 30 and 120 °C, the proportion of dimers decreased from 7 to 3.5%, while that of trimers varied between 1 and 0.1% and heavier oligomers were less than 0.3% at all temperatures. The identity of the oligomers changes as a function of silica concentrations, pH and salt content. Higher concentrations of silica result in larger, cage-like oligomers while highly alkaline pH reduced the size of the silica species to dimers and trimers (Svensson et al., 1986). Pressure also favoured the formation of oligomers (Zotov and Keppler, 2002).

Once a geothermal fluid reaches saturation with respect to amorphous silica, self-assembly of silica starts. The polymerisation reaction involves the condensation of silanol groups to form Si-O-Si bonds and therefore produces silica species with an increasing number of monomer units and size (Iler, 1979; Perry and Keeling-Tucker, 2000). Thus, fluids in which silica polymerises contain a mix of monomers but also a number of larger species, i.e., polymers. The self-assembly process seems to be very rapid and has been investigated experimentally (Iler, 1979; Harrison and Loton, 1995; Icopini et al., 2005) and through molecular simulation approaches (Bhattacharya and Kieffer, 2008; Schaffer and Thomson, 2008; Malani et al., 2010; Zhang et al., 2011; McIntosh, 2013; Noguera et al., 2015). These studies indicate that

overall, in the initial stages of silica self-assembly the dominant polymers are dimers followed by linear and circular oligomers (tetramers to heptamers). Linear oligomers were found to be more common around neutral pH while alkaline pH conditions favoured the formation of circular oligomers (Zhang et al., 2011), similarly to non-polymerising solutions.

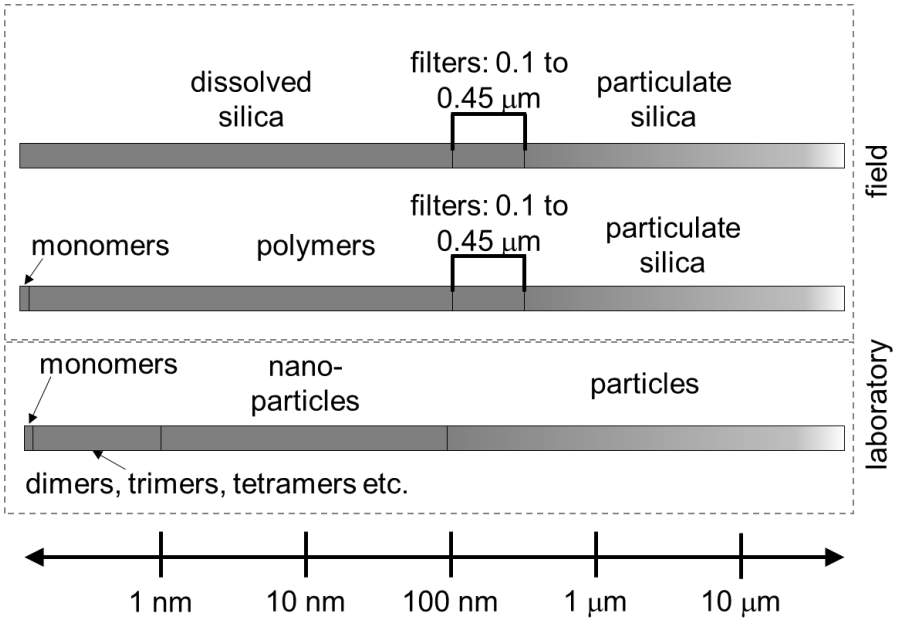

Figure 2.4: *Difference in definitions of silica species in laboratory and field experiments.*

The oligomers grow further by addition of monomers or coalescence of oligomers, resulting in larger (several tens of monomer units), often roughly spherical clusters. According to Iler (1979) the clusters consist of a mostly anhydrous core and a hydrated outer shell of SiOH groups. Depending on the physico-chemical conditions of the polymerising fluid (e.g., pH, temperature, silica concentration, ionic strength) the size of any SiO_2 particles formed can vary from one nanometre up to 25 μm (Goto, 1956; Iler, 1979; Icopini et al., 2005; Tobler et al., 2009; Tobler and Benning, 2013; Kley et al., 2014; van den Heuvel et al., in prep.b (Chapter 4)). The line between "polymers" and "particulate silica" is very difficult to draw as it depends on the type of study conducted. For researchers looking at high-resolution laboratory studies, "particulate silica" is anything that can be identified as solid object by scattering or electron imaging techniques, thus anything larger than a few nanometres (Figure 2.4). These particles contain a few hundreds to 1000 monomer units (Iler, 1979). Therefore, anything below this size but larger than silica mono-

mers is considered to be an oligomer or polymer (Figure 2.4). In field studies on the other hand, the term "particulate silica" is usually only used for silica species large enough to be removed by filtration. The most commonly used filter membranes have pore sizes of 0.1 to 0.45 μm, thus retaining only particles larger than 100 to 450 nm (Figure 2.4). Any silica species passing through the filter membranes are described as "dissolved silica" or, if monomeric silica is also determined and subtracted from the dissolved silica, as "polymeric silica" (Figure 2.4). This means that, in such studies, polymers range from dimers to entities containing up to 10^7 monomer units (Iler, 1979).

2.3 Precipitation mechanism and rates

Upon reaching amorphous silica solubility in a geothermal fluid, rapid precipitation takes place. Around hot springs these deposits are called silica sinters, around geysers they are referred to as geyserites and inside high-enthalpy geothermal power plants they are termed silica scales. Both hot springs and geothermal power plants are ideal study sites for detailed research into silica precipitation as the processes are occurring at the Earth's surface, the precipitates are fresh (no need to account for aging) and, in the case of geothermal power plants, take place under well-monitored physico-chemical conditions.

2.3.1 Nucleation, growth and aggregation – theoretical background

Thermodynamically, the formation of a solid phase from a supersaturated solution is due to a reduction of the Gibbs free energy of the system. There are two pathways for nucleation, homogeneous and heterogeneous nucleation. Homogeneous nucleation is the spontaneous and surface-independent formation of a solid phase in solution. Heterogeneous nucleation on the other hand describes the nucleation of a new phase on a previously existing surface. In order to form a nucleus, the supersaturated phase needs to self-assemble into clusters that will have a short lifespan and are usually re-dissolved again until they reach a certain critical size after which spontaneous growth sets in. According to the Classical Nucleation Theory (CNT) (e.g. Volmer and Weber, 1925; Farkas, 1927; Becker and Döring, 1935) the radius of the critical nucleus r^* in the case of homogeneous nucleation can be expressed as

$$r^*_{homo} = \frac{-2\sigma}{\Delta g} \tag{2.1}$$

and the free energy of the formation of the critical homogeneous nucleus ΔG* as

$$\Delta G^*_{homo} = \frac{16\pi\sigma^3}{3\,\Delta g^2} \tag{2.2}$$

where σ is the surface energy per unit area and Δg is the change in Gibbs free energy per unit volume of solid phase that has to be overcome. The critical radius as well as the critical energy depend on how fast the Gibbs free energy of the system is lowered due to cluster formation (volume term) and how fast the surface energy is increased due to solid-liquid interface reactions (surface term). Thus, the degree of oversaturation, temperature, the type of solvent and/or impurities in the system can all affect the size of a critical nucleus.

For the case of a heterogeneous nucleation (Benning and Waychunas, 2007) at a solid-liquid interface, the critical size and critical energy for the formation of a nuclei can be calculated according to:

$$r^*_{hetero} = -2\sigma_{SL}(\sin\theta)\Delta g \tag{2.3}$$

and

$$\Delta G^*_{hetero} = \frac{\Delta G_{homo}(2 - 3\cos\theta + \cos^3\theta)}{2} \tag{2-4}$$

where θ is the included angle of the nucleus edge as controlled by surface tension, σ_{SL} the interfacial energies for the nucleus-liquid and Δg the free energy change per unit volume of solid phase. As heterogeneous nucleation reduces the solid-liquid interface energy (and thus the surface term), it lowers the overall Gibbs free energy of the system more that homogeneous nucleation as is thus energetically favourable.

Classical growth theories assume an atom-by-atom or molecule-by-molecule attachment to a growing surface. There are several commonly used growth models: the Frank-van der Merwe model (Frank and Van der Merwe, 1949) assuming layer by layer growth, i.e., one layer is finished before the next one starts, the Volmer-Weber model (Volmer and Weber, 1925) in which the formation of islands precedes the formation of layers and the Stranski-Krastonov growth (Stranski and Krastanow, 1937), where growth sets off in layer-by-layer mode but shifts to an island mode later on. The growth rate of a nucleus depends on two steps: (1) the diffusion of the growth species to a surface and subsequent adsorption and (2) the incorporation of the growth species into the growing structure. If the first step is rate-limiting, diffusion controlled growth occurs. This happens in systems where large

concentrational gradients of the growth species between the solution and the particle surface exist or in viscous liquids. If the second step is slower, i.e., in solutions where the growth species is readily available at the particle surface growth is usually controlled by interfacial processes.

Once a particle is formed it can grow and aggregate. The aggregation process is dependent on overcoming the repulsive forces between individual particles (electrostatic, hydrophobic, van der Waals etc.) allowing them to stick together (Klein and Meakin, 1989; Lin et al., 1990). For particles with a sticking probability of 1 (= every collision leads to aggregation), the rate of aggregation only depends on the diffusion of particles. This process is called diffusion-limited colloid aggregation (DLCA) and rapidly produces relatively loose aggregates. If the sticking probability is < 1, the aggregation is described as reaction limited colloid aggregation (RLCA). Overall, RLCA processes are much slower than DLCA and result in the formation of much denser aggregates

2.3.2 Laboratory-based silica precipitation studies and simulations

As predicted by thermodynamics, upon reaching supersaturation with respect to amorphous silica, amorphous silica starts precipitating. The formation of amorphous silica occurs via the condensation of silica monomers (H_4SiO_4), also described as polymerisation. The mechanism can be described by bimolecular collisions of ionised and non-ionised molecules of monomeric silica and is catalysed by OH^- ions (Iler, 1979). *Ab initio* modelling by McIntosh (2013) showed that the transition states and thus the pathway of the condensation depend on the ionisation states of the individual molecules as some of the interactions are energetically favourable while others occur more rapidly. As the silica polymers grow in size, they become more negatively charged as the value of the dissociation constants determined under given physico-chemical conditions increase compared to the monomer (Iler, 1979 and references therein). The negative surface charge of large silica species (= polymers, (nano)particles and surfaces) means that they repel each other and are not likely to self-assemble. Monomers on the other hand will attach more readily due to their neutral charge. Furthermore, the possibility of interaction between the silanol groups of the monomers with the deprotonated silanol groups of the surface/particle promotes polymerisation (Bohlmann et al., 1976; Mroczek and McDowell, 1988; Bremere et al., 2000). However, geothermal waters always contain

certain amounts of multivalent cations (especially Ca, Fe, Al) which can act as flocculants, bridging the electrostatic repulsion between two negatively charged silica species. Thus, growth of polymers takes place primarily by addition of monomers at low ionic strength and is dominated by aggregation of individual polymers or particles at higher concentrations of salt (Figure 2.5 A; Iler, 1979).

The complexity of the polymerisation process of silica and its dependence on speciation possibly explains why there is a disagreement in literature over the kinetics of the process (reviewed by Tobler et al., 2009). The kinetic models were derived from the decrease of monomeric silica in polymerising solutions over time and gave reaction orders between 1 and 8. According to Tobler et al. (2009), this could indicate that the mechanism of silica polymerisation is depending on the physico-chemical conditions of the solution and cannot be described by a single kinetic model. Nevertheless, all studies agree that changing physico-chemical conditions affect the rate of silica polymerisation. An increase in solution pH has been shown to increase the rate of polymerisation, especially above pH 7 (Alexander, 1954; Goto, 1956; Iler, 1979; Weres et al., 1981; Gunnarsson and Arnórsson, 2005; Icopini et al., 2005). However, this positive effect is reduced in alkaline solution (pH > 9) because the higher solubility of silica at high pH counteracts the increasing polymerisation rates (Weres et al., 1981; Fleming, 1986). The degree of silica supersaturation of the solution also positively correlates with the rate of polymerisation (Weres et al., 1981; Gunnarsson and Arnórsson, 2005; Icopini et al., 2005; Tobler et al., 2009). The ionic strength of a solution, i.e., the salt content also affects the polymerisation rate (Crerar et al., 1981; Weres et al., 1981; Fleming, 1986; Gunnarsson and Arnórsson, 2005; Icopini et al., 2005). Batch experiments showed that the polymerisation of silica was accelerated at pH ≥ 9 in the presence of aluminium while in the pH range of 5 to 8 the presence of aluminium slowed polymerisation down (Yokoyama et al., 1991; Gallup, 1997). Iron on the other hand strongly accelerated the polymerisation of silica across the entire pH range due to its strong affinity for silica (Gallup, 1989). The effect of temperature on polymerisation has so far not been well constrained. Some authors found a fairly pronounced temperature effect (Alexander, 1954; Kitahara, 1960; Gunnarsson and Arnórsson, 2003) while Rothbaum and Rhode (1979) and Makrides et al. (1980) found that temperature had only very little effect on the polymerisation rate up to 105 °C. The apparent independence of reaction rate on temperature could potentially be attributed to the higher solubility of silica at higher temperatures which counteracts the faster polymerisation (Makrides et al.,

1980). Tobler and Benning (2013) could show that the polymerisation rate was increased when precipitation was induced by neutralisation of a high pH solution compared to fast cooling.

Before any silica polymers reach a critical nucleus size, they have a short lifespan and will rapidly re-dissolve (Iler, 1979; Tobler et al., 2009; Noguera et al., 2015). For amorphous silica it has been shown that the critical size can very between 0.5 and 2 nm (Iler, 1979; Icopini et al., 2005; Tobler et al., 2009; Noguera et al., 2015). Once this size is reached, the nuclei will grow spontaneously by addition of dissolved silica from the fluid and this is assumed to be governed by layer-by-layer attachment of monomers and potentially oligomers to the particle surface in three dimensions. (Matsoukas and Gulari, 1988). The process is controlled by the surface processes, i.e., not diffusion limited, and follows a first order kinetic rate law (Bohlmann et al., 1980; Fleming, 1986; Tobler et al., 2009). If the nuclei formed by homogeneous nucleation in the fluid, growth will result in the formation of silica particles (Tobler et al., 2009; Tobler and Benning, 2013) while if the nuclei formed via heterogeneous nucleation, the resulting silica precipitate will most likely result in a more continuous silica layer (Bohlmann et al., 1980).

The nucleation and growth process will take place until the solubility with respect to amorphous silica is reached. The final size of silica nanoparticles (Figure 2.4) formed by homogeneous nucleation and subsequent growth at ambient conditions is in the range of 5 to 10 nm (Tobler et al., 2009; Tobler and Benning, 2013). At elevated temperatures, alkaline pH, low ionic strength and constant addition of dissolved silica, the conditions as encountered in some geothermal systems, particles can grow larger (> 100 nm) due to a naturally occurring “buildup process” (Morris and Vossos, 1970). However, if the ionic strength is higher or there are flocculating agents present, particle growth is interrupted by premature aggregation of silica particles (Figure 2.5 A).

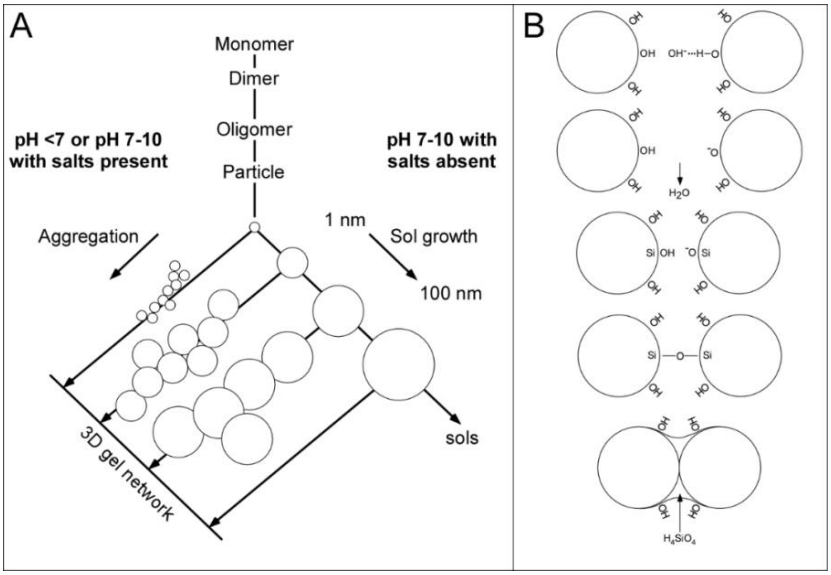

Figure 2.5: *Aggregation of silica particles: (A) Growth and aggregation/precipitation as a function of physico-chemical conditions and (B) mechanism of aggregation of silica particles with OH-groups as catalysts and subsequent cementation by the deposition of dissolved silica (both modified after Iler, 1979).*

The aggregation behaviour of silica particles is strongly dependant on the surface properties of the individual particles. Silica particles show a negative surface charge over most of the pH range ($pH_{IEP} < 2$; Parks, 1965). At acidic pH, where the surface charge density of the silica particles is low, aggregation is prevalent and can happen as soon as the first particles form (Figure 2.5 A). At neutral to alkaline pH the electrostatic repulsion limits the degree of aggregation and particles grow to larger sizes (Figure 2.5 A). However, if salt is present at concentrations higher than around 0.2-0.3 N (Iler, 1979), the surface charge is reduced and aggregation takes place (Figure 2.5 A). In geothermal systems aggregation will dominate over gelation in most cases due to the near neutral or alkaline pH and the often high concentrations of salts.

The attachment between two particles requires the presence of both, neutral hydroxyl groups as well as deprotonated hydroxyl groups at the surface of the particles. These two groups condense, releasing an OH^- ion, to form new Si-O-Si bonds connecting the particles (Figure 2.5 B; Iler, 1979). The mechanism is the same as during polymerisation (bimolecular collisions of ionised and non-ionised molecules of monomeric silica) thus it is also controlled by the same parameters, i.e., temperature, pH and degree of supersaturation. Where the particles are touching, monomeric silica is precipitated immediately as the solubility of silica

becomes zero due to the infinitely small negative radius of curvature in between the two particles (Figure 2.5 B; Iler, 1979). The cementation by monomeric silica stops once the neck between the particles has increased enough for the concentration to decrease below the solubility of amorphous silica again. For small particles (∅ 4 nm) this results in a neck diameter equal to ~80% of the particle diameter while for larger particles (∅ 20 nm) the neck diameter is only ~20% of the particle diameter. Thus, smaller particles are more strongly coalesced (Iler, 1979). A complicating factor is the fluid flow (hydrodynamics) in most geothermal systems. An approach called "ballistic aggregation" (Ramanlal and Sander, 1985) is needed in order to describe aggregation of silica particles under these conditions. Hawkins et al. (in prep.) showed that the ballistic aggregation of particles leads to the formation of fan-shaped structures under conditions of turbulent channel flow. The point of the fans is the initial deposition site and every additional collision leads to the attachment of another particle allowing the fans grow towards the flow, widening from bottom to top. The fans create turbulences immediately behind them and thus a shadowing effect arises, controlling the spacing of individual fans. Furthermore, the model by Hawkins et al. revealed that in a polydisperse particle size distribution scenario larger particles are preferentially aggregated into fans while smaller particles tend to remain in the fluid.

2.3.3 Applied studies

In the previous sections, the pathways and rates of amorphous silica precipitation as determined from detailed laboratory studies performed on simulated fluids have revealed that the process, despite its complexity, is relatively well understood. However, comparing these laboratory results to field observations (in hot springs or geothermal power plants) revealed several major discrepancies that will be addressed below.

2.3.3.1 Formation of silica sinters in hot springs

The term silica sinter is used to describe a chemical, mainly siliceous sedimentary rock deposited by natural precipitation from fluids emanating at Earth's surface due to rapid cooling. The rate of sinter formation is invariably linked to the rate of silica polymerisation and nanoparticle formation, and thus to the amount of dissolved

silica in the uprising fluid and the magnitude and rate of cooling. In addition, the loss of steam can lead to an increase in the silica concentration and pH which enhances silica precipitation. The presence of multivalent cations (Al and Fe) in the emerging fluid can equally accelerate sinter growth rates. Noteworthy, most terrestrial silica sinters found in thermal hot spring areas are formed sub-aerially (above the air-water interface) and therefore hydrodynamic processes including wave action, capillary action, diffusion and splash must also be invoked to fully explain their formation (Mountain et al., 2003; Handley et al., 2005; Tobler et al., 2008).

Abiotic sinter textures

Morphologies of silica precipitated around hot springs and geysers are very diverse and depend strongly on the type of spring (boiling vs. non-boiling, surging vs. non-surging) or, for geysers, on their eruption behaviour. This is primarily due to the fact that silica precipitation occurs predominantly at the air water interface where recurring wetting-evaporation cycles occur as well as other hydrodynamic processes including wave action, capillary action, diffusion and splash (Mountain et al., 2003; Handley et al., 2005; Tobler et al., 2008).

Despite the plethora of macroscopic sinter textures, there are only a few types of amorphous silica present in most fresh silica sinters: silica particles (a few tens of nm to 10+ microns), silica cement (macroscopically dense but often laminated at the sub-micron scale) and randomly shaped, dense shards of amorphous silica, so-called cryogenic opal A (COA) (White et al., 1964; Renaut et al., 1996; Braunstein and Lowe, 2001; Jones and Renaut, 2003; Lowe and Braunstein, 2003; Lynne et al., 2008; Tobler et al., 2008; Jones and Renaut 2010; Boudreau and Lynne, 2012). The silica particles form by homogeneous nucleation in the fluid due to cooling, acidification of fluid (microbial activity or degassing) or evaporation. They are on average a few tens of nanometres to ~5 μm in size (Braunstein and Lowe, 2001; Jones and Renaut, 2004; Jones and Renaut, 2007; Tobler et al., 2008; Jones and Renaut, 2010) and show a polydisperse size distribution. The aggregation of a large number of silica microspheres can lead to the formation of porous layers. Over time, the individual particles can become cemented together by the deposition of dissolved silica until the layer becomes very dense and the only visible trace of the particles remaining are pores with concave walls (Jones and Renaut, 2007). If the aggregation of particles takes place in a current instead, the resulting shapes are asymmetric ridges,

leaning towards the flow (Braunstein and Lowe, 2001). Again, deposition of dissolved silica results in cementation of the particles. The second type of silica is silica cement, deposited as a dense, micro- to millimetre thick layer onto pre-existing surfaces (e.g., plant or animal material, microbial surfaces or detrital grains) by heterogeneous nucleation. However, natural etching by acidic steam has revealed that many cements are finely (< 1 μm) laminated (Jones and Renaut, 2004). The individual laminae are not just characterised by slightly different solubilities (as revealed by preferential etching of some laminae) but also by different water contents and thus atomic numbers. Laminae can be attributed to periods of different growth conditions, i.e., wetter conditions during submersion (= eruption of geyser or overflow of hot spring) and subsequent drying out. The laminae likely form due to different precipitation rates during these two periods with wetter conditions resulting in faster precipitation and silica containing more water and vice versa (Jones and Renaut, 2004). The COA forms in winter, when there are only short periods during which nucleation and growth of silica are possible as the water freezes shortly after emerging from a hot spring or geyser (Channing and Butler, 2007). The growth of ice crystals causes the silica to be squeezed into the interstices between individual ice crystals, thus resulting in denser aggregates. COA can show a wide range of shard-like textures as they replicate the shape of the interstices in which they grow.

The different types of silica are not precipitated in equal amounts throughout the year but show seasonal variations. COA only forms in winter, where the geothermal fluids freeze upon emerging from the subsurface. If there is still liquid water in winter time, the formation of silica microspheres and the precipitation of silica cement can occur all year long. However, their precipitation is enhanced in summer when there is more microbial activity due to more sunshine and cooling and evaporation of the fluid are more gradual (Jones and Renaut, 2010).

Microbial communities in hot springs and their effect on silica sinter formation

Although silica precipitation is perceived as a purely inorganic process, many recent studies have shown that when polymerization and sinter formation occurs at Earth surface conditions, the presence, diversity and abundance of microorganisms and the role they play in silica sinter formation have to also be considered when discussing silica precipitating processes.

Neutral to alkaline (pH 7 – 9), high-temperature (60 – 95 °C) silica precipitating hot springs around the world exhibit an abundant diversity of thermophilic microorganisms, often dominated by bacterial species belonging to the order *Aquificales* and the genus *Thermus* (Brock and Freeze, 1969; Kristjansson and Alfredsson, 1983; Hudson et al., 1989; Chung et al., 2000; Reysenbach et al., 2000; Hjorleifsdottir et al., 2001; Takacs et al., 2001; Tobler and Benning, 2011). Other organisms in these ecosystems include members of the *Bacilli*, *Nitrospira*, *Thermotogales* and *Thernodesulfobacterium* group, as well as many unknown species. Archaeal species also exist in these ecosystems. Representatives of *Korarchaeota*, *Thermofilum* and uncultured *Crenarchaeota* are the most abundant, along with many unknown archaeal species (Barns et al., 1994; Reysenbach et al., 2000; Skirnisdottir et al., 2000; Meyer-Dombard et al., 2005; Kvist et al., 2007).

Several studies have (Skirnisdottir et al., 2000; Fouke et al., 2003; Meyer-Dombard et al., 2005; Purcell et al., 2007; Petursdottir et al., 2009; Tobler and Benning, 2011) linked the diversity of microbial communities with physico-chemical conditions of the studied geothermal waters and showed that the microbial abundance and community structure was directly controlled by the geochemical and hydrodynamic regime. These parameters included temperature, pH, sinter growth rates, and availability of energy sources and organic substrates. On a more local basis these studies also showed that historical factors (e.g., climate events, sea-level changes, volcanic eruptions) and geographical barriers can also play important roles.

While hot springs are unique environments for extremophilic microbial communities, the microbes themselves may both provide reactive interfaces for heterogeneous silica nucleation and surfaces for homogeneously formed silica particles to adhere to (Figure 2.6). As such, they can strongly influence the structure and texture of the silica sinters. The structural role microbes play in sinter formation and/or their simultaneous fossilisation has been investigated for decades (Schultze-Lam et al., 1995; Cady and Farmer, 1996; Jones et al., 2000; Guidry and Chafetz, 2003; Mountain et al., 2003; Handley et al., 2005), not only because modern hot springs provide an important window into ancient siliceous terrestrial environments (Cady and Farmer, 1996; Konhauser and Ferris, 1996) but also because they are critical to interpret hydrothermal sinter deposit found on Mars (Squyres et al., 2008) and to guide the search for potential Martian life. Overall, what has emerged from these studies is that sinter textures are highly dependent on the relative rates of silica pre-

cipitation and biofilm growth, the physico-chemical parameters triggering precipitation as well as the type of microorganisms thriving within these systems. For example, Tobler et al. (2008), showed that under conditions of very rapid sinter growth (e.g., 300 kg y^{-1} m^{-2} at a wastewater outflow at Reykjanes power plant) no bacteria was found while at moderate to low deposition rates, extensive biofilms were observed to develop and sinter fabrics were strongly influenced by the microbial mats.

Most microorganisms have no known metabolic requirement for silica, and thus the silicification of microorganisms in hot springs is mostly controlled by the physical nature of their surfaces. The microbial surface exhibits a wide variety of different functional groups (i.e., carboxyl, hydroxyl, phosphate and amine) and microbes often exude exopolymeric substances (EPS), including slimes, sheaths, or biofilms. Adsorption of silica onto this microbial envelope is less governed by electrostatic interactions, since they are both usually neutrally or negatively charged in neutral to alkaline geothermal fluids, but more by hydrophobic interactions, hydrogen bonding and cation bridging (e.g., Fe^{3+}, Al^{3+}) (Benning et al., 2005 and references therein). Important to note that in natural hot spring systems, the concentration of soluble silica often far exceeds that of cation bridge ions and thus the vast majority of silica precipitated will occur without the aid of a cation bridge.

While the deposition of silica onto the microbial surface appears mostly to be a passive process, the microbes actually seem to respond to the presence of supersaturated silica conditions. For example, silica-induced protein expression has been observed for a number of thermophilic species when exposed to silica concentrations ≥ 300 ppm SiO_2, including the cyanobacterium *Anabaena sp. PCC 7120* (Konhauser et al., 2008) and *Thermus* thermophiles species (Doi et al., 2009). These proteins seem to relate to membrane transport, such as iron (Doi et al., 2009) or heavy metals (Spada et al., 2002). However, it is still not clear how these particular responses benefit the microbe itself as they are ultimately becoming encased in a silica layer which ultimately fossilizes them (Figure 2.6 B; Ferris et al., 1986; Cady and Farmer, 1996; Jones et al., 1998; Phoenix et al., 2001; Mountain et al., 2003; Tobler et al., 2008). One response to exposure to supersaturated polymerising silica solution observed in *Calothrix* and *Sulfurihydrogenibium azorense,* was an increased production of exopolysaccharides in the EPS layer (Benning et al., 2004a; Benning et al., 2004b; Lalonde et al., 2005). The EPS of these two microbes, is characterized by a higher abundance of positively and neutrally charged functional groups, which fa-

cilitate interaction with the negatively charged silica nanoparticles, and thereby enhance bacterial silicification.

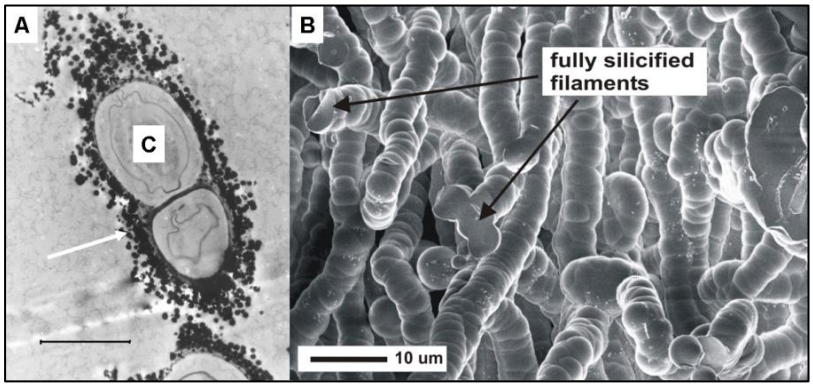

Figure 2.6: *(A) TEM photomicrograph of a naturally silicified microorganism (probably cyanobacteria) collected from the Strokkur hot spring, Iceland (Phoenix et al., 2001). The bacterial cells (C) have acted as a nucleation site/surface for the precipitation of the amorphous silica spheres (arrow). Scale bar = 5 μm. (B) Fully silicified filaments on slides collected after 25 months from an outflow channel at Krafla Power Station in Iceland (Tobler et al., 2008).*

These observations documented that microbes can indeed actively aid and enhance silica precipitation despite the ultimately detrimental effect silica precipitation and fossilization has on the life cycle of the microbes. The question however arises, whether a silica casing can actually help microbial survival in these harsh environments or if it is just a perfect way of preservation. Phoenix et al. (1999) argued that biosilicification is restricted to the surface of healthy microbial cells due to metabolic processes (e.g., photosynthesis) of the microbial cell (Figure 2.6 A). In addition, they showed that the sheath of certain cyanobacteria can act as a diffusion barrier for silica particles ≥ 11 nm, and that this in term inhibits internal mineralization. In a later study, Phoenix et al. (2000) showed that mineralised *Calothrix* cells remained both intact and functioning while encrusted in an extensive (~5 μm) silica crust, while unhealthy and damaged cells became silicified also intracellularly. This was a first indication which was later been experimentally demonstrated (Benning et al., 2004a; Benning et al., 2004b) that the production of thickened sheath may play a vital role for the microbes to survive in hot spring environments subjected to extensive silicification. In addition, a thin silica crusts can also protect microorganisms against damaging UV light, while the photosynthetically active radiation (PAR) can

still penetrate through the layer to ensure the perpetuation of photosynthesis (Figure 2.7).

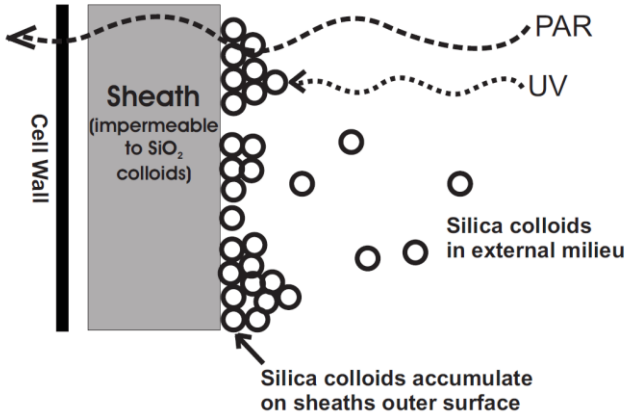

Figure 2.7: *Silicification model illustrating the advantages of the microbial sheath (Benning et al., 2005)*

Silica layers can also protect microbial biofilms against predation and intrusion by other microorganisms and due to the high water contents of amorphous silica (up to 18 wt.%) means that being encased in a hydrated silica layer also prevent microbes from dehydrating. Such protection mechanisms have also been proposed as potential scenarios for the survival of microorganisms in the silica-enriched, shallow-water environments in the Archean era, where high levels of UV radiation and fluctuating water levels prevailed (Phoenix et al., 2001).

2.3.3.2 Silica scaling in geothermal power plants

The study of silica precipitation in hot springs is of great importance to understand processes occurring naturally, both today and throughout the Earth's history. On the other hand, silica precipitation inside geothermal power plants is important from an applied point of view. Silica precipitation has been identified as one of the most common problems in high-enthalpy geothermal power plants, reducing the efficiency of geothermal energy production (Rothbaum et al., 1979; Fleming and Crerar, 1982; Harrar et al., 1982; Gunnarsson and Arnórsson, 2003; Demadis et al., 2007). As with unwanted mineral precipitation in other industrial systems, the terms "scaling" or "precipitation fouling" are often used to describe the process and "silica scale" to describe the resulting deposits (Figure 2.8).

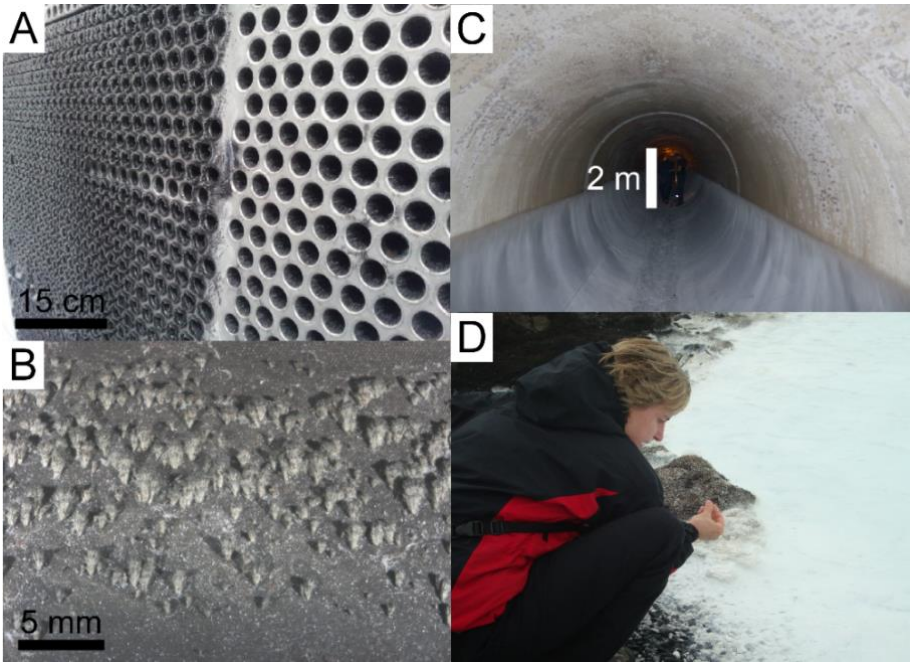

Figure 2.8: *Pictures of silica scaling in geothermal power plants in SW-Iceland: (A) tube sheet of a heat exchanger showing ring-shaped scales and (B) fan-shaped scales deposited onto a scaling plate used to monitor scaling inside in-use pipelines at Hellisheiði (Meier et al., 2014 (Chapter 3)), (C) silica scaling inside the retention tank at Nesjavellir (indicating the water-level when in use) and (D) silica deposits formed in waste water pools at Svartsengi.*

Silica scales can clog pipes and wells, reduce the efficiency of pumps and heat exchangers, shorten the lifetime moveable parts such as valves and can also increase the operational hazards due to the need of higher operational pressures. Silica precipitation also impairs the financial performance of a power plant due to the reduction in power generation, increased operating costs (e.g., additional costs for chemical additives, need for additional pumping capacity) and longer down-times required for cleaning and maintenance of the system (Demadis et al., 2007). Amorphous silica deposits are very hard and therefore more difficult to remove mechanically or chemically from equipment surfaces than other precipitates (e.g., carbonates). However, in most operational geothermal power plants, silica scaling issues have been minimized or alternative solutions for fluid handling have been implemented to the point where the scaling is not too detrimental for the efficient operation of the system. For example, at both the Reykjanes and Svartsengi geo-thermal power plants only the steam is used for power production due to the high salt contents in the geothermal fluids (Tobler et al., 2008). The separated water is not

used for the production of district heat but allowed to cool in waste water pools (Figure 2.8 D) where the supersaturated silica precipitates; a well-known phenomenon seen expressed in the bright blue colour of the pools at the Blue Lagoon.

Composition of silica scales

Similarly to hot springs, the dissolved silica that eventually turns into scales is derived from deep geothermal reservoirs where rock-water interactions occur (Figure 2.2). Such deep waters are usually rapidly pumped to the surface without depressurisation or cooling and this keeps the pipes up to the surface free of precipitates. Precipitation starts inside the surface installations once supersaturation with respect to amorphous silica is reached. This generally happens between 100 and 220 °C during flashing of the fluid (removal of steam results in an increase in concentration of dissolved solids in the separated water) or when the fluids are cooled in heat exchangers (reduced solubility). During precipitation, silica scales incorporate ions form the fluid (especially Al and Fe), resulting in impure amorphous silica. These impure precipitates are well-known as they have been observed in many high-enthalpy geothermal systems in Iceland (Thórhallsson et al., 1975), New Zealand (Rothbaum et al., 1979), Japan (Ito et al., 1977; Yokoyama et al., 1993), Greece (Karabelas et al., 1989), Indonesia (Gallup, 1997), the Philippines (Gallup, 1997) and the USA (Makrides et al., 1980; Gallup, 1997). These silica scales typically contain 0.5 to 12 wt.% Al_2O_3 and 0.5 to 10 wt.% Fe_2O_3 with aluminium generally being more abundant than iron. However, Rothbaum et al. (1979) showed that extensive corrosion (e.g., due to low pH and high H_2S contents in the fluid) can result in the formation of scales which contain up to 19 wt.% iron. When incorporated into the amorphous silica precipitates, both aluminium and iron are believed to be tetrahedrally coordinated, indicating that some of the Si^{4+} in the SiO_4 matrix may be replaced by Al^{3+} and Fe^{3+} or Fe^{2+} respectively and that Al-O-Si and Fe-O-Si bonds could have formed (Gallup, 1989; Yokoyama et al., 1993; Manceau et al., 1995; Gallup, 1998). Nevertheless, in such composites the charge balance is maintained by the inclusion of interstitial cations such as sodium, calcium and potassium that are ample in the fluids (Manceau et al., 1995; Gallup, 1997). In an experimental study Manceau et al. (1995) suggested that the iron-rich silica precipitates are more ordered compared to pure silica precipitates and that these show local ordering comparable to hisingerite, a poorly crystalline version of the smectite mineral

nontronite. Nevertheless, the solubility limit for Al- and Fe-containing silica precipitates are reached between 20 to 40 °C (Al) and 50 to 75 °C (Fe) higher than for pure silica precipitates (Gallup, 1989; Thórhallsson et al., 1975; Gallup, 1998;). These rather substantial differences indicate that in geothermal systems, such impure Al-Fe rich silica scales will still precipitate even at temperatures where the solutions are not anymore supersaturated with respect to pure amorphous silica.

Pathways of silica scaling

The precipitation mechanism of amorphous silica inside geothermal power plants as well as the factors controlling it have rarely been studied systematically and this is primarily due to the difficulties in accessing inside surfaces of geothermal pipelines. Naturally, the few data available on silica precipitation inside geothermal power plants was obtained within the framework of developing better mitigation strategies for silica scaling (e.g., Bohlmann et al., 1976; Rothbaum et al., 1979; Harrar et al., 1982; Henley, 1983; Carroll et al., 1998; Gunnarsson et al., 2010) or trying to manipulate precipitation in a way to produce a silica product of commercial interest (e.g., Gudmundsson and Einarsson, 1989; Potapov et al., 2011; Svavarsson et al., 2014).

Experiments conducted at geothermal power plants generally involve the use of a bypass as to not disrupt normal operations and allow access to both, solid and liquid samples. Studies conducted this way at different power plants in Iceland and New Zealand found that the microtextures of the scales deposited depended primarily on the dominant silica species (monomers vs. particles) in the fluid (Gudmundsson and Bott, 1979; Rothbaum et al., 1979; Carroll et al., 1998). If substantial amounts of polymerised or particulate silica were present, i.e., after aging, the scales consisted of relatively loose aggregates of small silica particles which were interpreted to have formed via homogeneous nucleation. In contrast, if monomeric silica was the dominant species the authors described a 'bumpy', dense silica layer which was interpreted to have formed via heterogeneous nucleation and direct deposition of monomeric silica. The work by Gudmundsson and Bott, Rothbaum et al. and Carroll et al. covered a large range of silica concentrations (500 to 900 mg/L), salinities (~ 3000 to 28'000 mg/L), pH (7.7 to 9.5) and temperatures (60 to 115 °C), indicating that the processes resulting in the textures observed are taking place over a wide range of physico-chemical conditions. However, the conditions

inside a bypass are not identical to those inside in-use geothermal pipelines because of the lower flow rates and the different hydrodynamic conditions due to the use of numerous valves and the smaller diameter of the pipes. Depending on the design of the bypass, additional artefacts such as cooling or oxygenation of the fluid can also be introduced (Rothbaum et al., 1979). Thus, the precipitation pathways determined from such studies are not necessarily representative of the behaviour of amorphous silica inside the actual geothermal power plant. However, in a recent study we confirmed the formation of both, a 'bumpy' silica layer and 3D structures composed of aggregated particles, inside in-use pipelines at the Hellisheiði power plant in SW-Iceland (van den Heuvel et al., in prep.b (Chapter 4)). Similarly to the studies conducted in the bypasses, we inferred from these findings that silica precipitated via both, the homogeneous and heterogeneous pathway (Figure 2.9). Homogeneous nucleation resulted in the formation of silica nanoparticles and even micron sized, smooth spherical particles in the geothermal fluid. The maximum diameter of these larger spherical particles was 20+ μm indicating that in geothermal systems like Hellisheiði the conditions for particle growth by addition of dissolved silica from the fast flowing fluid (400 L/s) was ideal. It is however important to note that the majority of these particles were much smaller (< 0.5 μm) suggesting that nucleation happened continuously. Furthermore, compared to the total silica in the system, the proportion of silica particles in solution was very small (< 0.05%, van den Heuvel et al., in prep.b (Chapter 4)) and the geothermal fluid composition was still dominated my monomeric silica species. Interestingly, the observed large particles seem to have been preferentially deposited on the surfaces due to the larger drag (e.g., Brown and Dunstall, 2000). Aggregation sometimes led to the formation fan- or ridge-shaped structures which further grew towards the flow and were cemented together by the amply available dissolved silica (Figure 2.9; Meier et al., 2014 (Chapter 3); Hawkins et al., in prep.; van den Heuvel et al., in prep.b (Chapter 4)). The formation of these structures was dominantly controlled by the hydrodynamic conditions (Brown and Dunstall, 2000; Dunstall et al., 2000; Hawkins et al., 2013; Hawkins et al., in prep.).

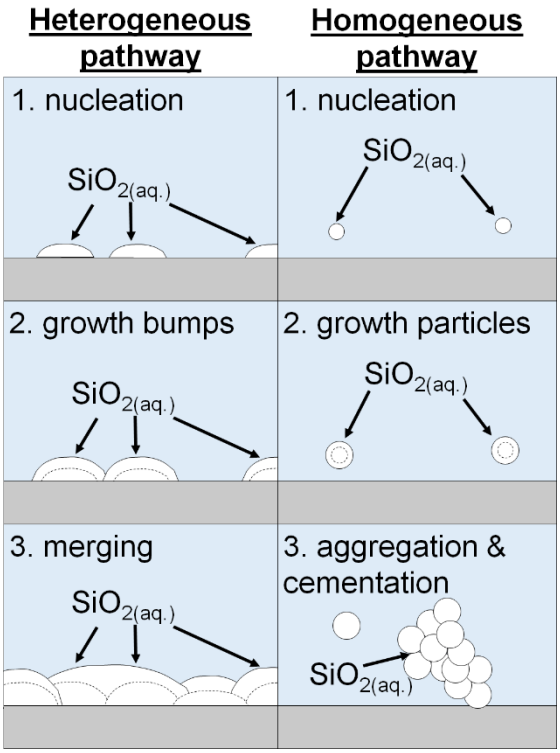

Figure 2.9: *Precipitates resulting from (A) the heterogeneous pathway and (B) the homogeneous pathway and (C) schematic of pathway (van den Heuvel et al., in prep.b (Chapter 4))*

The second, and by far the more dominant pathway of silica scale formation at Hellisheiði was by heterogeneous nucleation and growth on pre-existing surfaces. Once an amorphous silica nuclei formed on a surface they grew by addition of further dissolved silica, analogue to the homogeneous nuclei. This growth resulted in the formation of lens-shaped features, which, over time covered the surface completely, resulting in a continuous, uneven silica layer (Figure 2.9) (van den Heuvel et al., in prep.b (Chapter 4)). Both theoretical and experimental studies have demonstrated that the nucleation and growth of such silica layers on surfaces very much depends on the surface properties (e.g., composition, roughness etc.) of the substrate exposed to scaling (Harrar et al., 1982; Brown and Dunstall, 2000; van den Heuvel et al., 2016 (Chapter 6); van den Heuvel et al., in prep.a (Chapter 5)). Rothbaum et al. (1979) suggested that, in addition to fixed surfaces like pipeline walls, other mineral colloids (e.g., iron hydroxides or carbonates) could also enhance heterogeneous nucleation of silica. Furthermore, recent studies from Japan indicate that, similarly to hot springs, the presence of thermophilic microbes could enhance silica precipita-

tion in geothermal power plants as their surfaces act as additional sites for heterogeneous nucleation (Inagaki et al., 1997; Doi and Fujino, 2013).

Mitigation strategies for silica scaling

When comparing the two pathways of silica scaling, high supersaturation (= rapid silica polymerisation) and high salinities favour homogeneous nucleation while high flow rates, high temperatures, alkaline pH and low supersaturation favour heterogeneous nucleation (Harrar et al., 1982; Brown and Dunstall, 2000; Gunnarsson et al., 2010). Thus, by manipulating any of these factors, we should be able to affect silica precipitation and, potentially reduce or even prevent it. A wide range of approaches to mitigate silica scaling have been tested in various localities. Many of them proved to be successful for one or several given geothermal fields. However, applied to a different geothermal system, where conditions of silica scaling are different (e.g., other process conditions or solution chemistry) they often exhibited limited efficiency (Rothbaum et al., 1979; Henley, 1983; Gunnarsson et al., 2010; Mroczek et al., 2011). At present, no single, universally applicable solution has been found for the problem of silica scaling in geothermal systems and the choice of mitigation strategy for a given power plant strongly depends on fluid and steam chemistry, fluid temperature, economics and the power plant design.

One option to control silica scaling is to prevent silica saturation by keeping the temperature above the solubility limit of amorphous silica. However, impure varieties of amorphous silica can show substantially higher solubilities (see above) which would require even higher operating temperatures. While successful in preventing scaling, this method of silica management prevents the efficient use of a geothermal resource. Second stage boiling to produce low pressure steam, hot water production for space heating and industrial use or the use of a binary cycle to produce more electricity from the geothermal fluid are excluded by this mitigation approach. A growing number of geothermal power plants want to be able to go beyond the point of silica saturation to improve efficiency, highlighting the importance of a good silica management strategy for successful operation.

Another option to control silica saturation is by dilution of the geothermal fluid by water, thus lowering the driving force of silica scaling. Ideally, steam condensate from closed condensers is used, sometimes mixed with fresh water (Gunnarsson and Arnórsson, 2003; Gunnarsson et al., 2010). The use of fresh water

only would require huge amounts and the oxygenated water would promote the risk of magnesium silica scaling (Owen, 1975; Rothbaum et al., 1979; Henley, 1983; Gunnarsson and Arnórsson, 2005). The same is true for steam condensate obtained from open condensers. However, dilution reduces the overall energy output of a geothermal system due to cooling of the fluid or the pre-heating of the condensate.

Silica scaling can also be mitigated by reducing the rate of silica precipitation. One approach involves the acidification of the geothermal fluid. At low pH, the rate of silica self-assembly is slowed down and the negative surface charge of silica particles stabilised, preventing aggregation. This method has been showed to be effective against silica and iron-containing silica scaling in several geothermal fields worldwide (Rothbaum et al., 1979; Henley, 1983; Gallup, 1989; Gallup, 1998; Gallup, 2011;). However, the precipitation of aluminium-containing amorphous silica was not reduced by acidification of the fluid (Manceau et al., 1995), unless the pH was dropped ≤ 4 (Gallup, 1997). Controlling the rate of acid injection and precise measurement of the pH of the geothermal fluid is very important as too much acid will strongly enhance localised corrosion of pipes while not enough acid will not stop silica deposition (Addison et al., 2015). In addition to the difficulties controlling acid dosage, the costs for the required acids, usually HCl or H_4SO_4, can be high. Also, if injection wells receiving the spent acidified geothermal fluid are close to the production field, the acid can cause acidification of the reservoir fluid.

The precipitation rate of silica can also be lowered by controlling silica speciation in the fluid. Laboratory studies have identified that monomeric silica is more likely to deposit than polymeric silica (Bohlmann et al., 1976; Mroczek and McDowell, 1988; Bremere et al., 2000). This assumption was used by Yanagase et al. (1970) to design a mitigation strategy for silica scaling at Otake power plant, Japan using ageing of the geothermal fluid in a tank before being used for the generation of energy. The fluid was retained for one hour during which time the silica in solution polymerised. This reduced the downstream silica scaling by 90%. This approach is also successfully applied in geothermal power plants in Iceland, where it is combined with dilution by steam condensate (Gunnarsson and Arnórsson, 2005; Gunnarsson et al., 2010). In geothermal operations in New Zealand on the other hand, Rothbaum et al. (1979) showed that ageing of the solution did not reduce the amount of silica precipitation noticeably. The success of this silica management method depends to a large extent on the ionic strength of the brine. In high salinity

fluids aging is assumed to lead to enhanced precipitation as the cations present could act as flocculating agents cross-linking the negatively charged silica particles.

A third group of mitigation strategies involve the use of additives to control silica precipitation. The first group of additives are used to develop anti-scaling coatings which prevent the deposition of silica scales onto equipment surfaces. Sugama and Gawlik (2002) have studied carbon steel with a special anti-scaling coating. Without a special coating, corrosion products form on the surface of normal carbon steel. These phases show a strong affinity for silica and facilitate scaling. By coating the surface with an organic polymer, fewer and less adherent silica deposits form and therefore removal of these precipitates is easier. The second group of additives aims at removing the silica from solution by controlled precipitation. This has the advantage that the deposits are locally concentrated and often less adherent, making them easier to remove (Harrar et al., 1980). So far, crystals, gels, colloids or cationic precipitants have been tested with varying degrees of success (Harrar et al., 1980; Sugita et al., 1998; Ueda et al., 2003). The third group of additives are (in)organic inhibitors which try to keep dissolved silica in solution by preventing self-assembly or by acting as dispersants for silica particles (Harrar et al., 1982; Gallup, 2002; Demadis, 2005; Gallup and Barcelon, 2005; Demadis and Stathoulopoulou, 2006; Amjad and Zuhl, 2008; Bai et al., 2009). However, most of these potential inhibitors showed only limited efficiency when tested in laboratory and field experiments. Besides, many were not stable at high temperatures and over long time spans (Demadis and Stathoulopoulou, 2006; Amjad and Zuhl, 2008) and dosage of inhibitors was showed to be a challenge. Often inhibitors acted as flocculating agents upon overdosing and therefore increased precipitation of silica (Gallup, 2002; Demadis and Stathoulopoulou, 2006). Thus, owing to the shortcomings of most inhibitors and their formidable costs, other approaches to mitigate silica scaling are chosen in most geothermal fields at present. The development of inhibitors is still ongoing but to develop more efficient and universally applicable inhibitors, the interaction between the additives and silica at the molecular scale has to be understood better.

2.4 Conclusions and outlook

The nucleation and growth of silica both in solution as well as on surfaces has been investigated over a wide range of physico-chemical conditions in the last 70 years

and the processes, despite their complexity, are relatively well understood. Many of the physical, chemical or biological factors (e.g., temperature, pH, silica concentration, microbial presence, salinity etc.) found to control silica precipitation in laboratory analogue experiments also affect the precipitation of silica from natural geothermal fluids both in hot spring or power plant settings. However, in natural geothermal fluids all these parameters are in competition with one another and it is often difficult to isolate the parameters which affect silica precipitation most profoundly.

Despite this rather broad and seemingly comprehensive knowledge-base, there are still many open questions that need addressing in order to further our understanding of the mechanisms and rates of silica precipitation. Here we discuss several approaches and suggestions for further theoretical, laboratory and field studies that we assert are still needed to help progress this field in the future:

- Theoretical:
    - Molecular simulations to assess the fundamental interactions between different molecules to elucidate the molecular mechanisms of silica polymerisation or the interaction of silica with specific surfaces (microbial, corroded steel etc.).
    - Molecular simulations to understand the involvement of different polymeric species in the growth of homogeneous and heterogeneous nuclei.
    - Hydrodynamic simulations to address interactions between surfaces, particles and fluid flow properties to model possible precipitation patterns.

- Laboratory analogue studies:
    - *In-situ* and real-time experiments addressing the precipitation mechanisms and rates using high resolution microscopy (e.g., liquid-cell TEM, AFM) or scattering techniques (e.g., SAXS, DLS). These experiments should quantify (a) homogeneous nucleation and growth of particles in solution as a function of parameters not yet addressed (e.g., fluid flow rates, presence of organic compounds and even microbial species), and (b) heterogeneous surface nucleation and growth. Importantly in these experiments supersaturation should be induced through rapid cooling

of a fluid and not (as usually done as it is simpler) by neutralising of supersaturated high pH silica solutions.
    - Thermodynamic and kinetic data for impure silica as a function of both, aluminium and iron content.

- Field studies:
    - More highly controlled (both spatially and in a time resolved manner) studies of silica scaling inside in-use geothermal pipelines (not using bypasses) to see if the two pathways of silica precipitation are indeed taking place over a wide range of physic-chemical conditions.
    - Scaling plate and bypass studies to test novel materials and coatings as well as additives to develop better mitigation strategies for scaling control and corrosion prevention.

All laboratory and field approaches require a highly complementary and detailed monitoring of the physico-chemical conditions under which silica precipitation takes place as well as detailed characterisation of the textures and composition (abiotic and biotic) of the resulting solids. The significance of the proposed research will invariably drastically increase when several of these approaches are combined, and when especially simulations, laboratory and field-based observations can be better compared and contrasted.

References

Addison, S.J., Brown, K.L., von Hirtz, P.H., Gallup, D.L., Winick, J.A., Siega, F.L., Gresham, T.J., 2015. *Brine silica management at Mighty River Power, New Zealand*, Proceedings World Geothermal Congress, Melbourne.

Aines, R.D., Rossman, G.R., 1984. Water in minerals? A peak in the infrared. *Journal of Geophysical Research: Solid Earth* **89**, 4059-4071.

Alexander, G., 1954. The polymerization of monosilicic acid. *Journal of the American Chemical Society* **76**, 2094-2096.

Amjad, Z., Zuhl, R.W., 2008. *An evaluation of silica scale control additives for industrial water systems*, Proceedings of the NACE International Corrosion Conference and Expo, New Orleans.

Arnórsson, S., 1975. Application of the silica geothermometer in low temperature hydrothermal areas in Iceland. *American Journal of Science* **275**, 763-784.

Bai, S., Okaue, Y., Yokoyama, T., 2009. Depolymerization of polysilicic acid by tiron. *Polymer Degradation and Stability* **94**, 1795-1799.

Barns, S.M., Fundyga, R.E., Jeffries, M.W., Pace, N.R., 1994. Remarkable archaeal diversity detected in a Yellowstone National Park hot spring environment. *Proceedings of the National Academy of Sciences* **91**, 1609-1613.

Becker, R., Döring, W., 1935. Kinetische Behandlung der Keimbildung in übersättigten Dämpfen. *Annalen der Physik* **24**, 719-752.

Benning, L.G., Phoenix, V.R., Mountain, B.W., 2005. Biosilicification: the role of cyanobacteria in silica sinter deposition, *Symposia-Society for General Microbiology*. Cambridge University Press, Cambridge, p. 131.

Benning, L.G., Phoenix, V.R., Yee, N., Konhauser, K.O., 2004a. The dynamics of cyanobacterial silicification: an infrared micro-spectroscopic investigation. *Geochimica et Cosmochimica Acta* **68**, 743-757.

Benning, L.G., Phoenix, V.R., Yee, N., Tobin, M.J., 2004b. Molecular characterization of cyanobacterial silicification using synchrotron infrared micro-spectroscopy. *Geochimica et Cosmochimica Acta* **68**, 729-741.

Benning, L.G., Waychunas, G.A., 2007. Nucleation, growth, and aggregation of mineral phases: Mechanisms and kinetic controls, *Kinetics of Water-Rock Interaction*. Springer, pp. 259-333.

Bergna, H.E., Roberts, W.O., 2005. *Colloidal silica: Fundamentals and applications*. CRC Press, Boca Raton.

Bhattacharya, S., Kieffer, J., 2008. Molecular dynamics simulation study of growth regimes during polycondensation of silicic acid: from silica nanoparticles to porous gels. *The Journal of Physical Chemistry C* **112**, 1764-1771.

Bohlmann, E.G., Mesmer, R.E., Berlinski, P., 1980. Kinetics of silica deposition from simulated geothermal brines. *Society of Petroleum Engineers Journal* **20**, 239-248.

Bohlmann, E.G., Shor, A., Berlinski, P., 1976. *Precipitation and scaling in dynamic geothermal systems*. Oak Ridge National Laboratories, p. 21680.

Boudreau, A.E., Lynne, B.Y., 2012. The growth of siliceous sinter deposits around high-temperature eruptive hot springs. *Journal of Volcanology and Geothermal Research* **247**, 1-8.

Braunstein, D., Lowe, D.R., 2001. Relationship between spring and geyser activity and the deposition and morphology of high temperature (> 73 °C) siliceous sinter, Yellowstone National Park, Wyoming, USA. *Journal of Sedimentary Research* **71**, 747-763.

Bremere, I., Kennedy, M., Mhyio, S., Jaljuli, A., Witkamp, G.-J., Schippers, J., 2000. Prevention of silica scale in membrane systems: removal of monomer and polymer silica. *Desalination* **132**, 89-100.

Brock, T.D., Freeze, H., 1969. *Thermus aquaticus gen. n.* and *sp. n.*, a nonsporulating extreme thermophile. *Journal of Bacteriology* **98**, 289-297.

Brown, K.L., Dunstall, M., 2000. *Silica scaling under controlled hydrodynamic conditions*, Proceedings World Geothermal Congress, Beppu-Morioka, pp. 3039-3044.

Cady, S., Farmer, J., 1996. Fossilization processes in siliceous thermal springs: trends in preservation along thermal gradients. *Ciba Foundation Symposium* **202**, 150-170.

Carroll, S., Mroczek, E., Alai, M., Ebert, M., 1998. Amorphous silica precipitation (60 to 120 °C): Comparison of laboratory and field rates. *Geochimica et Cosmochimica Acta* **62**, 1379-1396.

Channing, A., Butler, I.B., 2007. Cryogenic opal-A deposition from Yellowstone hot springs. *Earth and Planetary Science Letters* **257**, 121-131.

Chen, C.-T.A., Marshall, W.L., 1982. Amorphous silica solubilities IV. Behavior in pure water and aqueous sodium chloride, sodium sulfate, magnesium chloride, and magnesium sulfate solutions up to 350 °C. *Geochimica et Cosmochimica Acta* **46**, 279-287.

Chung, A.P., Rainey, F.A., Valente, M., Nobre, M.F., da Costa, M.S., 2000. *Thermus igniterrae sp. nov.* and *Thermus antranikianii sp. nov.*, two new species from Iceland. *International Journal of Systematic and Evolutionary Microbiology* **50**, 209-217.

Coradin, T., Eglin, D., Livage, J., 2004. The silicomolybdic acid spectrophotometric method and its application to silicate/biopolymer interaction studies. *Journal of Spectroscopy* **18**, 567-576.

Crerar, D.A., Axtmann, E.V., Axtmann, R.C., 1981. Growth and ripening of silica polymers in aqueous solutions. *Geochimica et Cosmochimica Acta* **45**, 1259-1266.

Demadis, K.D., 2005. A structure/function study of polyaminoamide dendrimers as silica scale growth inhibitors. *Journal of Chemical Technology and Biotechnology* **80**, 630-640.

Demadis, K.D., Mavredaki, E., Stathoulopoulou, A., Neofotistou, E., Mantzaridis, C., 2007. Industrial water systems: problems, challenges and solutions for the process industries. *Desalination* **213**, 38-46.

Demadis, K.D., Stathoulopoulou, A., 2006. Solubility enhancement of silicate with polyamine/polyammonium cationic macromolecules: relevance to silica-laden process waters. *Industrial & Engineering Chemistry Research* **45**, 4436-4440.

Dickson, M.H., Fanelli, M., 2013. *Geothermal energy: Utilization and technology*. Routledge, London.

Doi, K., Fujino, Y., 2013. *Biomineralization in Geothermal Environments*, Thermophilic Microbes in Environmental and Industrial Biotechnology. Springer, pp. 233-247.

Doi, K., Fujino, Y., Inagaki, F., Kawatsu, R., Tahara, M., Ohshima, T., Okaue, Y., Yokoyama, T., Iwai, S., Ogata, S., 2009. Stimulation of expression of a silica-induced protein (Sip) in *Thermus thermophilus* by supersaturated silicic acid. *Applied and Environmental Microbiology* **75**, 2406-2413.

Dunstall, M., Zipfel, H., Brown, K.L., 2000. *The onset of silica scaling around circular cylinders*, Proceedings World Geothermal Congress, Beppu-Morioka.

Eaton, A.D., Clesceri, L.S., Rice, E.W., Greenberg, A.E., 2005. *Standard methods for the examination of water and wastewater*, 21st Edition ed. American Public Health Association, Washington.

Farkas, L., 1927. Keimbildungsgeschwindigkeit in übersättigten Dämpfen. *Zeitschrift für Physikalische Chemie* **125**, 236-242.

Ferris, F., Beveridge, T., Fyfe, W., 1986. Iron-silica crystallite nucleation by bacteria in a geothermal sediment. *Nature* **320**, 609-611.

Fleming, B.A., 1986. Kinetics of reaction between silicic acid and amorphous silica surfaces in NaCl solutions. *Journal of Colloid and Interface Science* **110**, 40-64.

Fleming, B.A., Crerar, D.A., 1982. Silicic acid ionization and calculation of silica solubility at elevated temperature and pH application to geothermal fluid processing and reinjection. *Geothermics* **11**, 15-29.

Flörke, O., 1991. Nomenclature of micro-and non-crystalline silica minerals, based on structure and microstructure. *Neues Jahrbuch Mineralogie, Abhandlungen* **163**, 19-42.

Flörke, O., Jones, J., Segnit, E., 1973. The genesis of hyalite. *Neues Jahrbuch für Mineralogie, Monatsheft* **2**, 82-89.

Fouke, B.W., Bonheyo, G.T., Sanzenbacher, B., Frias-Lopez, J., 2003. Partitioning of bacterial communities between travertine depositional facies at Mammoth Hot Springs, Yellowstone National Park, USA. *Canadian Journal of Earth Sciences* **40**, 1531-1548.

Fournier, R., 1985. The behavior of silica in hydrothermal solutions. *Reviews in Economic Geology* **2**, 45-61.

Fournier, R., Rowe, J., 1966. Estimation of underground temperatures from the silica content of water from hot springs and wet-steam wells. *American Journal of Science* **264**, 685-697.

Fournier, R.O., Marshall, W.L., 1983. Calculation of amorphous silica solubilities at 25 to 300 C and apparent cation hydration numbers in aqueous salt solutions using the concept of effective density of water. *Geochimica et Cosmochimica Acta* **47**, 587-596.

Fournier, R.O., Rowe, J.J., 1977. Solubility of amorphous silica in water at high temperatures and high pressure. *American Mineralogist* **62**, 1052-1056.

Frank, F., Van der Merwe, J., 1949. *One-dimensional dislocations. III. Influence of the second harmonic term in the potential representation, on the properties of the model*, Proceedings of the Royal Society of London A: Mathematical, Physical and Engineering Sciences. The Royal Society, pp. 125-134.

Gallup, D.L., 1989. Iron silicate scale formation and inhibition at the Salton Sea geothermal field. *Geothermics* **18**, 97-103.

Gallup, D.L., 1997. Aluminum silicate scale formation and inhibition: scale characterization and laboratory experiments. *Geothermics* **26**, 483-499.

Gallup, D.L., 1998. Aluminum silicate scale formation and inhibition (2): scale solubilities and laboratory and field inhibition tests. *Geothermics* **27**, 485-501.

Gallup, D.L., 2002. Investigations of organic inhibitors for silica scale control in geothermal brines. *Geothermics* **31**, 415-430.

Gallup, D.L., 2011. *pH modification scale control technology*, Proceedings International Workshop on Mineral Scaling, Manila, pp. 39-46.

Gallup, D.L., Barcelon, E., 2005. Investigations of organic inhibitors for silica scale control from geothermal brines–II. *Geothermics* **34**, 756-771.

Glass, B., 1984. Tektites. *Journal of Non-Crystalline Solids* **67**, 333-344.

Goto, K., 1956. Precipitation of silica in the presence of aluminum. *Bulletin of the Chemical Society of Japan* **29**, 740-741.

Graetsch, H., 1994. Structural characteristics of opaline and microcrystalline silica minerals. *Reviews in Mineralogy and Geochemistry* **29**, 209-232.

Gudmundsson, J., Bott, T., 1979. Deposition of silica from geothermal waters on heat transfer surfaces. *Desalination* **28**, 125-145.

Gudmundsson, S., Einarsson, E., 1989. Controlled silica precipitation in geothermal brine at the Reykjanes geo-chemicals plant. *Geothermics* **18**, 105-112.

Guidry, S.A., Chafetz, H.S., 2003. Depositional facies and diagenetic alteration in a relict siliceous hot-spring accumulation: examples from Yellowstone National Park, USA. *Journal of Sedimentary Research* **73**, 806-823.

Gunnarsson, I., Arnórsson, S., 2000. Amorphous silica solubility and the thermodynamic properties of H_4SiO_4 in the range of 0 to 350 °C at P_{sat}. *Geochimica et Cosmochimica Acta* **64**, 2295-2307.

Gunnarsson, I., Arnórsson, S., 2003. *Silica scaling: The main obstacle in efficient use of high-temperature geothermal fluids*, Proceedings International Geothermal Conference, Reykjavik, pp. 30-36.

Gunnarsson, I., Arnórsson, S., 2005. Impact of silica scaling on the efficiency of heat extraction from high-temperature geothermal fluids. *Geothermics* **34**, 320-329.

Gunnarsson, I., Ívarsson, G., Sigfússon, B., Thrastarson, E.Ö., Gíslason, G., 2010. *Reducing silica deposition potential in waste waters from Nesjavellir and Hellisheiði Power Plants, Iceland*, Proceedings World Geothermal Congress, Bali.

Handley, K., Campbell, K., Mountain, B., Browne, P., 2005. Abiotic–biotic controls on the origin and development of spicular sinter: *in-situ* growth experiments, Champagne Pool, Waiotapu, New Zealand. *Geobiology* **3**, 93-114.

Harrar, J., Locke, F., Otto Jr, C., Deutscher, S., Frey, W., Lorensen, L., Snell, E., Lim, R., Ryon, R., Quong, R., 1980. *Tests of proprietary chemical additives as antiscalants for hypersaline geothermal brine. Final report*. Lawrence Livermore Laboratories.

Harrar, J., Locke, F., Otto Jr, C., Lorensen, L., Monaco, S., Frey, W., 1982. Field tests of organic additives for scale control at the Salton Sea geothermal field. *Society of Petroleum Engineers Journal* **22**, 17-27.

Harrison, C.C., Loton, N., 1995. Novel routes to designer silicas: studies of the decomposition of $(M^{+})_2[Si(C_6H_4O_2)_3] \cdot H_2O$. Importance of M^{+} identity of the kinetics of oligomerisation and the structural characteristics of the silicas produced. *Journal of the Chemical Society, Faraday Transactions* **91**, 4287-4297.

Hawkins, C., Angheluta, L., Hammer, Ø., Jamtveit, B., 2013. Precipitation dendrites in channel flow. *Europhysics Letters* **102**, 54001.

Hawkins, C., van den Heuvel, D., Angheluta, L., Benning, L., Jamtveit, B., in prep. Simulation of silica particle aggegation from unidirectional flow in comparison with geothermal silica precipitates.

Heaney, P.J., 1994. Structure and chemistry of the low-pressure silica polymorphs. *Reviews in Mineralogy and Geochemistry* **29**, 1-40.

Henley, R., 1983. pH and silica scaling control in geothermal field development. *Geothermics* **12**, 307-321.

Herdianita, N., Browne, P., Rodgers, K., Campbell, K., 2000. Mineralogical and textural changes accompanying ageing of silica sinter. *Mineralium Deposita* **35**, 48-62.

Hjorleifsdottir, S., Skirnisdottir, S., Hreggvidsson, G., Holst, O., Kristjansson, J., 2001. Species composition of cultivated and noncultivated bacteria from short filaments in an Icelandic hot spring at 88 °C. *Microbial Ecology* **42**, 117-125.

Hochstein, M., 1990. *Classification and assessment of geothermal resources, Small geothermal resources: A guide to development and utilization*. UNITAR, New York, pp. 31-57.

Hudson, J.A., Morgan, H.W., Daniel, R.M., 1989. Numerical classification of Thermus isolates from globally distributed hot springs. *Systematic and Applied Microbiology* **11**, 250-256.

Icopini, G.A., Brantley, S.L., Heaney, P.J., 2005. Kinetics of silica oligomerization and nanocolloid formation as a function of pH and ionic strength at 25 °C. *Geochimica et Cosmochimica Acta* **69**, 293-303.

Iler, R.K., 1979. *The chemistry of silica: solubility, polymerization, colloid and surface properties, and biochemistry*. Wiley, London.

Inagaki, F., Hayashi, S., Doi, K., Motomura, Y., Izawa, E., Ogata, S., 1997. Microbial participation in the formation of siliceous deposits from geothermal water and analysis of the extremely thermophilic bacterial community. *FEMS Microbiology Ecology* **24**, 41-48.

Ito, J., Kubota, Y., Kurosawa, M., 1977. On the silica scale of the Onuma geothermal power plant. *Chinetsu* **14**, 173-179.

Jones, B., Renaut, R.W., 2003. Hot spring and geyser sinters: the integrated product of precipitation, replacement, and deposition. *Canadian Journal of Earth Sciences* **40**, 1549-1569.

Jones, B., Renaut, R.W., 2004. Water content of opal-A: implications for the origin of laminae in geyserite and sinter. *Journal of Sedimentary Research* **74**, 117-128.

Jones, B., Renaut, R.W., 2007. Microstructural changes accompanying the opal-A to opal-CT transition: New evidence from the siliceous sinters of Geysir, Haukadalur, Iceland. *Sedimentology* **54**, 921-948.

Jones, B., Renaut, R.W., 2010. Impact of seasonal changes on the formation and accumulation of soft siliceous sediments on the discharge apron of Geysir, Iceland. *Journal of Sedimentary Research* **80**, 17-35.

Jones, B., Renaut, R.W., Rosen, M.R., 1998. Microbial biofacies in hot-spring sinters: a model based on Ohaaki Pool, North Island, New Zealand. *Journal of Sedimentary Research* **68**, 413-434.

Jones, B., Renaut, R.W., Rosen, M.R., 2000. Stromatolites forming in acidic hot-spring waters, North Island, New Zealand. *Palaios* **15**, 450-475.

Jones, J., Segnit, E., 1969. Water in sphere-type opal. *Mineralogical Magazine* **37**, 357-361.

Karabelas, A., Andritsos, N., Mouza, A., Mitrakas, M., Vrouzi, F., Christanis, K., 1989. Characteristics of scales from the Milos geothermal plant. *Geothermics* **18**, 169-174.

Kitahara, S., 1960. The polymerization of silicic acid obtained by the hydrothermal treatment of quartz and the solubility of amorphous silica. *Review of Physical Chemistry Japan* **30**, 131-137.

Klein, R., Meakin, P., 1989. Universality in colloid aggregation. *Nature* **339**, 360-362.

Kley, M., Kempter, A., Boyko, V., Huber, K., 2014. Mechanistic studies of silica polymerization from supersaturated aqueous solutions by means of time-resolved light scattering. *Langmuir* **30**, 12664-12674.

Konhauser, K., Ferris, F., 1996. Diversity of iron and silica precipitation by microbial mats in hydrothermal waters, Iceland: Implications for Precambrian iron formations. *Geology* **24**, 323-326.

Konhauser, K., Lalonde, S., Phoenix, V., 2008. Bacterial biomineralization: Where to from here? *Geobiology* **6**, 298-302.

Kristjansson, J.K., Alfredsson, G.A., 1983. Distribution of *Thermus spp.* in Icelandic hot springs and a thermal gradient. *Applied and Environmental Microbiology* **45**, 1785-1789.

Kvist, T., Ahring, B.K., Westermann, P., 2007. Archaeal diversity in Icelandic hot springs. *FEMS Microbiology Ecology* **59**, 71-80.

Lalonde, S.V., Konhauser, K.O., Reysenbach, A.L., Ferris, F.G., 2005. The experimental silicification of *Aquificales* and their role in hot spring sinter formation. *Geobiology* **3**, 41-52.

Langer, K., Flörke, O., 1974. Near infrared absorption spectra (4000–9000 cm^{-1}) of opals and the role of ''water''in these SiO_2*nH_2O minerals. *Fortschritte der Mineralogie* **52**, 17-51.

Lin, M., Lindsay, H., Weitz, D., Ball, R., Klein, R., Meakin, P., 1990. Universal reaction-limited colloid aggregation. *Physical Review A* **41**, 2005.

Lowe, D.R., Braunstein, D., 2003. Microstructure of high-temperature (> 73 °C) siliceous sinter deposited around hot springs and geysers, Yellowstone National Park: the role of biological and abiological processes in sedimentation. *Canadian Journal of Earth Sciences* **40**, 1611-1642.

Lynne, B.Y., Campbell, K.A., Moore, J., Browne, P., 2008. Origin and evolution of the Steamboat Springs siliceous sinter deposit, Nevada, USA. *Sedimentary Geology* **210**, 111-131.

Makrides, A.C., Turner, M., Slaughter, J., 1980. Condensation of silica from supersaturated silicic acid solutions. *Journal of Colloid and Interface Science* **73**, 345-367.

Malani, A., Auerbach, S.M., Monson, P.A., 2010. Probing the mechanism of silica polymerization at ambient temperatures using Monte Carlo simulations. *The Journal of Physical Chemistry Letters* **1**, 3219-3224.

Manceau, A., Ildefonse, P., Hazemann, J., Flank, A., Gallup, D., 1995. Crystal chemistry of hydrous iron silicate scale deposits at the Salton Sea geothermal field. *Clays and Clay Minerals* **43**, 304-317.

Matsoukas, T., Gulari, E., 1988. Dynamics of growth of silica particles from ammonia-catalyzed hydrolysis of tetra-ethyl-orthosilicate. *Journal of Colloid and Interface Science* **124**, 252-261.

McIntosh, G.J., 2013. Theoretical investigations into the nucleation of silica growth in basic solution part I – ab initio studies of the formation of trimers and tetramers. *Physical Chemistry Chemical Physics* **15**, 3155-3172.

Meier, D.B., Gunnlaugsson, E., Gunnarsson, I., Jamtveit, B., Peacock, C., Benning, L., 2014. Microstructural and chemical variation in silica-rich precipitates at the Hellisheiði geothermal power plant. *Mineralogical Magazine* **78**, 1381-1389.

Meyer-Dombard, D., Shock, E., Amend, J., 2005. Archaeal and bacterial communities in geochemically diverse hot springs of Yellowstone National Park, USA. *Geobiology* **3**, 211-227.

Morris, M., Vossos, P.H., 1970. *Large particle silica sols and method of production*. Google Patents.

Mountain, B., Benning, L., Boerema, J., 2003. Experimental studies on New Zealand hot spring sinters: rates of growth and textural development. *Canadian Journal of Earth Sciences* **40**, 1643-1667.

Mroczek, E., Graham, D., Bacon, L., 2011. *Silica deposition experiments: past work and future research directions*, International Workshop on Mineral Scaling in Geothermal Environments, Manila.

Mroczek, E., McDowell, G., 1988. *Silica scaling field experiments*, New Zealand Geothermal Workshop, Auckland.

Noguera, C., Fritz, B., Clément, A., 2015. Precipitation mechanism of amorphous silica nanoparticles: a simulation approach. *Journal of Colloid and Interface Science* **448**, 553-563.

Owen, L., 1975. *Precipitation of amorphous silica from high-temperature hypersaline geothermal brines*. Lawrence Livermore Laboratories.

Parks, G.A., 1965. The isoelectric points of solid oxides, solid hydroxides, and aqueous hydroxo complex systems. *Chemical Reviews* **65**, 177-198.

Perry, C.C., Keeling-Tucker, T., 2000. Biosilicification: the role of the organic matrix in structure control. *JBIC Journal of Biological Inorganic Chemistry* **5**, 537-550.

Petursdottir, S.K., Bjornsdottir, S.H., Hreggvidsson, G.O., Hjorleifsdottir, S., Kristjansson, J.K., 2009. Analysis of the unique geothermal microbial ecosystem of the Blue Lagoon. *FEMS Microbiology Ecology* **70**, 425-432.

Phoenix, V., Konhauser, K., Adams, D., Ármannsson, H., 1999. Photosynthetic controls on the silicification of cyanobacteria, in: Ármansson, H. (Ed.), *Proceedings of the 5th International Symposium on Geochemistry of the Earth's Surface*. Balkema, Rotterdam, Reykjavik, pp. 275-278.

Phoenix, V., Konhauser, K., Adams, D., Bottrell, S., 2001. Role of biomineralization as an ultraviolet shield: Implications for Archean life. *Geology* **29**, 823-826.

Phoenix, V.R., Adams, D.G., Konhauser, K.O., 2000. Cyanobacterial viability during hydrothermal biomineralisation. Chemical *Geology* **169**, 329-338.

Potapov, V., Trutnev, N., Gorbach, V., Generalov, M., Romanova, I., 2011. Obtaining of silica nanopowders from natural hydrothermal solutions. *Theoretical Foundations of Chemical Engineering* **45**, 471-477.

Purcell, D., Sompong, U., Yim, L.C., Barraclough, T.G., Peerapornpisal, Y., Pointing, S.B., 2007. The effects of temperature, pH and sulphide on the community structure of hyperthermophilic streamers in hot springs of northern Thailand. *FEMS Microbiology Ecology* **60**, 456-466.

Ramanlal, P., Sander, L., 1985. Theory of ballistic aggregation. *Physical Review Letters* **54**, 1828.

Renaut, R.W., Jones, B., Rosen, M.R., 1996. Primary silica oncoids from Orakeikorako hot springs, North Island, New Zealand. *Palaios* **11**, 446-458.

Reysenbach, A.-L., Longnecker, K., Kirshtein, J., 2000. Novel bacterial and archaeal lineages from an *in-situ* growth chamber deployed at a Mid-Atlantic Ridge hydrothermal vent. *Applied and Environmental Microbiology* **66**, 3798-3806.

Rogers, A.F., 1946. Sand fulgurites with enclosed lechatelierite from Riverside County, California. *The Journal of Geology* **54**, 117-122.

Rothbaum, H., Anderton, B., Harrison, R., Rohde, A., Slatter, A., 1979. Effect of silica polymerisation and pH on geothermal scaling. *Geothermics* **8**, 1-20.

Rothbaum, H., Rohde, A., 1979. Kinetics of silica polymerization and deposition from dilute solutions between 5 and 180 °C. *Journal of Colloid and Interface Science* **71**, 533-559.

Sanders, J., 1964. Colour of precious opal. *Nature* **204**, 1151-1153.

Sanders, J., 1985. Structure of opals. *Le Journal de Physique Colloques* **46**, C3-1-C3-8.

Schaffer, C.L., Thomson, K.T., 2008. Density functional theory investigation into structure and reactivity of prenucleation silica species. *The Journal of Physical Chemistry C* **112**, 12653-12662.

Schultze-Lam, S., Ferris, F., Konhauser, K., Wiese, R., 1995. *In-situ* silicification of an Icelandic hot spring microbial mat: implications for microfossil formation. *Canadian Journal of Earth Sciences* **32**, 2021-2026.

Segnit, E., Stevens, T., Jones, J., 1965. The role of water in opal. *Journal of the Geological Society of Australia* **12**, 211-226.

Sjöberg, S., 1996. Silica in aqueous environments. *Journal of Non-Crystalline Solids* **196**, 51-57.

Skirnisdottir, S., Hreggvidsson, G.O., Hjörleifsdottir, S., Marteinsson, V.T., Petursdottir, S.K., Holst, O., Kristjansson, J.K., 2000. Influence of sulfide and temperature on species composition and community structure of hot spring microbial mats. *Applied and Environmental Microbiology* **66**, 2835-2841.

Sosman, R.B., 1965. *Phases of silica*. Rutgers University Press, New Brusnwick.

Spada, S., Pembroke, T.J., Wall, G.J., 2002. Isolation of a novel *Thermus thermophilus* metal efflux protein that improves *Escherichia coli* growth under stress conditions. *Extremophiles* **6**, 301-308.

Squyres, S., Arvidson, R.E., Ruff, S., Gellert, R., Morris, R., Ming, D., Crumpler, L., Farmer, J., Des Marais, D., Yen, A., 2008. Detection of silica-rich deposits on Mars. *Science* **320**, 1063-1067.

Stranski, I.N., Krastanow, L., 1937. Zur Theorie der orientierten Ausscheidung von Ionenkristallen aufeinander. *Monatshefte für Chemie/Chemical Monthly* **71**, 351-364.

Sugama, T., Gawlik, K., 2002. Anti-silica fouling coatings in geothermal environments. *Materials Letters* **57**, 666-673.

Sugita, H., Bando, Y., Nakamura, M., 1998. Removal of silica from geothermal brine by seeding method using silica gel. *Journal of Chemical Engineering of Japan* **31**, 150-152.

Svavarsson, H.G., Einarsson, S., Brynjolfsdottir, A., 2014. Adsorption applications of unmodified geothermal silica. *Geothermics* **50**, 30-34.

Svensson, I.L., Sjöberg, S., Öhman, L.-O., 1986. Polysilicate equilibria in concentrated sodium silicate solutions. *Journal of the Chemical Society, Faraday Transactions 1: Physical Chemistry in Condensed Phases* **82**, 3635-3646.

Swamy, V., Saxena, S.K., Sundman, B., Zhang, J., 1994. A thermodynamic assessment of silica phase diagram. *Journal of Geophysical Research: Solid Earth* **99**, 11787-11794.

Takacs, C.D., Ehringer, M., Favre, R., Cermola, M., Eggertsson, G., Palsdottir, A., Reysenbach, A.-L., 2001. Phylogenetic characterization of the blue filamentous

bacterial community from an Icelandic geothermal spring. *FEMS Microbiology Ecology* **35**, 123-128.

Tanakaa, M., Takahashib, K., 2001. Silicate species in high pH solution molybdate, whose silica concentration is determined by colorimetry. *Analytica Chimica Acta* **429**, 117-123.

Thórhallsson, S., Ragnars, K., Arnórsson, S., Kristmannsdóttir, H., 1975. *Rapid scaling of silica in two district heating systems*, Proceedings United Nations Symposium on the Development and Use of Geothermal Resources, San Fransico, pp. 1445-1449.

Tobler, D.J., Benning, L.G., 2011. Bacterial diversity in five Icelandic geothermal waters: temperature and sinter growth rate effects. *Extremophiles* **15**, 473-485.

Tobler, D.J., Benning, L.G., 2013. *In-situ* and time resolved nucleation and growth of silica nanoparticles forming under simulated geothermal conditions. *Geochimica et Cosmochimica Acta* **114**, 156-168.

Tobler, D.J., Shaw, S., Benning, L.G., 2009. Quantification of initial steps of nucleation and growth of silica nanoparticles: An *in-situ* SAXS and DLS study. *Geochimica et Cosmochimica Acta* **73**, 5377-5393.

Tobler, D.J., Stefansson, A., Benning, L.G., 2008. *In-situ* grown silica sinters in Icelandic geothermal areas. *Geobiology* **6**, 481-502.

Ueda, A., Kato, K., Mogi, K., Mroczek, E., Thain, I.A., 2003. Silica removal from Mokai, New Zealand, geothermal brine by treatment with lime and a cationic precipitant. *Geothermics* **32**, 47-61.

van den Heuvel, D., Gunnlaugsson, E., Benning, L., in prep.a. Surface roughness and composition control silica deposition from geothermal fluids. *Geochemical Transactions.*

van den Heuvel, D., Gunnlaugsson, E., Gunnarsson, I., Stawski, T., Peacock, C., Benning, L., in prep.b. Two pathways of amorphous silica precipitation control scaling inside in-use geothermal pipelines. *Geochimica et Cosmochimica Acta*.

van den Heuvel, D.B., Gunnlaugsson, E., Benning, L.G., 2016. *Passivation of metal surfaces against corrosion by silica scaling*, Proceedings Workshop on Geothermal Reservoir Engineering Stanford.

Volmer, M., Weber, A., 1925. Keimbildung in übersättigten Gebilden. *Zeitschrift für Physikalische Chemie* **119**, 277-301.

Weres, O., Yee, A., Tsao, L., 1981. Kinetics of silica polymerization. *Journal of Colloid and Interface Science* **84**, 379-402.

White, D.E., Thompson, G.A., Sandberg, C.H., 1964. *Rocks, structure, and geologic history of Steamboat Springs thermal area, Washoe County, Nevada*. US Government Printing Office.

Willey, J.D., 1974. The effect of pressure on the solubility of amorphous silica in seawater at 0 °C. *Marine Chemistry* **2**, 239-250.

Yanagase, T., Suginohara, Y., Yanagase, K., 1970. The properties of scales and methods to prevent them. *Geothermics* **2**, 1619-1623.

Yokoyama, T., Sato, Y., Maeda, Y., Tarutani, T., Itoi, R., 1993. Siliceous deposits formed from geothermal water. I. The major constituents and the existing states of iron and aluminium. *Geochemical Journal* **27**, 375-384.

Yokoyama, T., Takahashi, Y., Tarutani, T., 1991. Retarding and accelerating effects of aluminum on the growth of polysilicic acid particles. *Journal of Colloid and Interface Science* **141**, 559-563.

Zhang, X.-Q., Trinh, T.T., van Santen, R.A., Jansen, A.P., 2011. Mechanism of the initial stage of silicate oligomerization. *Journal of the American Chemical Society* **133**, 6613-6625.

Zotov, N., Keppler, H., 2002. Silica speciation in aqueous fluids at high pressures and high temperatures. *Chemical Geology* **184**, 71-82.

Chapter 3

Microstructural and chemical variation in silica-rich precipitates at the Hellisheiði geothermal power plant

Daniela B. van den Heuvel[1], Einar Gunnlaugsson[2], Bjørn Jamtveit[3]
Caroline L. Peacock[1], Liane G. Benning[1,4]

[1] *Cohen Geochemistry Group, School of Earth and Environment, University of Leeds, Leeds LS2 9JT, UK*
[2] *Reykjavik Energy, Baejarhals 1, 110 Reykjavik, Iceland*
[3] *Physics of Geological Processes, Department of Geoscience, University of Oslo, 0316 Oslo, Norway*
[4] *German Research Center for Geosciences, GFZ, 14473 Potsdam, Germany*

Abstract

Precipitation of amorphous silica (SiO_2) in geothermal power plants, although a common factor limiting the efficiency of geothermal energy production, is poorly understood and no universally applicable mitigation strategy to prevent or reduce precipitation is available. This is primarily due to the lack of understanding of the precipitation mechanism of amorphous silica in geothermal systems. In the present study data are presented about microstructures and compositions of precipitates formed on scaling plates inserted at five different locations in the pipelines at the Hellisheiði power station (SW-Iceland). Precipitates on these plates formed over 6 to 8 weeks of immersion in hot (120 or 60 °C), fast-flowing and silica-supersaturated geothermal fluids (~800 ppm of SiO_2). Although the composition of the precipitates is fairly homogeneous, with silica being the dominant component and Fe sulphides as a less common phase, the microstructures of the precipitates are highly variable

and dependent on the location within the geothermal pipelines. The silica precipitates have grown through aggregation and precipitation of silica particles that precipitated homogeneously in the geothermal fluid. Five main factors were identified that may control the precipitation of silica: (1) temperature, (2) fluid composition, (3) fluid-flow regime, (4) distance along the flow path, and (5) immersion time. On all scaling plates, a corrosion layer was found underlying the silica precipitates indicating that, once formed, the presence of a silica layer probably protects the steel pipe surface against further corrosion. Yet silica precipitates influence the flow of the geothermal fluids and therefore can limit the efficiency of geothermal power stations.

3.1 Introduction

In geothermal power plants around the world the polymerization of monomeric silica and the formation and deposition of amorphous silica (SiO_2) precipitates on pipes and other fluid-handling systems (most often referred to as 'scaling') have been identified as the most common problems limiting the efficiency of geothermal power stations (Gunnarsson and Arnórsson, 2003). Although precipitation of amorphous silica in natural geothermal settings has been studied extensively (e.g., Mountain et al., 2003; Tobler et al., 2008), the processes that occur at the water-fluid-handling equipment interfaces (e.g., scale formation on pipes) are not well understood. A wide range of approaches to mitigate amorphous silica-scale formation, such as pH control (e.g., Fleming and Crerar, 1982; Henley, 1983; Stapleton and Weres, 2011), dilution and acidification with steam condensate (Gunnarsson and Arnórsson, 2003); or the use of (in)organic inhibitors (e.g., Harrar et al., 1982; Gallup, 2002; Gallup and Barcelon, 2005; Amjad and Zuhl, 2008) have been applied in various geothermal power plants. However, due to the large variations in geothermal fluid conditions, no single method for adequately mitigating silica scaling exists (Mroczek et al., 2011). One of the limits to developing a universally applicable mitigation approach is the lack of a fundamental understanding of the pathways and mechanisms of precipitation of amorphous silica. This is partly due to the dearth of data on silica-scale microstructures and compositions. In the present study, the microstructures and compositional characteristics of silica-dominated precipitates that formed in the pipes of the Hellisheiði geothermal power station in SW-Iceland were investigated.

3.2 Materials and Methods

Silica precipitation was monitored using stainless steel scaling plates (5 x 2.5 cm) deployed at different points within the pipelines of the Hellisheiði geothermal power plant, but in all cases after the steam used for the production of electrical energy was separated (Figure 3.1). The chemical composition and pH of the separated water at sampling point 1 is monitored at regular intervals by the power plant operators. The separated water is cooled and filtered before the pH is measured and sample aliquots are taken for various analyses. For details of sample preservation and sampling containers see Arnórsson et al. (2006). The cations were analysed by ion chromatography (IC) at Reykjavik Energy while the anions were analysed using inductively coupled plasma-mass spectrometry at the University of Iceland. The concentration of H_2S is measured by titration with mercury acetate using dithizone as an indicator (Arnórsson et al., 2006).

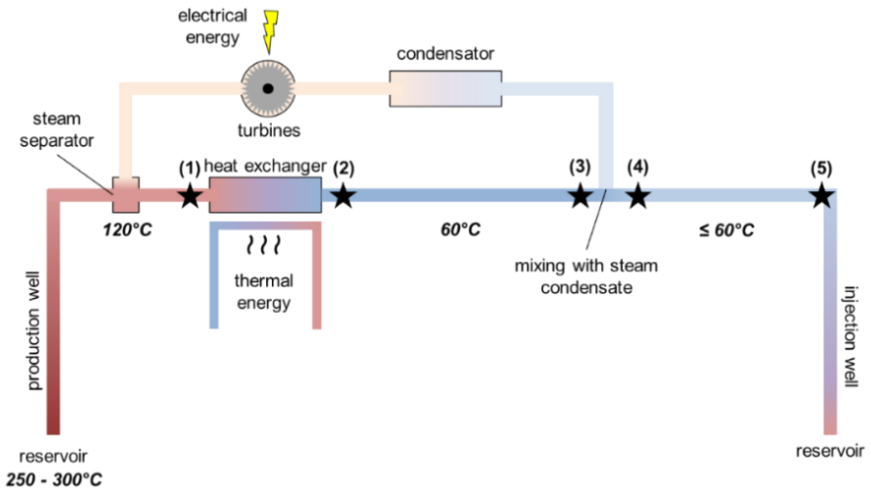

Figure 3.1: *System schematic of the Hellisheiði geothermal power station indicating the five points (*) where the scaling plates were immersed. The geothermal fluid at depth, being at up to 300 °C, is flowing up through production wells. In the steam separator the pressure is released and the geothermal fluid boils, separating the steam (used for the production of electrical energy) from the fluid. The remaining geothermal fluid (also called separated water) is passed through a heat exchanger where it heats up cold groundwater to be used for space heating. Some tens of metres further along the flow path, the geothermal fluid is mixed with steam condensate to dilute it before re-injecting it some hundreds of metres further downstream.*

The plates were inserted into the path of the flowing geothermal fluid for 6 (plates 2, 3 and 4) or 8 weeks (plates 1 and 5). After removal from the separated water, the plates were first dried at room temperature on-site, and, after shipping to Leeds (UK), were dried again at 30 °C for 24 h before further analysis.

Some precipitates were scraped off of one side of each plate using a plastic spatula and ground using an agate mortar and pestle. The powder was analysed by X-ray diffraction using a Bruker D8 diffractometer (XRD, $CuK_{\alpha 1}$; 5-90° 2θ; 0.01°/step) and the patterns were evaluated using the EVA software (Bruker, Version 3.0). The other side of the plates was coated with ~40 nm of gold and imaged using a field emission scanning electron microscope (FEG SEM, FEI Quanta 650 at 20 keV). Spot analyses and elemental mapping were performed using an energy dispersive spectrometer (EDS) and the Aztec software (Oxford Instruments, Version 2.2).

3.3 Results

The separated water from which precipitation occurred is a dilute, low-ionic-strength fluid with a high concentration of dissolved H_2S and a pH varying between 9.1 and 9.4 (Table 3.1). Depending on which production well is used, the waters contain between 700 and 800 ppm SiO_2 (Table 3.1). No data are currently available about solution compositions at the other sampling points. After 6-8 weeks of immersion, all scaling plates showed visible signs of precipitation. Although the XRD analyses revealed silica as the dominant precipitate in all cases, the microstructures of the precipitates were highly variable (Figure 3.2). Precipitation onto plate 1 occurred at 120 °C due to its position directly before the heat exchanger (Figure 3.1). The precipitates formed large (up to 1 – 2 mm) fan-shaped structures pointing towards the direction of the flow (Figure 3.2 & 3.3 A). The fans were composed of silica particles (~1 – 20 μm in diameter; Figure 3.3 F), while the rest of the plate was covered by individual silica spheres or idiomorphic Fe sulphides. The precipitates on plate 2 formed immediately after the heat exchanger (Figure 3.1) at 60 °C. They formed wave-shaped structures, oriented parallel to the flow (Figure 3.2), again consisting of larger, weakly aggregated silica spheres. These were overlying a film of smaller silica particles forming aggregates up to 50 μm in diameter (Figure 3.3 B). Plate 3 was located immediately before the point at which the geothermal fluid is mixed with steam condensate fluid (Figure 3.1), and was characterized by the smallest amount of silica precipitates (Figures 3.2 & 3.3 C).

Table 3.1: *Chemical composition of the separated water at sampling location 1 (Figure 3.1; before the heat exchanger, 120 °C). The data represent average values of measurements between September 2012 and January 2014 (n = 4). The variations in pH and concentration are due to the use of different production wells, tapping different parts of the aquifer, at different points in time.*

Separated water sample location 1 (before heat exchanger)	
pH	9.1 – 9.4
Concentration	(mg/kg)
H_2S	25.2 – 30.4
SiO_2 (total)	694.9 – 787.2
Na	194.6 – 209.4
K	26.1 – 36.6
Ca	0.74 – 1.05
Mg	< 0.03
Fe	< 0.25
Al	1.80 – 2.06
Cl	161.6 – 193.6
SO_4	16.2 – 54.6
F	1.2 – 1.6

The precipitates on plate 4 consisted of individual or connected flakes of a dark grey precipitate (Figures 3.2 & 3.3 D), which consisted of very small (< 1 μm) angular Fe sulphide aggregates and (0.1 μm) spherical silica particles (Figure 3.3 D; XRD results revealed mackinawite, greigite and pyrrhotite). The metal between the flakes was covered by spherical silica particles (0.1 – 0.5 μm in size) and idiomorphic, columnar sulphur crystals several μm long. Plate 5 was characterized by the largest amount of precipitate and was covered densely by grey ridges oriented perpendicular to the flow (Figure 3.2). These ridges (Figure 3.3 E) were composed of individual, small silica spheres (0.1 – 0.5 μm in diameter) that were occasionally interspersed with larger, smooth silica particles (up to 10 μm in diameter). Along the rims of some plates, a clear morphological (Figure 3.4 A) and compositional (Figure 3.5) layering was revealed. Underlying the silica precipitates (Figures 3.4 B & 3.5) was a layer composed of fine-grained, often idiomorphic Fe sulphides (Figures 3.4 C & 3.5). In some areas even the corrosion of the stainless steel plates was

observed in the form of rosette-shaped Fe oxides (Figure 3.4 D). Based on the shape of the mineral phase, this was probably hematite. Due to the small amount of these Fe sulphides and Fe oxides on the plates, a definitive mineralogical identification or quantification was not feasible.

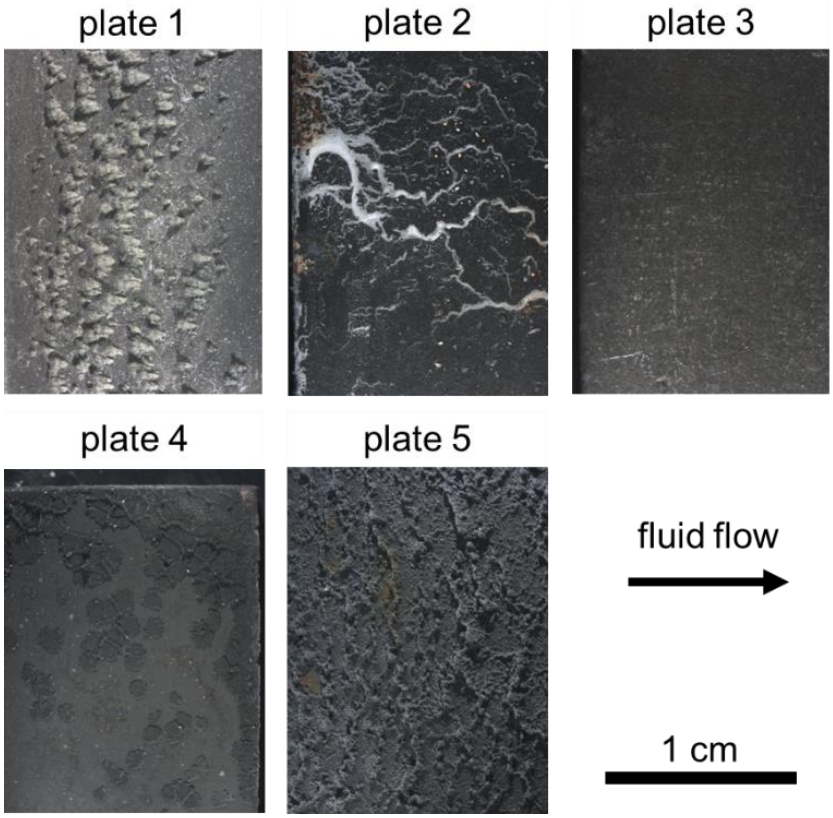

Figure 3.2: *Photographs of the scaling plates after immersion in the geothermal fluid for 6 (plates 2, 3 and 4) and 8 weeks (plates 1 and 5), respectively. The precipitates on each plate show distinct microstructures from fan-shaped (1) to wave-like (2) to thin films (3) and to dark flakes (4) or even ridge-shaped (5).*

3.4 Discussion

The results from this study of precipitates formed on scaling plates immersed in the fast-flowing geothermal waters in the pipes of the Hellisheiði geothermal power station revealed that the microstructures and compositions of precipitates varied considerably along the flow path. Distinct microstructures that range from fan-shaped to wave-like to individual flakes or even ridge-shaped precipitates were observed. The dominant phases present on the scaling plates were amorphous silica, Fe sulphides and rarely Fe oxides. Silica was present as spherical nanoparticles

which form by homogeneous nucleation (Tobler et al., 2009; Tobler and Benning, 2013) from the supersaturated geothermal fluids that contained ~800 ppm of silica. The data assembled indicate that once the particles that form in solution come into contact with the scaling plates (or the pipe surfaces) they are deposited. Monomeric silica will also polymerize continuously, cementing the particles together to form larger and larger clusters (Angcoy and Arnórsson, 2010).

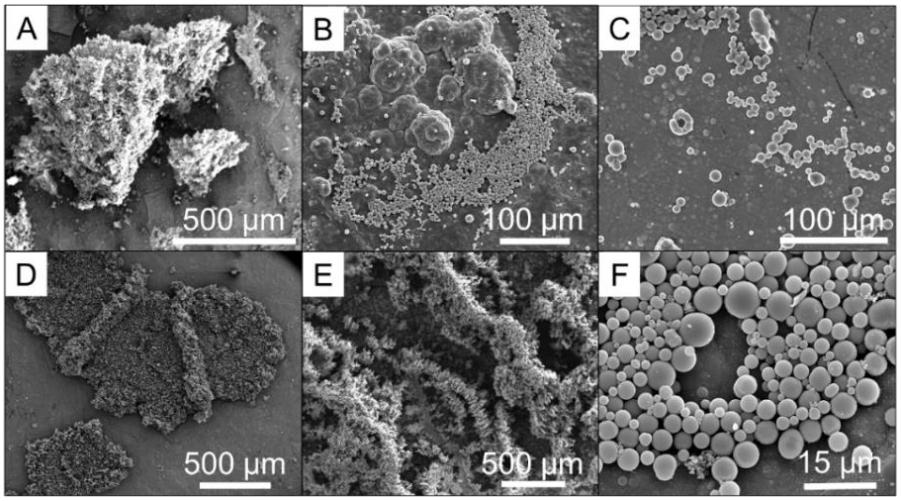

Figure 3.3: *FEG-SEM images showing the different microstructure of the precipitates on the scaling plates. The microstructures on plate 1 (A), plate 2 (B), plate 3 (C) and plate 5 (E) are formed by the aggregation of silica particles (F). On plate 4 (D) the precipitates are dominated by Fe sulphides.*

The iron phases (Fe sulphides and Fe oxides) largely represent corrosion products. The Fe could be sourced either from the plates or pipes themselves or from the geothermal fluid and when combined with H_2S from the geothermal fluid would precipitate as Fe sulphides, and upon oxidation probably transform to Fe oxides. The observed variations in composition and microstructures are the result of differences in physicochemical conditions in the power-plant pipelines. Although the data assembled so far cannot fully explain all our observations, five parameters have been identified that play a crucial role in controlling the precipitation regimes and modes of amorphous silica deposition on our scaling plates. These are:

(1) Variation in temperature: an increase in temperature results in greater rates of polymerization of monomeric silica and hence an increased rate of formation of amorphous silica nanoparticles (e.g., Alexander et al., 1954;

Kitahara, 1960; Tobler and Benning, 2013). At higher temperatures this effect could be counterbalanced by the greater solubility of amorphous silica and the resulting decrease in supersaturation (Makrides et al., 1980; Gunnarsson and Arnórsson, 2000).

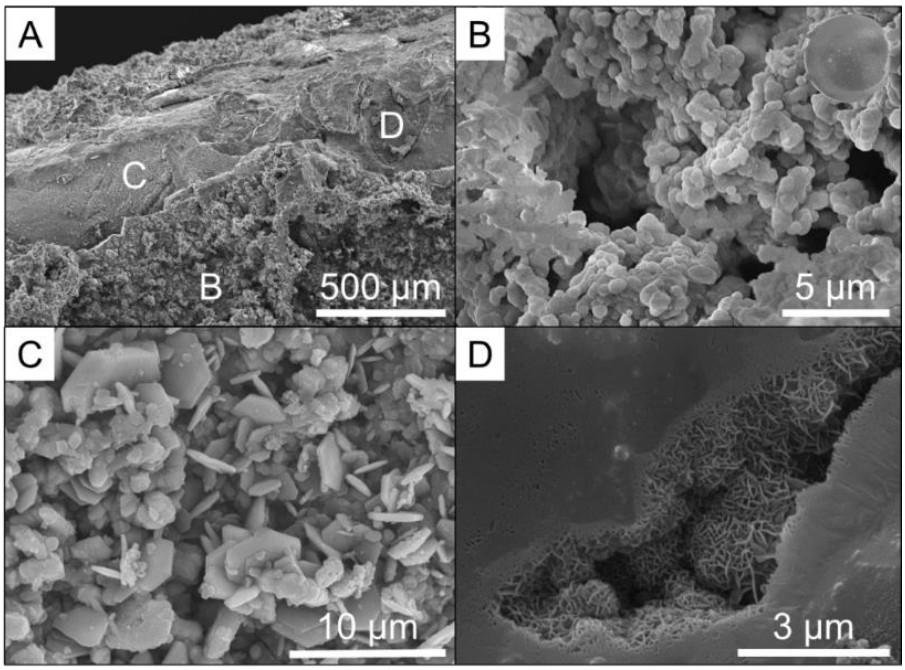

Figure 3.4: *(A) Different layers at the edge of plate 5 showing the top layer consisting of amorphous silica spheres, aggregated to form delicate structures (B). The silica layer covers a layer of Fe sulphides (C) probably a corrosion product of the scaling plate while underneath this layer, the metal of the scaling plate (D) was oxidized to Fe oxides.*

(2) Variation in fluid composition: the composition of the geothermal fluid is crucial for the composition of the phases formed on the scaling plates. The dominant phases on plate 4, for example, which formed immediately after the addition of steam condensate to the geothermal fluid (Figure 3.1), were Fe-sulphides. In this case, the precipitation of Fe sulphides was enhanced locally because of the mixing with steam condensate. The concentration of dissolved iron in the steam condensate is marginally greater than in the separated water (power-plant operators, pers. comm.). Therefore, when the Fe-rich steam condensate mixes with the H_2S from the geothermal fluid this may result in the very fast precipitation of Fe sulphides. The addition of condensate also decreased the concentration of silica and diluted the

geothermal fluid. Lower supersaturation of silica combined with reduced ionic strength of the geothermal fluid results in slower precipitation of silica (Fleming, 1986; Icopini et al., 2005). This may, in part, explain the smaller amount of amorphous silica on plate 4 compared to all the other plates.

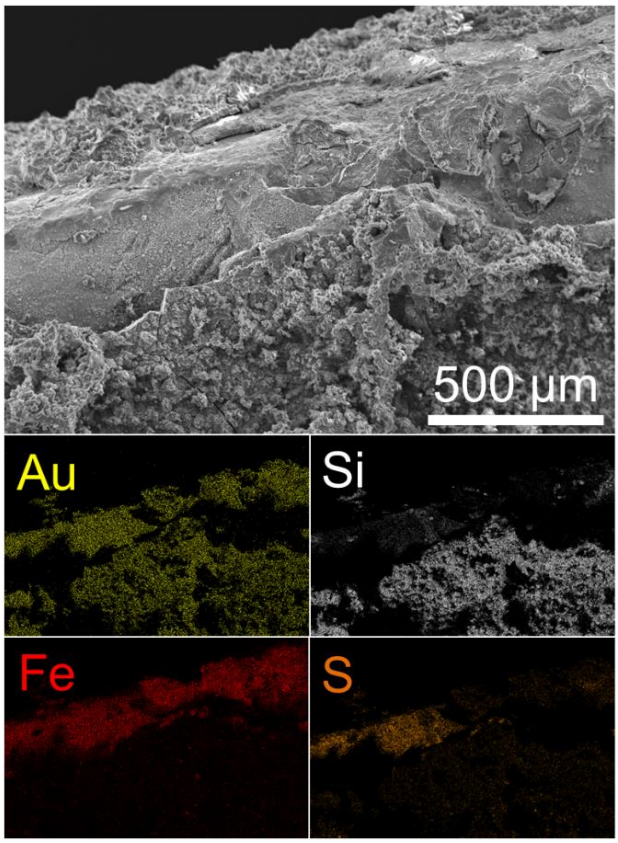

Figure 3.5: *Elemental maps of the layers on plate 5 described in Fig. 4 with the uppermost precipitation layer showing primarily Si which overlies the Fe sulphide layer (Fe and S maps) and the metal plate (Fe map). Dark areas on the Au map indicate areas where the topography of the sample resulted in a poor EDS signal. These areas will be dark in all elemental maps.*

(3) Fluid-flow regime: fan-shaped structures like those on plate 1 have recently been modelled by Hawkins et al. (2014). The authors used fluid dynamic modelling approaches and simulated the surface growth processes in a geothermal pipeline in the presence of non-homogeneous and non-laminar flow. Those authors found that the competition between advection and diffusion (Péclet number) and the turbulence characteristics (Reynolds number) define the exact geometry of the precipitates. The microstructures

found on plate 1 (Figures 3.2 & 3.3 A) are matched by the modelling results, thus confirming that fluid flow does indeed play a dominant role. However, why this microstructure was only observed on plate 1 (120 °C, before the heat exchanger) is not yet clear and further time-resolved immersion experiments that are in progress hope to address this.

(4) Distance along the flow path: the precipitation of silica is affected by the distance between a spot where the physicochemical conditions in the power-plant pipelines change drastically and the location of the scaling plate. An example is the effect of cooling the geothermal fluid from 120 to 60 °C in the heat exchanger: This temperature drop affects the rate of polymerization rate and it was shown by Tobler and Benning (2013) that it may take up to 3 h to reach steady state again. Hence, the precipitation conditions where plate 2 is located are different from the conditions further downstream where plate 3 is located. Another example are the differences between plates 4 and 5. The addition of steam condensate enhances precipitation of Fe sulphides (see above) onto plate 4. As plate 5 is located several hundred metres further downstream, the geothermal fluid at plate 5 had more time to react to the physicochemical disturbance and re-equilibrate. Thus, at plate 5, amorphous silica again becomes the primary precipitate.

(5) Immersion time: the amount of time for which the scaling plates are immersed in the geothermal fluid will have an effect on the amount of material precipitated and probably on the microstructures formed. In the present study, only precipitation after 6 to 8 weeks was studied but precipitation has been monitored since commissioning of the Hellisheiði power station in 2006. The rates of precipitation are not known, however. In order to investigate precipitation and the evolution of microstructures as a function of time, additional time-resolved experiments are in progress.

In spite of detailed evaluation of the microstructures and compositions of the precipitates on the individual plates, the exact contributions of the individual factors mentioned above remain unclear.

All precipitates were made up of different layers (Figures 3.4 & 3.5): (1) the stainless steel metal plate that in some cases was partly oxidized to Fe oxides; (2) the corrosion layer composed primarily of Fe sulphides; and (3) the main precipitation

layer composed mainly of spherical amorphous silica and, in the case of plates 1 and 4, Fe sulphides. The precipitation of amorphous silica (and Fe sulphides on plate 4), the corrosion of the plates and the related formation of Fe sulphides are probably concurrent processes both starting as soon as the plates are immersed in the geothermal fluids. The Fe sulphide corrosion layer was in most cases concealed under the silica precipitates, however, suggesting that before a protective amorphous silica layer could form, metal corrosion dominated. Once the precipitation layer became more continuous, further corrosion was passivated or at least slowed down by the amorphous silica (and Fe sulphides on plate 4) layer. Thus, the precipitation of amorphous silica does indeed limit the efficiency of geothermal power production by reducing the flow of geothermal fluid through the system (Gunnarsson and Arnórsson, 2003) but, its deposition in thin, variable structured layers also helps to limit the corrosion of the steel pipes. To explore this passivation effect, a longer-term (12 months), time-resolved, scaling-plate exposure study is already underway.

3.5 Conclusion

The results presented here provide the first detailed description of silica-rich precipitates in pipes from the Hellisheiði power station. The microstructure and composition of the precipitates vary considerably depending on the ambient physicochemical conditions in the power-plant pipelines. However, exactly how and why particular physicochemical conditions lead to a variety of microstructures in the silica precipitates is still unclear. Nevertheless, this study presents important findings which, combined with fluid chemical data, information about fluid flow and longer-term scaling-plate immersion experiments, will allow us to derive the first comprehensive model for silica precipitation in geothermal systems and this information will potentially help to reduce silica scaling in geothermal power plants.

Acknowledgements

The authors acknowledge the help of the staff at the Hellisheiði power station, especially Einar Örn Thrastarson, for their support with emplacing and removing the scaling plates from the pipes. The authors are also grateful to Richard Walshaw and Lesley Neve, University of Leeds, for their assistance with SEM and XRD analyses,

respectively. Comments by several members of the Cohen Geochemistry group at Leeds, by Thomas Rinder (Guest Associate Editor) and three anonymous reviewers have helped to improve this manuscript. This research was made possible by a Marie Curie grant from the European Commission in the framework of the MINSC ITN (Initial Training Research network), Project number 290040.

References

Alexander, G.B., Heston, W., Iler, R.K., 1954. The solubility of amorphous silica in water. *The Journal of Physical Chemistry* **58**, 453-455.

Amjad, Z., Zuhl, R., 2008. *An evaluation of silica scale control additives for industrial water systems*, Proceedings of the NACE International Corrosion Conference and Expo, New Orleans, pp. 3180-3192.

Angcoy, E., Arnórsson, S., 2010. *An experiment on monomeric and polymeric silica precipitation rates from supersaturated solutions*, Proceedings of the World Geothermal Congress, Bali.

Arnórsson, S., Bjarnason, J.Ö., Giroud, N., Gunnarsson, I., Stefánsson, A., 2006. Sampling and analysis of geothermal fluids. *Geofluids* **6**, 203-216.

Fleming, B., Crerar, D., 1982. Silicic acid ionization and calculation of silica solubility at elevated temperature and pH application to geothermal fluid processing and reinjection. *Geothermics* **11**, 15-29.

Fleming, B.A., 1986. Kinetics of reaction between silicic acid and amorphous silica surfaces in NaCl solutions. *Journal of Colloid and Interface Science* **110**, 40-64.

Gallup, D.L., 2002. Investigations of organic inhibitors for silica scale control in geothermal brines. *Geothermics* **31**, 415-430.

Gallup, D.L., Barcelon, E., 2005. Investigations of organic inhibitors for silica scale control from geothermal brines–II. *Geothermics* **34**, 756-771.

Gunnarsson, I., Arnórsson, S., 2000. Amorphous silica solubility and the thermodynamic properties of H_4SiO_4 in the range of 0 to 350 °C at P_{sat}. *Geochimica et Cosmochimica Acta* **64**, 2295-2307.

Gunnarsson, I., Arnórsson, S., 2003. *Silica scaling: The main obstacle in efficient use of high-temperature geothermal fluids*, Proceedings International Geothermal Conference, Reykjavik, pp. 30-36.

Harrar, J., Locke, F., Otto Jr, C., Lorensen, L., Monaco, S., Frey, W., 1982. Field tests of organic additives for scale control at the Salton Sea geothermal field. *Society of Petroleum Engineers Journal* **22**, 17-27.

Hawkins, C., Angheluta, L., Jamtveit, B., 2014. Hydrodynamic shadowing effect during precipitation of dendrites in channel flow. *Physical Review E* **89**, 022402.

Henley, R., 1983. pH and silica scaling control in geothermal field development. *Geothermics* **12**, 307-321.

Icopini, G.A., Brantley, S.L., Heaney, P.J., 2005. Kinetics of silica oligomerization and nanocolloid formation as a function of pH and ionic strength at 25 °C. *Geochimica et Cosmochimica Acta* **69**, 293-303.

Kitahara, S., 1960. The polymerization of silicic acid obtained by the hydrothermal treatment of quartz and the solubility of amorphous silica. *Review of Physical Chemistry Japan* **30**, 131-137.

Makrides, A.C., Turner, M., Slaughter, J., 1980. Condensation of silica from supersaturated silicic acid solutions. *Journal of Colloid and Interface Science* **73**, 345-367.

Mountain, B., Benning, L., Boerema, J., 2003. Experimental studies on New Zealand hot spring sinters: rates of growth and textural development. *Canadian Journal of Earth Sciences* **40**, 1643-1667.

Mroczek, E., Graham, D., Bacon, L., 2011. *Silica deposition experiments: past work and future research directions*, Proceedings International Workshop on Mineral Scaling in Geothermal Environments, Manila.

Stapleton, M., Weres, O., 2011. *Recent Developments in Geothermal Scale Control*, International Workshop on Mineral Scaling in Geothermal Environments, Manila.

Tobler, D.J., Benning, L.G., 2013. *In-situ* and time resolved nucleation and growth of silica nanoparticles forming under simulated geothermal conditions. *Geochimica et Cosmochimica Acta* **114**, 156-168.

Tobler, D.J., Shaw, S., Benning, L.G., 2009. Quantification of initial steps of nucleation and growth of silica nanoparticles: An *in-situ* SAXS and DLS study. *Geochimica et Cosmochimica Acta* **73**, 5377-5393.

Tobler, D.J., Stefansson, A., Benning, L.G., 2008. *In-situ* grown silica sinters in Icelandic geothermal areas. *Geobiology* **6**, 481-502.

Chapter 4

Two pathways of amorphous silica precipitation control scaling inside in-use geothermal pipelines

Daniela B. van den Heuvel[1], Einar Gunnlaugsson[2], Ingvi Gunnarsson[2], Tomasz M. Stawski[1,3], Caroline L. Peacock[1], Liane G. Benning[1,3]

[1] *Cohen Geochemistry Group, School of Earth and Environment, University of Leeds, Leeds LS2 9JT, UK*
[2] *Reykjavik Energy, Baejarhals 1, 110 Reykjavik, Iceland*
[3] *German Research Center for Geosciences, GFZ, 14473 Potsdam, Germany*

Abstract

Silica precipitation (= scaling) inside high-enthalpy geothermal power plants has previously been shown to be controlled by a combination of different physico-chemical factors. Yet a mechanistic understanding of the scaling occurring inside pipelines has been lacking. Here we report the results from the first ever time-resolved study of silica precipitation conducted inside in-use pipelines we left scaling plates to react with the fast flowing geothermal waters at four locations within the Hellisheiði power plant for 1 day to 10 weeks. The results revealed two distinct types of precipitates: (1) A continuous silica layer covering the scaling plates completely (even after just 1 day) that steadily grew in thickness and (2) 3D fan- or ridge-shaped aggregates which formed after longer exposure times and consisted of aggregated silica microspheres. The continuous layers grew by heterogeneous nucleation and subsequent growth by monomer addition while the formation of the 3D aggregates was dominated by homogeneous nucleation of particles in the fluid

and their subsequent aggregation and cementation into 3D structures. From the time-resolved data we determined silica precipitation rates of up to 1 gram per day per m^2. Our data helps improve our understanding of the silica scaling mechanism inside geothermal power plants and is crucial for the development of better mitigation strategies against silica scaling in the future.

4.1 Introduction

Amorphous silica is one of the most common phases to precipitate from high-enthalpy geothermal fluids that are rich in dissolved silica due to rock-water interactions in the geothermal reservoir. The maximum concentration of silica depends on the reservoir temperature and is controlled by quartz solubility or, if the temperature is below 110 °C, by the solubility of chalcedony (Fournier and Rowe, 1966; Arnórsson, 1975). Geothermal fluids can reach the surface naturally, i.e., by ascending along fractures, where they emerge as hot springs and geysers or by being pumped from the reservoir for the production of geothermal energy. In both cases the fluids are subjected to rapid cooling and depressurisation upon reaching the surface. This results in fluids which are supersaturated with respect to amorphous silica and consequent rapid precipitation. Around hot springs these deposits are called silica sinters, around geysers, geyserites and inside geothermal power plants silica scales.

The precipitation of amorphous silica has been investigated over a wide range of physico-chemical conditions over the last few decades and the process, despite its complexity, is relatively well understood. The formation of amorphous silica has been shown to occur via the condensation of silica monomers (H_4SiO_4) through nucleation, subsequent growth and aggregation and/or deposition (e.g., Iler, 1979; Rothbaum and Rohde, 1979; Icopini et al., 2005; Tobler et al., 2009). The precipitation of amorphous silica is enhanced by alkaline pH, elevated temperature, increasing ionic strength (especially the presence of Al and Fe) and high total silica concentration (Alexander et al., 1954; Goto, 1956; Kitahara, 1960; Iler, 1979; Crerar et al., 1981; Weres et al., 1981; Fleming, 1986; Gallup, 1997; Gunnarsson and Arnórsson, 2005; Icopini et al., 2005; Tobler and Benning, 2013). These physico-chemical factors are also expected to affect the precipitation of silica from natural geothermal fluids. However, in natural geothermal fluids all these parameters are in competition with one another and it is often difficult to isolate the parameter which

affects silica precipitation most strongly. In addition, complicating factors such as microbial activity in hot springs (e.g., Mountain et al., 2003; Tobler et al., 2008) or high flow in geothermal power plants (e.g., Meier et al., 2014 (Chapter 3)) make the understanding of these natural systems even more challenging. Therefore, the findings from laboratory studies cannot be applied directly to silica precipitation from natural geothermal fluids as shown by Carroll et al. (1998).

While silica sinter formation has been studied in depth in recent years (e.g., Braunstein and Lowe, 2001; Mountain et al., 2003; Jones and Renaut, 2004; Konhauser et al., 2004; Handley et al., 2005; Tobler et al., 2008), very few studies addressed the formation of amorphous silica inside geothermal power plants (e.g., Gudmundsson and Bott, 1979; Rothbaum et al., 1979; Carroll et al., 1998), despite the fact that silica scaling presents a huge problem for the energy production in geothermal systems (e.g., Gunnarsson and Arnórsson, 2003; Demadis et al., 2007). The main reason for the lack of such studies lies in the difficulties in accessing both, fluids and silica scales during production without being detrimental to normal operations. There have been some studies that aimed to circumvent these problems, by conducting experiments at geothermal power plants in bypass systems (Rothbaum et al., 1979; Harrar et al., 1982; Carroll et al., 1998). Yet, the conditions in such bypass systems are most often markedly different from those inside in-use geothermal pipelines because of lower flow rates, changes in temperatures, redox conditions or hydrodynamic regimes due to the variations in pipe geometries etc. (Rothbaum et al., 1979). Such changes lead to differences in precipitation pathways and/or rates, which are thus often difficult to translate to scaling processed occurring inside in-use pipelines. This means that control and potential silica-scaling mitigation strategies are not well informed.

Here we present the first ever *in-situ* and time-resolved study conducted inside actual geothermal pipelines of a high enthalpy geothermal power plant at Hellisheiði, SW-Iceland (Figure 4.1 A). All our experiments were carried out under conditions of normal operation and had access to both, fluid samples and precipitated solids. Silica precipitation was monitored using stainless steel scaling plates (Figure 4.1 B) deployed at different points within the pipelines of the Hellisheiði geothermal power plant for periods between 1 day and 10 weeks,. The results show that two largely independent pathways control silica precipitation and that continuous layers of silica form very rapidly on steel surfaces, yet over long time periods 3D structures will also form.

4.2 Materials and methods

Field deployments

The time-resolved deposition of silica scales on stainless steel scaling plates (5.4 x 2-2.5 cm) deployed between 1 day and 10 weeks (Table 4.1) was studied at four different locations within the Hellisheiði power plant (Figure 4.1): (1) several metres before the heat exchangers, (2) several metres after the heat exchangers, (3) several tens of metres downstream of location 2, just before mixing with condensed steam (equivalent to almost pure water) and (4) 500 m downstream from location 3 at the Húsmúli injection site. The locations were chosen because they differed with respect to physico-chemical conditions of the fluid (temperature, flow rate, silica concentration etc.) and this allowed us to study how these parameters affected silica precipitation.

At each location scaling plates made from unpolished S316 stainless steel (Figure 4.1 C & D) were attached to a sampling rod and inserted into the geothermal fluid through valves in the pipeline walls. The surfaces of the plates were aligned to be parallel to the flow.

The power plant operators monitor the temperatures and flow rates at each of the chosen sampling locations hourly to identify changes in production parameters and as a guide for when maintenance (e.g., heat exchanger cleaning) is required (Table 4.1). These continuous datasets helped make sure that the scaling plate deployments were started/finished during periods where no maintenance was required. At the end of each deployment, the plates were removed from the fluid, gently rinsed with distilled water to remove soluble salts and dried at 40 °C for 12 to 16 hours. For short deployments (1 day, 3 days and 1 week), the scaling plates were also weighted before and after the deployments in order to determine the mass of the precipitated silica. For deployments of 2 weeks or longer this was not feasible as in most cases some of the accumulated silica would have been either lost during deployment (high fluid flow) or during scaling plate handling post removal.

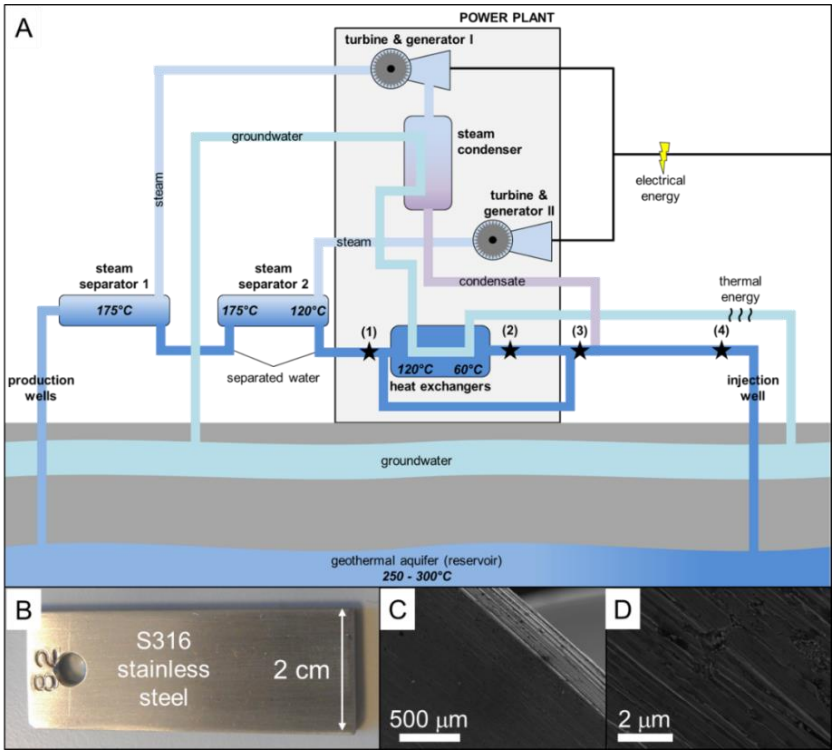

Figure 4.1: *(A) System schematic of the Hellisheiði geothermal power plant indicating the four sampling locations (stars) at which the scaling plates (B) were immersed. FEG-SEM images (C & D) showing the textures of the steel surface before deployment.*

At the beginning and end of each deployment, the separated water at each location was sampled to evaluate changes in fluid composition. The separated water was cooled down using a stainless steel cooling coil (total length ~5 m) attached to the pipeline valve and placed into a barrel filled with cold water. The temperature and pH of the cooled fluid (21 to 27 °C) were determined using a Metrohm Aquatrode plus pH electrode with a thermocouple. Fluid samples were collected first into two Teflon gas sampling bulbs (300 mL, rinsed 3x with separated water before use) and assuring no air remained trapped within the bulbs. These samples were used for analysis of dissolved CO_2 and H_2S. Subsequently a stainless steel holder containing single-use 0.2 µm polycarbonate filter membranes was used to collect filtered fluid samples. These sample aliquots were divided into three different parts. For cation analyses aliquots were transferred into 120 mL into Nalgene bottles containing 2.5 mL of ultrapure HNO_3, for anion analyses 60 mL were transferred into empty Nalgene bottles and, during selected deployments, 5 mL of the filtered waters were transferred into Nalgene bottles containing 20 mL of MilliQ water for analysis of monomeric silica. The filtration membranes were retained from

the 1 day, 3 days and 6 weeks sampling campaigns. For the same deployments, 2 L of separated water from the pipeline were filtered through ten pre-weighted 0.2 μm polycarbonate membranes each to assess the particles load in the fluid and 100 mL were filtered through an additional 0.2 μm polycarbonate membrane which was retained for electron microscope imaging. All collected filter membranes were dried at 40 °C for 12 to 16 hours and, for the pre-weighted filter membranes, weighted again post-drying.

Analyses of silica scales and filter membranes

All analyses of the collected solids were carried out at the University of Leeds unless stated otherwise. The silica deposited on each scaling plate and the materials deposited on the filter membranes were analysed by field emission gun scanning electron microscopy (FEG-SEM, FEI Quanta 650 at 15 keV, coated with ~40 nm of gold). A couple of selected filter membranes were also imaged at ultra-high resolution, using a low kV cold-field emission scanning electron microscope (CFE-SEM, Hitachi SU8230 at 2 kV). The FEG-SEM images were used to determine the dimensions of the observed silica structures by measuring widths and lengths of 70 to 100 structures or particles that had formed in the top side of each plate or filter manually. The elemental composition of the silica precipitates was determined by energy dispersive spectrometry (EDS; spot analyses and elemental mapping, AZtec software, Oxford Instruments, Version 2.2). On the scaling plates where enough material had precipitated, material was scraped off and analysed by X-ray diffraction (XRD; Bruker D8 diffractometer, CuKa1; 5 – 90° 2θ; 0.01°/step; data evaluation by the EVA software, Bruker, Version 3.0). XRD analyses of the materials on the filter membranes was done with the filters glued directly onto the XRD silicon holders. The internal structure, composition and thickness of the precipitated silica layer on the scaling plates from location 1 were investigated via two approaches. For high resolution work, focused ion beam (FIB) sections (15 × 10 × 0.15 μm) were prepared at the GeoForschungsZentrum in Potsdam, Germany from the 1 day, 3 day and 1 week scaling plates following the method described in Wirth (2009). The FIB foils were analysed using a high-resolution transmission electron microscope (HR-TEM, TECNAI F20 X-Twin, 200 kV) at the GFZ in Potsdam, Germany equipped with a Gatan Tridiem Imaging Filter and an EDAX X-ray analyser. Secondly, all scaling plates from location 1 were embedded in epoxy resin, cut along the width of the scaling

plates and polished (at the University of Bern) before being imaged by FEG-SEM as described above.

Table 4.1: *Duration and starting/end dates of individual scaling plate deployments as well as periods of disruptions. The cleaning of the heat exchangers in early October 2014 (after the 10 week and before the 2 week deployment) was part of regular and scheduled maintenance at the Hellisheiði power plant to remove the accumulated silica scales from the heat exchangers (done every 6 to 12 months).*

	Deployment [days]	Start date	End date
1 day	1	02/02/2015	03/02/2015
3 days	3	16/03/2015	19/03/2015
1 week	7	27/10/2014	03/11/2014
2 weeks	14	03/11/2014	17/11/2014
4 weeks	28	23/06/2014	21/07/2014
6 weeks	41	03/02/2015	16/03/2015
10 weeks	72	21/07/2014	01/10/2014
cleaning heat exchangers		06/10/2014	07/10/2014

Analyses of separated water

All analyses of the collected separated water samples were carried out at the University of Leeds unless stated otherwise. After collection, the samples were stored at 3 – 6 °C for maximum 2 days before analysis of the dissolved gases and monomeric silica and for maximum 3 weeks for the analysis of cations or anions. The concentrations of dissolved CO_2 and H_2S were analysed at Reykjavik Energy by total alkalinity titration (Metrohm 905 Titrando equipped with a Metrohm Aquatrode plus) and titration with mercury acetate using dithizone as an indicator (Arnórsson et al., 2006), respectively. The analytical uncertainties of these methods are ± 1% for total alkalinity titration and ± < 0.1% for titration of H_2S. The monomeric silica content was also analysed at Reykjavik Energy based on the method described by Gunnarsson et al. (2010) using a JENWAY 6300 spectrophotometer. The chloride concentrations were analysed by ion chromatography (IC) using a Thermoscientific Dionex system DX600, equipped with a AG16 (2 x 5 mm) and AS16 (2 x 250 mm) column,

with an analytical uncertainty of ±5%, based on multiple standard measurements. The concentrations of the major cations (Al, Ca, K, Na, Si) were analysed by inductively coupled plasma optical emission spectrometry (ICP-OES, Thermo Scientific iCAP7400; analytical uncertainty of < 4%) while the trace cations (Mg, Mn, Fe) were analysed by inductively coupled plasma mass spectrometry (ICP-MS, Thermo Scientific iCAPQc; analytical uncertainty of < 3%.).

Geochemical simulations

The composition of the separated water and the measured pH and temperatures were used as input parameters for geochemical simulations using PHREEQC (version 3.0, Parkhurst and Appelo, 2013) using the database phreeqc.dat updated with the thermodynamic data for amorphous silica by Gunnarsson and Arnórsson (2000) to obtain information on the *in-situ* pH and Eh conditions of the fluid inside the pipelines as well as the saturation indices (SI) of the compounds of interest.

4.3 Results

4.3.1 Composition of separated water

The four sampling locations differed with respect to fluid temperature, flow rate and fluid composition (Table 4.2). This was in a large part defined by their position within the Hellisheiði geothermal power station (Figure 4.1). Location 1 (before the heat exchangers) was characterised by fluids with temperatures of around 118 °C and a flow rate of nearly 430 L/s. The separated water at this location was a low ionic strength NaCl fluid containing ~800 mg/L SiO_2 and ~25 mg/L $CO_{2(aq)}$ and ~20 mg/L $H_2S_{(aq)}$. The pH measured after cooling of the fluid to ambient conditions was 9.4. According to geochemical simulations, the pH under *in-situ* conditions was 8.5 and the Eh -0.56 V. At location 2, after the separated water was cooled inside the heat exchangers (Figure 4.1), the fluid temperature was lower (~57 °C). Due to the differences in pipe geometry, the flow rate was also much lower (~215 L/s), although the fluid composition remained identical to location 1. The measured/calculated pH was 9.4/9.0 and the calculated Eh -0.46 V. These same conditions prevailed at location 3, further downstream from the heat exchangers (Figure 4.1), where temperature and flow rates were only marginally higher (~58 °C and ~295 L/s). Before loca-

tion 4, steam condensate was added to the fluid (around 0.4 L of condensate per 1 L of separated water). The condensate was hotter than the separated water, thus the temperature of the fluid at location 4 was higher (~73 °C). The addition of the condensate and differences in pipe geometry resulted in a higher flow rate of nearly 440 L/s at location 4. The biggest effect of the mixing with condensate was observed in the chemistry of the separated water as the steam condensate is nearly pure water. Thus, the concentration of all fluid components was lower at location 4 compared to the other locations (e.g., 550 mg/L of SiO_2 instead of 800 mg/L). The addition of the steam condensate also resulted in a slightly lower measured pH of 9.1 (calculated pH of 8.8). The Eh was comparable to locations 2 and 3.

Table 4.2: *Average and standard deviation of temperature, fluid composition, pH and Eh for each sampling location.*

		Loc. 1	Loc. 2	Loc. 3	Loc. 4
Temp.	[°C]	117.8 ± 0.4	56.6 ± 1.6	58.0 ± 5.3	72.5 ± 11.2
Flow rate	[L/s]	427 ± 75	214 ± 37	293 ± 29	437 ± 34
SiO_2	[mg/L]	802 ± 19	801 ± 30	794 ± 30	550 ± 76
Na	[mg/L]	204 ± 8	205 ± 9	207 ± 8	140 ± 10
Cl	[mg/L]	173 ± 12	171 ± 9	175 ± 6	120 ± 5
K	[mg/L]	34.7 ± 1.6	34.7 ± 1.7	35.1 ± 1.6	23.6 ± 1.2
CO_2	[mg/L]	25.4 ± 5.5	25.2 ± 4.8	23.8 ± 3.7	18.5 ± 3.8
H_2S	[mg/L]	19.2 ± 2.9	19.8 ± 2.5	20.5 ± 1.9	14.3 ± 2.7
Al	[mg/L]	1.99 ± 0.09	2.04 ± 0.11	2.04 ± 0.11	1.36 ± 0.07
Ca	[mg/L]	0.71 ± 0.13	0.70 ± 0.06	0.71 ± 0.04	0.50 ± 0.06
Fe	[µg/L]	28.5 ± 44.5	16.4 ± 13.1	21.6 ± 23.5	25.2 ± 29.5
Mg	[µg/L]	21.5 ± 21.5	19.6 ± 12.9	19.7 ± 14.2	22.1 ± 15.6
pH meas.[1)]		9.4 ± 0.2	9.4 ± 0.2	9.4 ± 0.2	9.1 ± 0.3
pH calc.[2)]		8.5 ± 0.1	9.0 ± 0.1	9.0 ± 0.1	8.8 ± 0.2
Eh[2)]	[V]	-0.56 ± 0.01	-0.46 ± 0.01	-0.47 ± 0.01	-0.48 ± 0.02

[1)] As measured at 21 to 27 °C

[2)] Derived from PHREEQC simulations at *in-situ* temperatures and with the analysed fluid compositions

Table 4.3: *Silica speciation in the separated water at Hellisheiði*

		Loc. 1	Loc. 2	Loc. 3	Loc. 4
SiO_2 (total)	[mg/L]	802 ± 19	801 ± 30	794 ± 30	550 ± 76
solubility[1)]	[mg/L]	465	204	209	261
saturation index[2)] amorphous SiO_2		0.10 ± 0.02	0.44 ± 0.02	0.42 ± 0.02	0.18 ± 0.08
Speciation [%]					
monomeric[3)]		85.0	81.4	75.5	85.8
"polymeric"[3)]		15.0	18.6	24.5	14.2
particulate [4)]		< 0.02	< 0.03	< 0.03	n/a
Particle sizes [μm][5)]					
in the fluid	mdn	0.2	0.1	0.1	n/a
	IQR	(0.1 – 0.3)	(0.1 – 0.3)	(0.1 – 0.2)	
on the plates	mdn	3.4	0.8	1.0	0.9
	IQR	(1.7 – 6.8)	(0.4 – 1.7)	(0.4 – 1.7)	(0.5 – 3.1)

1) Calculated based on Gunnarsson and Arnorsson (2000).

2) Derived from PHREEQC simulations using the *in-situ* temperatures and with the fluid compositions given in Table 4.2.

3) Determined by analysing fluid samples for total and monomeric silica ("polymeric silica" = total silica – monomeric silica).

4) Determined from the weight difference of the 10 filter membranes before/after sampling and a density of 2.25 mg/mm^3 for glass-like, high density amorphous silica (Mroczek et al., 2011).

5) Determined from manual measurement of silica particles in FEG-SEM images found on filter membranes or scaling plates; mdn = median, IQR = interquartile range (n = 70 to 100 objects per scaling plate or filter)

Calculating the saturation indices based on the measured fluid chemistry revealed that in all cases the separated waters were supersaturated with respect to amorphous silica (Table 4.3). The total silica reported in Table 4.2 represents the sum of all silica species: monomers (H_4SiO_4), polymers (dimers, trimers, tetramers etc.) and nanoparticulate silica (< 0.2 μm). Partitioning the various silica species reveals that in all cases monomeric silica was by far the dominant component (Table 4.3). The proportion of monomeric silica decreased along the flow path from 85% down to 75% from location 1 to 3. At the same time, the proportion of polymeric silica increased from 15 to 25%. The exception was location 4, despite the lower temperature

of the fluids and the dilution with steam condensate the percentage of monomeric silica was similar to location 1 (86%). The proportion of particulate silica as evaluated from the difference in weight of the filters accounted for less than 0.05% of the total silica (Table 4.3) with a marginally higher proportion at locations 2 and 3 compared to location 1. XRD and imaging of the filters revealed that in all cases the particulate silica on the filters consisted of amorphous silica spheres with mean particle sizes identical or smaller than the pore sizes of the filter membranes (0.2 μm) at locations 1 to 3. At all locations particle sizes varied between < 0.1 and 22.7 μm (Table 4.3, Figure 4.2 A). The larger particles could be subdivided into two groups: (1) particles with a relatively smooth surface (Figure 4.2 A & B) and (2) particles consisting of aggregates of much smaller particles (0.01 – 0.05 μm; Figure 4.2 A & B). In addition to the silica particles at locations 1 to 3, a few platy aluminosilicates were imaged (Figure 4.2 A) by FEG-SEM and confirmed as clinochlor by XRD analyses. Therefore, the percentages of particulate silica given in Table 4.3 are maximum values only. At location 4, silica particles were very rare and the abundance of aluminosilicates such as chamosite and clinochlore and the magnesium silicate sepiolite (identified by XRD and EDS analyses) was high (Figure 4.3 C).

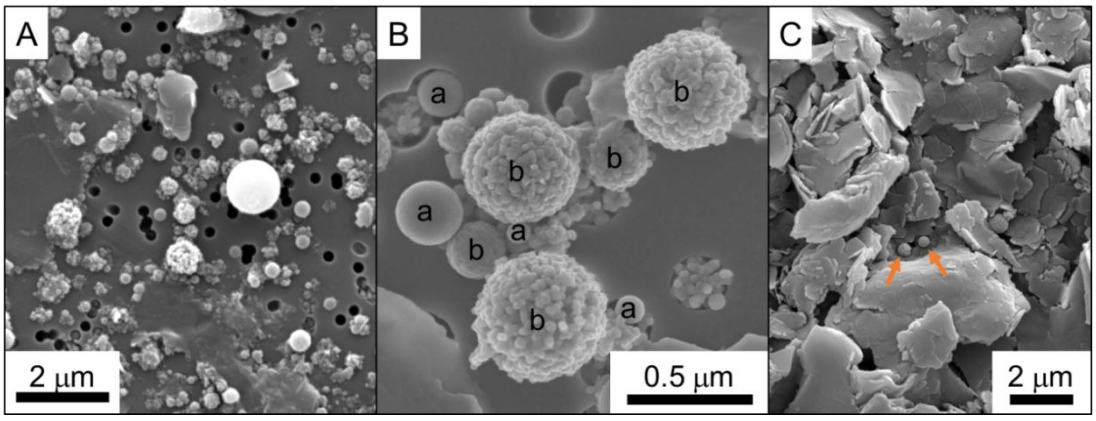

Figure 4.2: *FEG-SEM images of 0.2 μm polycarbonate filter membranes with (A & B) two types of silica particles (smooth particles and rough particle aggregates) from location 1 and (C) platy aluminosilicates with very few small silica spheres (arrows) from location 4.*

4.3.2 Composition and structure of silica scales

On all plates, independent of deployment time and location, precipitates were observed. The precipitates were identified as amorphous silica by XRD and EDS spot analyses. The amorphous silica precipitates were sometimes interspersed with min-

eral and metal flakes, identified as aluminium silicates (based on EDS) and in some samples confirmed to be clinochlor (by XRD). In addition to these distinct phases, EDS analyses also revealed that the precipitates silica also contained ions from the geothermal fluid (Na, Cl, S, Al, Fe etc.).

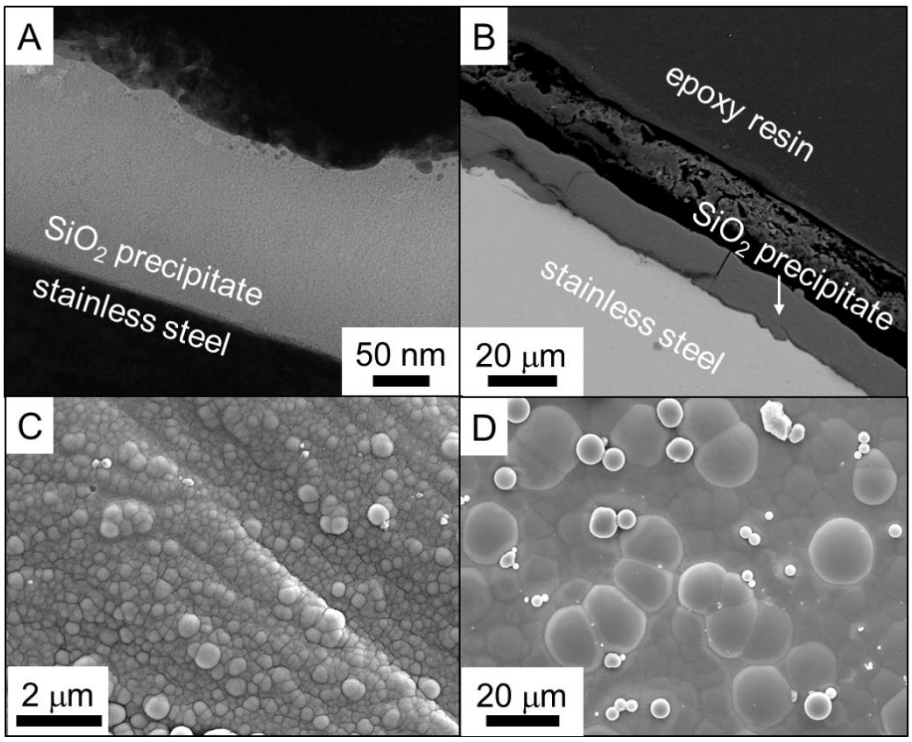

Figure 4.3: *Electron microscope images showing a cross section of the precipitation layer after (A) 1 day (FIB section imaged by TEM) and (B) 10 weeks (FEG-SEM image of a sample embedded in epoxy resin). Note the difference in scale. FEG-SEM images of the surface of scaling plates deployed for (C) 1 day and (D) 10 weeks, respectively. All samples were from location 1.*

The scaling plates were completely covered by a layer of amorphous silica precipitates, even after 1 day. The silica precipitation layer was very dense with a complete lack of internal structure (Figure 4.3 A & B). The thickness of the silica layer was similar around each plate with no differences between the individual faces of the plates (top *vs*. bottom, main face *vs.* edge) and increased over time (from 0.3 to 20.2 μm over 10 weeks at location 1). The surface of the precipitation layer was uneven and consisted of lens-shaped silica precipitates that we call 'bumps' hereafter (Figure 4.3 C & D). These bumps grew over time in size (areas as evaluated based on measuring lengths and widths) but decreased in numbers per area. The average

sizes of the bumps are shown in Figure 4.4 for each location. At all four locations rapid growth during the short deployments was followed by a decreasing growth during the longer deployments. The increase in bump size was fastest at locations 1 and 2, where the area of individual bumps grew from 0.05 μm^2 after 1 day to around 75 μm^2 over the course of 10 weeks. At location 3, the growth was slower and the bumps only grew to a size of maximum 15 μm^2. Although silica bumps were observed at location 4, their growth was very slow and even after 10 weeks the bumps only reached a size of 0.1 μm^2. These measurements were all done on the top side of the scaling plates. For the 1 week deployment the bumps sizes were also measured on the bottom side of the scaling plates at all four locations to confirm that their average sizes were identical to those observed on the top side (Figure 4.4).

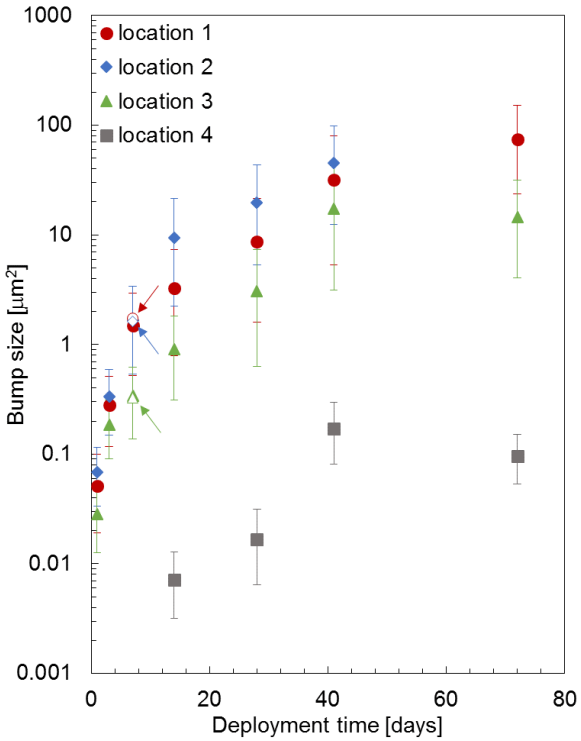

Figure 4.4: *Increase in average bump size over time at all four locations as evaluated based on lengths and widths of 70 to 100 bumps on each plate (note logarithmic scale). The empty symbols (highlighted by arrows) represent the bump sizes measured on the underside of the 1 week deployment at locations 1 to 3.*

In many cases, on top of the bumpy silica layer, individual or merged silica spheres were observed (Figure 4.5). These spherical particles looked identical to the

particles found on the filters (Figure 4.2), but on average they were markedly larger (Table 4.3). The spatial distribution of the particles on the plates seemed completely random with some plates containing only few particles, while other having larger areas covered by silica particles. In some instances, neighbouring particles were cemented together (Figure 4.5 A) or to the surface of the existing silica layer (Figure 4.5 B) by dissolved silica or possibly also silica nanoparticles. A very small number of particles were observed to become incorporated into the surface layer (Figure 4.5 C).

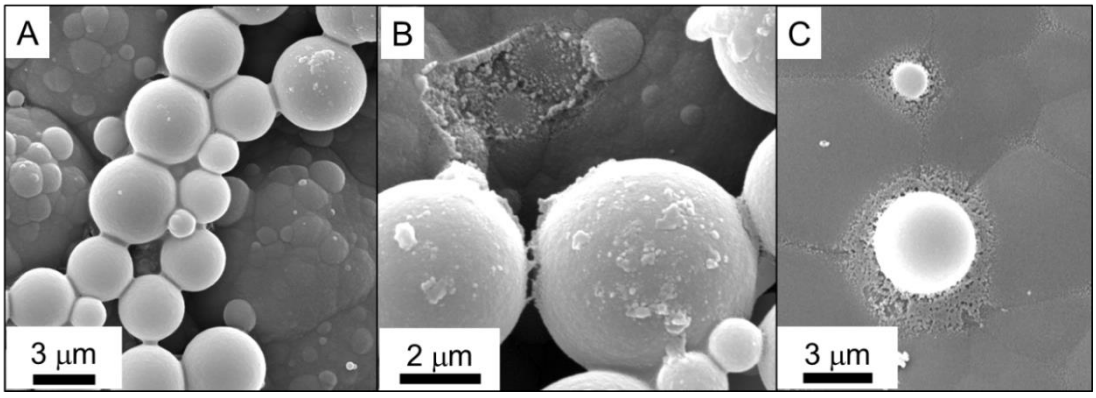

Figure 4.5: *FEG-SEM images showing particles deposited onto the bumpy silica precipitation layer where they were (A) cemented together and/or (B) cemented to the surface or (C) (rarely) incorporated into the silica layer.*

In addition to being deposited onto the surface of the scaling plates individually or as small clusters (Figure 4.5), silica particles were also found to aggregate into three dimensional fan- to ridge-shaped structures (Figure 4.6 A to C). These structures were all pointing towards the direction of the flow and they were cemented together resulting in a globular texture (Figure 4.6 D). Such 3D fans were dominantly found on the plates deployed for 4 and 10 weeks and on the upwards facing plate, along the edge oriented towards the flow (Figure 4.6 A). At location 1, single fans, mostly found along the edge of the plate, grew up to 700 µm high during the 4 week deployment (Figure 4.6 A). On the 10 week scaling plate from location 1, such fans were also found growing on the surface of the plate and there they formed ridges that were up to 10 mm long and 1mm high (Figure 4.6 B & C). At locations 2 and 3, fewer fans were present and they only grew to maximum 300 and 500 µm after 4 and 10 weeks, respectively. 3D structures were not found on any scaling plate deployed for 6 weeks, independent of the location.

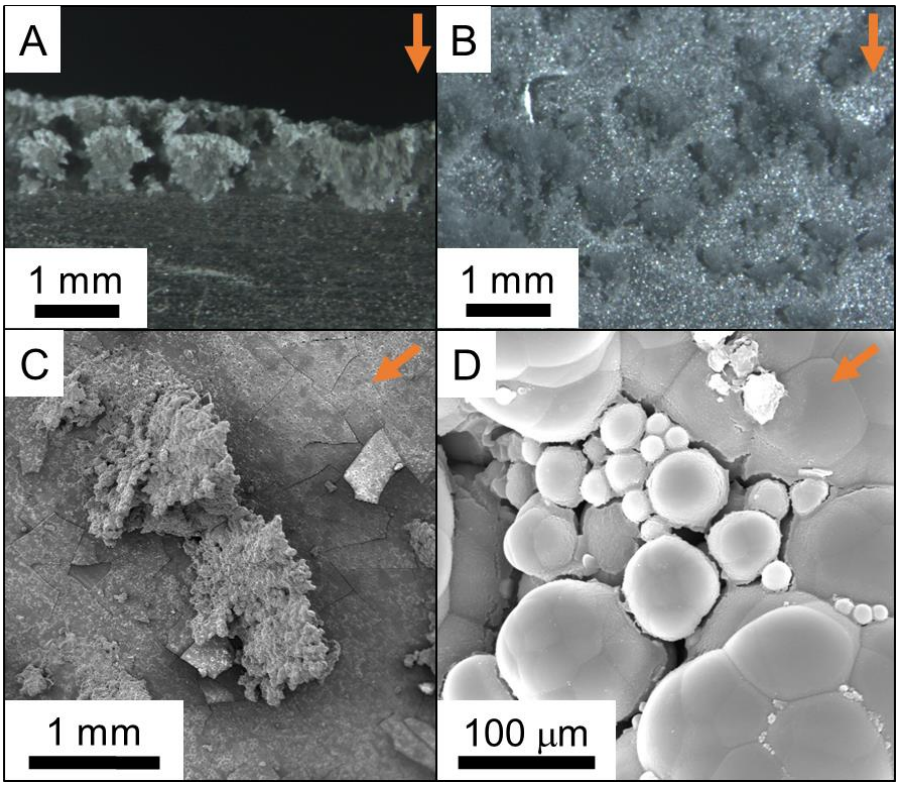

Figure 4.6: *Microphotographs showing the 3D, fan-shaped structures found on the location 1 scaling plates from the 4 and 10 week deployments (A) along the edge of the plate and (B) on the surface of the plates. The (C) fans consisted of spherical aggregates that grew as a function of time by addition of (D) individual particles which were then cemented together. Flow direction indicated by arrows.*

4.4 Discussion

Silica was by far the most abundant component in the separated water at Hellisheiði with a concentration of around 800 mg/L before and 550 mg/L after the addition of steam condensate and the deposits were predominantly identified as amorphous silica. According to the results from our initial study at Hellisheiði (Meier et al., 2014 (Chapter 3)), the precipitation of silica on scaling plates was controlled by an interplay between temperature, fluid composition, fluid flow regime, distance along flow path and immersion time, yet we could not separate the contribution of each of these parameters. By doing a time-resolved scaling plate study, involving a more thorough characterisation of the physico-chemical conditions under which precipitation occurred, we have gained a much deeper understanding of the silica precipitation mechanisms and the factors controlling them as well as the first ever silica precipitation rates from Hellisheiði.

4.4.1 Precipitation pathways

We observed two different silica microtextures on the scaling plates (Figure 4.7): bumpy silica layers and 3D structures consisting of individual silica microspheres. While the silica layers were identified on all scaling plates grew continuously in thickness, the 3D structures were only observed during the 4 and 10 week deployments at locations 1 to 3. This indicates that their formation was controlled by different processes/pathways.

The formation of silica species is a consequence of polymerisation of monomers, a process that proceeds via the condensation and hydration of a deprotonated silanol group to form Si-O-Si bonds (Iler, 1979). Polymerisation is occurring continuously inside the pipelines at Hellisheiði as shown by the decreasing proportion of monomeric silica between locations 1 and 3 (Table 4.3). At location 4 their relative amount has increased again, indicating that the dilution led to the partial depolymerisation of silica polymers in the fluid.

Silica polymerisation can take place at the scaling plate-separated water interface or in the fluid. If occurring at the interface, it can be described as heterogeneous nucleation and results in the formation of the bumpy silica layer. If occurring in the fluid, the process is called homogeneous nucleation and results in the formation of silica microspheres (Benning and Waychunas, 2007). In both cases, once the nuclei have reached a critical size, previously found to be between < 0.5 and 2 nm (Iler, 1979; Tobler et al., 2009; Noguera et al., 2015), they grow spontaneously by the addition of silica from solution. Monomers are the dominant growth species due to their predominantly neutral charge (K_a ~$10^{-8.8}$ at 120 °C; Seward, 1974; Fleming and Crerar, 1982) in the slightly alkaline pH regime of the separated water at Hellisheiði (Bohlmann et al., 1976; Mroczek and McDowell, 1988; Bremere et al., 2000). In contrast, silica polymers have a higher dissociation constant ($K_a > 10^{-8}$; Dugger et al., 1964; Hair and Hertl, 1970). Thus, the surface of the nuclei as well as any polymers formed in solution will be negatively charged and their aggregation will be prevented by electrostatic repulsion. This is in agreement with what we observed in the current study. The smooth (at the resolution studied here) appearances of the silica bumps (Figure 4.3) and the scarcity of particles partly embedded in the silica layer (Figure 4.5 C) suggest that the silica layer, once formed by heterogeneous nucleation, grew by the addition of monomeric silica. The equally smooth appearance of one group of silica particles (Figure 4.5 A & B) as well as the material cementing the

particles together and to the silica layer (Figures 4.5 & 4.6) are in accordance with the growth by addition of monomeric silica. However, the separated water contains low concentrations of multivalent cations (Table 4.2) which can act as flocculants, potentially also helping with the attachment of large, negatively charged silica species to the silica layer or into the 3D aggregates.

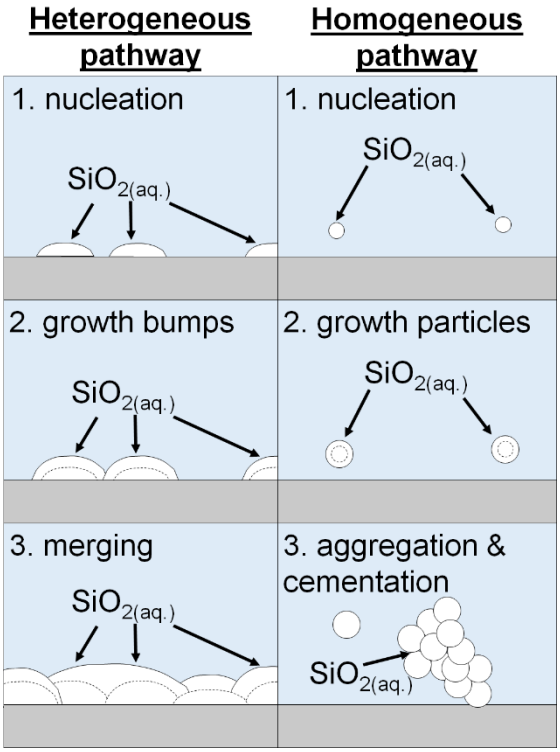

Figure 4.7: *Schematic of the two precipitation pathways inside the pipelines at Hellisheiði.*

The heterogeneous nucleation of silica was found to be predominantly controlled by surface properties of the scaling plates, especially roughness (van den Heuvel et al., in prep. (Chapter 5)). As the scaling plates were all prepared from identical S316 stainless steel, we did not expect to see a difference in nucleation behaviour between the four locations. However, once nuclei had formed, their growth was controlled by silica-silica interactions and thus enhanced by the same parameters which increase silica polymerisation rates such as high total silica concentrations, high percentage of monomers, elevated temperature and alkaline pH (Alexander et al., 1954; Goto, 1956; Kitahara, 1960; Bohlmann et al., 1980; Crerar et al., 1981; Weres et al., 1981; Fleming, 1986; Bremere et al., 2000; Gunnarsson and Arnórsson, 2003; Gunnarsson and Arnórsson, 2005; Icopini et al., 2005; Tobler et al.,

2009). In order to assess the effect of the different parameters, we compared the growth rate of the bumps (Figure 4.4) and the physico-chemical conditions of the fluid (Tables 4.2 & 4.3) at the different locations. Based on the slow growth of bump sizes at location 4, we could conclude that the total silica concentration had the strongest effect on growth rate. The other parameters at location 4 were similar to location 1 (monomer content, pH), location 3 (distance to the nearest disturbance) or in between the values for the other locations (temperature) and would thus not have explained the much slower growth observed. The higher growth rate at location 1 compared to locations 2 and 3 was strongly affected by the elevated temperature which increased the rate of monomer attachment (Alexander et al., 1954; Kitahara, 1960). Thus the precipitation rates at locations 2 and 3 should be substantially lower. While this was true for location 3, the growth rate at location 2 was very similar to location 1. This was attributed to the rapid cooling of the fluid in the heat exchangers only a few metres upstream of location 2. Thus, the deposition rates of monomeric silica at location 2 were similar to the conditions before the heat exchangers (which explains the similarities to location 1) and not yet representative of the new physico-chemical conditions (explaining the discrepancy to location 3). The other parameters controlling silica polymerisation according to previous studies, i.e., pH and monomer content, seemed to be of little importance under the conditions observed in the separated water at Hellisheiði. The bumps were also investigated for their shapes and sizes relative to flow direction and top/bottom side of the scaling plates. No correlation was found, indicating that neither flow rate/direction nor gravity affect heterogeneous nucleation and bump growth.

Independent of the location and thus the physico-chemical conditions, the growth of the bumps slowed down as a function of time (Figure 4.4). This was due to the decreasing number of bumps with increasing deployment time. Over time, the deposition of dissolved silica resulted in the merging of smaller bumps to form fewer but bigger bumps (Figures 4.3 C & D & 4.7). This in turn resulted in fewer bump boundaries which, compared to the bumps themselves, are preferential deposition sites for dissolved silica. This preferential deposition is due to the small turbulences created when the fluid flows along the bumpy layer (Hawkins et al., 2013). The same turbulences also favour the deposition of silica microspheres along these depressions (Figure 4.3 D).

Homogeneous nucleation and particle growth were only controlled by the physico-chemical conditions of the fluid. Under ambient conditions and up to 60 °C

particles grow to ≤ 10 nm in laboratory experiments (Goto, 1956; Icopini et al., 2005; Iler, 1979; Tobler and Benning, 2013; Tobler et al., 2009). However, at alkaline pH and in the absence of salts, particles can grow to sizes of 100 nm (Iler, 1979). While this could explain the nanoparticles which make up the spherical aggregates observed on the filter membranes (Figure 4.2 B), it does not explain the 20+ μm particles with smooth surfaces (Figure 4.2 A). They likely formed due to the favourable conditions for growth inside the pipelines (alkaline pH, elevated temperature, constant re-supply of dissolved silica and in the absence of salts) which are similar to the conditions in the industrial "build-up process" developed for the production of large particle silica sols (Morris and Vossos, 1970). However, these particles only account for a small proportion of the particulate silica, indicating that the build-up process was rare or slow.

Large particles were deposited preferentially as evidenced by the larger average particle size on the plates (especially at location 1) compared to the filter membranes (Table 4.3). The difference is smaller at locations 2 and 3, indicating that the particles grew larger at higher temperatures and/or that the fluid got depleted with respect to large particles along the flow path. During certain deployments the deposition of particles led to the formation of fans and ridges (Figure 4.6). Their structure was very similar to the dendritic precipitates predicted by hydrodynamic simulations by Hawkins et al. (2013), suggesting that the fluid flow regime likely controlled the resulting morphologies. The individual particles were cemented together by the deposition of dissolved silica. This occurred in the embayment between particles, where the solubility of amorphous silica was zero due to the infinitely small negative radius of curvature at the contact point (Iler, 1979). The 3D structures grew largest at location 1, likely due to the larger average size of particles deposited, and were absent at location 4 where there were only few silica particles in the fluid. The structures were only observed during the 4 and 10 week deployments which were done between June and early October 2014 (Table 4.1). Only a few days after the 10 week deployment was finished, the heat exchangers were cleaned as part of regular maintenance work at Hellisheiði. After the cleaning, the flow rate increased substantially at location 1 (up to 590 L/s) and less dramatically at location 2 (up to 300 L/s) while remaining close to average at the two remaining locations. This could indicate that there is a threshold flow rate above which no formation of 3D structures occurs.

4.4.2 Precipitation rates

Apart from describing the textures of the silica scales and inferring their precipitation pathways, we used our time resolved data to estimate the heterogeneous growth rates of the silica scales via two different approaches (Figure 4.8): (1) we quantified the amount of silica deposited on the plates (in mg) from the 1 day, 3 day and 1 week deployments at each location and (2) we measured the average thickness of the precipitation layer for the 1+ week deployments at location 1.

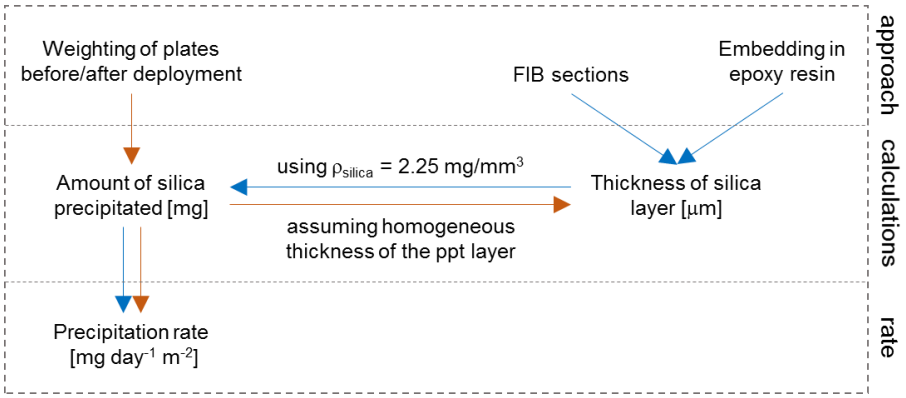

Figure 4.8: *Two approaches to determine the precipitation rates of the bumpy silica layer: (1) weighting of the plates (orange) and (2) measuring the thickness of the precipitated layer from FIB sections and the samples embedded in epoxy (blue).*

For the first approach, the amount of silica precipitated was measured by weighting of the scaling plates before and after the deployments. This was converted to a volume using a density of ρ_{SiO2} = 2.25 mg/mm^3 for a high density vitreous scale (Mroczek et al., 2011) and, because the cross sections (Figure 4.3 A & B) revealed that the silica layers were of roughly constant thickness around the plate, we could calculate the thickness of the precipitates. We also used the amount of silica precipitated and the surface areas of the individual scaling plates to calculate precipitation rates (Table 4.4).

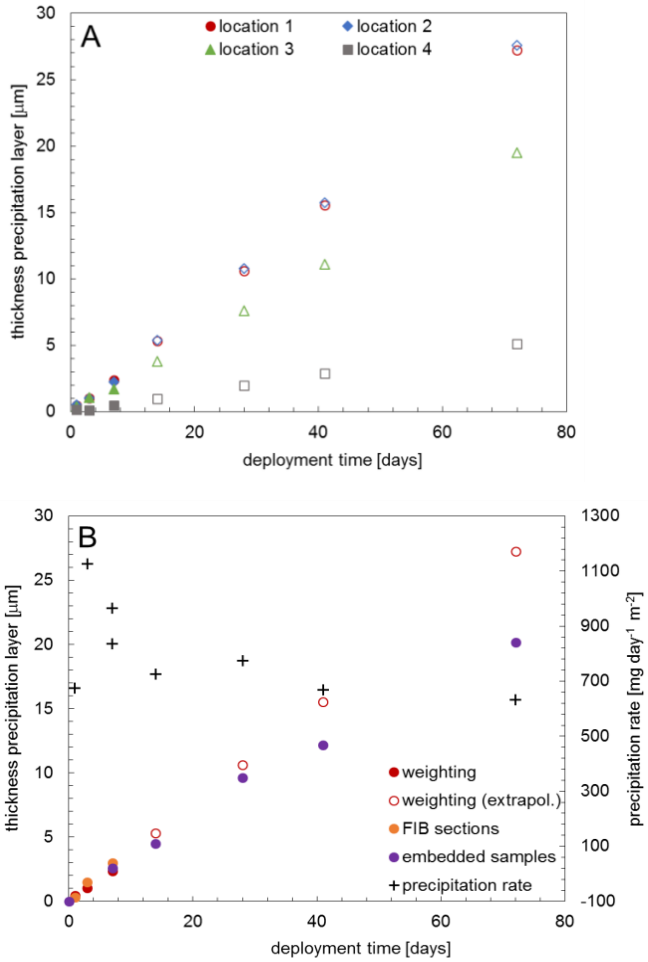

Figure 4.9: *Growth of the silica precipitation layer over time: (A) thickness of silica layer calculated based on the weight of silica and a density of 2.25 mg/mm³ (Mroczek et al., 2011) at all locations up to 1 week (solid symbols) and a linear extrapolation up to 10 weeks (empty symbols) and (B) the thickness of the silica layer at location 1 as determined/calculated by weighting (red) thickness measurements from FIB sections (orange) and embedded samples (purple) by electron microscopy and the calculated precipitation rates in mg day⁻¹ m⁻².*

The amount of silica increased four- to fivefold from 1 day to 1 week at all locations. However the absolute values differed substantially between the locations. The accumulation of silica was fastest at locations 1 and 2, where the calculated thickness of the silica layer increased from 0.5 to nearly 2.5 µm. At location 3 the increase was slower (0.4 to 1.7 µm) and at location 4 only little silica was deposited (< 0.1 to 0.5 µm). Based on the data obtained, the thickness of silica precipitated up to 10 weeks was extrapolated linearly using an average precipitation rate calculated

for each location (Figure 4.9 A). However, the precipitation rates in Table 4.4 are decreasing from the 1 day to the 1 week deployment. Thus, the linear extrapolation likely overestimates the actual precipitation. This was confirmed by the thicknesses measured from FIB sections and the samples embedded in epoxy resin at location 1 (Table 4.5). Up to 1 week, the measured thicknesses agreed well with the ones extrapolated (Table 4.4, Figure 4.9 B). For longer deployments, the measured thicknesses started to deviate from the extrapolation (Figure 4.9 B) and the silica precipitation layer after 10 weeks was nearly a third thinner (~20 μm) than predicted (~27.5 μm). The decrease in silica precipitation was also observed in the calculated precipitation rates (Table 4.5, Figure 4.9 B) and the increase of bump size (Figure 4.4). Thus, the extrapolated values represent a 'worst case' scenario and a maximum silica deposition rate. Why the growth/precipitation rates slows down as a function of time is not well understood, yet our data indicates that the growth of the silica layer may have led to an increase in depositional surface area while the rate of silica attachment to the surface remained unchanged. This would suggest that the growth of the silica layer is controlled by the rate of attachment of dissolved silica from the solution and not diffusion controlled. This is in line with previous findings from Bohlmann et al. (1980) and Weres et al. (1981). However, to fully differentiate these various possible reasons more, detailed measurements and longer deployment experiments are needed.

Our data showed that precipitation was fastest at locations 1 and 2 and slowest at location 4. This is in conflict with the saturation indices (SIs) calculated by PHREEQC (Table 4.3). According to the SIs, precipitation should be fastest at locations 2 and 3 (highest SIs = highest driving force for precipitation). However, the SI is a purely thermodynamic concept which is only of limited use in a system as dynamic as a geothermal power plant where changes in the physico-chemical conditions (e.g., cooling in the heat exchangers, dilution by steam condensate) occur rapidly and over short distances. These changes resulted in a non-equilibrated fluid whose behaviour cannot be predicted by SIs alone. Even if kinetics would be taken into account to simulate the precipitation, the accuracy of the predictions would likely not improve substantially as the kinetics of silica polymerisation are still highly contentious (reviewed by Tobler et al., 2009). The simulated results will thus strongly depend on the kinetic model chosen and are not necessarily representative of silica precipitation in a given geothermal system. Overall, this indicates that geo-

chemical models are currently only of limited use in predicting silica precipitation in geothermal systems.

Table 4.4: *Calculation of thickness of precipitation layer based on weighting scaling plates before and after deployment for all four locations.*

	Amount of silica precipitated		Thickness of layer [μm][3)]	precipitation rate [mg day^{-1} m^{-2}][4)]
	[mg][1)]	[mm^3][2)]		
Location 1				
1 day	2.5	1.1	0.5	1027
3 days	5.7	2.5	1.0	515
1 week	13.2	5.9	2.4	267
Location 2				
1 day	2.8	1.2	0.5	3347
3 days	5.6	2.5	1.0	1450
1 week	12.3	5.5	2.2	511
Location 3				
1 day	2.0	0.9	0.4	2108
3 days	5.8	2.6	1.0	248
1 week	11.4	5.1[5)]	1.7	161
Location 4				
1 day	0.8	0.3	0.1	1524
3 days	0.6	0.3	0.1	631
1 week	3.2	1.4[5)]	0.5	464

1) Calculated based on the weight difference of the scaling plate before and after deployment

2) Calculated based on a density of 2.25 mg/mm^3 for glass-like, high density amorphous silica (Mroczek et al., 2011).

3) Calculated assuming a constant thickness of the silica layer around the whole plate.

4) Calculated using the amount precipitated and the surface area of the scaling plates.

5) Scaling plates 2.5 cm wide (all other scaling plates were 2 cm wide). Taken into account when calculating the thickness of the layer and the precipitation rate.

4.4.3 Implications

Silica precipitates with morphologies similar to the bumpy silica layers and 3D particle aggregates described from the Hellisheiði pipelines have been described at oth-

er power plants in Iceland and New Zealand (Thórhallsson et al., 1975; Gudmundsson and Bott, 1979; Rothbaum et al., 1979; Carroll et al., 1998), silica sinters from Iceland (Jones and Renaut, 2010) and laboratory experiments mimicking the growth of silica veins (Okamoto et al., 2010). This indicates that the combination of homogeneous and heterogeneous precipitation modes for amorphous silica as observed at Hellisheiði is widespread and happens in both, natural and man-made geothermal systems over a range of total silica concentrations (250 to 900 mg/L), temperatures (20 to 200 °C), pH (7.2 to 10.2) and salinities (200 to 25'000 mg/L). Nevertheless, our results are unique because, in addition to determining the pathways by which silica scaling occurs, we also identified and partly quantified the factors controlling the two pathways as well as the precipitation rates. These findings will help to develop better mitigation strategies (e.g., additives) for silica scales as formed in geothermal power plants, thus improving the overall performance of geothermal power production.

Table 4.5: *Thicknesses of precipitated silica layer at location 1 from FIB sections and samples embedded in epoxy as well as calculated precipitation rates.*

	measured [μm]		Amount of silica [mg][1)]	precipitation rate [mg day^{-1} m^{-2}][2)]
	FIB sections	embedded		
1 day	0.3	-	1.7	675
3 days	1.5	-	8.3	1125
1 week	3.0	2.6	16.6 / 14.4	965 / 836
2 weeks	-	4.5	24.9	725
4 weeks	-	9.6	53.2	773
6 weeks	-	12.2	67.4	669
10 weeks	-	20.2	111.7	632

[1)] Calculated based on a density of 2.25 mg/mm^3 for glass-like, high density amorphous silica (Mroczek et al., 2011) and the volume of silica precipitated assuming a constant thickness of the precipitation layer all around the scaling plates.

[2)] Calculated using the amount precipitated and the surface area of the scaling plates.

4.5 Conclusions

This study represents the first ever time-resolved silica precipitation study inside a high-entropy, low-salinity geothermal power station while in use. We have studied

the physico-chemical conditions of the separated water at the Hellisheiði power plant in detail and characterised the precipitates at the (sub)micron scale. Our results showed that silica precipitated via two pathways: (1) heterogeneous nucleation and growth of a bumpy silica layer by addition of monomeric silica and (2) homogeneous nucleation of particles in the fluid which growth by addition of monomeric silica and were deposited to form 3D fan- and ridge-shaped structures. The heterogeneous pathway was predominantly controlled by surface properties, total silica concentration and temperature. The nucleation and growth stages in the homogeneous pathway were primarily controlled by temperature and total silica concentration. The subsequent deposition on the other hand was strongly controlled by the fluid flow rate and regime.

We also presented the first ever precipitation rates for the heterogeneous pathway in this study (up to 1 g day^{-1} m^{-2}). They were derived from weighting of the scaling plates before and after the deployments and measuring the thickness of the precipitation layer. Precipitation was fastest at locations 1 and 2 but the precipitation rates were halved from the first few days to 10 weeks. Comparing our results with previous studies we concluded that the homogeneous and heterogeneous pathway are not unique to Hellisheiði power plant but occur under a wide range of physic-chemical fluid conditions.

Acknowledgments

This research was made possible by a Marie Curie grant from the European Commission in the framework of the MINSC ITN (Initial Training Research network), Project number 290040 and the 2014 PhD Student Grant by the International Geothermal Association (IGA) awarded to D.B. van den Heuvel. We thank Tony Windross and Stephen Burgess for preparation of all scaling plates and Halldór Bergmann for his help with the deployments. We are grateful for the fluid analyses done at Reykjavik Energy and by Stephen Reid and Fiona Keay at the University of Leeds. We thank Anja Schreiber and Richard Wirth at the GFZ Potsdam for preparation of FIB foils and subsequent analyses by TEM. We also acknowledge analytical support by Lesley Neve (XRD) and Richard Walshaw (SEM), both University of Leeds. We would like to thank Hari Williams (University of Leeds), Thomas Aebi and Nadine Lötscher (both University of Bern) for help with embedding of the samples in resin and the subsequent cutting and polishing.

References

Alexander, G.B., Heston, W., Iler, R., 1954. The solubility of amorphous silica in water. *The Journal of Physical Chemistry* **58**, 453-455.

Arnórsson, S., 1975. Application of the silica geothermometer in low temperature hydrothermal areas in Iceland. *American Journal of Science* **275**, 763-784.

Arnórsson, S., Bjarnason, J.Ö., Giroud, N., Gunnarsson, I., Stefánsson, A., 2006. Sampling and analysis of geothermal fluids. *Geofluids* **6**, 203-216.

Benning, L.G., Waychunas, G.A., 2007. Nucleation, growth, and aggregation of mineral phases: Mechanisms and kinetic controls, *Kinetics of Water-Rock Interaction*. Springer, pp. 259-333.

Bohlmann, E., Shor, A., Berlinski, P., 1976. *Precipitation and scaling in dynamic geothermal systems*. Oak Ridge National Laboratories, p. 21680.

Bohlmann, E.G., Mesmer, R.E., Berlinski, P., 1980. Kinetics of silica deposition from simulated geothermal brines. *Society of Petroleum Engineers Journal* **20**, 239-248.

Braunstein, D., Lowe, D.R., 2001. Relationship between spring and geyser activity and the deposition and morphology of high temperature (> 73 °C) siliceous sinter, Yellowstone National Park, Wyoming, USA. *Journal of Sedimentary Research* **71**, 747-763.

Bremere, I., Kennedy, M., Mhyio, S., Jaljuli, A., Witkamp, G.-J., Schippers, J., 2000. Prevention of silica scale in membrane systems: removal of monomer and polymer silica. *Desalination* **132**, 89-100.

Carroll, S., Mroczek, E., Alai, M., Ebert, M., 1998. Amorphous silica precipitation (60 to 120 °C): Comparison of laboratory and field rates. *Geochimica et Cosmochimica Acta* **62**, 1379-1396.

Crerar, D.A., Axtmann, E.V., Axtmann, R.C., 1981. Growth and ripening of silica polymers in aqueous solutions. *Geochimica et Cosmochimica Acta* **45**, 1259-1266.

Demadis, K.D., Mavredaki, E., Stathoulopoulou, A., Neofotistou, E., Mantzaridis, C., 2007. Industrial water systems: problems, challenges and solutions for the process industries. *Desalination* **213**, 38-46.

Dugger, D.L., Stanton, J.H., Irby, B.N., McConnell, B.L., Cummings, W.W., Maatman, R.W., 1964. The Exchange of Twenty Metal Ions with the Weakly

Acidic Silanol Group of Silica Gel1, 2. *The Journal of Physical Chemistry* **68**, 757-760.

Fleming, B., Crerar, D., 1982. Silicic acid ionization and calculation of silica solubility at elevated temperature and pH application to geothermal fluid processing and reinjection. *Geothermics* **11**, 15-29.

Fleming, B.A., 1986. Kinetics of reaction between silicic acid and amorphous silica surfaces in NaCl solutions. *Journal of Colloid and Interface Science* **110**, 40-64.

Fournier, R., Rowe, J., 1966. Estimation of underground temperatures from the silica content of water from hot springs and wet-steam wells. *American Journal of Science* **264**, 685-697.

Gallup, D.L., 1997. Aluminum silicate scale formation and inhibition: scale characterization and laboratory experiments. *Geothermics* **26**, 483-499.

Goto, K., 1956. Effect of pH on polymerization of silicic acid. *The Journal of Physical Chemistry* **60**, 1007-1008.

Gudmundsson, J.S., Bott, T.R., 1979. Deposition of silica from geothermal waters on heat transfer surfaces. *Desalination* **28**, 125-145.

Gunnarsson, I., Arnórsson, S., 2000. Amorphous silica solubility and the thermodynamic properties of H_4SiO_4 in the range of 0 to 350 °C at P_{sat}. *Geochimica et Cosmochimica Acta* **64**, 2295-2307.

Gunnarsson, I., Arnórsson, S., 2003. *Silica scaling: The main obstacle in efficient use of high-temperature geothermal fluids*, Proceedings International Geothermal Conference, Reykjavik, pp. 30-36.

Gunnarsson, I., Arnórsson, S., 2005. Impact of silica scaling on the efficiency of heat extraction from high-temperature geothermal fluids. *Geothermics* **34**, 320-329.

Hair, M.L., Hertl, W., 1970. Acidity of surface hydroxyl groups. *The Journal of Physical Chemistry* **74**, 91-94.

Handley, K., Campbell, K., Mountain, B., Browne, P., 2005. Abiotic–biotic controls on the origin and development of spicular sinter: *in-situ* growth experiments, Champagne Pool, Waiotapu, New Zealand. *Geobiology* **3**, 93-114.

Harrar, J., Locke, F., Otto Jr, C., Lorensen, L., Monaco, S., Frey, W., 1982. Field tests of organic additives for scale control at the Salton Sea geothermal field. *Society of Petroleum Engineers Journal* **22**, 17-27.

Hawkins, C., Angheluta, L., Hammer, Ø., Jamtveit, B., 2013. Precipitation dendrites in channel flow. *Europhysics Letters* **102**, 54001.

Icopini, G.A., Brantley, S.L., Heaney, P.J., 2005. Kinetics of silica oligomerization and nanocolloid formation as a function of pH and ionic strength at 25 C. *Geochimica et Cosmochimica Acta* **69**, 293-303.

Iler, R.K., 1979. *The chemistry of silica: solubility, polymerization, colloid and surface pro perties, and biochemistry*. Wiley, London.

Jones, B., Renaut, R.W., 2004. Water content of opal-A: implications for the origin of laminae in geyserite and sinter. *Journal of Sedimentary Research* **74**, 117-128.

Jones, B., Renaut, R.W., 2010. Impact of seasonal changes on the formation and accumulation of soft siliceous sediments on the discharge apron of Geysir, Iceland. *Journal of Sedimentary Research* **80**, 17-35.

Kitahara, S., 1960. The polymerization of silicic acid obtained by the hydrothermal treatment of quartz and the solubility of amorphous silica. *Review of Physical Chemistry Japan* **30**, 131-137.

Konhauser, K.O., Jones, B., Phoenix, V.R., Ferris, G., Renaut, R.W., 2004. The microbial role in hot spring silicification. *AMBIO: A Journal of the Human Environment* **33**, 552-558.

Meier, D., Gunnlaugsson, E., Gunnarsson, I., Jamtveit, B., Peacock, C., Benning, L., 2014. Microstructural and chemical variation in silica-rich precipitates at the Hellisheiði geothermal power plant. *Mineralogical Magazine* **78**, 1381-1389.

Morris, M., Vossos, P.H., 1970. *Large particle silica sols and method of production*. Google Patents.

Mountain, B., Benning, L., Boerema, J., 2003. Experimental studies on New Zealand hot spring sinters: rates of growth and textural development. *Canadian Journal of Earth Sciences* **40**, 1643-1667.

Mroczek, E., Graham, D., Bacon, L., 2011. *Silica deposition experiments: past work and future research directions*, Proceedings International Workshop on Mineral Scaling in Geothermal Environments, Manila.

Mroczek, E., McDowell, G., 1988. *Silica scaling field experiments*, New Zealand Geothermal Workshop, Auckland.

Noguera, C., Fritz, B., Clément, A., 2015. Precipitation mechanism of amorphous silica nanoparticles: a simulation approach. *Journal of Colloid and Interface Science* **448**, 553-563.

Okamoto, A., Saishu, H., Hirano, N., Tsuchiya, N., 2010. Mineralogical and textural variation of silica minerals in hydrothermal flow-through experiments: Implications for quartz vein formation. *Geochimica et Cosmochimica Acta* **74**, 3692-3706.

Parkhurst, D.L., Appelo, C., 2013. *Description of input and examples for PHREEQC version 3: a computer program for speciation, batch-reaction, one-dimensional transport, and inverse geochemical calculations*. US Geological Survey.

Rothbaum, H., Anderton, B., Harrison, R., Rohde, A., Slatter, A., 1979. Effect of silica polymerisation and pH on geothermal scaling. *Geothermics* **8**, 1-20.

Rothbaum, H., Rohde, A., 1979. Kinetics of silica polymerization and deposition from dilute solutions between 5 and 180 °C. *Journal of Colloid and Interface Science* **71**, 533-559.

Seward, T., 1974. Determination of the first ionization constant of silicic acid from quartz solubility in borate buffer solutions to 350 °C. *Geochimica et Cosmochimica Acta* **38**, 1651-1664.

Thórhallsson, S., Ragnars, K., Arnórsson, S., Kristmannsdóttir, H., 1975. *Rapid scaling of silica in two district heating systems*, United Nations Symposium on the Development and Use of Geothermal Resources, San Fransico, pp. 1445-1449.

Tobler, D.J., Benning, L.G., 2013. *In-situ* and time resolved nucleation and growth of silica nanoparticles forming under simulated geothermal conditions. *Geochimica et Cosmochimica Acta* **114**, 156-168.

Tobler, D.J., Shaw, S., Benning, L.G., 2009. Quantification of initial steps of nucleation and growth of silica nanoparticles: An *in-situ* SAXS and DLS study. *Geochimica et Cosmochimica Acta* **73**, 5377-5393.

Tobler, D.J., Stefansson, A., Benning, L.G., 2008. *In-situ* grown silica sinters in Icelandic geothermal areas. *Geobiology* **6**, 481-502.

van den Heuvel, D., Gunnlaugsson, E., Benning, L., in prep. Surface roughness and composition control silica deposition from geothermal fluids. *Geochemical Transactions*.

Weres, O., Yee, A., Tsao, L., 1981. Kinetics of silica polymerization. *Journal of Colloid and Interface Science* **84**, 379-402.

Wirth, R., 2009. Focused Ion Beam (FIB) combined with SEM and TEM: Advanced analytical tools for studies of chemical composition, microstructure and crystal structure in geomaterials on a nanometre scale. *Chemical Geology* **261**, 217-229.

Chapter 5

Surface roughness and composition control silica deposition from geothermal fluids

Daniela B. van den Heuvel[1], Einar Gunnlaugsson[2], Liane G. Benning[1,3]

[1] *Cohen Geochemistry Group, School of Earth and Environment, University of Leeds, Leeds LS2 9JT, UK*
[2] *Reykjavik Energy, Baejarhals 1, 110 Reykjavik, Iceland*
[3] *German Research Center for Geosciences, GFZ, 14473 Potsdam, Germany*

Abstract

Precipitation of amorphous silica (SiO_2) in geothermal power plants has been shown to occur via homogeneous nucleation in the fluid as well as heterogeneous nucleation on pre-existing surfaces. While the factors facilitating homogeneous nucleation are fairly well known, the effect of surface properties on the heterogeneous pathway are less well understood.

In this study we present data from a 10 week study of the precipitation of amorphous silica on three different surfaces (volcanic glass, non-precious opal and carbon steel) inside pipelines at the Hellisheiði power station (SW-Iceland). We found that regardless of the surface properties, heterogeneous nucleation dominated and lead to the formation of lens-shaped silica precipitates ('bumps') distributed across all surfaces. On smooth surfaces (volcanic glass and opal), short exposure (≤ 2 weeks) resulted in isolated silica bumps that became joined together only upon growth during longer exposure to the geothermal fluid. On rough surfaces (carbon steel), the density of the bumps was much higher and even after one day the surfac-

es were completely covered by silica. Despite these differences, the growth rate of the silica bumps was identical for all surfaces, indicating that growth was controlled by silica-silica interaction rather than silica-surface interactions.

Our results show that the choice of material for geothermal pipelines does affect the amount of silica scaling in geothermal pipelines. We also show that smoother or polished pipeline surfaces would be far more effective in reducing silica scaling inside a geothermal power station and this would help increase their efficiency.

5.1 Introduction

Silica scaling, i.e., the unwanted precipitation of amorphous silica (SiO_2) inside pipelines and onto other fluid-handling equipment, is a major issue in high-enthalpy geothermal power stations such as the ones in Iceland. The dissolution of silicate minerals in the deep geothermal reservoirs leads to geothermal fluids generally containing high concentrations of dissolved silica. For example, some of the fluids in one of Iceland's high temperature areas (Hengill) contain up to 1200 ppm SiO_2 (Scott et al., 2014). When these deep fluids are flashed and cooled during power generation, silica becomes highly supersaturated and this leads to rapid precipitation of amorphous silica. Worldwide in geothermal power production such silica precipitates lead to decreased production efficiency and thus a wide range of approaches have been tested with the aim to mitigate amorphous silica-scale formation. These include pH control (Fleming and Crerar, 1982; Henley, 1983), dilution with steam condensate (Gunnarsson and Arnórsson, 2003), ageing of the fluids before reinjection (Yanagase et al., 1970; Gunnarsson et al., 2010) or the use of (in)organic additives as potential inhibitors (Harrar et al., 1982; Gallup, 2002; Gallup and Barcelon, 2005; Amjad and Zuhl, 2008). However, due to the large variations in fluid chemistries and operational conditions between geothermal power plants, a universal method for adequately mitigating silica scaling does still not exists.

Studies on the precipitation of amorphous silica from geothermal fluids (Rothbaum et al., 1979; Carroll et al., 1998; Gunnarsson et al., 2010; van den Heuvel et al., in prep. (Chapter 4)) have suggested that upon rapid cooling of the fluids, polymerisation occurs and large 3D nuclei form. Experimental and modelling evidence has confirmed that these nuclei form through the self-condensation of silica monomers (H_4SiO_4) and that they grow to a critical size below which they rapidly

re-dissolve (Iler, 1979; Tobler et al., 2009; Noguera et al., 2015). Such nuclei can form and evolve both in solution (= homogeneous nucleation) or on surfaces (= heterogeneous nucleation) (Benning and Waychunas, 2007). Homogeneous nucleation has been studied in great detail both experimentally (Iler, 1979; Crerar et al., 1981; Icopini et al., 2005; Tobler et al., 2009) and in natural geothermal settings (Carroll et al., 1998; Mountain et al., 2003; Tobler et al., 2008; van den Heuvel et al., in prep. (Chapter 4)). Heterogeneous nucleation on the other hand has received very little attention and has only recently been described in detail for the first time in a geothermal system (van den Heuvel et al., in prep. (Chapter 4)). In order to quantitatively assess silica precipitation via the heterogeneous pathway inside geothermal pipelines, the effect of the pipeline wall properties on silica scaling at the interface needs to be understood. Therefore we have investigated the effect of surface composition and roughness and the effect of surface-fluid interactions on silica scaling. We studied the precipitation of silica onto three different surfaces: volcanic glass, opal and carbon steel and demonstrate that surface roughness is the most important parameter controlling the initial heterogeneous deposition of silica. We also show that once the surfaces have been covered by a continuous layer of silica any subsequent growth is controlled by silica-silica interactions, resulting in similar deposition rates for all surfaces. Our findings support the search for more suitable materials for reducing silica scaling in geothermal power plants.

5.2 Materials and methods

To study silica precipitation, we exposed scaling plates with different surfaces to the geothermal fluids at two locations inside the pipelines of the Hellisheiði geothermal power plant (SW-Iceland). Both locations were downstream from the steam separators, where the steam used for powering of turbines is separated from the water used for the production of thermal heat. This is where, due to the drop in temperature, silica saturation is usually reached for the first time. Location A is inside a pipeline located < 10 m before the heat exchanger and through which ~120 °C hot fluids flow, while location B is located several metres after the heat exchanger and contains ~60 °C hot fluids. At both locations, two 5.4 x 2 cm large S316 stainless steel scaling plates were inserted into the pipelines via specialist valves. These plates were exposed to the fast (up to 400 L/s) flowing geothermal fluid for up to 10 weeks. We chose three different substrates to address the compositional differences and

prepared these as coupons (2 x 1.3 cm) that were glued onto scaling plates using Loctite Hysol 9455 epoxy adhesive (Figure 5.1 A, left). The coupons consisted of (1) volcanic glass (VG) of rhyolitic composition from south Iceland, (2) non-precious opal (OPA) from Coober Peedy, Australia and (3) S275 carbon steel (Table 5.1).

Table 5.1: *Surface finish and compositions of the three types of coupons used in this study.*

	volcanic glass[1]		opal[1]		carbon steel (S275)[2]	
Finish	polished		polished		unpolished	
Composition [%]	SiO_2	69.5	SiO_2	92.5	Fe	> 98.0
	Al_2O_3	13.7	Al_2O_3	2.1	Mn	< 1.6
	Na_2O	4.8	Na_2O	0.3	C	< 0.25
	CaO	1.5	CaO	0.5	Si	< 0.05
	K_2O	3.5	K_2O	0.2	S	< 0.05
	MgO	0.2	MgO	0.1	P	< 0.04
	Fe_2O_3	5.1	Fe_2O_3	0.2		
	LOI	0.1	LOI	3.7		

[1] Composition derived from the XRF analyses with LOI (loss ion ignition) at 1050 °C

[2] Composition as provided by the manufacturer (RS Components)

The volcanic glass was chosen to represent the hyaloclastites making up the reservoir of the Hellisheiði geothermal field. However, the chosen rhyolitic glass is not an exact match for the more basaltic lithologies encountered at Hellisheiði (Alfredsson et al., 2013) but the surface properties and the behaviour of rhyolitic and basaltic glasses in solution has been shown to be comparable (Declercq et al., 2013). The opal was chosen to represent a different form of amorphous silica but with almost equivalent composition to the silica scales formed in Icelandic power plants (Meier et al., 2014 (Chapter 3); van den Heuvel et al., in prep. (Chapter 4)) or natural hot springs (Schultze-Lam et al., 1995; Tobler et al., 2008). The tinned S275 carbon steel was used as a readily-available, relatively corrosion resistant analogue for the high-grade carbon steel (P235GH) from which the pipelines at Hellisheiði are fabricated. The secondary goal for the choice of these materials was to test the effect of surface roughness onto the precipitation modes. Therefore, the two natural materials, the porous volcanic glass and the dense opal coupons were highly polished, while the S275 steel coupons were used as provided by the manufacturer (Table 5.1).

For comparison, at each location we also deployed a S316 stainless steel scaling plate without any coupons glued on (van den Heuvel et al., in prep. (Chapter 4)).

The so prepared scaling plates were left to react with the geothermal fluids inside the pipelines for between 1 day and 10 weeks at both locations. At the beginning and end of each deployment, the fluids were sampled by filtration through 0.2 μm polycarbonate filters and aliquots of the filtered fluids were preserved for analysis of anions, cations and dissolved gases (Arnórsson et al., 2006). All analyses were carried out at the University of Leeds unless otherwise stated. Anions (Cl) were analysed by ion chromatography (IC, Thermo Scientific Dionex DX600), major cations (Al, Ca, K, Na, Si) by inductively coupled plasma-optical emission spectroscopy (ICP-OES, Thermo Scientific iCAP7400) and trace cations (Mg, Mn, Fe) by inductively coupled plasma-mass spectrometry (ICP-MS, Thermo Scientific iCAPQc). The concentration of dissolved gases was measured by titration at Reykjavik Energy according to the methods described by Arnórsson et al. (2006). The *in-situ* fluid temperatures were obtained from the power plant operators who monitor temperature every hour.

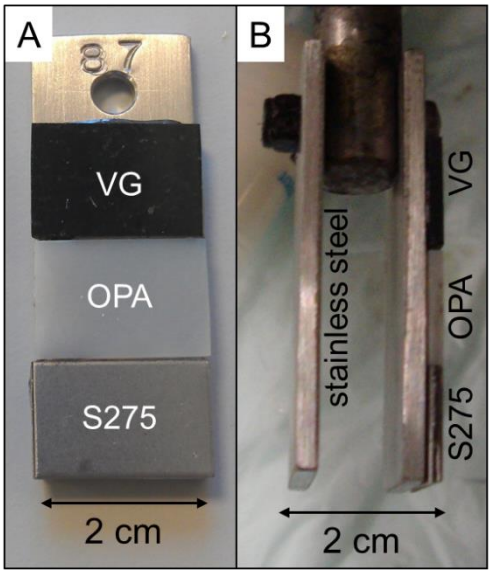

Figure 5.1: *Photographs of scaling plates before deployment (A) top view showing the different substrates and (B) side view illustrating the two plates (one stainless steel with glued on coupons and one pure stainless steel). Shown in B is also the attachment of the plates to the sampling rod used to insert the plates into the geothermal pipelines.*

Equivalent coupons of each substrate were imaged pre-deployment using a field emission gun scanning electron microscope (FEG-SEM, FEI Quanta 650 at 15 keV). In addition, the chemical analysis of the major and trace elements of the volcanic glass and the opal were performed on pressed powder tablets (32 mm diameter, 4 g sample + 0.9 g Hoechstwax as binder) using a Philipps WD-XRF PW2400 and the UniQuant 5 software (Omaga Data Systems) at the University of Fribourg. At the end of each deployment, the plates were removed from the fluid and dried at 30 °C for 24 h. Subsequently, they were photographed and where possible, precipitates from one half of each coupon were scraped off with a plastic spatula. These materials were ground using an agate mortar and pestle and the powders analysed by X-ray diffraction (XRD, Bruker D8, CuKα1; 5 – 90° 2θ, 0.01°/step). All coupons/plates were then coated with ~40 nm of gold and imaged and analysed using FEG-SEM (see above) and EDS (spot analyses, AZtec software, Oxford Instruments, Version 2.2). The EDS analyses were used to confirm the elemental compositions of the precipitates, while the FEG-SEM images were used to determine the dimensions of the individual morphological characteristics by measuring 70 to 150 individual features on each coupon.

5.3 Results

5.3.1 Composition of the geothermal fluid

The fluids from which silica precipitation occurred were low ionic strength fluids containing ~800 mg/L SiO_2 (Table 5.2). Silica was present as dissolved silica (76 – 86% monomeric, 14 – 24% polymeric; van den Heuvel et al., in prep. (Chapter 4)) and as silica particles that varied hugely in size (diameters between < 0.1 and 22.7 μm) but which had a mean particle size of 0.2 μm at location A and 0.1 μm at location B (van den Heuvel et al., in prep. (Chapter 4)). Other major components were ~270 mg/L NaCl, 25 mg/L $CO_{2[aq]}$ and 20 mg/L $H_2S_{[aq]}$ (Table 5.2). The biggest difference between location A and B was temperature and flow rate which were both higher at location A (~120 °C and > 400 L/s) compared to location B (~60 °C and < 300 L/s; Table 5.2).

5.3.2 Silica precipitation onto coupon surface

On all coupon surfaces precipitation of amorphous silica was observed. The samples were immersed for 1 day, 1 week, 2 weeks, 4 weeks, 6 weeks and 10 weeks. Unfortunately, some of the glued-on coupons were lost during deployments (volcanic glass: location A at 6 and 10 weeks, location B at 6 weeks; opal: location A at 6 weeks; S275 steel: location A at 1 week).

Table 5.2: *Average and standard deviation of temperature, flow rate and fluid composition for locations A and B.*

		Loc. A	Loc. B
Temp.	[°C]	117.8 ± 0.4	58.0 ± 5.3
Flow rate	[L/s]	427 ± 75	293 ± 29
SiO_2	[mg/L]	802 ± 19	794 ± 30
Na	[mg/L]	204 ± 8	207 ± 8
Cl	[mg/L]	173 ± 12	175 ± 6
CO_2	[mg/L]	25.4 ± 5.5	23.8 ± 3.7
H_2S	[mg/L]	19.2 ± 2.9	20.5 ± 1.9
K	[mg/L]	34.7 ± 1.6	35.1 ± 1.6
Al	[mg/L]	1.99 ± 0.09	2.04 ± 0.11
Ca	[mg/L]	0.71 ± 0.13	0.71 ± 0.04
Fe	[µg/L]	28.5 ± 44.5	21.6 ± 23.5
Mg	[µg/L]	21.5 ± 21.5	19.7 ± 14.2

Prior to deployment, the polished volcanic glass coupons were characterised by smooth surfaces with a few scratches and numerous tube-like or spherical pores/vesicles (Figure 5.2 A) that were a few micrometres to 2 mm in size. At the end of the individual deployments, the surfaces of the volcanic glass coupons were partly covered by lens-shaped amorphous silica structures hereafter called 'bumps' (Figure 5.2 B to E). For the short deployments (i.e., up to 2 weeks), the majority of these bumps were isolated with only a few joined together (Figure 5.2 B & C). Evaluating the time dependent development of these features revealed that the initial growth of the bump sizes (areas as evaluated based on measuring lengths and widths of bumps on each coupon) was rapid but slowed down for longer deploy-

ments (Figure 5.3). Furthermore, the increase of the bump sizes was faster at location A compared to location B. In addition to the bumps, individual silica particles were observed on the volcanic glass surfaces and in the vesicles (Figure 5.2 E). These silica particles were all spherical and ranged from < 0.5 to around 20 μm in size with an average of ~3.4 μm at location A and ~1.0 μm at location B.

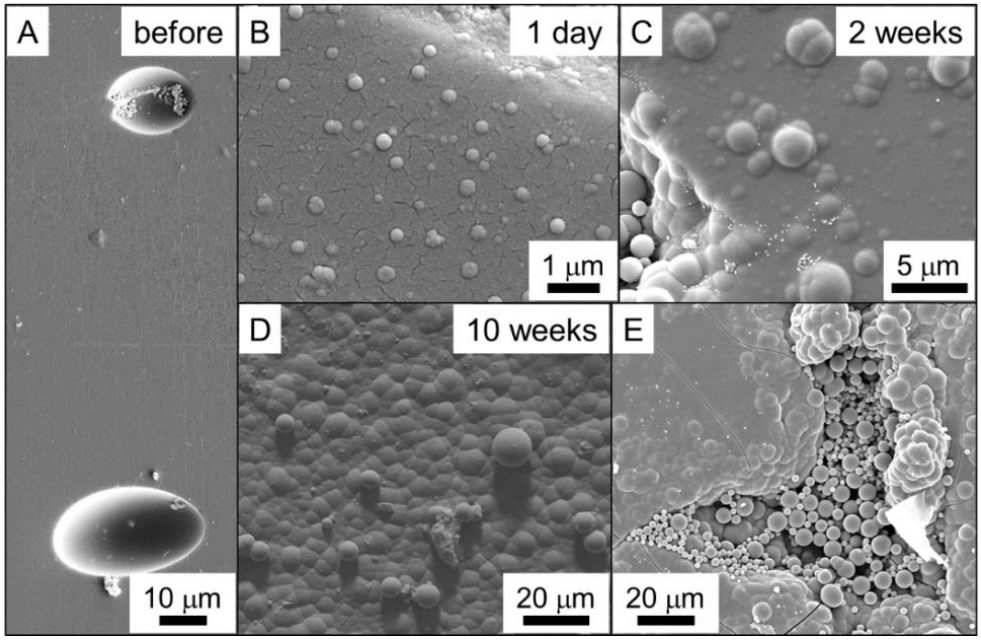

Figure 5.2: *FEG-SEM microphotographs of the volcanic glass surface (A) before deployment, (B) after 1 day, (C) after 2 weeks, (D) after 10 weeks and (E) a close-up of a vesicle filled by silica microspheres.*

In contrast to the volcanic glass, the polished opal, although also very smooth pre-deployment (Figure 5.4 A), did not have any vesicles or other morphological features. However, in some cases, during deployments small parts of the opal coupons chipped off along the edges, leaving typical conchoidal fractures. Post-deployment, the morphologies of amorphous silica deposits on the opal coupons were nearly identical to those observed on the volcanic glass coupons: isolated bumps that became joined together and grew over time as well as individual silica spheres with sizes comparable to those on the volcanic glass coupons (Figure 5.3 & 5.4). Silica particles were deposited on the smooth opal surfaces but when conchoidal fractures were present they were often found to be preferentially deposited along these conchoidal fractures (Figure 5.4).

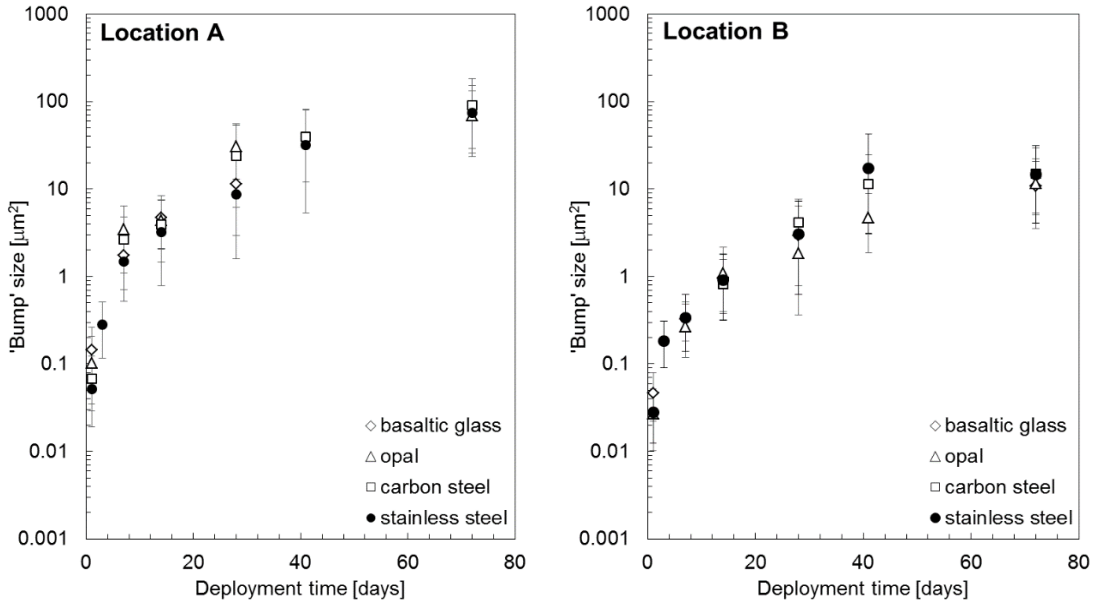

Figure 5.3: *Growth of bump size (areas as evaluated based on measuring lengths and widths of bumps on each coupon) as a function of time at location A (left) and B (right) for all surfaces. The stainless steel data are from van den Heuvel et al. (in prep. (Chapter 4).*

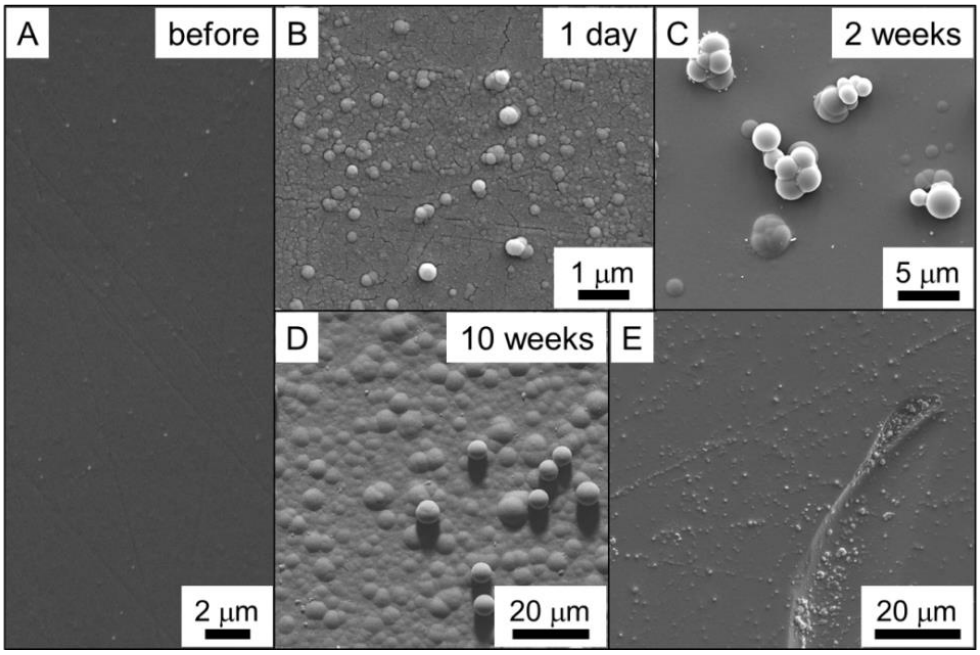

Figure 5.4: *FEG-SEM microphotographs of the opal surface (A) before deployment, (B) after 1 day, (C) after 2 weeks, (D) after 10 weeks and (E) close-up of a conchoidal fracture and deposited silica microspheres.*

Finally, the surfaces of the S275 carbon steel coupons, because they were not polished prior to deployment, contained many irregular patterns with ridges and swirls that created a rough topography (Figure 5.5 A), which was in stark contrast to the smooth surfaces of the volcanic glass (Figure 5.2 A) and opal (Figure 5.4 A). Nevertheless, the precipitation of amorphous silica also resulted in the coverage of the carbon steel surfaces with silica bumps and individual silica particles. In contrast to the smooth volcanic glass and opal surfaces, the S275 steel coupons were however completely covered by bumps even after 1 day. The increase of these bump sizes as a function of time (Figure 5.3) was indistinguishable from the other surfaces, again with growth at location A faster than location B. Furthermore, variably shaped corrosion minerals (needles, flowers, blades) were found to break through the silica layers in some places (Figure 5.5 E). These minerals were identified in a previous study (van den Heuvel et al., 2016 (Chapter 6)) to be iron sulphides (mackinawite and greigite) and their oxidation products (the iron oxides hematite and goethite).

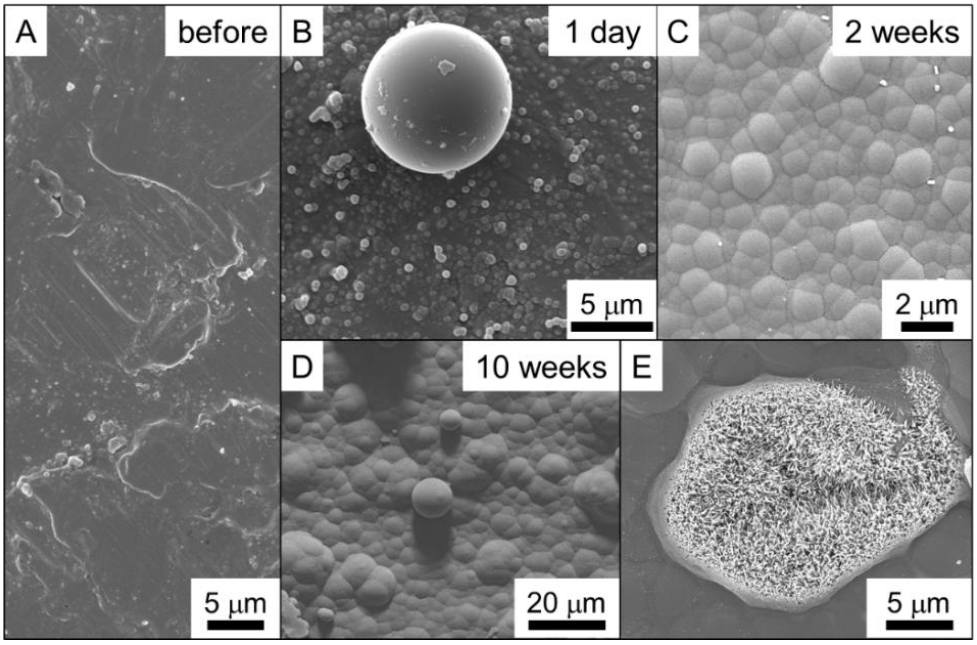

Figure 5.5: *FEG-SEM microphotographs of the carbon steel surface (A) before deployment, (B) after 1 day, (C) after 2 weeks, (D) after 10 weeks and (E) close-up of a Fe-sulphide "flower" (= corrosion product) breaking through the silica layer (from van den Heuvel et al., 2016 (Chapter 6)).*

5.4 Discussion

5.4.1 Interactions between the coupons and the fluid

The observed and above described silica precipitation features were not the only expected interactions between the coupons and the geothermal fluids. Declerq et al. (2013) showed that volcanic glass is highly reactive, especially at elevated temperatures, and that over the course of a few days dissolution is non-stoichiometric and leads to the rounding of edges and the precipitation of non-identified secondary minerals. However, in this study the volcanic glass coupons did not reveal any changes to their surface texture (although this is likely also a consequence of our observation approach through FEG-SEM images only) indicating limited dissolution. This difference may be due to the much lower specific surface area of our coupons (3.5 cm^2/g) compared to the volcanic glass powder used by Declerq et al. (2013) (~4300 cm^2/g). Furthermore, the continuous coverage of the coupon surfaces with silica, also decreased the ability for dissolution of the underlying volcanic glass to occur. In contrary, the opal coupons were not expected to dissolve as the fluids were supersaturated with respect to amorphous silica (= opal).

The biggest change in surface characteristics, aside from the silica precipitation features, was visible following the interaction between the S275 carbon steel and the geothermal fluids. We observed, even after short deployment times of 1 day, corrosion features (Figure 5.5 E), that were a consequence of the interactions between the carbon steel and the fluids that contain high concentration of H_2S and NaCl (van den Heuvel et al., 2016 (Chapter 6)). Nevertheless, corrosion of the deployed carbon steel coupons at both locations A and B was limited (Figure 5.5) compared to other sites (van den Heuvel et al., 2016 (Chapter 6)). The reduced corrosion can be explained as a consequence of the rapid silica precipitation (Figure 5.5) and the formation of a continuous silica layer that covered the whole coupon even after 1 day of reaction in the geothermal fluid. This continuous layer helped to passivate the carbon steel surfaces against further corrosion (van den Heuvel et al., 2016 (Chapter 6)).

5.4.2 Pathways of silica precipitation

Silica scaling occurred because, as the geothermal fluids passed through the steam separators, they became supersaturated with respect to amorphous silica. Despite the differences in coupon surface texture/roughness, reactivity and composition, silica precipitation was remarkably similar on volcanic glass, opal and carbon steel. Both, precipitate morphologies (bumps; Figures 5.2, 5.4 & 5.5) and the increase in bump sizes (Figure 5.3) were nearly equivalent and were also near-identical to observations made on stainless steel plates deployed together with the coupons (van den Heuvel et al., in prep. (Chapter 4)).

The presence of individual silica particles indicates homogeneous nucleation in the fluid, while the textures and morphologies observed on the coupons (bumps) indicate heterogeneous nucleation and growth on all available surfaces. Conceptually these can be represented as in the schematic shown in Figure 5.6.

In the case of a heterogeneous process the two main parameters that are known to affect nucleation are chemical composition and roughness of the interacting surface. The effect of surface chemistry has for example been evaluated through the use of different mineral types for nucleating ice (Murray et al., 2012; Zolles et al., 2015). The efficiency with which ice crystals nucleated was highly dependent on structure matching between the mineral surface and the newly forming ice nuclei. In our study we infer that the nucleation of amorphous silica on silica-based surfaces (volcanic glass and opal) is due to the structural similarities. The abundance of surface silanol groups on the opal and volcanic glass surfaces allows the formation of Si-O-Si bonds with the dissolved silica leading to the observed silica bumps and their growth into layers. Conversely, the nucleation efficiency of the carbon steel, purely based on chemical properties, should be far lower than the two silica-based surfaces due to the much larger chemical discrepancies between these surfaces and the precipitating silica. However, the much rougher surface enhances heterogeneous nucleation as it has a higher surface area and a variety of nooks which act as preferential nucleation sites (Eastwood et al., 2008; Murray et al., 2012). In addition, the topography of the rough steel surfaces results in turbulent flow at the steel-fluid interface which enhances deposition of silica (Hawkins et al., 2013). This is in agreement with our findings from the smooth surfaces: On the volcanic glass and the opal, the bumps were preferentially lined up along superficial scratches (Fig-

ure 5.4 E & 5.6), which happened during sample preparation or subsequent handling, and which provide nucleation sites as well as causing small turbulences.

On all surfaces, irrespective of chemical composition and roughness, once formed the bumps grew by addition of dissolved silica. This is controlled by silica-silica interactions and independent of the surface on which the initial silica deposition occurred (Figure 5.3).

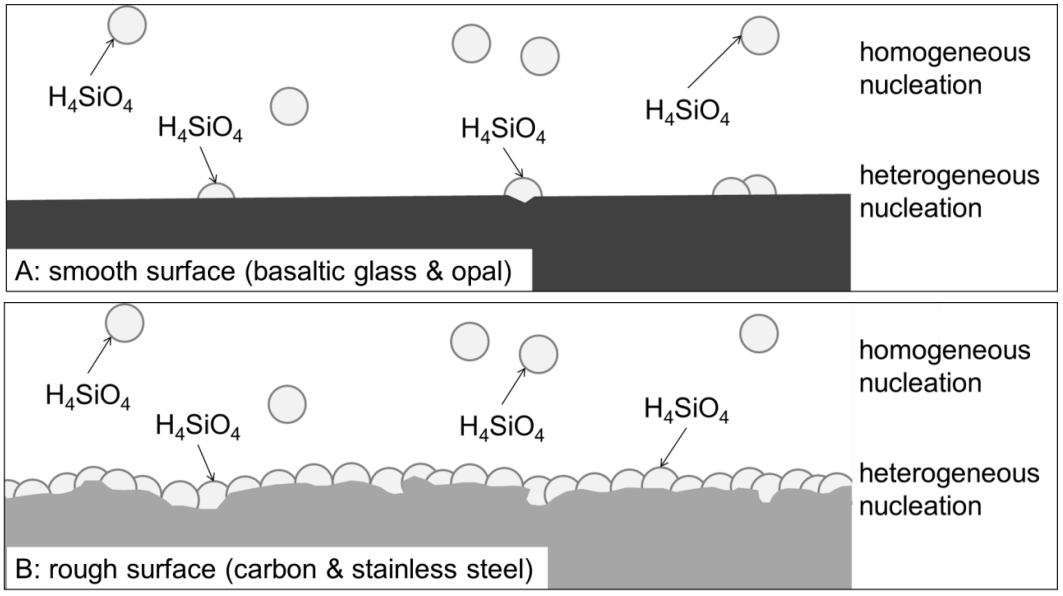

Figure 5.6: *Heterogeneous and homogeneous nucleation of silica in the presence of (A) a smooth surface offering few nucleation sites and (B) a rough surface offering plenty of nucleation sites.*

We also observed homogeneous nucleation of particles in the fluid of the Hellisheiði power plant. These particles deposited on the surfaces of the coupons after the silica layers formed. Homogeneous nucleation as a process has a higher energy barrier compared to heterogeneous nucleation on a surface (Benning and Waychunas, 2007), yet the presence of silica particles in the separated water at the Hellisheiði power plant suggests that homogeneous nucleation nevertheless occurs widely. This is not surprizing as the conditions are highly favourable for polymerisation of silica (elevated temperatures, highly supersaturated with respect to amorphous silica but low ionic strength) which is inductive of spontaneous nucleation and growth of amorphous silica as shown in numerous experimental and field studies (Iler, 1979; Icopini et al., 2005; Tobler et al., 2008; Tobler et al., 2009; van den

Heuvel et al., in prep. (Chapter 4)). The growth of the so formed amorphous silica particles is also proceeding mostly by monomer addition (Iler, 1979; Tobler et al., 2009). The deposition of the silica particles is seemingly controlled by surface topography, as evidenced for example by the filled vesicles in the volcanic glass (Figure 5.2 E) and the preferential deposition of particles along the conchoidal fractures on the opal coupons (Figure 5.4 E). These topographic features resulted in local turbulences in the fluid which enhanced their precipitation. Larger particles were preferentially deposited due to higher drag.

5.4.3 Impact on the search for mitigation strategies

The findings from the present study indicate that the surface roughness is a crucial factor controlling both pathways of silica deposition: heterogeneous nucleation and growth of a bumpy layer as well as deposition of homogeneously nucleated silica particles. Our results suggest that smooth surfaces show the smallest amount of silica deposition while rough surfaces cause the accumulation of more substantial amounts of silica scale. This is interesting for the design of future geothermal power plants, as polishing of surfaces could potentially reduce the deposition of silica and help mitigating the scaling problem.

An additional approach is the development of anti-scaling coatings. Sugama and Gawlik (2002) found that polytetrafluoroethylene blended polyphenylenesulfide coatings showed promising results in the prevention of silica scaling. These coatings create an anti-oxidant and hydrophobic surface which prevents the formation of a high-surface area corrosion layer and thus retains the smoothness of the steel. While polishing and coating could represent mitigation strategies for flat surfaces such as pipelines, it would not help with silica scaling in valves, orifices and around other flow obstacles onto which silica would readily deposit due to their surface textures (e.g., welding seams, bolts) and the turbulent flow. In order to assess the effectiveness of modifying surface roughness by polishing and/or coatings, testing at a larger scale and for time periods of 10+ weeks would be required.

5.5 Conclusions

Silica in geothermal pipelines can precipitate via heterogeneous or homogeneous nucleation. Both pathways are strongly affected by the surface properties: Rough

surfaces provide a plethora of nucleation sites for the heterogeneous pathway while nucleation sites on smooth surfaces were fewer. In both cases, the nuclei grew by addition of dissolved silica (controlled by silica-silica interactions), resulting in the formation of a bumpy silica layer. Homogeneous nucleation on the other hand led to the formation and growth of silica particles in the fluid. Their deposition was also controlled by surface properties as they were preferentially deposited onto surfaces with a high topographical relief. These results indicate that manipulating the surface properties of materials used for the construction of geothermal pipelines could represent a potential mitigation strategy for silica scaling.

Acknowledgments

This research was made possible by a Marie Curie grant from the European Commission in the framework of the MINSC ITN (Initial Training Research network), Project number 290040, the 2014 PhD Student Grant by the International Geothermal Association (IGA) awarded to DBH and a UK Natural Environment Research Council grant (NE/J008745/1) awarded to LGB. We thank GT Opals in Coober Peedy for providing the opal samples and Tony Windross, Stephen Burgess and Hari Williams for preparation of all plates and coupons. We are grateful to Gisela Weibel at the University of Bern for XRF analyses. We would like to thank the local staff at Hellisheiði, especially Halldór Bergmann, for help with sampling and are grateful to the laboratory staff at Reykjavik energy and Stephen Reid, Fiona Keay and Richard Walshaw at the University of Leeds for fluid analyses as well as for support with scanning electron microscopy.

References

Alfredsson, H.A., Oelkers, E.H., Hardarsson, B.S., Franzson, H., Gunnlaugsson, E., Gislason, S.R., 2013. The geology and water chemistry of the Hellisheiði, SW-Iceland carbon storage site. *International Journal of Greenhouse Gas Control* **12**, 399-418.

Amjad, Z., Zuhl, R., 2008. *An evaluation of silica scale control additives for industrial water systems*, Proceedings of the NACE International Corrosion Conference and Expo, New Orleans, pp. 3180-3192.

Arnórsson, S., Bjarnason, J.Ö., Giroud, N., Gunnarsson, I., Stefánsson, A., 2006. Sampling and analysis of geothermal fluids. *Geofluids* **6**, 203-216.

Benning, L.G., Waychunas, G.A., 2007. Nucleation, growth, and aggregation of mineral phases: Mechanisms and kinetic controls, *Kinetics of Water-Rock Interaction*. Springer, pp. 259-333.

Carroll, S., Mroczek, E., Alai, M., Ebert, M., 1998. Amorphous silica precipitation (60 to 120 °C): Comparison of laboratory and field rates. *Geochimica et Cosmochimica Acta* **62**, 1379-1396.

Crerar, D.A., Axtmann, E.V., Axtmann, R.C., 1981. Growth and ripening of silica polymers in aqueous solutions. *Geochimica et Cosmochimica Acta* **45**, 1259-1266.

Declercq, J., Diedrich, T., Perrot, M., Gislason, S.R., Oelkers, E.H., 2013. Experimental determination of rhyolitic glass dissolution rates at 40–200 °C and 2<pH<10.1. *Geochimica et Cosmochimica Acta* **100**, 251-263.

Eastwood, M.L., Cremel, S., Gehrke, C., Girard, E., Bertram, A.K., 2008. Ice nucleation on mineral dust particles: Onset conditions, nucleation rates and contact angles. *Journal of Geophysical Research: Atmospheres* **113**.

Fleming, B., Crerar, D., 1982. Silicic acid ionization and calculation of silica solubility at elevated temperature and pH application to geothermal fluid processing and reinjection. *Geothermics* **11**, 15-29.

Gallup, D.L., 2002. Investigations of organic inhibitors for silica scale control in geothermal brines. *Geothermics* **31**, 415-430.

Gallup, D.L., Barcelon, E., 2005. Investigations of organic inhibitors for silica scale control from geothermal brines–II. *Geothermics* **34**, 756-771.

Gunnarsson, I., Arnórsson, S., 2003. *Silica scaling: The main obstacle in efficient use of high-temperature geothermal fluids*, Proceedings International Geothermal Conference, Reykjavik, pp. 30-36.

Gunnarsson, I., Ívarsson, G., Sigfússon, B., Thrastarson, E.Ö., Gíslason, G., 2010. *Reducing silica deposition potential in waste waters from Nesjavellir and Hellisheiði Power Plants, Iceland*, Proceedings World Geothermal Congress, Bali.

Harrar, J., Locke, F., Otto Jr, C., Lorensen, L., Monaco, S., Frey, W., 1982. Field tests of organic additives for scale control at the Salton Sea geothermal field. *Society of Petroleum Engineers Journal* **22**, 17-27.

Hawkins, C., Angheluta, L., Hammer, Ø., Jamtveit, B., 2013. Precipitation dendrites in channel flow. *Europhysics Letters* **102**, 54001.

Henley, R., 1983. pH and silica scaling control in geothermal field development. *Geothermics* **12**, 307-321.

Icopini, G.A., Brantley, S.L., Heaney, P.J., 2005. Kinetics of silica oligomerization and nanocolloid formation as a function of pH and ionic strength at 25 °C. *Geochimica et Cosmochimica Acta* **69**, 293-303.

Iler, R.K., 1979. *The chemistry of silica: solubility, polymerization, colloid and surface pro perties, and biochemistry*. Wiley, London.

Meier, D., Gunnlaugsson, E., Gunnarsson, I., Jamtveit, B., Peacock, C., Benning, L., 2014. Microstructural and chemical variation in silica-rich precipitates at the Hellisheiði geothermal power plant. *Mineralogical Magazine* **78**, 1381-1389.

Mountain, B., Benning, L., Boerema, J., 2003. Experimental studies on New Zealand hot spring sinters: rates of growth and textural development. *Canadian Journal of Earth Sciences* **40**, 1643-1667.

Murray, B., O'Sullivan, D., Atkinson, J., Webb, M., 2012. Ice nucleation by particles immersed in supercooled cloud droplets. *Chemical Society Reviews* **41**, 6519-6554.

Noguera, C., Fritz, B., Clément, A., 2015. Precipitation mechanism of amorphous silica nanoparticles: a simulation approach. *Journal of Colloid and Interface Science* **448**, 553-563.

Rothbaum, H., Anderton, B., Harrison, R., Rohde, A., Slatter, A., 1979. Effect of silica polymerisation and pH on geothermal scaling. *Geothermics* **8**, 1-20.

Schultze-Lam, S., Ferris, F., Konhauser, K., Wiese, R., 1995. *In-situ* silicification of an Icelandic hot spring microbial mat: implications for microfossil formation. *Canadian Journal of Earth Sciences* **32**, 2021-2026.

Scott, S., Gunnarsson, I., Arnórsson, S., Stefánsson, A., 2014. Gas chemistry, boiling and phase segregation in a geothermal system, Hellisheiði, Iceland. *Geochimica et Cosmochimica Acta* **124**, 170-189.

Sugama, T., Gawlik, K., 2002. Anti-silica fouling coatings in geothermal environments. *Materials Letters* **57**, 666-673.

Tobler, D.J., Shaw, S., Benning, L.G., 2009. Quantification of initial steps of nucleation and growth of silica nanoparticles: An *in-situ* SAXS and DLS study. *Geochimica et Cosmochimica Acta* **73**, 5377-5393.

Tobler, D.J., Stefansson, A., Benning, L.G., 2008. *In-situ* grown silica sinters in Icelandic geothermal areas. *Geobiology* **6**, 481-502.

van den Heuvel, D.B., Gunnlaugsson, E., Benning, L.G., 2016. *Passivation of metal surfaces against corrosion by silica scaling*, Proceedings Workshop on Geothermal Reservoir Engineering Stanford.

van den Heuvel, D.B., Gunnlaugsson, E., Gunnarsson, I., Stawski, T.M., Peacock, C.L., Benning, L.G., in prep. Two pathways of amorphous silica precipitation control scaling inside in-use geothermal pipelines. *Geochimica et Cosmochimica Acta*.

Yanagase, T., Suginohara, Y., Yanagase, K., 1970. The properties of scales and methods to prevent them. *Geothermics* **2**, 1619-1623.

Zolles, T., Burkart, J., Häusler, T., Pummer, B., Hitzenberger, R., Grothe, H., 2015. Identification of ice nucleation active sites on feldspar dust particles. *The Journal of Physical Chemistry A* **119**, 2692-2700.

Chapter 6

Passivation of metal surfaces against corrosion by silica scaling

Daniela B. van den Heuvel[1], Einar Gunnlaugsson[2], Liane G. Benning[1,3]

[1] *Cohen Geochemistry Group, School of Earth and Environment, University of Leeds, Leeds LS2 9JT, UK*
[2] *Reykjavik Energy, Baejarhals 1, 110 Reykjavik, Iceland*
[3] *German Research Center for Geosciences, GFZ, 14473 Potsdam, Germany*

Abstract

In high-enthalpy geothermal systems the precipitation of amorphous silica (SiO_2) is the most common scaling problem. Together with corrosion, silica scaling affects the efficiency of geothermal power plants through increased maintenance costs and reduced equipment lifetimes. Despite their crucial importance for the development of better mitigation strategies, the relationship and inter-dependencies between scaling and corrosion are poorly understood. Here we present data from a time resolved study where the development of both silica precipitates and corrosion features on S316 stainless plates and S275 carbon steel coupons immersed in geothermal waters at the Hellisheiði power plant (SW-Iceland) were followed for between 1 day and 10 weeks. We chose four locations that differ with respect to fluid temperatures (55 to 120 °C) and silica concentration (550 to 800 ppm) and characterized the morphologies and textures of the precipitating silica and the corrosion products by high resolution imaging, while the solid precipitates and corrosion products were identified by X-ray diffraction (XRD) and energy dispersive spectroscopy (EDS). Silica precipitates were observed on all plates as uneven layers and rounded

'bumps' covering the plates completely, even after 1 day. With time and regardless of prevailing conditions, the size of the individual 'bumps' increased. Where silica precipitation was high, the carbon steel revealed only minor signs of corrosions, while where silica precipitation was minor ubiquitous corrosion was observed. The corrosion products were composed of iron sulphides (mackinawite and greigite), as well as their oxidized products (elemental sulphur, goethite and hematite). We show that in environments where silica precipitation is slow, corrosion dominates, while once an initial amorphous silica layer formed fast this will protect the underlying carbon steel from further reaction with the geothermal fluids and therefore from continuing corrosion. Thus, silica scaling can indeed act as a passivating agent for steel surfaces prone to corrosion.

6.1 Introduction

Geothermal fluids are often rich in dissolved solids and gases, leading to two challenges which have to be overcome in order to run a high enthalpy geothermal power plants efficiently: scaling, i.e., the unwanted precipitation of minerals inside pipelines and other fluid-handling equipment, and corrosion. Both of these processes can result in the clogging of pipelines, heat exchangers and wells and reduce the lifetime of pumps and turbines. They also impair the financial performance of a power plant due to the reduction in power generation, increased operating costs (e.g., additional costs for anti-scaling treatments or more corrosion-resistant materials or need for additional pumping capacity) and longer and more regular downtimes required for cleaning and maintenance of the system.

In the high-enthalpy systems of Iceland, the biggest challenge is amorphous silica scaling (Gunnarsson and Arnórsson, 2003). Silica is very abundant in most geothermal waters with concentrations of more than 1200 ppm SiO_2 in the geothermal fluids of the Hengill area, Iceland (Scott et al., 2014). Once silica supersaturation is reached, precipitation, especially under conditions of high ionic strength, was observed to be very rapid with rates of over 300 kg $year^{-1}$ m^{-2} in the wastewater drains at the Reykjanes geothermal field (Tobler et al., 2008). Silica scales can also be very hard and are not easily dissolved and therefore difficult to remove from equipment surfaces. In addition, conventional approaches to mitigate scaling, such as inhibitor addition have so far proven less effective against silica scaling (Demadis et al., 2007). Although precipitation of amorphous silica in natural geothermal set-

tings has been studied extensively (e.g., Mountain et al., 2003; Tobler et al., 2008), the processes inside in-use geothermal pipelines have only recently been investigated for the first time (van den Heuvel et al., in prep.a (Chapter 5); van den Heuvel et al., in prep.b (Chapter 4)). One of the factors complicating the understanding of silica precipitation onto steel surfaces is corrosion of the pipes and other fluid handling equipment. Corrosion can affect scaling, resulting in silica scales enriched in iron and/or containing inclusions of iron or other metal sulphides or oxides (Rothbaum et al., 1979; Deutscher et al., 1980). Furthermore, corrosion can also enhance precipitation due to the creation of higher surface areas (Harrar et al., 1982; Neofotistou and Demadis, 2004). In high enthalpy geothermal systems, corrosion is usually a consequence of the reactions between corrosive dissolved gas (most often hydrogen sulphide, $H_2S_{(aq)}$ e.g., ~20 ppm of $H_2S_{(aq)}$ in the separated water at the Hellisheiði power plant; Meier et al., 2014 (Chapter 3)) and metal surfaces. This reaction most often leads to the formation of metal sulphides. Under fully reducing conditions, studies in geothermal systems have shown that mackinawite (non-stoichiometric FeS) is the dominant mineral phase forming as a corrosion product (Soylemezoglu and Harper, 1982; Tang et al., 2010). Other iron sulphides such as greigite, troilite, pyrrhotite and pyrite have been observed under slightly more oxidized conditions. Under even more oxidizing conditions even iron (hydr)oxides (goethite, hematite, magnetite) have been observed (Soylemezoglu and Harper, 1982; Richter et al., 2006), although these could be simply an oxidation product of the former sulphides.

Scaling in geothermal systems, especially when occurring rapidly, can limit the extent of corrosion (Braithwaite and Lichti, 1980; Lichti et al., 1981). In a recent study, based on a single time point we (Meier et al., 2014 (Chapter 3)) suggested that corrosion in the pipes of Hellisheiði occurred before the build-up of substantial silica layers. However, where more silica precipitation occurred corrosion was prevented or at least slowed down. If silica scaling could be controlled, this could potentially represent a cheap and easy way to reduce the issues related to corrosion in silica-rich geothermal systems. The problem however lies in the fact that, the mechanism and temporal relationships between scale formation and corrosion are still poorly quantified. With this study, we took the first step in this direction by evaluating the temporal changes in silica scaling and corrosion of carbon steel, deployed inside the pipelines at Hellisheiði for different periods of time (between 1 day and 10 weeks). Our results allowed us to quantify how rapid silica scaling occurred. We show that silica scaling resulted in the formation of a dense layer of amorphous sili-

ca that quickly isolated the steel surfaces from the reacting geothermal fluids. This way, in some cases, the silica cover strongly reduced and even prevented further corrosion.

6.2 Materials and methods

Silica precipitation and corrosion were monitored using stainless steel scaling plates (5 x 2 cm) deployed at four different points within the pipelines of the Hellisheiði geothermal power plant (Figure 6.1): (1) inside the power plant but before the heat exchangers, (2) inside the power plant but after the heat exchangers, (3) outside the power plant and (4) at the Húsmúli injection site, after mixing with steam condensate. All these deployment points were located in pipes that carried fluid following steam separation for use in the production of electrical energy. After the removal of the steam the separated water reached supersaturation with respect to amorphous silica and precipitation occurred. The four locations differed with respect to temperature, fluid flow rate and concentration of dissolved silica and H_2S_{aq} (Table 6.1).

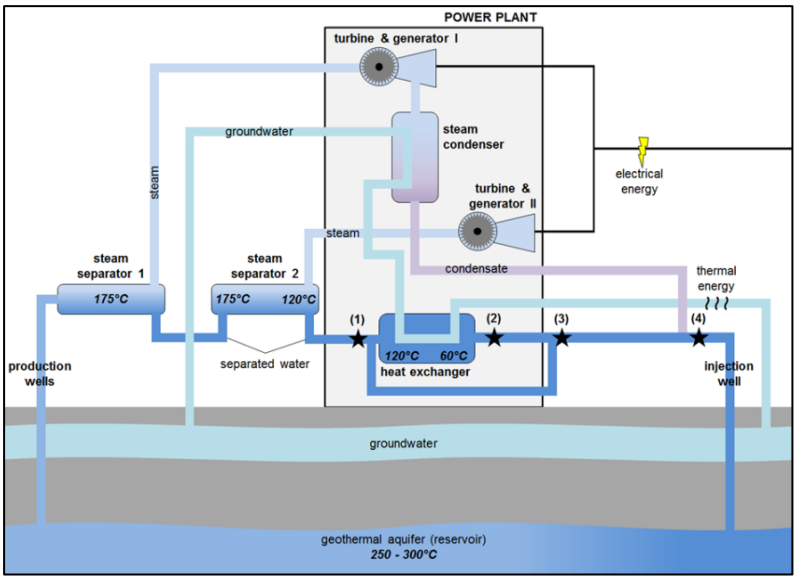

Figure 6.1: *Schematic of the Hellisheiði geothermal power station indicating the four locations (*) at which the scaling plates were immersed. Full details and schematics of the Hellisheiði power plant are available at http://www.or.is/vinnsluras.*

At each location two scaling plates (wiped clean with ethanol and stored in individual tubes until deployment) were inserted into pipes into the fast (up to

400 L/s) flowing fluid. The bottom plate was a S316 stainless steel plate (Figure 6.2 A, left), while the top plate consisted of an equivalent S316 stainless steel plate onto which 3 different 2 x 1.3 cm coupons were glued (Figure 6.2A, right) using Loctite Hysol 9455 epoxy adhesive. These coupons were used to assess the effects that varying substrate composition and surface roughness have on silica precipitation and corrosion. The coupons consisted of (a) basaltic glass from south Iceland, (b) opal from Coober Peedy, Australia and (c) S275 carbon steel (Figure 6.2 A, right). In the current paper we focus primarily on the processes observed on the S275 carbon steel coupons and compared them with the results from the S316 stainless steel plates (presented in van den Heuvel et al., in prep.b (Chapter 4)). All other substrates are part of another publication (van den Heuvel et al., in prep.a (Chapter 5)). The S275 carbon steel contained 0.25% carbon, 1.6% manganese, 0.05% silicon, 0.04% phosphorus and 0.05% sulphur.

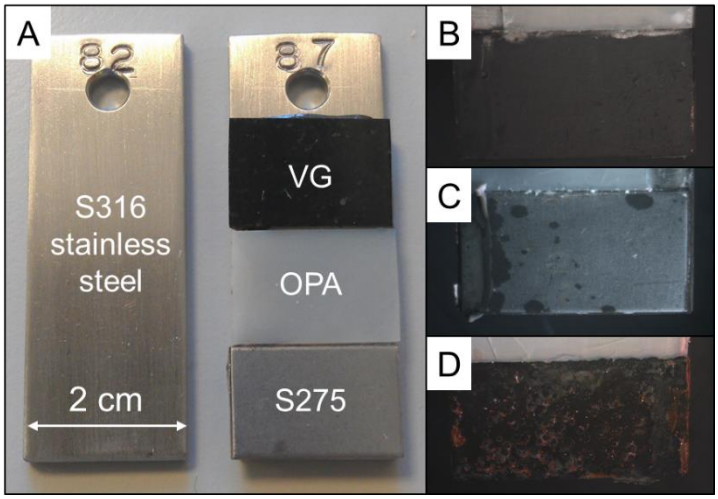

Figure 6.2: *Photographs of scaling plates before (A) and after the deployments (B-D). For each deployment, two scaling plates were prepared (A): S316 stainless steel scaling plate (left) and S316 stainless steel scaling plate with volcanic glass (VG), opal (OPA) and carbon steel (S275) coupons glued onto its surface (right). During some deployments, the carbon steel corroded showing homogeneous blackening (B), patchy corrosion (C) or the formation of a thick layer of corrosion products (D).*

Each set of scaling plates was deployed for between 1 day and 10 weeks. At the beginning and end of each deployment, the separated water was sampled at each location through a valve and immediately filtered through 0.2 µm polycarbonate filters. The pH was measured at temperatures of 23 to 27 °C and sample ali-

quots were collected for analysis of anions, cations and dissolved gases (for details of sample preservation and sampling containers see Arnórsson et al., 2006). The *in-situ* fluid temperatures at each location were obtained from the power plant operators. Anions were analysed by ion chromatography (IC) and cations by inductively coupled plasma-mass spectrometry (ICP-MS) at the University of Leeds. The concentration of dissolved gases was measured by titration at Reykjavik Energy according to the methods described by Arnórsson et al. (2006). The filters were retained, dried and the solids on the filters analysed by X-ray diffraction (XRD, Bruker D8, CuKα_1; 5-90° 2θ, 0.01°/step) at the University of Leeds. XRD patterns were evaluated using the EVA software (Bruker, Version 3.0). The compositions of the separated waters, as well as the pH and temperatures were used as inputs for geochemical simulations with PHREEQC (version 3.0; Parkhurst and Appelo, 2013) using the database phreeqc.dat updated with the latest thermodynamic data for amorphous silica (Gunnarsson and Arnórsson, 2000).

After set periods of time the plates were removed from the fluid and dried at 30 °C for 24 h. They were photographed and where possible, precipitates and/or corrosion products from half of each scaling plate or coupon were scraped off with a plastic spatula. These materials were ground using an agate mortar and pestle and the powders analysed by XRD as described above. All plates were then coated with ~40 nm of gold and the precipitates or corrosion features were imaged using a field emission scanning electron microscope (FEG SEM, FEI Quanta 650 at 20 keV). Spot analyses were performed using an energy dispersive spectrometer (EDS) and spectral information evaluated using the AZtec software (Oxford Instruments, Version 2.2). The SEM images were used to determine the size of the observed morphological features by measuring at least 100+ individual features on each coupon or plate manually and determining their mean dimensions.

6.3 Results

6.3.1 Composition of geothermal fluid

The sampling locations differed with respect to the fluid temperature, composition of the separated water and thus pH and Eh (Table 6.1). The temperatures decreased from 118 °C before the heat exchanger (location 1) to just under 60 °C at locations 2 and 3. The fluid composition was more or less constant with ~800 ppm SiO_2 and

nearly 400 ppm NaCl for these three locations. Dissolved gases were also abundant with around 25 ppm CO_2 and 20 ppm H_2S (Table 6.1).

Table 6.1: *Average and standard deviation of measured temperatures, measured fluid compositions and pH, calculated pH, Eh saturation indices and* in-situ *solubility for each sampling location (from van den Heuvel et al., in prep.b (Chapter 4)).*

		Loc. 1	Loc. 2	Loc. 3	Loc. 4
Temp.	[°C]	117.8 ± 0.4	56.6 ± 1.6	58.0 ± 5.3	72.5 ± 11.2
CO_2	[ppm]	25.4 ± 5.5	25.2 ± 4.8	23.8 ± 3.7	18.5 ± 3.8
H_2S	[ppm]	19.2 ± 2.9	19.8 ± 2.5	20.5 ± 1.9	14.3 ± 2.7
SiO_2	[ppm]	802 ± 19	801 ± 30	794 ± 30	550 ± 76
Na	[ppm]	204 ± 8	205 ± 9	207 ± 8	140 ± 10
Cl	[ppm]	173 ± 12	171 ± 9	175 ± 6	120 ± 5
K	[ppm]	34.7 ± 1.6	34.7 ± 1.7	35.1 ± 1.6	23.6 ± 1.2
Al	[ppm]	1.99 ± 0.09	2.04 ± 0.11	2.04 ± 0.11	1.36 ± 0.07
Ca	[ppm]	0.71 ± 0.13	0.70 ± 0.06	0.71 ± 0.04	0.50 ± 0.06
Fe	[ppb]	28.5 ± 44.5	16.4 ± 13.1	21.6 ± 23.5	25.2 ± 29.5
Mg	[ppb]	21.5 ± 21.5	19.6 ± 12.9	19.7 ± 14.2	22.1 ± 15.6
pH meas. [1)]		9.4 ± 0.2	9.4 ± 0.2	9.4 ± 0.2	9.1 ± 0.3
pH calc.[2)]		8.5 ± 0.1	9.0 ± 0.1	9.0 ± 0.1	8.8 ± 0.2
Eh[2)]	[V]	-0.56 ± 0.01	-0.46 ± 0.01	-0.47 ± 0.01	-0.48 ± 0.02
Amorphous silica					
Solubility [3)]	[ppm]	470	210	210	260
Saturation index [2)]		0.1	0.4	0.4	0.2

[1)] As measured at 21 to 27 °C

[2)] Derived from PHREEQC simulations at *in-situ* temperatures and with the given fluid compositions

[3)] Calculated according to Gunnarsson and Arnórsson (2000)

The measured fluid pH is identical for locations 1 to 3. However, the calculated pH using PHREEQC is lower in all cases as it is re-calculated to reflect the *in-situ* temperatures. The difference in pH is biggest (nearly 1 log unit) at location 1 where the fluid is hottest and less than half a log unit at the cooler locations 2 and 3. The Eh is lower at the highest temperature (location 1) and similar at all other locations. Location 4 was different due to the addition of steam condensate (Figure 6.1). The condensate was hotter than the separated water and its addition lead to dilution

of the SiO_2 and H_2S concentrations (~550 ppm and 14 ppm respectively; Table 6.1). The calculated pH and Eh values fell in between those of the other locations (8.8 and -0.5 V respectively, Table 6.1). Overall, location 1, 2 and 3 were fairly similar yet, location 4 was by far the most diverse in terms of temperature, pH, Eh and fluid composition.

Electron microscopic images of the materials captured by the filters revealed the presence of spherical particles, which at locations 1 to 3 varied in size between 0.05 and 25 μm (0.3 to 0.7 μm on average). EDS identified these as silica. In addition, small platy phases on the filters were identified by EDS analyses to primarily consist of Al and Si and complementary XRD analyses suggested these to be the alumosilicate clinochlor. At location 4, such silica particles were very sparse, but platy alumosilicates were abundant. XRD identified them as chamosite and clinochlore and the magnesium silicate sepiolite. At all locations, on the filters we also found small (< 2 μm) metal rich (identified by EDS) flakes, which were transported along in the fluid and likely originated from the corrosion of the pipelines or valves

6.3.2 Description of mineral phases and corrosion features on scaling plates

We compare here features observed on the S316 scaling plates (described in detail in van den Heuvel et al., in prep.b (Chapter 4)) and the S275 coupons from each location with immersion times of 1 day, 1 week, 2 weeks, 4 weeks, 6 weeks and 10 weeks. At location 2, all glued on S275 carbon steel coupons were lost during deployments. At the remaining three locations, all but one (location 3, 1 week) S275 carbon steel coupons were recovered (Table 6.2).

At location 1, regardless of deployment time no or only minor macroscopically distinguishable traces of corrosion were visible (Table 6.2) on the S275 carbon steel coupons. Microphotographs however, revealed that the coupon surfaces were largely covered by an uneven layer of amorphous silica (identified by XRD) that consisted primarily of rounded 'bumps' and individual spherical silica particles (Figure 6.3 A & B). The diameter of these 'bumps' increased from 0.3 μm after 1 day to over 12 μm after 10 weeks (Figure 6.3 A & B , Figure 6.4 A). This is identical to the change in size of amorphous silica 'bumps' determined on the stainless steel plates from the same location (van den Heuvel et al., in prep.b (Chapter 4)). In addition, silica microspheres identical to those observed on the filters were found on the silica-coated steel surfaces (Figure 6.3 A). Furthermore, variably shaped corrosion min-

erals (needles, flowers, blades plates), were found to break through the silica layers in some places (Figure 6.3 C to E). Due to this localized appearance, the exact nature of these mineral phases could not be identified by XRD. However, their morphologies together with multiple EDS spot analyses (solely Fe and, in most cases, S) and combined with the bulk XRD confirmed these phases to be iron sulphides (mackinawite and greigite) and their oxidation products (the iron oxides hematite and goethite).

Table 6.2: *Stereo microscope (black) and scanning electron microscopy (in grey) observations of corrosion features and shapes of products. At locations 1 and 3 an uneven silica layer was the dominant precipitate.*

	Loc. 1	Loc. 3	Loc. 4
1 day	no corrosion needles, bladed, platy	homogeneous[1)] dense, bladed	patchy[2)] tubular, bladed
1 week	no corrosion needles, bladed	– –	homogeneous tubular, bladed, platy
2 weeks	patchy only silica	patchy only silica	continuous layer[3)] blistered, dense
4 weeks	no corrosion needles	no corrosion needles	homogeneous tubular, bladed, flowers
6 weeks	patchy flowers	homogeneous only silica	continuous layer blistered, dense
10 weeks	no corrosion needles	patchy only silica	continuous layer blistered, dense, bladed

[1)] Homogeneous blackening of the steel coupon without a noticeable increase in thickness and no apparent change in surface texture (Figure 6.2 B)

[2)] Individual dark to orange patches surrounded by (macroscopically) uncorroded steel (Figure 6.2 C)

[3)] Formation of a dark brown to orange continuous layer with a noticeably increased thickness and a much more irregular surface compared to the S275 steel (Figure 6.2 D)

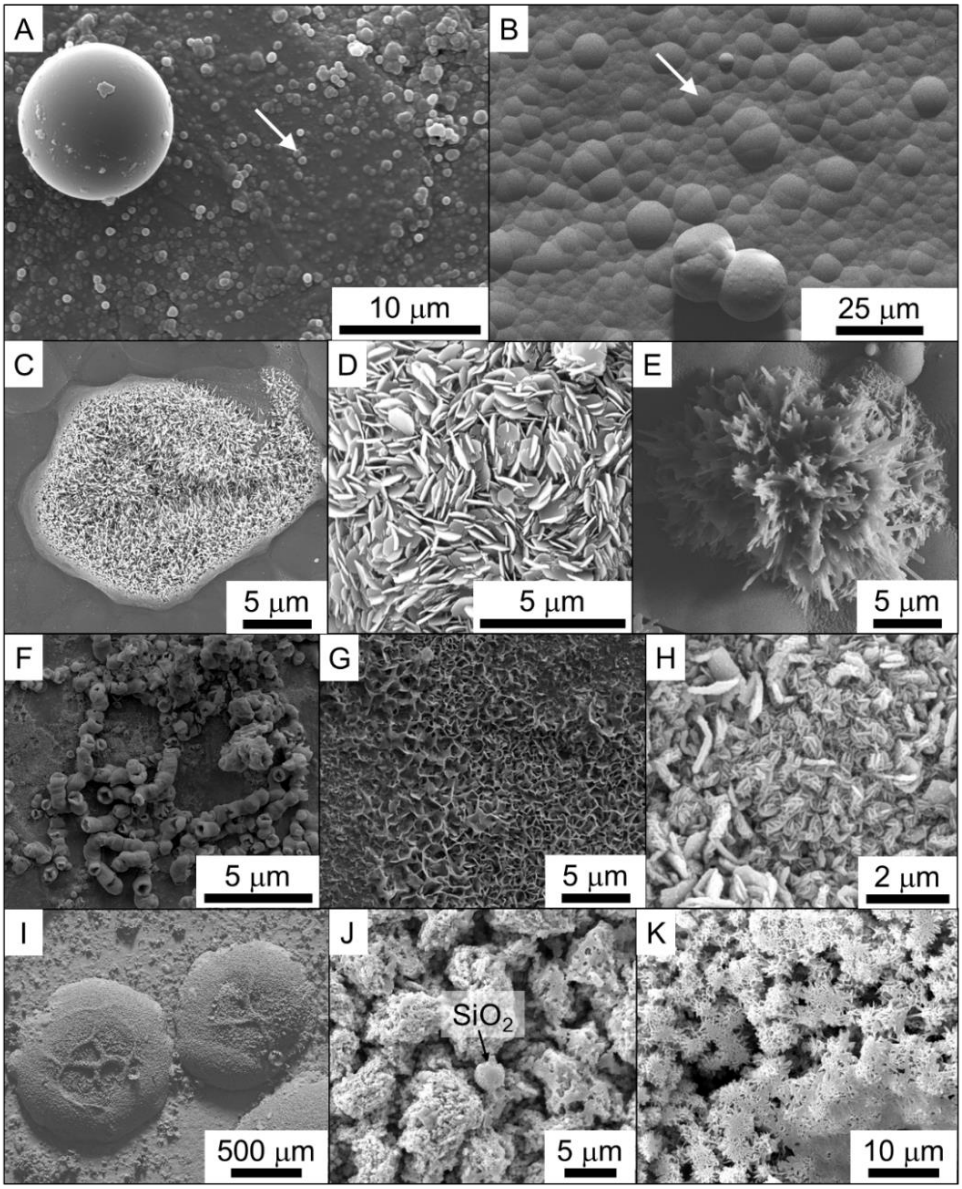

Figure 6.3: *SEM microphotographs of amorphous silica textures and corrosion morphologies observed on the S275 carbon steel coupons. At locations 1 the plates were dominated by an uneven layer of amorphous silica with the size of individual 'bumps' (arrows) increasing over time (A = 1 day & B = 6 weeks). Individual spherical silica particles between 0.5 to 25 µm were also often seen (A & B). At location 3 both, the silica 'bumps' and the individual particles were slightly smaller. Variously shaped Fe-sulphides and/or oxides (EDS, not shown) were found: needle-shaped (C), platy (D) or flower-shaped habits (E). At location 4, corrosion was dominant and expressed as two main textures: homogeneous blackening of the steel and formation of a thick layer of corrosion products consisting of tubular structures (F) surrounded by bladed (G) and platy crystals (H) of Fe-sulphides and/or –oxides. The thick corrosion layers all showed blistering (I) and the formation of dense (J) Fe-sulphides and/or –oxides. Flower- or rosette-shaped aggregates (K) were encountered less frequently. No silica scaling 'bumps' and very few silica spheres (arrow in J) were observed at location 4.*

The S275 carbon steel coupons recovered from location 3 were more intensely corroded compared to location 1 with two of the plates completely and homogeneously blackened and two more showing patchy corrosion (Figure 6.2 B). However, microscopically only sample 3-1d showed abundant corrosion features with dense or bladed mineral habits covering the coupon surface (Figure 6.3 C to E). These corrosion minerals were similar to location 1 (iron sulphides and its oxidation products). Most other recovered coupons at location 3 were absolutely free of corrosion features even at the microscopic level. They were however, all characterized by the same uneven, bumpy, amorphous silica layer as in location 1. The individual 'bump' diameters increased from 0.2 μm after 1 day to over 5 μm after 10 weeks (Figure 6.3 A & B, Figure 6.4 B). Similar to location 1, some amorphous silica microspheres were also observed on top of the continuous silica layers.

Finally, on the coupons from location 4 totally different surface features were observed. All S275 carbon steel coupons showed clear and ubiquitous signs of corrosion. This includes the complete blackening of the carbon steel as well as the formation of thicker (estimated to be up to 0.5 mm), black and dark orange-brown corrosion layers (Figure 6.2 B to D). On all samples characterized by homogeneous blackening of the carbon steel, tubular structures (Figure 6.3 F) composed of aggregates of bladed crystals were observed. In-between these structures, the coupon surfaces was covered by bladed and platy crystals (Figures 6.3 G & H). The thick corrosion layers were characterized by large (up to 2 mm) blister-shaped structures (Figure 6.3 I) that consisted of dense aggregates and, more rarely, of flower- or rosette-shaped minerals (Figure 6.3 J & K). The minerals that formed these corrosion layers were mackinawite (FeS), greigite (Fe_3S_4), hematite (Fe_2O_3), goethite (FeOOH) and elemental sulphur as confirmed not just through their morphologies but also through EDS analyses and XRD bulk analyses. Amorphous silica, the dominant component at locations 1 and 3 was largely absent. Occasionally, spherical silica particles several micrometres in size were found incorporated into the corrosion layers (Figure 6.3 J).

6.4 Discussion

6.4.1 Mineral scaling

At locations 1 to 3, even after 1 day rapid silica scaling resulted in the complete coverage of the scaling plates and coupons. As predicted by PHREEQC calculations the solutions were all supersaturated with respect to amorphous silica. The saturation indices (SI) varied between 0.1 at location 1, 0.4 at locations 2 and 3 and 0.2 at location 4. Thus, theoretically, the scaling potential was lowest at location 1. However, the faster increase in 'bump' diameters at location 1 compared to location 3 indicated that the rate of silica deposition at this location was higher. This could be due to the elevated temperature (nearly 120 °C), which, despite increasing solubility, results in enhanced deposition of monomeric silica, i.e., growth (Makrides et al., 1980; Gunnarsson and Arnórsson, 2003; Tobler and Benning, 2013). The almost fully absent silica at location 4 is attributed to the more dilute conditions and thus much lower silica concentration (~550 pm) and the prevalence of corrosion at this location.

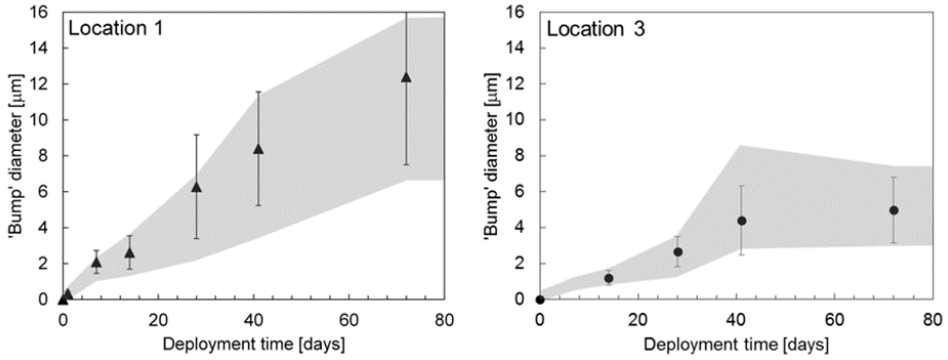

Figure 6.4: *Increase of 'bump' diameters on the S275 stainless steel coupon as a function of time at location 1 (left) and location 3 (right). The data points correspond to the average diameters of 100+ individual 'bumps', while the error bars correspond to the standard deviations. The grey surfaces shown the average 'bump' diameter ± standard deviation as determined from the S316 stainless steel plates (van den Heuvel et al., in prep.b (Chapter 4)). The overlap between the date from S275 steel coupons and the S316 steel plates indicate that the growth of the silica scaling layers was independent of the underlying steel surface properties.*

Silica can be deposited from a supersaturated solution by two pathways: molecular deposition and particle deposition (Weres et al., 1981; van den Heuvel et al., in prep.b (Chapter 4)). Molecular deposition is the direct deposition of silica mono-

mers (and potentially small polymers) onto a surface. This process results in the formation of the uneven surfaces consisting of adjoined silica 'bumps' with sizes that increase as a function of time. The increase is faster in the initial stages of precipitation (up to ~40 days) and seemingly slows down as time progresses (Figure 6.4). The similar shapes in the growth profiled between the 'bumps' formed on the S316 stainless steel plates (Figure 6.4, shaded areas) and those formed on the S275 carbon steel coupons (Figure 6.4, data points) suggests that under the conditions studied here the surface properties of the steel substrates have no effect on molecular deposition. Particle deposition requires the formation of silica particles by homogeneous nucleation first (Iler, 1979; Tobler et al., 2009; Tobler and Benning, 2013). Once such silica nanoparticles form in solution they can be deposited onto any available surface (Figure 6.3 A & B) or remain in the fluid where they can grow further by a naturally occurring "buildup" (Morris and Vossos, 1970) in which silica nanoparticles present in the fluid grow by Ostwald ripening through the constant addition of monomeric and polymeric silica. If deposited, the particles are cemented to the underlying surface or other particles by the continual coalescence through the amply available aqueous monomeric silica (Meier et al., 2014 (Chapter 3)). Together, these two mechanisms make up the silica scales observed. Based on the scantiness of individual silica particles on the plates compared to the silica deposited in the 'bumps' we suggest that molecular deposition is the dominant mechanisms responsible for the bulk of the silica scales formed on the plates and coupons (van den Heuvel et al., in prep.b (Chapter 4)).

6.4.2 Corrosion of the S275 carbon steel coupons

Dissolved gases are the primary corrosion species in geothermal fluid. At Hellisheiði, the following species could potentially be involved in the corrosion of the S275 carbon steel: dissolved oxygen, carbon dioxide ($CO_{2(aq)}$) and hydrogen sulphide ($H_2S_{(aq)}$). Based on the measured fluid compositions and temperatures, Eh values of -0.45 to -0.6 V, were obtained by PHRREQC, indicating strongly reducing conditions and negligible concentration of dissolved oxygen *in-situ*. However, a recent study Richter et al. (2007) showed that operational changes and maintenance procedures can result in a sudden increase in dissolved oxygen concentrations in certain parts of the pipelines, leading to rapid localized corrosion. Therefore, some corrosion caused by dissolved oxygen cannot be excluded, especially during the longer de-

ployments. The second corrosion species present at Hellisheiði is carbon dioxide (CO_2). When dissolved in water it forms carbonic acid (H_2CO_3) which can then interact with the steel surface to oxidize iron and precipitate siderite ($FeCO_3$) (Mundhenk et al., 2013). The absence of siderite and the high pH of the fluids (Table 6.1) indicates that this corrosion mechanism did not take place inside the pipelines at Hellisheiði. The predominant corrosion products were sulphides resulting from the interactions between the carbon steel surfaces and the ~20 ppm dissolved hydrogen sulphide (Table 6.1).

The anoxic conditions in the pipelines of Hellisheiði suggested that the only iron sulphide to form should be mackinawite (Benning et al., 2000). Mackinawite formed as a corrosion product due to the interaction of the $H_2S_{(aq)}$-rich fluids and the steel coupons during the prolonged exposure of the coupons to the geothermal fluids. The second iron sulphide identified, greigite, is a common intermediate in the usually rapid transformation of mackinawite to pyrite (Benning et al., 2000; Hunger and Benning, 2007). This transformation when occurring fast can also result in the formation of elemental sulphur (Benning et al., 2000). However, in order to transform mackinawite to greigite, slightly oxic conditions are needed. We identified two possible scenarios:

(1) Any change in operating conditions or maintenance during prolonged exposure of the coupons could result in the introduction of short pulses of increased dissolved oxygen into the geothermal fluid (Richter et al., 2006) This oxygen would lead to the rapid transformation of mackinawite into greigite as shown by Cahill et al. (2000) and Csákberényi-Malasics et al. (2012) with elemental sulphur as a by-product (Benning et al., 2000). Once the conditions return to anoxic, the transformation would be stopped, and mackinawite would continually precipitate.

(2) The transformation of mackinawite to greigite only takes place when the steel coupons are removed from the fluid. Although the coupons were immediately placed into centrifuge tubes and sealed after sampling, they were not kept strictly anaerobic. As the transformations of mackinawite occurs extremely fast in oxic conditions, it is possible that the partial transformation of mackinawite to greigite took place in the thin film of water covering the coupons upon removal from the geothermal fluids and before drying.

Both scenarios could also lead to the formation of the observed iron (hydr)oxides goethite and hematite. However, these minerals could also have formed during aerobic sample storage and analyses. Nevertheless, the fact that both, mackinawite and greigite were still present in the samples clearly indicated that upon oxidation of the upper most layer of iron sulphides, the oxidation products hematite and goethite seemingly formed a protective layer thus preserving the original iron sulphides even under ambient conditions and over time periods of weeks to months although mackinawite and greigite are not stable at ambient aerobic conditions (Benning et al., 2000).

6.4.3 Scaling vs. corrosion

When both, scaling and corrosion occur at the same location concurrently, they invariably will affect each other. The formed corrosion products influenced the precipitation of amorphous silica in that it changed the morphology and properties of the steel coupon surface. Harrar et al. (1982) found that this resulted in faster initial scale formation onto mild steel compared to inert surfaces such as Teflon or the superalloy Hastelloy. The authors did not discuss the reasons for this observation. However, they inferred that the higher surface area of the corrosion phases likely resulted in higher molecular deposition rates as well as making the trapping of colloidal silica more likely. For longer exposure times and higher scaling rates the effect disappeared (Harrar et al., 1982). This is in line with the findings of this study, where we showed that when silica scaling dominates (i.e., locations 1 and 3), the scaling onto partially corroded S275 carbon steel is identical to the scaling observed onto S316 stainless steel (Figure 6.4 data points compared with grey areas).

Conversely, the precipitation of silica can impact the corrosion of the metal surfaces and this has been shown in several power plants (Braithwaite and Lichti, 1980; Lichti et al., 1981; Meier et al., 2014 (Chapter 3)). When silica scales form fast, they can act as a barrier, isolating the steel surfaces from the fluid. The dense structure of such silica scales will subsequently impair fluid transport through the silica layer and slow down and potentially inhibit further corrosion. This is evidenced in the samples from location 1 where, based on the concentration of H_2S and the fluid temperature, corrosion rates should be highest. However, only limited corrosion was observed at location 1 even after 10 weeks. Similarly, at location 3, which although at lower temperatures was characterized by almost identical chemical

conditions, corrosion was limited (Table 6.2). Only few coupons at location 3 showed macroscopic signs of uniform or patchy corrosion but when observed at high resolution no obvious corrosion products were seen. This indicates that, at least in some cases, corrosion likely took place immediately after immersion of the coupons and before the initial stages of silica precipitation and that any continual corrosion was stopped or slowed once a complete layer of silica covered the coupons. Finally, the biggest difference was observed for the coupons deployed at location 4, where the silica precipitation is less important (van den Heuvel et al., in prep.b (Chapter 4)), and thus corrosion dominated because a protective silica layer was absent. As a consequence, the corrosion of the S275 carbon steel was much more uniform and extensive, sometimes even forming thick layers of iron phases when deployed for longer times (Table 6.2; Figure 6.2 D).

6.5 Conclusion

Concurrent mineral scaling and corrosion processes have been observed in geothermal systems before but up to date only a small number of studies have evaluated the relationship between these two processes. By characterizing the temporal relationship between silica scaling and corrosion at the Hellisheiði power station we demonstrate that both, scaling and corrosion took place within a day of placing the scaling plates into the geothermal fluid. Where silica scaling was rapid (locations 1 and 3), corrosion was very limited to non-existent, while at location 4, where silica precipitation is less important, corrosion of the S275 steel is the dominant process.

Our data shown that where silica scaling passivates exposed surfaces, it can prevent or at least drastically reduce corrosion of steel surfaces. Such fast silica scaling could thus represent a means to protect steel surfaces susceptible to corrosion in a cheap and fast way. However, silica scaling in geothermal power plants is inherently difficult to control and so far none of the employed approaches such as pH modification, dilution, controlled polymerization and/or precipitation as well as the use of (in)organic inhibitors allowed for a universally applicable mitigation strategy to be developed. Furthermore, even if perfect control of amorphous silica precipitation would be feasible in the future, the problem of localized corrosion associated with uneven steel surfaces or cracks in the precipitation layer for further fluid attach remain.

Although our work has advanced our understanding of the inter-dependencies between silica scaling and metal corrosion, the challenge for the future remains to see if controlled silica scaling may become a possible strategy to deal with corrosion of steel surfaces in high-enthalpy geothermal power plants.

References

Arnórsson, S., Bjarnason, J.Ö., Giroud, N., Gunnarsson, I., Stefánsson, A., 2006. Sampling and analysis of geothermal fluids. *Geofluids* **6**, 203-216.

Benning, L.G., Wilkin, R.T., Barnes, H., 2000. Reaction pathways in the Fe–S system below 100 °C. *Chemical Geology* **167**, 25-51.

Braithwaite, W., Lichti, K., 1980. Surface corrosion of metals in geothermal fluids at Broadlands, New Zealand. *Geothermal Scaling and Corrosion, ASTM STP* **717**, 81-112.

Cahill, C., Benning, L., Barnes, H., Parise, J., 2000. *In-situ* time-resolved X-ray diffraction of iron sulfides during hydrothermal pyrite growth. *Chemical Geology* **167**, 53-63.

Csákberényi-Malasics, D., Rodriguez-Blanco, J.D., Kis, V.K., Rečnik, A., Benning, L.G., Pósfai, M., 2012. Structural properties and transformations of precipitated FeS. *Chemical Geology* **294**, 249-258.

Demadis, K.D., Mavredaki, E., Stathoulopoulou, A., Neofotistou, E., Mantzaridis, C., 2007. Industrial water systems: problems, challenges and solutions for the process industries. *Desalination* **213**, 38-46.

Deutscher, S., Ross, D., Quong, R., Harrar, J.E., 1980. *Studies of the dissolution of geothermal scale*. Lawrence Livermore Laboratory.

Gunnarsson, I., Arnórsson, S., 2000. Amorphous silica solubility and the thermodynamic properties of H_4SiO_4 in the range of 0 to 350 °C at P_{sat}. *Geochimica et Cosmochimica Acta* **64**, 2295-2307.

Gunnarsson, I., Arnórsson, S., 2003. *Silica scaling: The main obstacle in efficient use of high-temperature geothermal fluids*, Proceedings International Geothermal Conference, Reykjavik, pp. 30-36.

Harrar, J., Locke, F., Otto Jr, C., Lorensen, L., Monaco, S., Frey, W., 1982. Field tests of organic additives for scale control at the Salton Sea geothermal field. *Society of Petroleum Engineers Journal* **22**, 17-27.

Hunger, S., Benning, L.G., 2007. Greigite: a true intermediate on the polysulfide pathway to pyrite. *Geochemical Transactions* **8**, 1-20.

Iler, R.K., 1979. *The chemistry of silica: solubility, polymerization, colloid and surface pro perties, and biochemistry*. Wiley, London.

Lichti, K.A., Soylemezoglu, S., Cunliffe, K.D., 1981. *Geothermal corrosion and corrosion products*, Proceeding of the New Zealand Geothermal Workshop, pp. 103-108.

Makrides, A.C., Turner, M., Slaughter, J., 1980. Condensation of silica from supersaturated silicic acid solutions. *Journal of Colloid and Interface Science* **73**, 345-367.

Meier, D., Gunnlaugsson, E., Gunnarsson, I., Jamtveit, B., Peacock, C., Benning, L., 2014. Microstructural and chemical variation in silica-rich precipitates at the Hellisheiði geothermal power plant. *Mineralogical Magazine* **78**, 1381-1389.

Morris, M., Vossos, P.H., 1970. *Large particle silica sols and method of production. Google Patents*.

Mountain, B., Benning, L., Boerema, J., 2003. Experimental studies on New Zealand hot spring sinters: rates of growth and textural development. *Canadian Journal of Earth Sciences* **40**, 1643-1667.

Mundhenk, N., Huttenloch, P., Sanjuan, B., Kohl, T., Steger, H., Zorn, R., 2013. Corrosion and scaling as interrelated phenomena in an operating geothermal power plant. *Corrosion Science* **70**, 17-28.

Neofotistou, E., Demadis, K.D., 2004. Use of antiscalants for mitigation of silica (SiO_2) fouling and deposition: fundamentals and applications in desalination systems. *Desalination* **167**, 257-272.

Parkhurst, D.L., Appelo, C., 2013. *Description of input and examples for PHREEQC version 3: a computer program for speciation, batch-reaction, one-dimensional transport, and inverse geochemical calculations*. US Geological Survey.

Richter, S., Hilbert, L.R., Thorarinsdottir, R., 2006. On-line corrosion monitoring in geothermal district heating systems. I. General corrosion rates. *Corrosion Science* **48**, 1770-1778.

Rothbaum, H., Anderton, B., Harrison, R., Rohde, A., Slatter, A., 1979. Effect of silica polymerisation and pH on geothermal scaling. *Geothermics* **8**, 1-20.

Scott, S., Gunnarsson, I., Arnórsson, S., Stefánsson, A., 2014. Gas chemistry, boiling and phase segregation in a geothermal system, Hellisheiði, Iceland. *Geochimica et Cosmochimica Acta* **124**, 170-189.

Soylemezoglu, S., Harper, R., 1982. Oxygen ingress into geothermal steam and its effect on corrosion of low carbon steel at Broadlands, New Zealand. *Geothermics* **11**, 31-42.

Tang, J., Shao, Y., Guo, J., Zhang, T., Meng, G., Wang, F., 2010. The effect of H_2S concentration on the corrosion behavior of carbon steel at 90 °C. *Corrosion Science* **52**, 2050-2058.

Tobler, D.J., Benning, L.G., 2013. *In-situ* and time resolved nucleation and growth of silica nanoparticles forming under simulated geothermal conditions. *Geochimica et Cosmochimica Acta* **114**, 156-168.

Tobler, D.J., Shaw, S., Benning, L.G., 2009. Quantification of initial steps of nucleation and growth of silica nanoparticles: An *in-situ* SAXS and DLS study. *Geochimica et Cosmochimica Acta* **73**, 5377-5393.

Tobler, D.J., Stefansson, A., Benning, L.G., 2008. *In-situ* grown silica sinters in Icelandic geothermal areas. *Geobiology* **6**, 481-502.

van den Heuvel, D., Gunnlaugsson, E., Benning, L., in prep.a. Surface roughness and composition control silica deposition from geothermal fluids. *Geochemical Transactions*.

van den Heuvel, D., Gunnlaugsson, E., Gunnarsson, I., Stawski, T., Peacock, C., Benning, L., in prep.b. Two pathways of amorphous silica precipitation inside in-use pipelines of a high-enthalpy, low salinity geothermal power plant *Geochimica et Cosmochimica Acta*.

Weres, O., Yee, A., Tsao, L., 1981. Kinetics of silica polymerization. *Journal of Colloid and Interface Science* **84**, 379-402.

Chapter 7

Formation of silica-lysozyme composites via co-precipitation and adsorption

Daniela B. van den Heuvel[1], Tomasz M. Stawski[1,2], Dominique J. Tobler[3], Richard Wirth[2], Caroline L. Peacock[1],Liane G. Benning[1,2]

[1] *Cohen Geochemistry Group, School of Earth and Environment, University of Leeds, Leeds LS2 9JT, UK*
[2] *German Research Center for Geosciences, GFZ, 14473 Potsdam, Germany*
[3] *Nano-Science Center, Department of Chemistry, University of Copenhagen, Copenhagen 2100, Denmark*

Abstract

Interactions between silica and proteins are crucial for the formation of biosilica as well as for the production of novel functional materials for a range of industrial applications. The proteins control both precipitation pathway and the properties of the resulting silica-organic composites. Here we present data on the formation of silica-lysozyme composites through two different synthesis approaches (co-precipitation *vs.* adsorption) and show that the chemical and structural properties of these composites when analysed using a combination of synchrotron-based scattering, spectroscopic, electron microscopy and surface characterization techniques vary dramatically. We document that while lysozyme was not incorporated into nor did its presence alter the molecular structure of silica, it enhanced the aggregation of silica particles and its presence affected the composition and structure of the composites. The difference to pure silica samples increased with increasing lysozyme content for both co-precipitation and adsorption composites. Yet, the absolute changes differ

substantially between these two sets of composites. Our results improve the understanding of how organic macromolecules interact with dissolved and nanoparticulate silica and how these interactions control the formation pathway of silica hybrid materials.

7.1 Introduction

Over the last few years interactions between silica particles and organic molecules, and protein-silica interaction in particular, have sparked renewed interest due to the dominant role of proteins in biological processes (e.g., biosilicification: Coombs and Volcani, 1968; Simpson and Volcani, 1981; Perry and Keeling-Tucker, 2000; Otzen, 2012) and because silica-organic composites have proven to be crucial in a plethora of material science applications (e.g., drug delivery, electroluminescence, optics etc.) (Sumper and Brunner, 2006; Slowing et al., 2007; Piao et al., 2008; Wang et al., 2013). Nevertheless, a molecular understanding of how the synthesis pathways leading to silica-protein composites affects the final hybrid materials is still lacking.

In this study, we use the protein lysozyme to study the formation pathways of silica-lysozyme composites. Lysozyme is a small prolate ellipsoidal protein (3 x 4.5 nm) with a molecular mass of 14.3 kDa. It consists of 129 amino acids, including 6 lysine and 11 arginine residues exposed at the surface of the molecule (Appendix C, Figure C.1; Canfield, 1963; Jollès et al., 1963) This gives the molecule an overall positive surface charge over a large pH range (pH_{IEP} = 11.1; Haynes and Norde, 1994) making electrostatic interactions with the negatively charged silica monomers, nanoparticles and surfaces possible (Coradin et al., 2003; Bharti et al., 2011; Kumar et al., 2011). Lysozyme has been used previously in the study of silica-protein composites (Coradin et al., 2003) as its physicochemical properties are extremely well studied, which makes it an ideal model protein, and due to its overall similarity to silaffins. Silaffins are a group of small proteins (4 to 17 kDa) characterized by an abundance of basic amino acids such as arginine and lysine. Together with long-chain polyamines (LCPA) and proteins of the cingulin and silicidin groups, they control silica precipitation inside diatoms and are believed to also control the characteristics of the resulting solid cell walls (Sumper and Brunner, 2008). The interaction between these organic molecules and silica occurs mainly by electrostatic interaction of primary amino groups ($-NH_2$) with silica (Sumper and Brunner, 2008; Otzen, 2012), although hydrophobic interactions may also contribute. The pos-

itively charged amino groups attract the partly deprotonated monosilicic acid ($H_3SiO_4^-$) and/or negatively charged colloidal silica and are inferred to enhance concentration locally and therefore facilitate precipitation and aggregation.

Adsorption of lysozyme onto silica surfaces can result in the partial loss of secondary and tertiary lysozyme structure, i.e., the conversion of alpha helices to beta sheets and the deformation of the overall shape of the lysozyme molecule, resulting in more oblate molecules (Norde and Favier, 1992; Billsten et al., 1995; Vertegel et al., 2004; Kubiak-Ossowska and Mulheran, 2010; Felsovalyi et al., 2011). The structural changes become more significant when lysozyme is adsorbed onto non-flat surfaces (Kubiak and Mulheran, 2009; Gagner et al., 2011; Hao et al., 2014). Due to the partial unfolding, the more hydrophobic core of the lysozyme molecule is exposed, leading to hydrophobic interactions between unfolded adsorbed amino acid chains in order to minimize contact with water (Gagner et al., 2011). Thus, the adsorption of lysozyme onto silica and subsequent aggregation to form a composite is believed to be controlled by electrostatic as well as hydrophobic interactions. Lysozyme likely incorporates into the precipitate during this process, leading to composites with different properties compared to purely inorganic silica precipitates (Gordon et al., 2009).

In this study, we have investigated the composition and microstructures of silica-lysozyme composites formed by co-precipitation and adsorption. In the co-precipitation experiments lysozyme was added to a solution of dissolved inorganic silica before initializing polymerization. Lysozyme could thus potentially interact with the polymerizing silica during nucleation, particle growth and aggregation. For the adsorption experiments, lysozyme was added to a solution containing already formed silica nanoparticles, where the presence of lysozyme could only affect particle aggregation. By comparing the results of these two sets of experiments, we were able to differentiate between the effects of lysozyme on polymerization and particle growth and its effect on aggregation of inorganic silica. Our dataset also represents the first thorough characterisation of silica-lysozyme hybrid composites. We show that lysozyme becomes incorporated into the silica precipitates and that the concentration of lysozyme in solution strongly affects the properties of the precipitates. We describe the mechanisms involved in these two processes and infer their role in biosilicification and other possible applications.

7.2 Results and Discussion

7.2.1 Composition of silica-lysozyme composites

The pure silica and all silica-lysozyme composites, regardless whether produced through co-precipitation or adsorption, revealed only a single broad X-ray diffraction (XRD) peak at ~24° 2θ (Appendix C, Figure C.2), indicating their amorphous character. Pair distribution functions (PDFs) derived from synchrotron-based high-energy X-ray diffraction (HEXD) confirmed the amorphous nature of all samples (attenuation of PDF plot at < 10 Å and only very small coherent scattering domains; Figure 7.1).

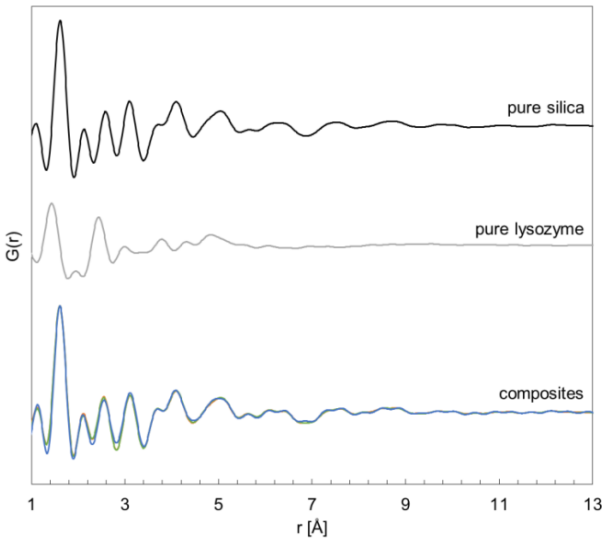

Figure 7.1: *PDFs for pure silica, pure lysozyme and silica-lysozyme composites formed by co-precipitation.*

The PDF for pure silica revealed a dominant peak at ~1.7 Å (Si-O), followed by a series of smaller peaks up to 6 Å (Si-Si, O-O) (Bowron, 2008; Dyer et al., 2010). The PDF of the pure lysozyme on the other hand showed dominant peaks at ~1.5 and 2.3 Å (C-C overlapping with C-N and C-O) (Wang et al., 2007). The peak positions and G(r) of the composite samples were identical to pure silica (Figure 7.1). The absence of any trace of lysozyme in the PDFs of the composite samples was due to the much lower scattering power of lysozyme, which rendered it "invisible" in the presence of silica. Nevertheless, if the presence of lysozyme altered the silica

structure at the molecular level, a shift in the peak positions in the PDFs of the composite samples would be expected. Instead, no changes in the atom pair-distances were seen for the composites.

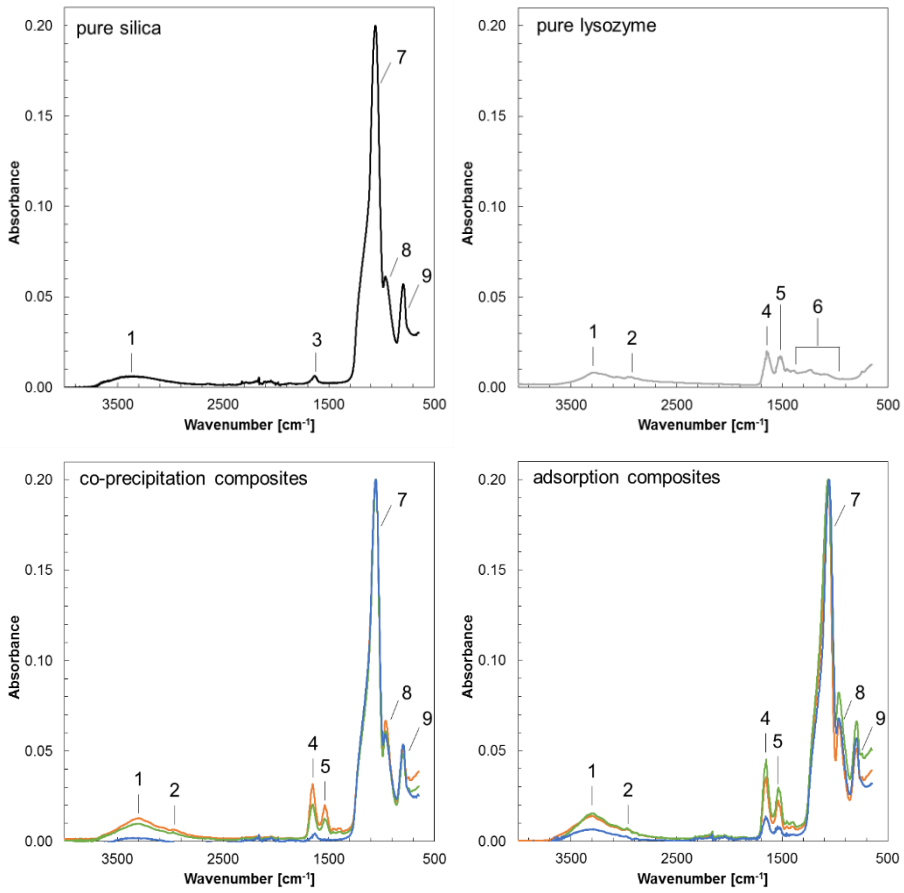

Figure 7.2: *FTIR spectra of pure silica, pure lysozyme and the composites formed by co-precipitation and adsorption (blue: 100 ppm added, green: 500 ppm added, orange: 1000 ppm added). The frequencies and band assignments are in accordance with Benning et al. (2004) and are listed in Appendix C, Table C.1.*

In order to identify the mode in which the lysozyme was associated with the silica in the composites, aliquots of the bulk samples were analysed using Fourier transform infrared (FTIR) spectroscopy (Figure 7.2; Appendix C, Table C.1). The FTIR spectra of pure silica showed prominent bands at 750 to 1300 cm^{-1}, corresponding to stretching and vibration of the siloxane and silane bonds. In the spectra of pure lysozyme the characteristic bands were at 1200 to 1700 cm^{-1} and corresponded to the vibrations of amide groups and stretching of carboxylic and nucleic acids. Both, the pure silica and lysozyme showed a broad band at ~3300 – 3400 cm^{-1} that

corresponded to vibrations of water. The FTIR spectra of the composite samples exhibited all bands described above for pure silica and lysozyme. Additionally, they showed a clear increase in the relative absorbance of the amide bands (~1650 and ~1540 cm^{-1}) compared to the main silica band (1060 cm^{-1}) with an increase in the amount of lysozyme added during the composite formation, from CoP_100 to 1000 and Ads_100 to 500/1000 (Appendix C, Table C.2).

In order to quantify the amount of lysozyme associated with the composites, the carbon content of the composites was analysed (Appendix C, Table C.2). For both composite types, the results show that the amount of lysozyme associated with the composites increased with increasing lysozyme concentration in solution (Figure 7.3). In the co-precipitation composites the increase of lysozyme associated with the silica was gradual, reaching a maximum lysozyme content of 27 wt.% when co-precipitated in the presence of 1000 ppm lysozyme. During the adsorption experiments more lysozyme got associated with the composites compared to co-precipitation and a plateau of ~32 wt.% lysozyme content was reached around 500 ppm lysozyme added to the colloidal silica solution. Thereafter, an increase in the added lysozyme content did not result in more lysozyme being associated with the adsorption composites.

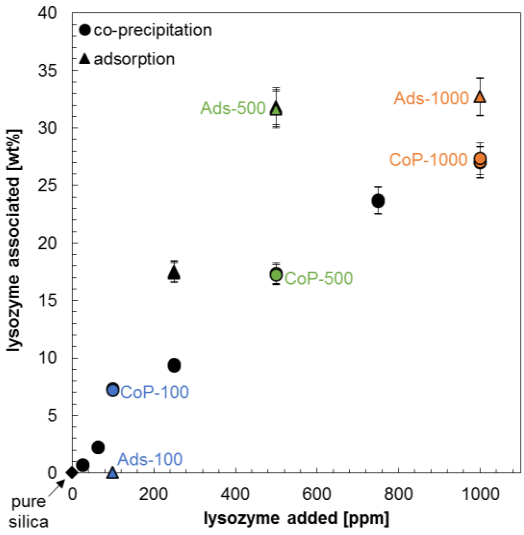

Figure 7.3: *Relationship between the concentrations of lysozyme added to the dissolved/ colloidal silica solution at the beginning of the co-precipitation (circles) and adsorption experiments (triangles) and the amount of lysozyme associated with the composites. Labelled are the pure silica sample (black diamond) and the composites on which most analyses were carried out (coloured symbols).*

The plateau value was investigated by comparing the maximum number of lysozyme molecules, which can adsorb onto silica particles (theoretical jamming limit Θ_{∞}, derived from a random sequential adsorption model onto spherical particles) (Adamczyk, 1996; Adamczyk and Belouschek, 1991; Feder, 1980) to the calculated surface coverage. This was based on the amount of lysozyme associated with the composites (Appendix C, Table C.3). The results indicated that $\Theta_{side\text{-}on}$ for Ads_500 and Ads_1000 were nearly identical to the jamming limit Θ_{∞}, indicating that the plateau observed in Figure 7.3 was likely due to the completion of a randomly packed monolayer with molecules in side-on orientation. The presence of a threshold concentration, after which an increase in lysozyme concentration had no further effect on the amount of lysozyme has also been observed in previous studies on lysozyme adsorption onto silica nanoparticle (9 and 20 nm respectively). The derived jamming values were also interpreted as the completion of a single lysozyme monolayer on the surface of the silica particles (Vertegel et al., 2004; Kumar et al., 2014). Several studies also reported lysozyme bilayers with side-on orientation on silica and no adsorption plateaus, even at concentrations > 1000 ppm. However, all these studies were conducted on flat silica surfaces (Wahlgren et al., 1995; Su et al., 1998a; Su et al., 1998b) or large (100 nm) silica nanoparticles (Vertegel et al., 2004). The stronger electrostatic interactions between these larger surfaces and the lysozyme result in stronger attractive forces, which allow the inter particle repulsions to be overcome. This is supported by the results of Su et al. (1998b) who showed that bilayer formation was prevented at pH 4 where silica-lysozyme attractive forces were weak due to the reduction of the surface charge density of silica when its isoelectric point (IEP, pH 1-2) was approached. For the co-precipitation composites no plateau in the amount of associated lysozyme was reached, even at the highest concentration (max. surface coverage ~49% of the jamming limit), indicating that the association of lysozyme with silica particles corresponds to approximately half the monolayer coverage (Appendix C, Table C.3).

7.2.2 Structure of silica lysozyme composites

High-resolution transmission electron microscopy (HR-TEM) bright-field images of the pure silica and the composite precipitates looked almost identical and showed aggregates of nanospheres (Figure 7.4 A to C). In these images, silica and lysozyme could not be differentiated, even at the highest resolution. The carbon and silicon

elemental maps based on electron energy loss spectroscopy (EELS; Figure 7.4 D & E) revealed relatively well mixed domains with some areas with higher carbon concentrations (in red; for differentiation between carbon support grid and carbon in lysozyme see Appendix C, Figure C.3). In both types of composites such carbon rich areas were distributed relatively homogeneously throughout the precipitate (Figure 7.4 D & E).

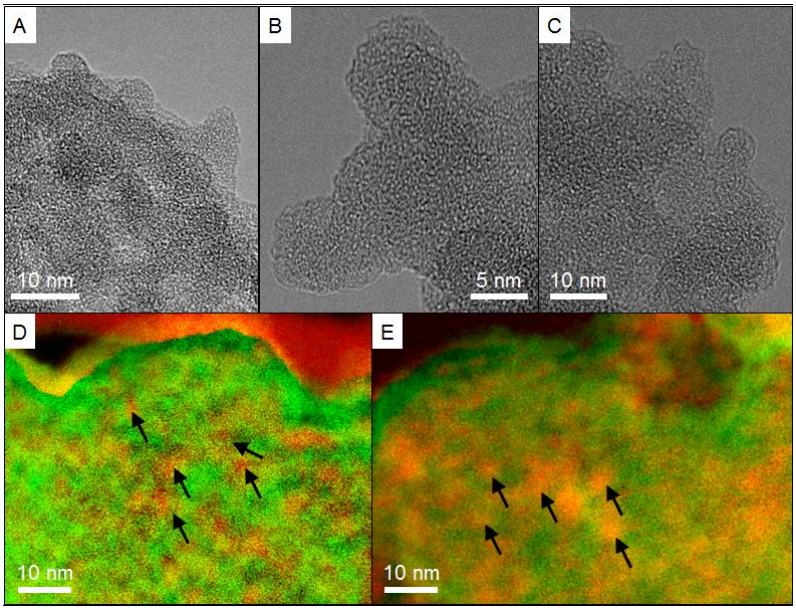

Figure 7.4: *HR-TEM phase contrast images of (A) pure silica, (B) CoP_100 and (C) Ads_100 and overlapped EELS maps collected at the carbon K-edge (red, ~290 eV) and the silicon K-edge (green, ~1840 eV) for (D) CoP_100 and (E) Ads_100.*

These seemingly distinct silicon *vs.* carbon rich areas in the EELS maps do not represent distinct lysozyme nanoparticles, because the average size and shape of these red regions were smaller than the average dimensions of native lysozyme molecules (3 x 4.5 nm: Canfield, 1963; Jollès et al., 1963). However, especially in the adsorption composite (Figure 7.4 E) some of these areas are larger than 10 nm. These areas could represent lysozyme oligomers that either formed in solution and became incorporated into the composites (Sophianopoulos and Van Holde, 1964; Bruzzesi et al., 1965) or that formed due to hydrophobic interactions between unfolded, adsorbed lysozyme (Gagner et al., 2011).

To obtain size information on silica-lysozyme particles and aggregates in suspension, we analysed these samples by small angle X-ray scattering (SAXS). In the pure silica system the mean diameter of silica nanoparticles was found to be

5.1 nm with a skew to larger diameters of up to nearly 20 nm (based on a McSAS fit; Pauw et al., 2013; Breßler et al., 2014; Appendix C, Figure C.4). In the log $I(q)$ *vs.* log q representation, at low q the intensity follows a near-q^0 dependence (plateau), indicating that the silica particles did not aggregate in solution in the absence of lysozyme (Figure 7.5 A).

The measured pattern of pure lysozyme were directly compared to the simulated scattering curve of lysozyme generated in FoXS (Schneidman-Duhovny et al., 2010; Schneidman-Duhovny et al., 2013) based on the molecular structure from Wang et al. (2007) The increase in intensity at $q > 0.2$ nm^{-1} corresponded to particle aggregation of lysozyme (Figure 7.5 A). Overall, the average intensity of scattering from silica nanoparticles was nearly two orders of magnitude higher compared to lysozyme at the concentrations used in our experiments. This indicated that, because silica strongly dominated the measured intensity, lysozyme remained invisible in the composites. This was highlighted by the pink pattern in Figure 7.5 A that represents the mathematical summation of the scattering contributions from silica and lysozyme, i.e., assuming no interactions between these two entities. This pattern falls within the experimental uncertainty region of the pure silica pattern. The patterns of the two composite samples (Figure 7.5 B) look distinctly different to the pure silica pattern and the calculated mixed pattern, indicating interaction between the silica particles and lysozyme molecules during composite formation. The most striking features in the composite SAXS patterns were the strong increase in intensity at $q < 0.5$ nm^{-1} and the correlation peaks at q ~1.5 nm^{-1} for the co-precipitation and q ~1.2 nm^{-1} for the adsorption composites. The increasing intensity at low q values indicated the contribution of a structure factor to the data, i.e., the aggregation of silica in the presence of lysozyme. The correlation peaks formed due to the increasing number of particle-particle interactions which corresponded to typical distances between individual silica particles of d ~4.2 nm for the co-precipitation composite and d ~5.2 nm for the adsorption composite. For the adsorption composite this length scale corresponded to the average silica particle diameter determined from the pure silica system (Appendix C, Figure C.4), which is in line with the absence of lysozyme during particle growth. For the co-precipitation composite, on the other hand, the smaller inter-particle distance suggested the formation of smaller silica particles. However, the correlation peak positions depend to a certain degree on the local volume fraction of particles within the aggregates, since particles pack more closely together at increased volume fractions (Kinning and Thomas, 1984; Appen-

dix C, Figure C.5). The absence of an increase in peak intensity or narrowing of the correlation peak in the co-precipitation sample indicated that the effect of a local increase in volume fraction was minor with respect to the peak shift being related to the formation of smaller silica particles. However, in order to fully differentiate between the effect of smaller particle sizes and increased local volume fraction, fitting of the data by an advanced model would be necessary. Thus, the *d*-value of 4.2 nm represented a maximum silica particle size in co-precipitation composites.

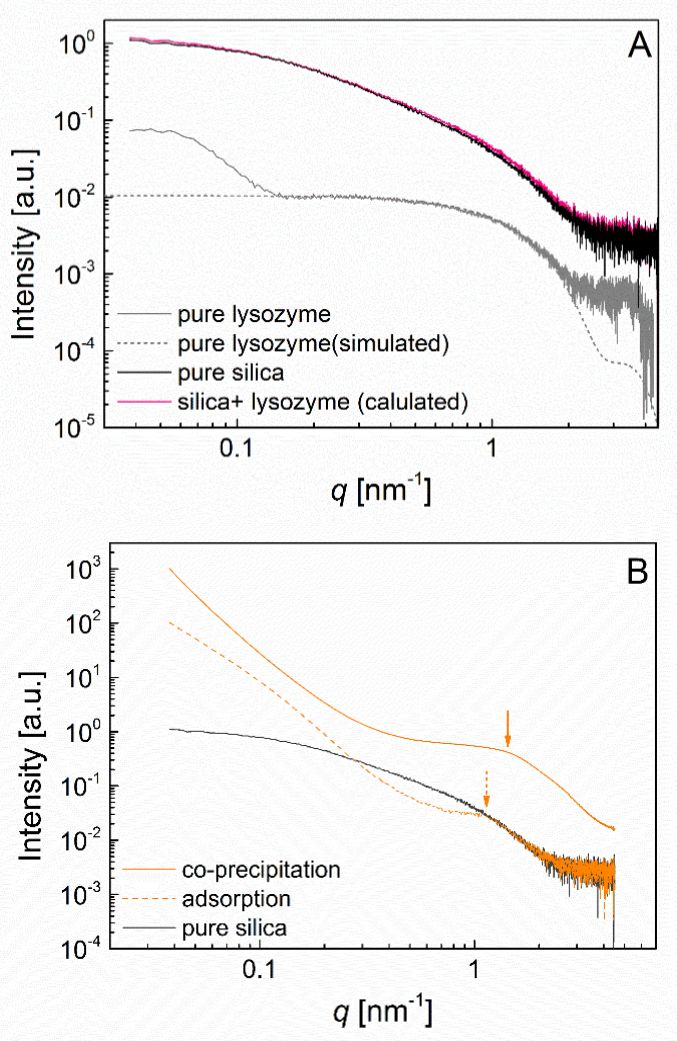

Figure 7.5: *Small angle X-ray scattering (SAXS) patterns (A) pure silica (black), pure lysozyme (grey) fitted by a scattering curve based on entry 2VB1 (Wang et al., 2007) in the Protein Database PDB (dot-dash grey), and the mathematical summation of the silica and lysozyme patterns (pink); (B) patterns representative of co-precipitated composites (CoP_1000, orange) and adsorption composites (Ads_1000, dashed orange) and pure silica (black) for comparison.*

Neither of the inter-particle distances determined for the composite samples could accommodate for lysozyme molecules in between silica particles (since the lysozyme molecules are 3 x 4.5 nm in size, and the correlation peak would thus be expected at q ~0.8 nm^{-1}). The same was observed by Kumar et al. (2011) when analysing silica-lysozyme aggregates by small-angle neutron scattering. These authors attributed the "missing" space between particles as an indication for the loss of structural coherence of the lysozyme molecule upon adsorption to multiple silica spheres. This was supported by other studies showing that lysozyme can lose substantial amounts of its secondary and tertiary structure, especially when adsorbed to non-flat surfaces (Kubiak and Mulheran, 2009), porous media (Hao et al., 2014) or in between nanoparticles (Gagner et al., 2011).

7.2.3 Surface properties of silica-lysozyme composites

The specific surface area (SSA; Figure 7.6) of pure silica as obtained by nitrogen adsorption was around 350 m^2/g which is smaller than the theoretical SSA of 566 m^2/g calculated by assuming monodisperse hard spheres with a diameter of 5.3 nm as determined by SAXS. This difference is most likely a consequence of drying of the experimental samples prior to SSA analyses, a process during which the monosilicic acid left in solution cements the particles together thereby reducing porosity and connectivity between pores, resulting in an overall smaller SSA. The amount of incorporated lysozyme (as determined by total carbon analyses, Figure 7.3) affected the SSA. A higher SSA, compared to pure silica, was observed for samples with lysozyme contents < 10 wt.%, but at values ≥ 10 wt.%, the SSA linearly decreased with increasing incorporated lysozyme. The decrease in SSA was a little steeper for the composites formed by co-precipitation than for the ones formed by adsorption. The higher SSA at low lysozyme contents (in comparison to the pure system) was likely due to additional surfaces, i.e., the lysozyme molecules, but at higher lysozyme contents this effect diminished because the relative amounts of lysozyme trapped in between the silica nanoparticles became larger (Figure 7.3). This likely resulted in denser composites, with smaller pores and a larger number of closed pores.

We also evaluated the ζ-potential over the pH range between 2.5 and 10 through potentiometric titrations. Our data showed that the surfaces of the pure silica precipitates were negative over the whole measured pH range with a pH_{IEP} < 2 (Figure 7.7, dotted lines), which agreed well with previously reported pH_{IEP} for non-

modified silica nanoparticles (Parks, 1965; Iler, 1979). Pure lysozyme on the other hand was positively charged over most of the measured pH range with a pH_{IEP} of ~9.5 (Figure 7.7, dashed lines). This was lower than the pH_{IEP} = 11.1 previously reported for lysozyme (Haynes & Norde, 1994) and was most likely due to impurities (buffer salts and other proteins from egg white) present in the crystalline lysozyme (Thomas et al., 1996), which affected the ζ-potential measurements.

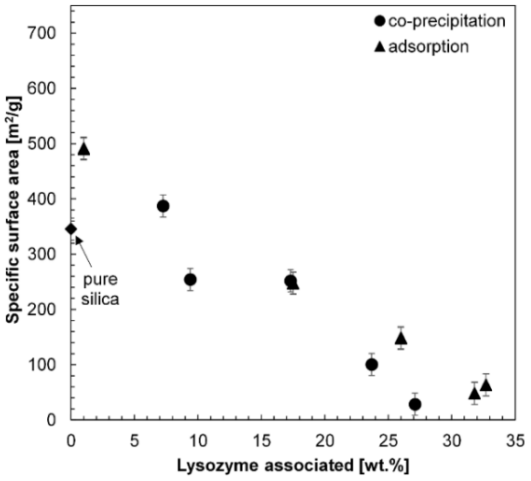

Figure 7.6: *Specific surface area (SSA) of pure silica (diamonds), co-precipitation composites (spheres) and adsorption composites (triangles) as a function of lysozyme content. Errors represent values derived from multiple measurements of the same sample.*

The co-precipitation composites showed pH_{IEP} values that fell in between pure silica and lysozyme. For example, silica co-precipitated in the presence of 100 ppm lysozyme had a pH_{IEP} ~5 - 5.5, while for silica co-precipitated with 1000 ppm lysozyme the pH_{IEP} increased to 8 - 8.5 (Figure 7.7 A). This matched results from previous studies (Haynes and Norde, 1995; Rezwan et al., 2005), where it was found that composite systems had characteristic pH_{IEP} values in between those of the end-members. The co-precipitation composites also showed a different pH dependency of the ζ-potential compared to pure silica and lysozyme (Figure 7.7 A). In the acidic pH range, the composite ζ-potential trend was similar to that of pure lysozyme, although the sample co-precipitated with 100 ppm lysozyme had a lower overall surface charge compared to pure lysozyme. This was likely due to the incomplete coverage of the silica nanoparticles by lysozyme, allowing the negative silica surface to contribute to the measured ζ-potential. In contrast, the samples co-

precipitated at higher lysozyme concentrations showed higher surface charge densities than pure lysozyme at acidic to neutral pH values. This shows that, while the surface properties of the composites were controlled by lysozyme, conformational changes of the protein molecules and/or preferential orientation of the lysozyme on the silica particles resulted in slightly different parts of the lysozyme molecule being exposed to the solution (Norde and Favier, 1992; Su et al., 1998a; Su et al., 1998b; Vertegel et al., 2004; Kubiak-Ossowska and Mulheran, 2010). At higher pH, the surface charge of the composite co-precipitated with 100 ppm lysozyme was nearly identical to pure silica likely due to the decreasing surface charge of the adsorbed lysozyme molecules.

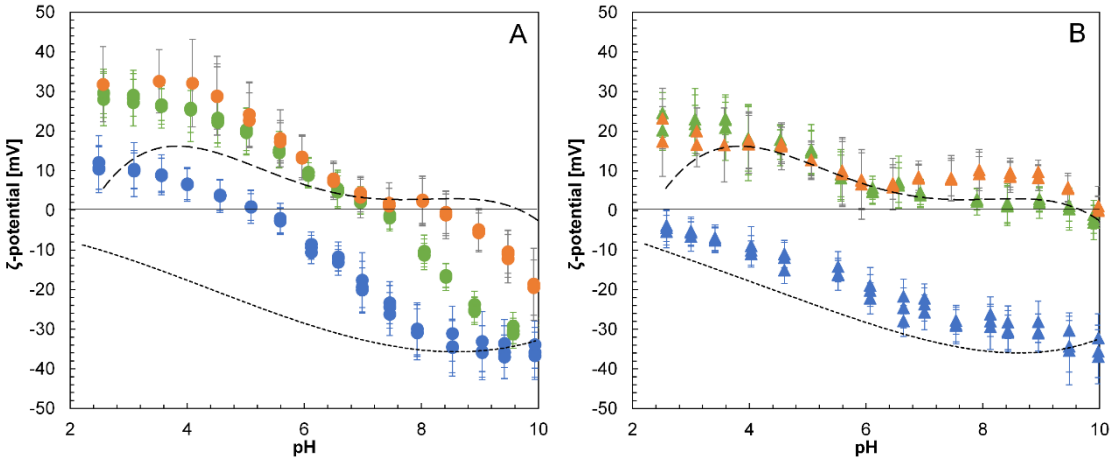

Figure 7.7: *ζ-potential as a function of pH for silica nanoparticles (dotted line) and lysozyme (dashed line) and for composites formed by co-precipitation (A) and composites formed by adsorption (B). Composite results are given for samples with 100 ppm (blue), 500 ppm (green) and 1000 ppm (orange) lysozyme added.*

At higher lysozyme concentration, the ζ-potential evolution largely followed the trend of lysozyme, yet at pH > 9 the trend was closer to that of pure silica. The surface charge densities of the adsorption composites (Figure 7.7 B) were completely different from the co-precipitation composites (Figure 7.7 A). The composite formed by adsorption of 100 ppm lysozyme showed a very similar trend to pure silica, slightly less negative likely due to the minor contribution of positively charged lysozyme. At higher concentrations of lysozyme, the adsorption composites largely matched the trend of pure lysozyme and this is likely because lysozyme covered the silica surfaces as a randomly packed monolayer (as shown above). Overall, the

ζ-potential results suggested that although the trends observed in the adsorption composites could simply be a consequence of lysozyme present, the interactions in the co-precipitation composites were more complex.

7.2.4 Pathways of silica-lysozyme composites

The presence of lysozyme during the formation of silica precipitates results in the formation of silica-lysozyme composites. Lysozyme was not incorporated into the composites nor did its presence alter the molecular structure of the silica particles. However, its presence enhanced the aggregation of the silica nanoparticles and affected the composite composition and structure. We observed a clear trend between the amount of lysozyme associated with the composites and the change in their properties. While these overall trends hold true for both the composites formed by co-precipitation and adsorption, the absolute changes between composites and pure silica differ substantially between these two sets of samples. These results clearly highlight the importance of quantitatively assessing the self-assembly pathway, properties and structures of silica-lysozyme composites.

Based on the complementary data sets presented above we have deducted that the pathway of silica precipitation in the absence and presence of lysozyme follows a series of steps (Figure 7.8). For pure silica the reaction starts with polycondensation of monosilicic acid, followed by particle growth and particle aggregation (Figure 7.8 A; Iler, 1979; Tobler et al., 2009). In the co-precipitation experiments, where lysozyme was added to a silica solution before initializing polymerization, interaction between the larger lysozyme molecules during silica polymerization was followed by particle growth and aggregation (Figure 7.8B). Lysozyme interacts with depolymerized silica monomers ($H_3SiO_4^-$) and polymeric species due to electrostatic interactions (Coradin et al., 2003). The adsorption of silica species onto polypeptides enhances the polymerization of silica by locally increasing their number density (Coradin et al., 2003). We showed from the SAXS data that besides the effect on silica polymerization, the presence of lysozyme also affected the growth and final size of the formed silica nanoparticles. The silica particles in the co-precipitation sample were smaller than those in the adsorption composite. This effect is interpreted as being a consequence of the positively charged lysozyme enhancing silica particle aggregation and might therefore cause the negatively charged silica particles to aggregate before they reach their full size and (2) the adsorption of silica monomers

and small polymers onto the surface of the lysozyme molecules could reduce the amount of dissolved silica species available for growth of particles. For the adsorption experiments, where lysozyme was added to a solution containing silica nanoparticles, the only effect observed was in particle aggregation (Figure 7.8 C).

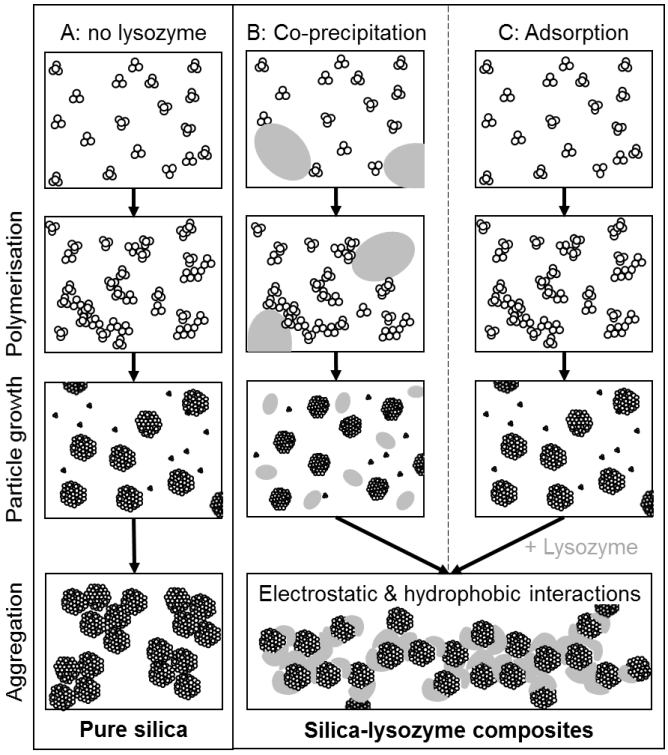

Figure 7.8: *Differences in pathways of formation for pure silica precipitation (A) and silica-lysozyme composites (B and C).*

7.3 Summary and Conclusion

This study showed that by controlling two simple parameters, the timing of the interaction between silica and protein (i.e., at which step during silica formation the proteins are added) and the ratio of silica to lysozyme, composites with variable properties formed. This is interesting for the understanding of biosilica as both these parameters are easily controlled inside a living cell and, by using a combination of different proteins and long-chain polyamines for different functions, allow the over 100'000 species of diatoms and sponges to form a wide range of biosilica with specific properties. Despite enormous efforts over the last few decades, the level of control on morphology and properties of silica that diatoms achieve has not been replicated in experimental studies, especially not at conditions similar to the ones inside

diatoms (ambient temperature and pressure, slightly acidic pH, short time-spans). Biomimetic studies focusing on the mechanism of interaction between an organic molecule and silica, like the present one, continue to support these efforts and eventually will allow us to control silica-organic composites to a degree comparable with organisms.

7.4 Methods

Preparation of silica lysozyme-composites

Sodium metasilicate ($Na_2SiO_3 \cdot 5\ H_2O$, technical grade), hen egg white lysozyme (crystalline, powdered), HCl (37% fuming, analytical grade) and 1 M NaOH (analytical grade) were obtained from Sigma Aldrich. Stock solutions of pure silica (1000 ppm, pH ~12.5) and pure lysozyme (5 wt.%, pH ~3.5) were prepared by dissolving the required amount of silica/lysozyme in ultrapure deionised water (MilliQ, ~18.2 MΩ cm).

For the co-precipitation experiments, the silica stock solution was acidified first to pH 9.5 – 10 with 37% HCl, before adding variable amounts of lysozyme stock solution to obtain solutions ranging from 25 to 1000 ppm lysozyme (Appendix C, Table C.2). The pre-acidification step was performed in order to prevent damage to the lysozyme molecule at highly alkaline pH. The solutions were then acidified to pH = 7.1 ± 0.1 and placed in an orbital shaker for 12 to 16 hours. For the adsorption experiments the 1000 ppm silica stock solution was neutralized (pH = 7.1 ± 0.1) in a single step by adding 37% HCl and left to polymerize in an orbital shaker for 12 to 16 hours. Variable amounts of lysozyme stock solution were then added to these solutions containing silica nanoparticles to obtain solutions ranging from 100 to 1000 ppm lysozyme (Appendix C, Table C.2). The mixtures were again left in an orbital shaker for 12 to 16 hours.

Characterization of colloidal suspensions

The pure silica and composite colloidal solutions were analysed by synchrotron-based small angle X-ray scattering (SAXS) at the BioSAXS beamline P12 of the EMBL at PETRA III (DESY, Germany; Blanchet et al., 2015). Measurements were performed by using a monochromatic X-ray beam at 10 keV and two-dimensional

scattered intensities were collected at small-angles with a Dectris Pilatus 2M (2D large area pixel-array detector). Transmission was measured by means of a photo-diode installed in the beam-stop of the SAXS detector. A sample-to-detector distance of ~3 m allowed for a usable q-range of ~$0.04 < q < 4.5$ nm^{-1}. The scattering-range at small-angles was calibrated against silver behenate and dry collagen standards. The samples were loaded into an automated sample changer (Round et al., 2015) and transferred to an in-vacuum quartz capillary (ID 1.7 mm, wall thickness 50 μm) for analyses. The acquisition time per frame was 1 s for the co-precipitation, and 50 ms for the adsorption experiments. Furthermore, we also measured a series of backgrounds and reference samples including an empty capillary and a capillary filled with water, silica stock solution and lysozyme stock solution. SAXS data processing and reduction included primarily masking of undesired pixels, normalizations and correction for transmission, background subtraction and data integration to 1D. These steps were performed automatically post-data collection at P12. Additionally, the ζ-potential was determined on subsamples of the colloidal solutions of pure silica and composites as well as the lysozyme stock solution (1000 ppm) using a Malvern Zetasizer Nano ZS and DTS1070 cells. The pH was adjusted to values between pH 2 and 10 with dilute HCl or NaOH to a separate aliquot of sample. Each sample was measured three times.

Characterization of washed and dried precipitates

At the end of the co-precipitation and adsorption experiments, the silica-lysozyme mixtures were transferred into an oven and the aqueous solvent evaporated at 40 °C for ~48 hours. The dried powders were washed 5 times with MilliQ water to remove excess lysozyme and salts followed by a final drying step at 40 °C (omitted for the sample aliquots used for PDF analyses). These samples were stored at 4 °C until further analysis. The dry solids were analysed by powder X-day diffraction (XRD, Bruker D8, Cu Kα radiation, 0.3° min^{-1} from 5° to 90°) and XRD patterns were evaluated using the EVA software (Bruker, Version 3.0). In addition, wet aliquots of solids were analysed by synchrotron-based total scattering (high-energy X-ray diffraction, HEXD, PDF, ~60 keV, λ = 0.21280 Å) at beamline 11-ID-B at the Advanced Photon Source at Argonne National Laboratory (USA) by using a Perkin Elmer amorphous silicon detector. A CeO_2 standard was used to calibrate the sample-to-detector distance and to align the detector with the incident beam path and a water-

filled capillary was measured for background corrections. The data reduction was done using the software Fit-2D (Hammersley, 1998), while the total scattering measurements were background corrected and converted to pair distribution function (PDF) plots using PDFgetX2 (Qiu et al., 2004). Further details on the performed PDF analysis can be found in Tobler et al. (2015). The molecular formulae used to obtain the reduced structure factor functions were $SiO_2 \cdot 0.5\,H_2O$ for silica and $C_{613}H_{959}N_{193}O_{185}S_{10}$ for lysozyme. The PDFs for all silica-lysozyme composites and the pure silica and lysozyme samples were calculated from the Fourier transform of the reduced structure function truncated at ~17.7 $Å^{-1}$. Dry samples were also analysed by Fourier transform infrared spectroscopy (FTIR, A2 Technology Microlab, 1024 scans co-added, range 4000 to 650 cm^{-1}, resolution 4 cm^{-1}) with spectra processed using the Nicolet FTIR OMNIC software, E.S.P. 5.1. The amount of lysozyme associated with the composites was quantified by determining the total carbon content in solids by mass spectrometry (DELTAplusXL ThermoFisher) with a Carlo-Erba NC2500. From these analyses the lysozyme content was calculated using the molecular formula $C_{613}H_{959}N_{193}O_{185}S_{10}$ and molecular weight of 14'313 g/mol for lysozyme (ProtParam based on UniProtKB entry P00698; Gasteiger et al., 2005). The theoretical monolayer equivalent surface coverage (jamming limit Θ_∞) was calculated according to the RSA model for the adsorption onto spherical particles developed by Adamczyk and Belouschek (1991)

$$\Theta_\infty = 0.547 * \left(1 + \frac{r}{R}\right)^2 \tag{7.1}$$

with r being the radius of the adsorbing species and R the radius of the spheres onto which it adsorbed. For the adsorption of lysozyme onto silica nanoparticles this equation can be rewritten as

$$\Theta_{\infty,end-on} = 0.770 * \left(1 + \frac{r_{lys,a}}{R_{SiO2}}\right)^2 \tag{7.2}$$

assuming that the radius of the adsorbing spheres corresponds to the short semi-axis of the lysozyme molecule ($r_{lys,a}$) and by substituting the prefactor 0.547 derived from the adsorption of spheres (Feder, 1980) by the prefactor 0.770 derived from the adsorption of prolate spheroids with an aspect ratio of 1.5 (Adamczyk, 1996), thus approximating a monolayer composed of lysozyme molecules purely in end-on adsorption and

$$\Theta_{\infty,side-on} = 0.770 * \left(1 + \frac{r_{lys,c}}{R_{SiO2}}\right)^2 \tag{7.3}$$

if the radius of the adsorbing spheres corresponds to the long semi-axis of the lysozyme molecule ($r_{lys,c}$), thus approximating a monolayer composed of lysozyme molecules purely in side-on orientation. Together, these values correspond to an upper and lower limit of the jamming coverage of lysozyme on silica. The absolute surface coverage values Θ for lysozyme on silica particles for the individual composites can be calculated based on the surface area of the silica particles ($R_{SiO2,CoP}$ = 4.2 nm and $R_{SiO2,Ads}$ = 5.2 nm as derived from SAXS) and the number of lysozyme molecules per silica particle derived from the lysozyme content associated with the individual composites.

Particle sizes of silica in the composites as well as the composite textures and morphologies were evaluated by high-resolution transmission electron microscopy (HR-TEM, TECNAI F20 X-Twin, 200 kV) combined with energy electron loss spectroscopy (EELS, using a Gatan GIF detector) and energy dispersive spectrometry (EDS, using a SiLi detector). The Brunauer–Emmett–Teller (BET) specific surface area (SSA) (Brunauer et al., 1938) of the composites and pure silica samples (0.05 to 0.2 g) was determined by N_2 sorption at 77 K on a Micromeritics Gemini VII 2390a in the relative pressure range of 0.0503 to 0.3005 p/p^0. Samples were degassed at room temperature for 24 h prior to analyses.

References

Adamczyk, Z., 1996. Random sequential adsorption of spheroidal particles: kinetics and jamming limit. *The Journal of Chemical Physics* **105**, 5562-5573.

Adamczyk, Z., Belouschek, P., 1991. Localized adsorption of particles on spherical and cylindrical interfaces. *Journal of Colloid and Interface Science* **146**, 123-136.

Benning, L.G., Phoenix, V., Yee, N., Tobin, M., 2004. Molecular characterization of cyanobacterial silicification using synchrotron infrared micro-spectroscopy. *Geochimica et Cosmochimica* **Acta** 68, 729-741.

Bharti, B., Meissner, J., Findenegg, G.H., 2011. Aggregation of silica nanoparticles directed by adsorption of lysozyme. *Langmuir* **27**, 9823-9833.

Billsten, P., Wahlgren, M., Arnebrant, T., McGuire, J., Elwing, H., 1995. Structural changes of T4 lysozyme upon adsorption to silica nanoparticles measured by circular dichroism. *Journal of Colloid and Interface Science* **175**, 77-82.

Blanchet, C.E., Spilotros, A., Schwemmer, F., Graewert, M.A., Kikhney, A., Jeffries, C.M., Franke, D., Mark, D., Zengerle, R., Cipriani, F., 2015. Versatile sample environments and automation for biological solution X-ray scattering experiments at the P12 beamline (PETRA III, DESY). *Journal of Applied Crystallography* **48**, 431-443.

Bowron, D., 2008. An experimentally consistent atomistic structural model of silica glass. *Materials Science and Engineering: B* **149**, 166-170.

Breßler, I., Pauw, B.R., Thünemann, A., 2014. *McSAS: A package for extracting quantitative form-free distributions*. arXiv preprint arXiv:1412.1900.

Brunauer, S., Emmett, P.H., Teller, E., 1938. Adsorption of gases in multimolecular layers. *Journal of the American Chemical Society* **60**, 309-319.

Bruzzesi, M.R., Chiancone, E., Antonini, E., 1965. Association-Dissociation Properties of Lysozyme*. *Biochemistry* **4**, 1796-1800.

Canfield, R.E., 1963. The amino acid sequence of egg white lysozyme. *Journal of Biological Chemistry* **238**, 2698-2707.

Coombs, J., Volcani, B., 1968. Studies on the biochemistry and fine structure of silica shell formation in diatoms. *Planta* **80**, 264-279.

Coradin, T., Coupé, A., Livage, J., 2003. Interactions of bovine serum albumin and lysozyme with sodium silicate solutions. C*olloids and Surfaces B: Biointerfaces* **29**, 189-196.

Coradin, T., Durupthy, O., Livage, J., 2002. Interactions of amino-containing peptides with sodium silicate and colloidal silica: a biomimetic approach of silicification. *Langmuir* **18**, 2331-2336.

Dyer, L., Fawell, P.D., Newman, O., Richmond, W.R., 2010. Synthesis and characterisation of ferrihydrite/silica co-precipitates. *Journal of Colloid and Interface Science* **348**, 65-70.

Feder, J., 1980. Random sequential adsorption. *Journal of Theoretical Biology* **87**, 237-254.

Felsovalyi, F., Mangiagalli, P., Bureau, C., Kumar, S.K., Banta, S., 2011. Reversibility of the Adsorption of Lysozyme on Silica. *Langmuir* **27**, 11873-11882.

Gagner, J.E., Lopez, M.D., Dordick, J.S., Siegel, R.W., 2011. Effect of gold nanoparticle morphology on adsorbed protein structure and function. *Biomaterials* **32**, 7241-7252.

Gasteiger, E., Hoogland, C., Gattiker, A., Wilkins, M. R., Appel, R. D., Bairoch, A., 2005. Protein identification and analysis tools on the ExPASy server. *The Proteomics Protocols Handbook*, 571-607.

Gordon, R., Losic, D., Tiffany, M.A., Nagy, S.S., Sterrenburg, F.A., 2009. The glass menagerie: diatoms for novel applications in nanotechnology. *Trends in Biotechnology* **27**, 116-127.

Hammersley, A., 1998. FIT2D V9. *129 Reference Manual V3. 1. Inter Rep ESRF98HA01*, ESRF, Grenoble.

Hao, D.-X., Huang, Y.-D., Wang, K., Wei, Y.-P., Zhou, W.-Q., Li, J., Ma, G.-H., Su, Z.-G., 2014. Multiscale evaluation of pore curvature effects on protein structure in nanopores. *Journal of Materials Chemistry B* **2**, 1770-1778.

Haynes, C.A., Norde, W., 1994. Globular proteins at solid/liquid interfaces. *Colloids and Surfaces B: Biointerfaces* **2**, 517-566.

Haynes, C.A., Norde, W., 1995. Structures and stabilities of adsorbed proteins. *Journal of Colloid and Interface Science* **169**, 313-328.

Iler, R.K., 1979. *The chemistry of silica: solubility, polymerization, colloid and surface properties, and biochemistry*. Wiley, London.

Jollès, J., Jauregui-Adell, J., Bernier, I., Jollès, P., 1963. La structure chimique du lysozyme de blanc d'oeuf de poule: étude détaillée. *Biochimica et Biophysica Acta* **78**, 668-689.

Kinning, D.J., Thomas, E.L., 1984. Hard-sphere interactions between spherical domains in diblock copolymers. *Macromolecules* **17**, 1712-1718.

Kubiak-Ossowska, K., Mulheran, P.A., 2010. Mechanism of hen egg white lysozyme adsorption on a charged solid surface. *Langmuir* **26**, 15954-15965.

Kubiak, K., Mulheran, P.A., 2009. Molecular dynamics simulations of hen egg white lysozyme adsorption at a charged solid surface. *The Journal of Physical Chemistry B* **113**, 12189-12200.

Kumar, S., Aswal, V.K., Callow, P., 2014. pH-dependent interaction and resultant structures of silica nanoparticles and lysozyme protein. *Langmuir* **30**, 1588-1598.

Kumar, S., Aswal, V.K., Kohlbrecher, J., 2011. SANS and UV–vis spectroscopy studies of resultant structure from lysozyme adsorption on silica nanoparticles. *Langmuir* **27**, 10167-10173.

Norde, W., Favier, J.P., 1992. Structure of adsorbed and desorbed proteins. *Colloids and Surfaces* **64**, 87-93.

Otzen, D., 2012. The role of proteins in biosilicification. *Scientifica* **2012**.

Parks, G.A., 1965. The isoelectric points of solid oxides, solid hydroxides, and aqueous hydroxo complex systems. *Chemical Reviews* **65**, 177-198.

Pauw, B.R., Pedersen, J.S., Tardif, S., Takata, M., Iversen, B.B., 2013. Improvements and considerations for size distribution retrieval from small-angle scattering data by Monte Carlo methods. *Journal of Applied Crystallography* **46**, 365-371.

Perry, C.C., Keeling-Tucker, T., 2000. Biosilicification: the role of the organic matrix in structure control. *JBIC Journal of Biological Inorganic Chemistry* **5**, 537-550.

Piao, Y., Burns, A., Kim, J., Wiesner, U., Hyeon, T., 2008. Designed fabrication of silica-based nanostructured particle systems for nanomedicine applications. *Advanced Functional Materials* **18**, 3745-3758.

Qiu, X., Thompson, J.W., Billinge, S.J., 2004. PDFgetX2: a GUI-driven program to obtain the pair distribution function from X-ray powder diffraction data. *Journal of Applied Crystallography* **37**, 678-678.

Rezwan, K., Meier, L.P., Gauckler, L.J., 2005. Lysozyme and bovine serum albumin adsorption on uncoated silica and AlOOH-coated silica particles: the influence of positively and negatively charged oxide surface coatings. *Biomaterials* **26**, 4351-4357.

Round, A., Felisaz, F., Fodinger, L., Gobbo, A., Huet, J., Villard, C., Blanchet, C.E., Pernot, P., McSweeney, S., Roessle, M., 2015. BioSAXS Sample Changer: a robotic sample changer for rapid and reliable high-throughput X-ray solution scattering experiments. *Acta Crystallographica Section D: Biological Crystallography* **71**, 67-75.

Schneidman-Duhovny, D., Hammel, M., Sali, A., 2010. FoXS: a web server for rapid computation and fitting of SAXS profiles. *Nucleic Acids Research* **38**, W540-W544.

Schneidman-Duhovny, D., Hammel, M., Tainer, J.A., Sali, A., 2013. Accurate SAXS profile computation and its assessment by contrast variation experiments. *Biophysical Journal* **105**, 962-974.

Simpson, T.L., Volcani, B.E., 1981. *Silicon and siliceous structures in biological systems*. Springer, New York.

Slowing, I.I., Trewyn, B.G., Giri, S., Lin, V.Y., 2007. Mesoporous silica nanoparticles for drug delivery and biosensing applications. *Advanced Functional Materials* **17**, 1225-1236.

Sophianopoulos, A., Van Holde, K., 1964. Physical studies of muramidase (lysozyme) II. pH-dependent dimerization. *Journal of Biological Chemistry* **239**, 2516-2524.

Su, T., Lu, J., Thomas, R., Cui, Z., Penfold, J., 1998a. The effect of solution pH on the structure of lysozyme layers adsorbed at the silica-water interface studied by neutron reflection. *Langmuir* **14**, 438-445.

Su, T.J., Lu, J.R., Thomas, R.K., Cui, Z.F., Penfold, J., 1998b. The adsorption of lysozyme at the silica–water interface: a neutron reflection study. *Journal of Colloid and Interface Science* **203**, 419-429.

Sumper, M., Brunner, E., 2006. Learning from diatoms: nature's tools for the production of nanostructured silica. *Advanced Functional Materials* **16**, 17-26.

Sumper, M., Brunner, E., 2008. Silica biomineralisation in diatoms: the model organism Thalassiosira pseudonana. *ChemBioChem* **9**, 1187-1194.

Thomas, B., Vekilov, P., Rosenberger, F., 1996. Heterogeneity determination and purification of commercial hen egg-white lysozyme. *Acta Crystallographica Section D: Biological Crystallography* **52**, 776-784.

Tobler, D.J., Rodriguez-Blanco, J.D., Dideriksen, K., Bovet, N., Sand, K.K., Stipp, S.L., 2015. Citrate effects on amorphous calcium carbonate (ACC) structure, stability, and crystallization. *Advanced Functional Materials* **25**, 3081-3090.

Tobler, D.J., Shaw, S., Benning, L.G., 2009. Quantification of initial steps of nucleation and growth of silica nanoparticles: An *in-situ* SAXS and DLS study. *Geochimica et Cosmochimica Acta* **73**, 5377-5393.

Vertegel, A.A., Siegel, R.W., Dordick, J.S., 2004. Silica nanoparticle size influences the structure and enzymatic activity of adsorbed lysozyme. *Langmuir* **20**, 6800-6807.

Wahlgren, M., Arnebrant, T., Lundström, I., 1995. The adsorption of lysozyme to hydrophilic silicon oxide surfaces: comparison between experimental data and models for adsorption kinetics. *Journal of Colloid and Interface Science* **175**, 506-514.

Wang, J., Dauter, M., Alkire, R., Joachimiak, A., Dauter, Z., 2007. Triclinic lysozyme at 0.65 A resolution. *Acta Crystallographica. Section D, Biological Crystallography* **63**, 1254-1268.

Wang, Y., Cai, J., Jiang, Y., Jiang, X., Zhang, D., 2013. Preparation of biosilica structures from frustules of diatoms and their applications: current state and perspectives. *Applied Microbiology and Biotechnology* **97**, 453-460.

Chapter 8

Summary and discussion

8.1 Silica scaling at the Hellisheiði power plant

In this thesis I have described the first ever *in-situ* study of silica scaling in an in-use geothermal power plant. Scaling was monitored using small (2-2.5 x 5 cm) metal plates inserted into the separated water pipelines through valves at four locations within the Hellisheiði power plant: (1) before the heat exchangers, (2) after the heat exchangers, (3) immediately before mixing with steam condensate and (4) at the Húsmúli injection site (Figure 8.1). For the initial study (Chapter 3) I also analysed scales on a plate deployed at a location in between condensate addition and injection (Figure 8.1), yet this location could not be used for the long term studies because the section of the pipeline was replaced by a valve-free section during maintenance work in 2013. As we only obtained one sample from this location, the focus of this final chapter will mainly be on the four main sampling locations where the bulk of the time resolved work (Chapters 4, 5 and 6) has been carried out. The naming of the locations in this summary chapter will follow the numbers assigned to each location in Chapter 4 (bold in Figure 8.1).

At each of the four locations we deployed stainless steel scaling plates for between 1 day and 10 weeks. The resulting precipitates were characterised in detail for their compositions and microtextures. An integral part of understanding silica precipitation inside the Hellisheiði pipelines was the detailed characterisation of the separated water (especially silica speciation) at each location paired with information on the temperature and flow rate.

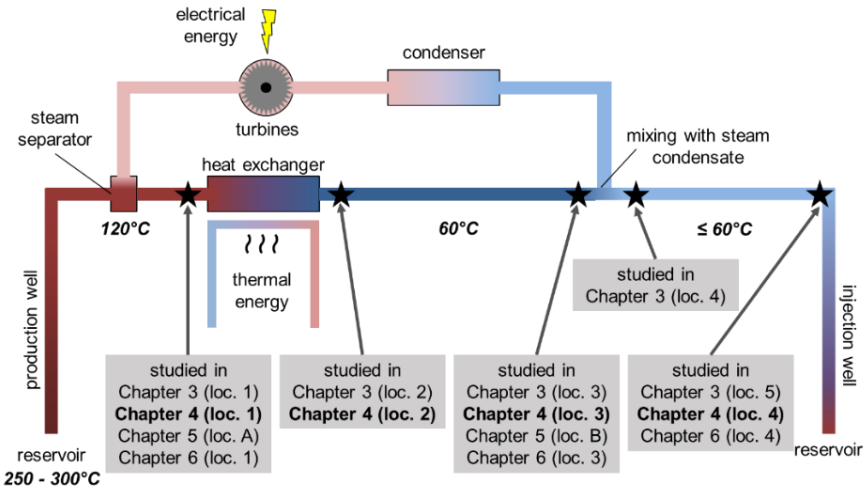

Figure 8.1: *Schematic of the Hellisheiði geothermal power plant indicating all the locations at which scaling plates were immersed as part of this PhD thesis.*

8.1.1 Characterisation of the separated water

The separated water at Hellisheiði is a dilute geothermal fluid, with silica being the main component, followed by Na, Cl, Ca and dissolved gases (H_2S, CO_2) (e.g., Table 4.2). Before the addition of condensate (locations 1 to 3), the fluid was characterized throughout the deployments by a fairly constant ~800 mg/L aqueous SiO_2, and was thus strongly supersaturated with respect to amorphous silica. The constant concentration along the flow path suggested that any removal of silica by precipitation in the fluid, was minor and did not affect the fluid composition with respect to dissolved silica. The concentration only changed due to dilution of the separated water by the addition of steam condensate after location 3 (reduced to ~550 mg/L).

Most of the silica in solution was present as silica monomers (H_4SiO_4) (Table 4.3). However, the proportion of monomeric silica decreased along the flow path from 85% before the heat exchanger to ~75% at location 3 while the proportion of "polymeric" silica increased from 15 to 25% over the same distance, indicating continuous polymerisation of silica. The proportion of particles in solution was below 0.05% of the total silica at all locations. However, the average size of particles decreased slightly downstream either because of preferential deposition of larger particles or because particle growth was reduced at the lower temperatures after the fluid was cooled in the heat exchanger. The dilution of the separated waters after addition of condensate lead to the proportion of monomers to increase again to 86%.

It is noteworthy to mention that both, the temperature and flow rates differed substantially between the different locations. Temperature varied between 55 and 118 °C while flow rated varied between 210 L/s to a maximum of 430 L/s (e.g., Table 4.2). Changes in these parameters occurred over relatively short distances and these rapid changes (e.g., forced cooling in the heat exchangers) put the system in a state of disequilibrium, at least temporarily (Chapter 4).

8.1.2 Composition of the deposited silica scales

The analysis of all samples showed the presence of silica only as amorphous silica. The presence of aluminosilicates on the filter membranes (Figure 4.3) or as small inclusions in the amorphous silica layers was minor and not related to the silica scale formation processes themselves. Furthermore, the precipitated amorphous silica contained minute ionic impurities (e.g., Na, Ca or Cl) as identified in EDS point analyses of the precipitates (Chapter 4). In addition to the dominant silica scales, iron sulphide phases were also observed on some plates from the initial study (location 1, 2 and 5; Chapter 3) and on the carbon steel coupons (Chapter 6).

8.1.3 Microtextures of the deposited silica scales and the two pathways of silica precipitation

In the first study conducted at Hellisheiði (Chapter 3) we described a range of microtextures that spanned from fan-shaped to wave-like to a film or even ridge-shaped precipitates. These variations were attributed to differences in the physico-chemical conditions within the power plant pipelines:

(1) variations in temperature, which will affect the rate of self-assembly (higher polymerisation rates at higher temperature),

(2) variations in fluid composition, which controls if amorphous silica precipitates or Fe sulphide corrosion products formed preferentially,

(3) the fluid flow regime, which controls the variable morphology of the precipitated structures,

(4) the distance along the flow path as this could lead to non-equilibrated fluids downstream of locations where major changes are occurring (cooling in the heat exchanger or dilution by steam condensate) and

(5) the immersion time of the scaling plates.

However, the exact contributions of each individual factors remained unclear in this initial study. This was addressed through the time-resolved study (Chapter 4) where the range of silica microtextures was much smaller and the precipitates could be subdivided into two types:

(1) an uneven silica layer consisting of individual 'bumps' the sizes of which increased as a function of time and onto which individual silica microspheres were deposited randomly

(2) 3D structures (fan- or ridge shaped), which grew towards the flow and which consisted of aggregated and cemented silica microspheres.

The silica layer was observed on all scaling plates, even after only 1 day of immersion, and both, the bump size and the thickness of the layer increased over time. The increase was not linear but slowed down as a function of time. The 3D structures on the other hand were only observed during the 4 and 10 week deployments at locations 1 to 3. This suggested that the two structures formed via two different processes/pathways.

Silica precipitation was a consequence of polymerisation of monomers and was taking place continuously inside the pipelines at Hellisheiði. Silica polymerisation took place at the scaling plate-separated water interface or in the fluid. When occurring at the interface it could be described as heterogeneous nucleation and resulted in the formation of the bumpy silica layer. When occurring in the fluid, the process was described as homogeneous nucleation and resulted in the formation of silica microspheres. In both cases the nuclei grew spontaneously by the addition of monomeric silica from solution. The heterogeneous nucleation of silica was found to be predominantly controlled by surface properties of the scaling plates, especially roughness (Chapter 5), while the subsequent growth was enhanced by high total silica concentrations and elevated temperature. Homogeneous nucleation and particle growth were only controlled by the physico-chemical conditions of the fluid, i.e., alkaline pH, elevated temperature, constant re-supply of dissolved silica and the

absence of salts. The deposition of particles was controlled by the fluid flow rate and likely the fluid flow regime. Larger particles were preferentially deposited due to larger drag. Homogeneously nucleated particles were also deposited onto the silica layers, preferentially along flow obstacles (vesicles in the volcanic glass or conchoidal fractures on the opal; Chapter 5).

In addition to the mechanism, this time-resolved study allowed us to derive the first ever heterogeneous growth rates of silica scales precipitated inside in-use geothermal pipelines (< 1 g day^{-1} m^{-2}). We could show that the precipitation was fastest at locations 1 and 2 and slowest at location 4. Again, total silica concentration and temperature were identified to have the biggest impact on the precipitation rate. In addition, our results show that the rapid changes in physico-chemical conditions (e.g., cooling in the heat exchangers) and the high flow rates resulted in a fluid in disequilibrium at location 2. Thus, the precipitation rate observed there did not yet represent the physico-chemical conditions of the fluid. This highlighted the importance of good kinetic models for the precipitation of amorphous silica, especially when trying to predict silica scaling using geochemical simulations.

8.1.4 Discrepancies between initial and time-resolved scaling plate study

When comparing the findings from the initial study (Chapter 3) with the findings from the time-resolved study (Chapter 4), the following discrepancies became obvious:

- *Composition of the precipitates:* During the initial study we found amorphous silica to be the dominant component on the scaling plates, closely followed by Fe sulphides. During the time-resolved experiments amorphous silica was by far the dominant phase encountered on the stainless steel scaling plates. Fe sulphides were only found as corrosion products (see below).
- *Presence of a bumpy silica layer:* For the time-resolved study, this type of precipitate was found on all scaling plates, irrespective of the location or deployment length. During the initial study however, a similar layer was only observed at locations 2 and 3. At the other two locations the rest of the plates were covered by individual silica spheres and idiomorphic Fe sulphides.
- *Corrosion of scaling plates:* Corrosion of the scaling plates was abundant at locations 1 and 5 during the initial study. During the time-resolved study, cor-

rosion was only observed on the S275 carbon steel coupons (predominantly at location 4) but never on the stainless steel scaling plates themselves.

Together these points suggest that the steel used for the preparation of some of the plates deployed during the initial study (locations 1, 5 and potentially also location 2) was not stainless steel as assumed but carbon steel instead. More specifically, it was likely non-tinned carbon steel as, based on the corrosion behaviour at location 1, it was less corrosion-resistant that the S275 carbon steel used for the preparation of the coupons. This assumption is reasonable as the power plant operators have used either stainless steel or carbon steel for the preparation of scaling plates in the past. Overall, this was a lucky coincidence as otherwise we might not have included the S275 carbon steel as a coupon on our scaling plates for the studies performed in Chapter 5 and 6.

8.1.5 Implications for the operation of other geothermal power plants

Silica precipitates with morphologies similar to the bumpy silica layers and 3D particle aggregates described from the Hellisheiði pipelines have been described at other power plants in Iceland and New Zealand (Carroll et al., 1998; Gudmundsson and Bott, 1979; Rothbaum et al., 1979; Thórhallsson et al., 1975), silica sinters from Iceland (Jones and Renaut, 2010) and laboratory experiments mimicking the growth of silica veins (Okamoto et al., 2010). This indicates that the combination of homogeneous and heterogeneous precipitation modes for amorphous silica as observed at Hellisheiði is widespread and happens in both, natural and man-made geothermal systems over a range of total silica concentrations (250 to 900 mg/L), temperatures (20 to 200 °C), pH (7.2 to 10.2) and salinities (200 to 25'000 mg/L). Nevertheless, our results are unique because, in addition to determining the pathways by which silica scaling occurs, we also identified and partly quantified the factors controlling the two pathways. These findings will help to develop better mitigation strategies (e.g., additives) for silica scales as formed in geothermal power plants, thus improving the overall performance of geothermal power production.

Our results indicate that, in order to fully control silica precipitation from geothermal fluids, both the heterogeneous and homogeneous pathway need to be inhibited. One option is to preventing the fluid from reaching supersaturation with respect to amorphous silica, e.g., by keeping the fluid temperature above the solu-

bility limit. However, this method of silica management prevents the efficient use of a geothermal resource as no second stage boiling or hot water production for space heating and industrial can be done. Mitigation of both pathways of silica scaling could also be achieved by reducing the rate of silica polymerisation. This can be done by acidification of the geothermal fluid (Henley, 1983; Gallup, 1998). At low pH, the rate of silica polymerisation is slowed down and the negative surface charge of silica particles stabilised, preventing aggregation. Controlling the rate of acid injection and precise measurement of the pH of the geothermal fluid is very important as too much acid will strongly enhance localised corrosion of pipes while not enough acid will not stop silica deposition. The polymerisation rate of silica can also be lowered by controlling silica speciation in the fluid. Monomeric silica is more likely to deposit than polymeric silica, thus by aging the fluid, scaling potential is reduced (Yanagase et al., 1970). The success of this silica management method depends to a large extent on the ionic strength of the brine. In high salinity fluids aging leads to enhanced precipitation as the cations present act as flocculating agents.

Another option is the use of additives. While there is currently no inhibitor preventing polymerisation of silica, there are dispersants preventing the aggregation of silica particles (Harrar et al., 1982; Gallup, 2002; Demadis, 2005). This could prevent the formation of 3D aggregates. Potentially, this is sufficient to largely mitigate the problem of silica scaling in geothermal power plants as the 3D structures lead to turbulent flow along the fluid-pipeline interface (Hawkins et al., 2013; Hawkins et al., 2014), leading to increased flow friction and lower flow rates at constant operating pressures. This explains why we saw a higher flow rate after cleaning of the heat exchangers (Chapter 4). This effect cannot be excluded for the silica layer but is likely much less severe due to the smoother nature of the silica layer. In Chapter 6 we even concluded that the formation of a thin silica layer could be beneficial as it could potentially passivate the pipeline surfaces against corrosion.

8.2 Interactions between silica and biomolecules

As part of this thesis I also studied the interaction between the protein lysozyme and a polymerising silica solution (co-precipitation) and a between lysozyme and a pre-formed silica nanoparticle suspension (adsorption). Through these experiments I could produce a set of novel hybrid composites which were characterised by a wide range of techniques. This allowed us to draw conclusions regarding their for-

mation and aggregation pathway. The results showed that in both cases, lysozyme primarily interacted with silica nanoparticles and adsorbed onto their surface due to electrostatic interactions. This led to bridging aggregation, where one lysozyme molecule connected two silica particles. The adsorption of lysozyme onto silica particles also led to conformational changes in the lysozyme. This exposed the hydrophobic core of the protein. In order to limit the contact of thee hydrophobic amino acid residues with the surrounding water, such deformed lysozyme molecules aggregated. Hence, the formation of silica-lysozyme composites was controlled by silica-lysozyme interactions but also by lysozyme-lysozyme aggregation.

A clear trend between the amount of lysozyme associated with the composites and the change in composite properties, especially surface charge and the specific surface area, was observed. While these overall trends held true for both the composites formed by co-precipitation and adsorption, the absolute changes between composites and pure silica differed substantially between the two sets of composites. One explanation may lie in the fact that in the co-precipitation experiments lysozyme interacted with smaller silica particles that were aggregated before reaching their full size. This is indicated by the SAXS data, which suggest smaller silica particles in the co-precipitated composited.

Overall, this biomolecule-silica interaction study showed that by controlling two simple parameters, silica-lysozyme ratios and the timing of their interaction, the properties of the resulting hybrid material could be controlled. This is interesting for both biosilicification (of diatoms and microbes) as well as industrial synthesis as both these parameters can be controlled inside or in the immediate surroundings of a living cell, as well as in industrial syntheses.

References

Carroll, S., Mroczek, E., Alai, M., Ebert, M., 1998. Amorphous silica precipitation (60 to 120 °C): Comparison of laboratory and field rates. *Geochimica et Cosmochimica Acta* **62**, 1379-1396.

Demadis, K.D., 2005. A structure/function study of polyaminoamide dendrimers as silica scale growth inhibitors. *Journal of Chemical Technology and Biotechnology* **80**, 630-640.

Gallup, D.L., 1998. Aluminum silicate scale formation and inhibition (2): scale solubilities and laboratory and field inhibition tests. *Geothermics* **27**, 485-501.

Gallup, D.L., 2002. Investigations of organic inhibitors for silica scale control in geothermal brines. *Geothermics* **31**, 415-430.

Gudmundsson, J.S., Bott, T.R., 1979. Deposition of silica from geothermal waters on heat transfer surfaces. *Desalination* **28**, 125-145.

Harrar, J., Locke, F., Otto Jr, C., Lorensen, L., Monaco, S., Frey, W., 1982. Field tests of organic additives for scale control at the Salton Sea geothermal field. *Society of Petroleum Engineers Journal* **22**, 17-27.

Hawkins, C., Angheluta, L., Hammer, Ø., Jamtveit, B., 2013. Precipitation dendrites in channel flow. *Europhysics Letters* **102**, 54001.

Hawkins, C., Angheluta, L., Jamtveit, B., 2014. Hydrodynamic shadowing effect during precipitation of dendrites in channel flow. *Physical Review E* **89**, 022402.

Henley, R., 1983. pH and silica scaling control in geothermal field development. *Geothermics* **12**, 307-321.

Jones, B., Renaut, R.W., 2010. Impact of seasonal changes on the formation and accumulation of soft siliceous sediments on the discharge apron of Geysir, Iceland. *Journal of Sedimentary Research* **80**, 17-35.

Okamoto, A., Saishu, H., Hirano, N., Tsuchiya, N., 2010. Mineralogical and textural variation of silica minerals in hydrothermal flow-through experiments: Implications for quartz vein formation. *Geochimica et Cosmochimica Acta* **74**, 3692-3706.

Rothbaum, H., Anderton, B., Harrison, R., Rohde, A., Slatter, A., 1979. Effect of silica polymerisation and pH on geothermal scaling. *Geothermics* **8**, 1-20.

Thórhallsson, S., Ragnars, K., Arnórsson, S., Kristmannsdóttir, H., 1975. *Rapid scaling of silica in two district heating systems*, San Francisco, pp. 1445-1449.

Yanagase, T., Suginohara, Y., Yanagase, K., 1970. The properties of scales and methods to prevent them. *Geothermics* **2**, 1619-1623.

Chapter 9

Work in progress

Besides the results presented above as thesis chapters I am either leading or am part of three further studies that are still ongoing, with their status briefly outlined below.

9.1 Modelling of aggregation of silica particles

One of the studies in progress is a collaboration with Christopher Hawkins, Luiza Angheluta and Bjørn Jamtveit from the University of Oslo on the formation of the fan-shaped precipitates observed on the scaling plates.

Hawkins et al. (2013) had previously investigated the effect of fluid flow (laminar and non-laminar) on the precipitation pattern on pipe walls. Their models predicted the formation of dendrites oriented towards the flow. The fact that these structures showed striking resemblances to our fan-shaped aggregates lead us to initiate a collaboration on a modelling study with the team in Oslo. Our goal was to develop a more representative model based on ballistic aggregation in a unidirectional flow, i.e., a fluid containing particles which move freely in one direction until they collide with a surface or another particle. The model revealed that both in 2D and 3D (Figure 9.1), aggregation will lead to intricate fan-shaped structures over time. These fans are near-identical to our observations from the scaling plates from location 1 (Figure 3.3 A and Figure 4.6).

The inclination of the precipitates formed during simulations depends on the relative rates of attachment and detachment. When the attachment and detachment rates were identical, the precipitates grew towards the flow at a low angle (Figure 9.1 B) while, if the attachment rate was higher than the detachment rate, the an-

gle between the pipe surface and the simulated precipitates was close to 45° (Figure 9.1 C). As most fan-shaped aggregates on the real scaling plates grew at an angle of 30 to 60° (Figure 4.6), we could conclude that the attachment rate of particles was higher than the detachment rate during our scaling plate deployments. This was likely due to the instantaneous precipitation of silica around the point of contact between two particles where there was an infinitely small negative radius of curvature and the solubility was zero (Iler, 1979). This cementation of particles has been observed in all the 3D aggregates on the scaling plates.

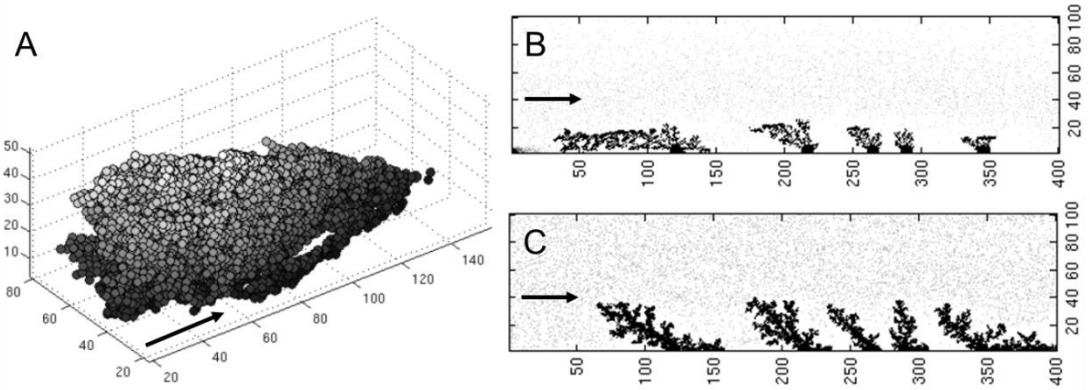

Figure 9.1: *Results of simulations based on ballistic aggregation of particles from a flowing fluid. (A) 3D representation of a single fan-shaped structure, (B) growth of fans under conditions of equal attachment/detachment rates and (C) growth under condition of faster attachment over detachment. In all figures the flow direction is indicated by an arrow (courtesy of Christopher Hawkins, University of Oslo)*

In addition, Christopher's simulation assessed the effect of polydispersity. This was because we observed silica particles ranging in sizes from 0.01 up to 25 μm in the separated water at Hellisheiði (Table 4.3). Particles of all sizes were aggregated to form the observed fan-shaped structures, however, large particles were preferentially incorporated into the fan-shaped aggregates. This was confirmed by the simulations which predicted a size distribution skewed towards larger particles as they are preferentially deposited due to the higher drag.

The model set up by Christopher already predicts the formation of the fan-shaped precipitates well. It would be interesting to expand the model to also include the more complex flow field around an orifice such as the openings in the tube sheet and see, if the overlap between simulation and the observed silica rings (Chap-

ter 9.2) is equally good. However, currently there are no concrete plans in place for further collaboration as Christopher has finished his PhD.

9.2 Silica scaling in a heat exchanger

The second study in progress is the detailed characterisation of silica precipitates that formed inside the heat exchangers at Hellisheiði (Figure 9.2 A). Like the separated water throughout the Hellisheiði power plant, the fluid flowing through the heat exchangers is supersaturated with respect to amorphous silica, resulting in the formation of silica scales (Figure 9.2 B & C). Over time the amount of heat transferred decreases due to these deposits. In addition, the operational pressure needed to maintain the flow rate has to be increased. Therefore, the heat exchangers need to be cleaned at regular intervals (every 6 to 12 months) to maintain the efficient operation of the power plant. During one of these routine cleaning operations in late 2012, samples of the silica scales removed from different locations within the heat exchangers were collected by the power plant operators. These samples represent a unique dataset as they have precipitated from a fluid of constant composition (no changes observed between in- and outflow composition, e.g., Table 4.2), during a given amount of time. The only two variables are thus temperature and flow regime. Due to the constant monitoring, the temperature profile along the flow path is very well known and the fluid flow regime can be derived from the geometry of the heat exchanger. Overall, the physico-chemical conditions under which these deposits precipitated are very well understood.

Using both light and scanning electron microscopy (SEM), two types of microstructures were identified: (1) silica rings on the openings of the tube sheets (Figure 9.2 B) and (2) silica fans on flat surfaces (Figure 9.2 C). They formed at different locations within the heat exchanger due to hydrodynamic differences. Similarly to the 3D structures formed within the pipelines at Hellisheiði (Chapter 3 and 4), both, the rings and fans consisted of rounded aggregates made up of individual silica spheres which were cemented together (Figure 9.2 D & E). Although they appeared dark grey in colour, they were both composed of amorphous silica only, according to XRD. In an attempt to characterize the 3D structures better, I analysed the porosity and pore size distribution on a single sample by NMR porosimetry (Appendix A) and showed that this sample had a porosity of 8.4% and an average pore size of 3.4 nm. In the near future we plan to analyse more samples by NMR and also to

dissolve the samples in NaOH and analyse the solutions by ICP-MS to quantify the impurities which have been incorporated into the precipitates and result in their dark colour.

In order to obtain additional information on the composition of the samples, we also sent aliquots of these solids as well as fluid samples from location 1 (before the heat exchanger) and location 2 (after the heat exchanger) to the University of New Mexico for analysis of triple oxygen isotopes and to the GFZ Potsdam for analysis of silicon isotopes. Whilst providing further information on the sample formation, these well-characterised samples precipitated under well-documented conditions will also help to study the fractionation of oxygen and silicon isotopes in the silica-water system as a function of temperature. Most of the samples have been analysed and data processing is currently underway but this is beyond the scope of this thesis.

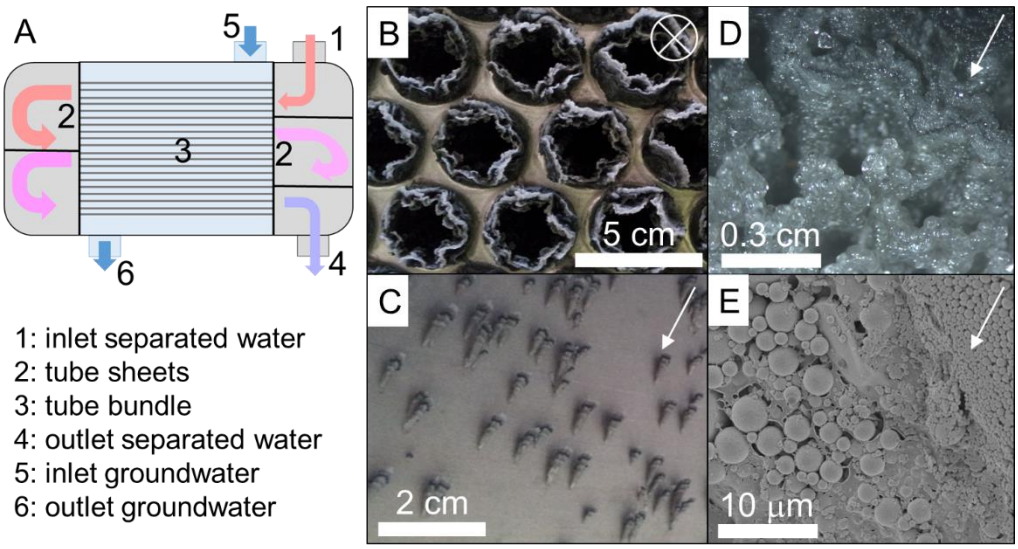

Figure 9.2: *Silica scales from the heat exchanger at the Hellisheiði power plant: (A) schematic of an individual heat exchanger unit with (B) scales formed around individual openings of the tube sheet and (C) on the flat walls of the inlet. Both types of precipitates consist of (D) marble-like aggregates which are composed of (E) individual, (sub)micrometre-sized silica particles cemented together by the deposition of dissolved silica.*

9.3 *In-situ* and real-time formation of silica-lysozyme composites

The detailed study of the silica-lysozyme composites allowed us to draw certain conclusions regarding the interactions between the two entities. We also collected additional, *in-situ* and real-time data during our SAXS beamtime in August 2015.

Scattering data was collected during the first few minutes of the adsorption experiments (Chapter 7) at 50 ms/frame. This was necessary as the electrostatic interactions between the negatively charged silica particles and positively charged lysozyme molecules are very rapid. We could clearly observe the evolution of the structure factor, $S(q)$ characterising the interparticle interactions thus giving information about aggregation process in the silica-lysozyme system. Currently we are analysing the data set using the Fourier transform techniques to obtain the real-space radial distribution $g(r)$ functions from $S(q)$ (lead by Tomasz M. Stawski, GFZ Potsdam). Our preliminary analysis suggests the aggregation process of silica in the presence of lysozyme involves a rapid formation of a loose extended network (fractal-like) in the first step, followed by the local densification within this network (increase in local packing of particles) leading to the formation of correlated (i.e., semi-ordered) aggregates of nanoparticles. This densification is likely due to the increasing size of the aggregates (outside the SAXS range) which leads to a collapse of the delicate fractal-like structures.

References

Hawkins, C., Angheluta, L., Hammer, Ø., Jamtveit, B., 2013. Precipitation dendrites in channel flow. *Europhysics Letters* **102**, 54001.

Iler, R.K., 1979. *The chemistry of silica: solubility, polymerization, colloid and surface properties, and biochemistry*. Wiley, London.

Chapter 10

Outlook

There are still many open questions in the field of silica precipitation under geothermal conditions that need addressing in order to further our understanding of the mechanisms and rates of silica precipitation. Here we discuss several approaches and suggestions for further theoretical, laboratory and field studies that we assert are still needed to help progress this field in the future:

- Theoretical:
  - Molecular simulations to understand the involvement of different polymeric species in the growth of homogeneous or heterogeneous nuclei.
  - Molecular simulations to assess the fundamental interactions between silica and other molecules (e.g., additional biomolecules) or specific surfaces (microbial, corroded steel etc.).
  - Hydrodynamic simulations to address interactions between surfaces, particles and fluid flow properties to model possible precipitation patterns.

- Laboratory analogue studies:
  - *In-situ* and real-time experiments addressing the precipitation mechanisms and rates using high resolution microscopy (e.g., liquid-cell TEM, AFM) or scattering techniques (e.g., SAXS, DLS). These experiments should quantify (a) homogeneous nucleation and growth of particles in solution as a function of parameters not yet addressed (e.g., fluid flow rates, presence of organic compounds and even microbial species), and (b) heterogeneous surface nucleation and growth. Importantly in these

experiments supersaturation should be induced through rapid cooling of a fluid and not (as usually done as it is simpler) by neutralising of supersaturated high pH silica solution.
    - Thermodynamic and kinetic data for impure silica as a function of both, aluminium and iron content.

- Field studies:
    - More highly controlled (both spatially and in a time resolved manner) studies of silica scaling inside in-use geothermal pipelines (not using bypasses) to see if the two pathways of silica precipitation are indeed taking place over a wide range of physic-chemical conditions.
    - Scaling plate and bypass studies to test novel materials and coatings as well as additives to develop better mitigation strategies for scaling control and corrosion prevention.

All laboratory and field approaches require a highly complementary and detailed monitoring of the physico-chemical conditions under which silica precipitation takes place as well as detailed characterisation of the textures and composition (abiotic and biotic) of the resulting solids. The significance of the proposed research will invariably drastically increase when several of these approaches are combined, and when especially simulations, laboratory and field-based observations can be better compared and contrasted.

Appendix A

Non-standard methods used for the study of silica scales from Hellisheiði

Focused ion beam sections

Focused ion beam (FIB) sections were used to obtain cross sections of the scaling plates deployed at location 1 for 1 day, 3 days and 1 week (Chapter 4).

A FIB instrument is a scanning electron microscope with an added capability of a finely focused gallium ion beam (e.g., Giannuzzi and Stevie, 1999; Wirth, 2009) that can be used to cut sections out of a solid sample. The beam is generated at 5 to 50 keV from a liquid metal ion source (LMIS) in which a gallium reservoir is in contact with a tungsten tip. The Ga, liquid above 30 °C, flows to the tip and is extracted by a high electric field. The thus generated beam is highly focusable and has a diameter of between ~5 and 500 nm, which leads to a highly accurate and spatially precisely controllable beam for the cutting of sections using the FIB technique.

FIB instruments are primarily used for the preparation of cross sections for imaging using scanning or transmission electron microscopy. However, FIB can also be used for direct imaging of a sample by detecting the electrons sputtered from the sample upon penetration of the Ga beam. These techniques are described in detail in Stevie et al. (1995) and Phaneuf (1999) and will not be elaborated on further. Here I only describe the FIB "lift-out" (LO) technique that I used in my work. Using this approach trenches are sputtered away on either side of the desired cross-section,

which is then milled until it is electron transparent (Overwijk et al., 1993; Wirth, 2009). Using a tungsten needle (Giannuzzi et al., 1997), the thin foil is removed and placed onto a TEM support grid. Ticker foils (> 1 μm) can be produced for other techniques such as SEM. The whole process of spot identification, sample preparation and removal is monitored using an SEM. The major advantages of this technique compared to the standard TEM foil preparation is the very limited amount of sample preparation required, the speed of the method and the small amount of material wasted.

The FIB sections studied in Chapter 4 were prepared using a FEI FIB200 instrument at the GFZ Potsdam. Foils with a size of 15 × 10 × 0.15 μm were sputtered with a Ga ion beam accelerated to 30 keV. No preparation was required as the samples were already coated with 40 nm of gold from SEM imaging. The FIB foils were then placed onto holey carbon copper grids and analysed using a high-resolution transmission electron microscope at the GeoForschungsZentrum in Potsdam (HR-TEM, TECNAI F20 X-Twin, 200 kV) equipped with a Gatan Tridiem Imaging Filter and an EDAX X-ray analyser.

Nuclear magnetic resonance porosimetry

Nuclear magnetic resonance (NMR) was used and will be used in the near future to obtain porosity values and pore size distributions of the samples collected from the heat exchanger at Hellisheiði during routing cleaning (Chapter 9.2).

NMR porosimetry is used to determine the porosity and pore size distribution of a sample immersed in water by measuring the spin states of hydrogen atoms in water (Gallegos et al., 1987; Drago et al., 1995; Stallmach and Kärger, 1999). Hydrogen can show two possible spin states m = ½ and m = - ½. If a magnetic field is applied, the spin of the hydrogen atom is aligned in parallel to the magnetic field (= 1st magnetisation). Then a radio frequency pulse is used to perturb the alignment of the hydrogen atoms (2nd magnetisation). After this pulse, the hydrogen atoms return to equilibrium orientation, i.e., orientation along the primary magnetic field. This process is called relaxation and the time required to reach equilibrium again is denoted as T_2 and measured by NMR. T_2 depends on the surroundings of a hydrogen atom and can be expressed as

$$\frac{1}{T_2} = \rho \frac{s}{v} \tag{A.1}$$

where ρ is the surface relaxation strength (i.e., how easy magnetisation is attenuated by the surface) and $\frac{S}{V}$ is the surface-to-volume ratio of the pore. Microscopically the volume of a single pore filled by water can be divided into two regions: surface area S and bulk volume V. The surface area S is a thin layer with a thickness of a few molecules close to the pore wall surface. The bulk volume is the remaining part of the pore volume and usually dominates the overall pore volume. The relaxation time T_2 is significantly shorter for a hydrogen atom in the surface area, compared to an atom in the bulk volume as each contact with a surface increases the loss of the non-equilibrium spin and helps the atom to return to the equilibrium orientation (Gallegos et al., 1987; Davies and Packer, 1990; Kleinberg et al., 1994). Hence, T_2 depends on the pore size the hydrogen atom is in. For small pores the non-equilibrium orientation is lost faster than for large pores or the water surrounding the sample. The average T_2 corresponds to the average pore size while studying the T_2 distribution gives information on the pore size distribution. If plotted versus the normalised signal, the plot shows peaks for each group of pores (e.g., small, intermediate and large). The peak height (= intensity of the signal) is proportional to the frequency of the corresponding pore size, i.e., higher peaks for more common pores (Figure A.1).

NMR T_2 relaxation time measurements were performed on a water saturated samples using a MARAN ULTRA (Oxford Instruments), with a 2 MHz operating frequency. The Carr-Purcel-Meiboom-Gill (CPMG) pulse sequence was used to generate the magnetisation decay with an echo spacing of 0.1 ms, and repeat delay of 10 s between successive scans. The decaying magnetisation was mapped to a T_2 distribution using the WinDXP programme software provided by Oxford Instruments. The signal amplitude was calibrated using standards with a known volume of doped water. Based on the average T_2 and a surface relaxivity of 3 μm s^{-1} for silica, the average pore size was calculated. Using the same surface relaxivity and the cumulative normalised signal (not shown), we could calculate the proportions of the individual groups of pores, e.g., small, intermediate and large (Figure A.1).

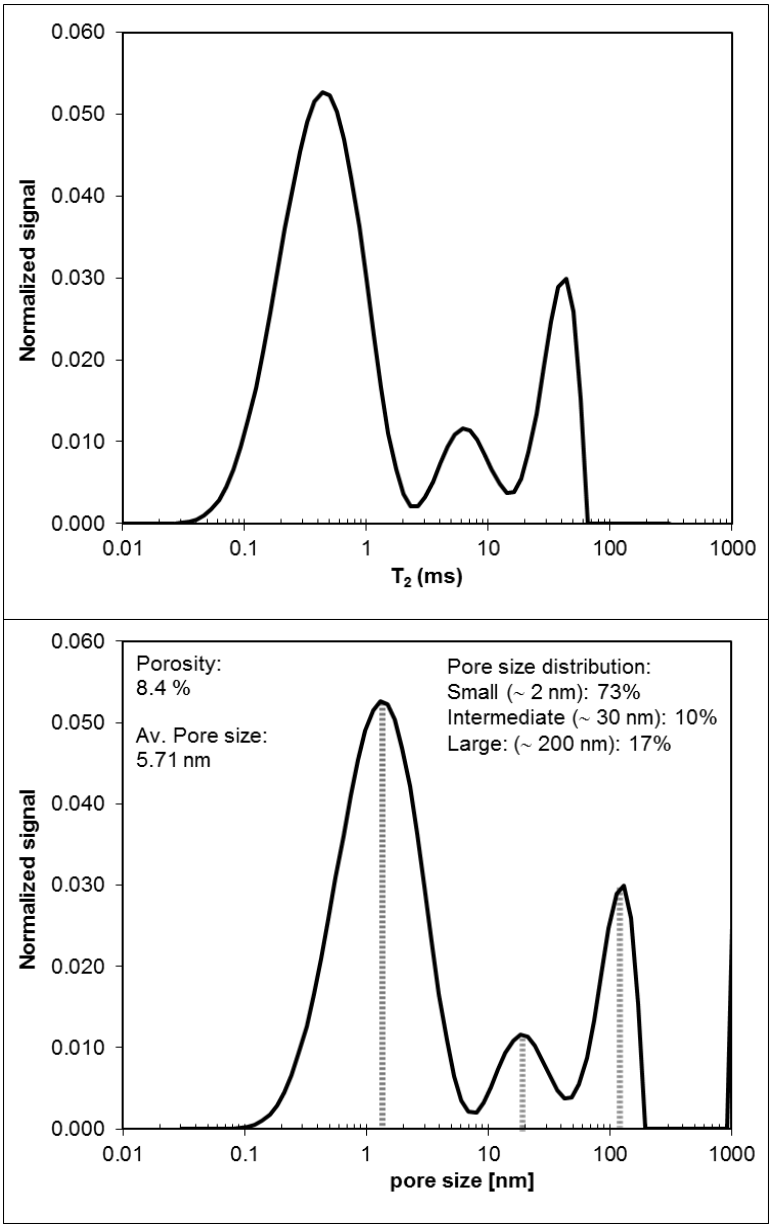

Figure A.1: *Distribution of T_2 (top) as measured during NMR porosimetry and the signal converted to pore sizes (bottom) using a surface relaxivity of $\rho = 3\ \mu m\ s^{-1}$. Each peak corresponds to one group of pores (small, intermediate, large) and the peak height to the abundance of the group of pores.*

References

Davies, S., Packer, K., 1990. Pore-size distributions from nuclear magnetic resonance spin-lattice relaxation measurements of fluid-saturated porous solids. I. Theory and simulation. *Journal of Applied Physics* **67**, 3163-3170.

Drago, R.S., Ferris, D.C., Burns, D.S., 1995. Pore-resolved NMR porosimetry. *Journal of the American Chemical Society* **117**, 6914-6920.

Gallegos, D.P., Munn, K., Smith, D.M., Stermer, D.L., 1987. A NMR technique for the analysis of pore structure: application to materials with well-defined pore structure. *Journal of Colloid and Interface Science* **119**, 127-140.

Giannuzzi, L., Drown, J., Brown, S., Irwin, R., Stevie, F.A., 1997. Focused ion beam milling and micromanipulation lift-out for site specific cross-section TEM specimen preparation, *MRS Proceedings*. Cambridge Univ Press, p. 19.

Giannuzzi, L., Stevie, F.A., 1999. A review of focused ion beam milling techniques for TEM specimen preparation. *Micron* **30**, 197-204.

Kleinberg, R., Kenyon, W., Mitra, P., 1994. Mechanism of NMR relaxation of fluids in rock. *Journal of Magnetic Resonance, Series A* **108**, 206-214.

Overwijk, M., Van den Heuvel, F., Bulle-Lieuwma, C., 1993. Novel scheme for the preparation of transmission electron microscopy specimens with a focused ion beam. *Journal of Vacuum Science & Technology B* **11**, 2021-2024.

Phaneuf, M., 1999. Applications of focused ion beam microscopy to materials science specimens. *Micron* **30**, 277-288.

Stallmach, F., Kärger, J., 1999. The potentials of pulsed field gradient NMR for investigation of porous media. *Adsorption* **5**, 117-133.

Stevie, F.A., Shane, T., Kahora, P., Hull, R., Bahnck, D., Kannan, V., David, E., 1995. Applications of focused ion beams in microelectronics production, design and development. *Surface and Interface Analysis* **23**, 61-68.

Wirth, R., 2009. Focused Ion Beam (FIB) combined with SEM and TEM: Advanced analytical tools for studies of chemical composition, microstructure and crystal structure in geomaterials on a nanometre scale. *Chemical Geology* **261**, 217-229.

Appendix B

Non-standard methods used for the study of silica-lysozyme composites Focused ion beam sections

Silicomolybdate method for analysis of monomeric silica

We tried to use the silicomolybdate method during the co-precipitation synthesis of the silica-lysozyme composites (Chapter 7) to monitor the polymerisation process of silica in the presence of lysozyme by following the change in monomeric silica concentration in the reacting solutions.

To determine monomeric silica concentration in solution, spectrophotometric methods can be used. The most common methods are the molybdate yellow and molybdate blue method, used for different concentrations of dissolved silica (Eaton et al., 2005). The molybdate yellow method is used in the concentration range from 1 to about 25 ppm. Both methods involve the reaction of molybdic acids with monosilicic acid to form silico-12-molybdic acids (a type of heteropoly acid; Coradin et al., 2004) which accommodate one silicon atom in a cage-like structure ofF MoO_6-octahedra (Figure B.1). Thus, in theory, only silica monomers can form the silicomolybdic complexes. However, several studies have shown that small oligomers can dissolve during the analyses and are thus also analysed by the molybdosilicate methods (Iler, 1979; Coradin et al., 2004; Tanakaa and Takahashib, 2001). Many studies thus use the term "molybdate-reactive silica" to describe the results obtained by the molybdate methods.

The silicomolybdic acids absorb light at specific wavelengths and therefore the solutions are distinctly coloured. They are analysed quantitatively for their optical density using a UV-Vis spectrophotometer. According to the Beer-Lambert law, the absorbance of a solution is directly proportional to the concentration of the absorbing species in solution and the path length of the light. Thus, for a fixed path length, UV-Vis spectrophotometry can be used to determine the concentration of the absorber (silicomolybdic acids) in the solution.

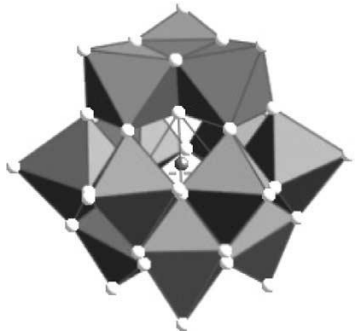

Figure B.1: *Structure of the silicomolybdic acid cluster. The silicon atom (in red) is surrounded by twelve MoO_6 octahedra (oxygen atoms in white). Hydrogen atoms are not shown (from Coradin et al., 2004).*

The molybdate methods are commonly used to follow the decrease in "molybdate-reactive silica" and infer the polymerisation process of silica (Icopini et al., 2005; Iler, 1979; Tobler et al., 2009; Weres et al., 1981) which we had planned to do as well. We collected sample aliquots (2 mL) from the polymerising solution (co-precipitation experiments, Chapter 7) at specific time intervals (0 to 180 min) and after filtration through 0.2 μm syringe filters these were added to 0.1 mL 1M HCl. The HCl allowed us to 'stabilize' the monomeric silica content for later analysis. This is because the formation and breaking of siloxane bonds are known to be very slow at low pH and therefore further polymerisation or depolymerisation is assumed to be prevented (Alexander, 1954; Alexander et al., 1954; Coradin et al., 2004; Tarutani, 1970). Nevertheless, sample analysis was performed within 60 minutes of their removal from the reacting solution. For the molybdic acid reagent 1.5 N (0.75 M) sulphuric acid (H_2SO_4) and a molybdate stock solution (100 g/L $H_{24}Mo_7N_6O_{24} \cdot 4H_2O$ and 47 g/L H_4NOH) were prepared and mixed 2:1:5 with deionised water. The molybdic acid reagent was always prepared on the day of the analyses as it is not stable over longer time periods. For analysis, 20 mL of

molybdic acid reagent were mixed with 5 mL of sample diluted with MilliQ to measurable range (≤ 24 ppm), shaken vigorously and left to equilibrate for 10 minutes. The coloured solutions were analysed on an Uvikon XL UV-Vis spectrophotometer at a wavelength of 410 nm and compared against silica standards.

Unfortunately, in stark contrast to solutions at the same silica concentrations but with no lysozyme added, all solutions containing lysozyme turned strongly turbid within 10 to 60 minutes of starting the co-precipitation reactions. This was due to the formation of silica nanoparticles. These nanoparticles show a negative surface charge and thus interacted with the positively charged lysozyme molecules (Chapter 7) to form aggregates. Initially it was assumed that these aggregates could be removed by filtration as many were big enough to appear as millimetre-sized floccules. However, filtration either did not remove enough of the silica nanoparticles and/or lysozyme or forced the aggregates apart so they passed through the filter nevertheless. In any case, the filtered and acidified samples turned turbid again within minutes. The turbidity was much weaker than in the non-filtered solutions. However, even slightly turbid solutions will strongly distort the results obtained by the spectrophotometric silicomolybdate method. Thus, despite lengthy testing of different filters and the timing of the filtration, we did not manage to adjust the method in a way suitable for our purposes.

Small-angle X-ray scattering

Small-angle X-ray scattering (SAXS) was used to determine the particle size of silica in the co-precipitation and adsorption silica-lysozyme composites as well as the particle-particle interactions (Chapter 7).

SAXS is a characterisation technique based on the elastic scattering of X-rays by nano-sized objects recorded at very low angles, typically 0.1 to 10°. Using SAXS we can obtain a series of structural parameters about the solid entities in a sample such as size, size distribution (polydispersity), geometric shape, and agglomeration in the size range of 0.1 to ≤ 500 nm but typically < 100 nm (Bras, 1998; Riekel et al., 2000; Craievich, 2002; Stawski and Benning, 2013; ten Elshof et al., 2015). A typical set up in shown in Figure B.2: The incident beam is collimated and falls onto the sample in a holder (usually a quartz capillary). The X-ray sources for SAXS can be conventional laboratory X-ray lamps or synchrotron X-ray radiation. The major advantage of synchrotron radiation is the high intensity of the beam, and hence the

reduced measurement time. This allows the realisation of *in-situ* experiments in which processes happening in solution (i.e., particle growth and aggregation) can be followed in real-time (< 100 ms to hours). Independent of the source, most of the incident X-rays are passing right through the sample and are absorbed by the beam stop. Only a small proportion of photons is scattered at small angles when passing through the sample and is detected by a 2D detector as a function of the so-called scattering angle 2θ. The scattered intensity depends on the volume fraction of the scatterers in solution as well as the scattering contrast (= difference in average electron density) between the solid entity and the surrounding solvent.

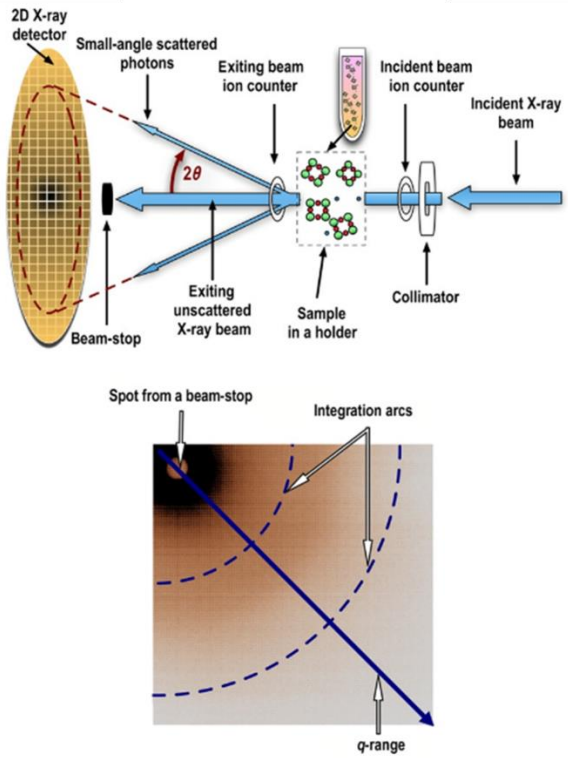

Figure B.2: *(A) Set up of a typical SAXS experiment and (B) example of a scattering pattern from a sample containing agglomerated particles in solution recorded with a 2D SAXS detector (from Stawski and Benning, 2013).*

Typically the scattering intensity is measured as a function of the scattering vector q (nm^{-1}), which is dependent on the scattering angle 2θ and the wavelength λ (nm) of the incident beam via

$$q = \left(\frac{4\pi}{\lambda}\right) \sin\theta \qquad \text{(B.1)}$$

In order to obtain the maximum information from a SAXS measurement, the q-range must be adjusted before each SAXS experiment to the range expected based on the expected maximum and minimum particle size: $q_{min} = \pi/D_{max} < q < q_{max} = \pi/D_{min}$ (Glatter and Kratky, 1982). The q-range can be adjusted by changing the wavelength of the incident X-ray beam, the sample-to-detector distance, the area of the detector as well as the position of beam on a detector (Stawski and Benning, 2013). To calibrate the q-range, i.e., obtain absolute units, a standard with a well-known scattering pattern is measured. Common standards are silver behenate or wet rat tail collagen.

The first step in the processing of SAXS data is reduction of the 2D scattering pattern to a 1D scattering curve by integrating over all angles starting at $q = 0$ (Guinier and Fournet, 1955; Glatter and Kratky, 1982; Craievich, 2002). Then, the measured intensities need to be corrected for fluctuations in the incident X-ray beam, scattering from the beam stop and other artefacts shown on the detector by masking these areas on the detector image. Finally the data are normalized against transmission and time as well as the scattering from the capillary and the solvent is subtracted as background.

Data interpretation, e.g., deriving information about particle size and shape, interactions, or polydispersity is based on the study of different regions or features of a scattering pattern. The scattering vector q is inversely proportional to size, thus information on the smallest features (e.g., surface of a particle, Porod's law) is found in the high q-range while information on the interactions between particles (so-called structure factor $S(q)$) can be found in the low q domain. At intermediate q, information on the particles themselves (size, shape and internal structure) is found (so-called form factor $P(q)$). Thus, even before detailed data analysis we can already obtain a certain amount of information by studying the shape of a scattering curve (Figure B.3):

- The plateau reached at low q values ($q < 0.1$ nm^{-1}) indicates that no aggregation occurred in the black system (in the q-range studied). The increasing intensity in the same q-range for the orange system indicates that the particles are aggregated.
- The correlation peak in the orange system (arrow) is due to particle-particle interactions in a non-dilute (i.e., aggregated system). Its position at q ~1.2 nm^{-1} corresponds to typical distances between individual particles of d ~5.2 nm (according to Equation B.1).

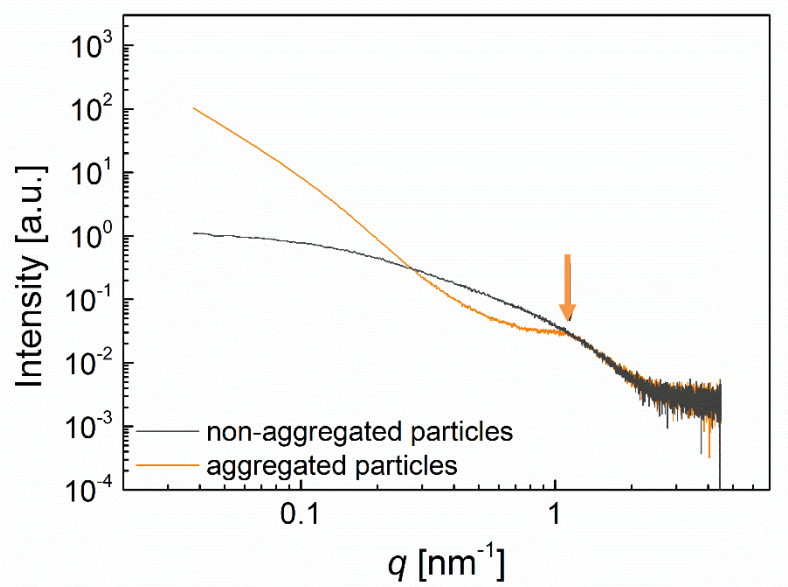

Figure B.3: *Example of two different scattering curves for a solution containing particles ~5 nm in size. The black curve represents a solution in which the particles are not aggregated while the orange one represents a solution containing particle aggregates. The arrow marks the correlation peak formed due to the increasing number of particle-particle interactions with typical distances.*

Detailed data interpretation requires fitting of the data by physical models as a part of the structural information is lost during the measurement due to the so called "phase problem". This problem arises as detectors can only detect the amplitude (related to the intensity) of the scattered photons but not their phase, which carries a lot of information on the structure. Thus, in order to solve the phase problem, we need to fit the measured data by physical models which were developed for certain systems (e.g., monodisperse spheres). In order to pick the correct model, some parameters of the system (e.g., particle size or shape) need to be derived from other characterisation techniques such as microscopy or have to be assumed. For detailed discussion of SAXS data fitting see Pauw (2013) and ten Elshof et al. (2015).

Our pure silica particles and biomimetic silica-lysozyme composites (Chapter 7) were analysed by synchrotron-based SAXS at the BioSAXS beamline P12 of the EMBL at PETRA III (DESY, Germany) (Blanchet et al., 2015). Measurements were performed by using a monochromatic X-ray beam at 10 keV and two-dimensional scattered intensities were collected at small-angles with a Dectris Pilatus 2M (2D large area pixel-array detector). Transmission was measured by means of a photodiode installed in the beam-stop of the SAXS detector. A sample-to-

detector distance of ~3 m allowed for a usable q-range of ~0.04 < q < 4.5 nm^{-1}. The scattering-range at small-angles was calibrated against silver behenate and dry collagen standards. The silica and composite colloidal solutions, were loaded into an automated sample changer (Round et al., 2015) and transferred to an in-vacuum quartz capillary (ID 1.7 mm, wall thickness 50 μm) for analyses. The acquisition time per frame was 1 s for the co-precipitation, and 50 ms for the adsorption experiments. Furthermore, we also measured a series of backgrounds and reference samples including an empty capillary and a capillary filled with water, silica stock solution and lysozyme stock solution. SAXS data processing and reduction included primarily masking of undesired pixels, normalizations and correction for transmission, background subtraction and data integration to 1D. These steps were performed automatically post-data collection at P12. Information on particle size distribution of the pure silica precipitates was derived from the software package MCSAS v.1.0.1 (Pauw, 2013; Breßler et al., 2014) while the position of the correlation peak in the composite patterns was evaluated based on a hard-sphere model in Percus-Yevick approximation (Kinning and Thomas, 1984).

ζ-potential measurements

The ζ-potential was determined for the pure colloidal silica solution and the lysozyme stock solution to understand the electrostatic interactions between these two components. In addition, the ζ-potentials of the composites were investigated in order to obtain information about the structure of the composites (Chapter 7).

The ζ-potential is defined as the electric potential at the slipping plane of a particle in solution (Figure B.4). The slipping plane (also called shear plane) is located within the electrical double layer (EDL) and indicates the layer below which molecules attached to the surface remain attached during movement. In other words, zeta potential is the potential difference between the freely moving solute and the stationary layer of solute attached to the dispersed particle. The ζ-potential is caused by the net surface charge contained below the slipping plane and the location of that plane. Thus, while not identical to the surface charge, it is widely used for quantification of the magnitude of the charge. The location of slipping plane and thus the ζ-potential strongly depend on the ionic strength of the solution (closer at higher ionic strength).

The ζ-potential is measured by applying an electric field across a colloidal solution. Particles within the dispersion will, depending on their ζ-potential, migrate toward the oppositely charged electrode with a velocity proportional to the magnitude of the zeta potential. This electrophoretic mobility is measured and subsequently converted to the ζ-potential of the colloidal solution using the Smoluchowski theory (Smoluchowski, 1903). No mobility suggests that there is no net charge at the slipping plane of a particle in solution. This point is described as the isoelectric point (e.g., Bray et al., 2014).

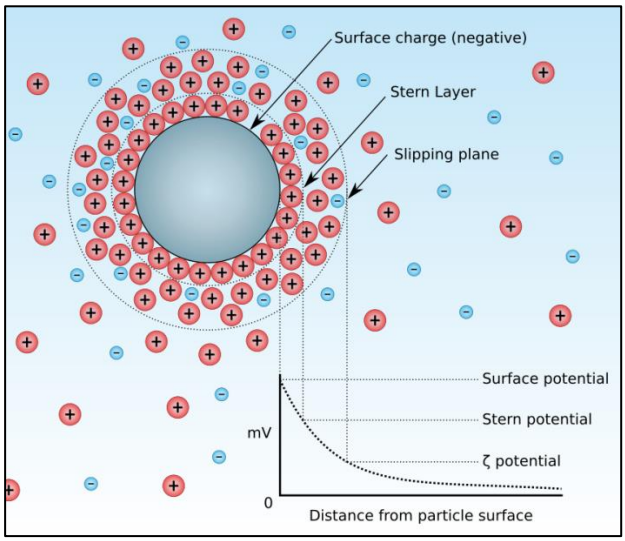

Figure B.4: *Schematic of the density of ions and the electrical potential as a function of distance away from a negatively charged particle in solution (source: Wikipedia, May 2016)*

In our experiments we investigated the ζ-potential of a colloidal silica, lysozyme and several composite solutions in 0.01 M NaCl solutions. For the silica colloids and the composites, we re-dispersed dried precipitates in 0.01 M NaCl solutions. This was done to avoid the effect of salts derived from the precipitation process (Na from the sodium metasilicate and Cl from the HCl used to neutralise the high pH silica stock solution). For the composites drying and re-suspension also removed any surplus lysozyme in solution and not associated with the composites which could affect the measured ζ-potential. We measured the ζ-potential in the range between pH 2 and 10 at 0.5 pH unit intervals. For each measurement point, we took 10 mL of solution, adjusted the pH by adding the required amount of 0.1 to 2M HCl or NaOH and measured the ζ-potential three times using a Malvern Zetasizer Nano ZS and DTS1070 cells. Fresh solution was taken for each data point

to prevent dilution and/or changes in ionic strength due to the continued addition of acid or base.

High-energy X–ray diffraction and conversion to pair distribution function

High-energy X–ray diffraction (HEXD) was performed in order to obtain total scattering data of the pure silica precipitates and the silica-lysozyme composites. The collected data was then transformed to a pair distribution function (PDF) by Fourier transformation yielding information on the molecular structure of amorphous silica and the silica-lysozyme composites (Chapter 7).

When doing X–ray diffraction (XRD) on amorphous or microcrystalline materials, the resulting diffraction patterns will be diffuse, i.e., without any sharp Bragg peaks. However, using the atomic PDF approach (Billinge, 2004; Billinge and Kanatzidis, 2004; Billinge and Levin, 2007; Billinge, 2008), these non-Bragg type patterns can be Fourier transformed to obtain structural information on the sample. To do this reliably and without artefacts the diffraction pattern has to cover a broad q-range (scattering vector, Equation B.1). To achieve this (45 - 100 keV), high-energy X-rays with small wavelengths (λ = 0.12 – 0.27 Å) are needed. The data is corrected for sample adsorption, background scattering and then converted from total scattering data to PDFs. The atomic PDF, *G(r)*, is defined as

$$G(r) = 4\pi r[\rho(r) - \rho_0] \quad \text{(B.2)}$$

with r being a radial distance, $\rho(r)$ the atomic pair-density and ρ_0 the average atomic number (Billinge, 2004). This function "gives information about the number of atoms in a spherical shell of unit thickness at a distance r from a reference atom" (Billinge and Kanatzidis, 2004). Atom-to-atom distances which appear repeatedly are represented by peaks in a PDF. For crystalline materials, these peaks are repeated due to the periodicity which results in the same atomic distances being represented over and over again (Figure B.5). PDFs where the peaks attenuate after several Ångströms (Figure B.5) can be interpreted twofold: (1) no long-range (e.g., 10 Å) structure is present in the sample due to its amorphous or highly disordered nature or (2) it could be crystalline but the size of the individual crystals is very small. For the second case, the attenuation length can be used to determine the size of crystalline regions (Kodama et al., 2006).

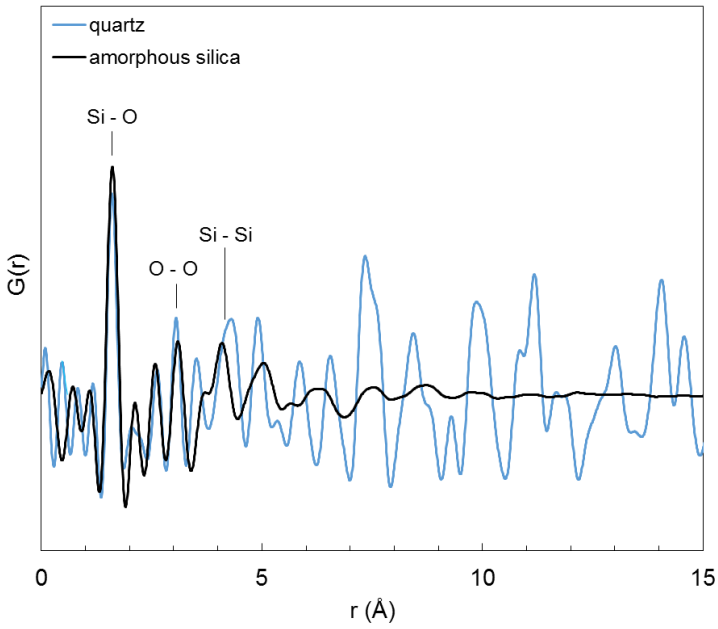

Figure B.5: *Pair distribution functions derived from total scattering of amorphous silica (black) and quartz (blue). The attenuation of the signal > 10Å for the amorphous silica pattern is due to the short-range structure of the material.*

The silica precipitates and the silica-lysozyme composites in Chapter 7 were analysed at beamline 11-ID-B at the Advanced Photon Source at Argonne National Laboratory (USA) by synchrotron-based total scattering (HEXD, ~60 keV, λ = 0.21280 Å). A CeO_2 standard was used to calibrate the sample-to-detector distance and to align the detector with the incident beam path. Before analyses, a water-filled capillary was measured and used for background corrections. The data reduction was done using the software Fit-2D (Hammersley, 1998)while the total scattering measurements were background corrected and converted to pair distribution function (PDF) plots using PDFgetX2 (Qiu et al., 2004). The molecular formulae used to obtain the reduced structure factor functions were $SiO_2 \cdot 0.5\,H_2O$ for silica and $C_{613}H_{959}N_{193}O_{185}S_{10}$ for lysozyme. The PDFs for all silica-lysozyme composites and the pure silica and lysozyme samples were calculated from the Fourier transform of the reduced structure function truncated at ~17.7 $Å^{-1}$. Total scattering was only performed for pure silica and the composited formed by co-precipitation. The composites formed by the adsorption pathway involved the interaction of lysozyme with silica colloids. The lysozyme could thus not affect the silica structure at the molecular scale and analysing them by HEXD was deemed fruitless.

References

Alexander, G., 1954. The polymerization of monosilicic acid. *Journal of the American Chemical Society* **76**, 2094-2096.

Billinge, S.J., 2004. The atomic pair distribution function: past and present. *Zeitschrift für Kristallographie-Crystalline Materials* **219**, 117-121.

Billinge, S.J., 2008. Nanoscale structural order from the atomic pair distribution function (PDF): There's plenty of room in the middle. *Journal of Solid State Chemistry* **181**, 1695-1700.

Billinge, S.J., Kanatzidis, M., 2004. Beyond crystallography: the study of disorder, nanocrystallinity and crystallographically challenged materials with pair distribution functions. *Chemical Communications* **7**, 749-760.

Billinge, S.J., Levin, I., 2007. The problem with determining atomic structure at the nanoscale. *Science* **316**, 561-565.

Blanchet, C.E., Spilotros, A., Schwemmer, F., Graewert, M.A., Kikhney, A., Jeffries, C.M., Franke, D., Mark, D., Zengerle, R., Cipriani, F., 2015. Versatile sample environments and automation for biological solution X-ray scattering experiments at the P12 beamline (PETRA III, DESY). *Journal of Applied Crystallography* **48**, 431-443.

Bras, W., 1998. An SAXS/WAXS beamline at the ESRF and future experiments. *Journal of Macromolecular Science, Part B: Physics* **37**, 557-565.

Bray, A.W., Benning, L.G., Bonneville, S., Oelkers, E.H., 2014. Biotite surface chemistry as a function of aqueous fluid composition. *Geochimica et Cosmochimica Acta* **128**, 58-70.

Breßler, I., Pauw, B.R., Thünemann, A., 2014. *McSAS: A package for extracting quantitative form-free distributions.* arXiv preprint arXiv:1412.1900.

Coradin, T., Eglin, D., Livage, J., 2004. The silicomolybdic acid spectrophotometric method and its application to silicate/biopolymer interaction studies. *Journal of Spectroscopy* **18**, 567-576.

Craievich, A., 2002. Synchrotron SAXS studies of nanostructured materials and colloidal solutions: a review. *Materials Research* **5**, 1-11.

Eaton, A.D., Clesceri, L.S., Rice, E.W., Greenberg, A.E., 2005. *Standard methods for the examination of water and wastewater*, 21st Edition ed. American Public Health Association, Washington.

Glatter, O., Kratky, O., 1982. *Small angle scattering*. Academic, New York.

Guinier, A., Fournet, G., 1955. *Small angle X-rays*. John Wiley & Sons, New York.

Hammersley, A., 1998. *FIT2D V9. 129 Reference Manual V3.1*. Internal Report ESRF98HA01, ESRF, Grenoble.

Icopini, G.A., Brantley, S.L., Heaney, P.J., 2005. Kinetics of silica oligomerization and nanocolloid formation as a function of pH and ionic strength at 25 °C. *Geochimica et Cosmochimica Acta* **69**, 293-303.

Iler, R.K., 1979. *The chemistry of silica: solubility, polymerization, colloid and surface properties, and biochemistry*. Wiley, London.

Kinning, D.J., Thomas, E.L., 1984. Hard-sphere interactions between spherical domains in diblock copolymers. *Macromolecules* **17**, 1712-1718.

Kodama, K., Iikubo, S., Taguchi, T., Shamoto, S.i., 2006. Finite size effects of nanoparticles on the atomic pair distribution functions. *Acta Crystallographica Section A: Foundations of Crystallography* **62**, 444-453.

Pauw, B.R., 2013. Everything SAXS: small-angle scattering pattern collection and correction. *Journal of Physics: Condensed Matter* **25**, 383201.

Qiu, X., Thompson, J.W., Billinge, S.J., 2004. PDFgetX2: a GUI-driven program to obtain the pair distribution function from X-ray powder diffraction data. *Journal of Applied Crystallography* **37**, 678-678.

Riekel, C., Burghammer, M., Müller, M., 2000. Microbeam small-angle scattering experiments and their combination with microdiffraction. *Journal of Applied Crystallography* **33**, 421-423.

Round, A., Felisaz, F., Fodinger, L., Gobbo, A., Huet, J., Villard, C., Blanchet, C.E., Pernot, P., McSweeney, S., Roessle, M., 2015. BioSAXS Sample Changer: a robotic sample changer for rapid and reliable high-throughput X-ray solution scattering experiments. *Acta Crystallographica Section D: Biological Crystallography* **71**, 67-75.

Smoluchowski, M., 1903. Contribution to the theory of electro-osmosis and related phenomena. *Bulletin International de l'Academie des Sciences de Cracovie* **3**, 184-199.

Stawski, T.M., Benning, L.G., 2013. SAXS in Inorganic and Bioinspired Research. *Research Methods in Biomineralization Science* **532**, 95-127.

Tanakaa, M., Takahashib, K., 2001. Silicate species in high pH solution molybdate, whose silica concentration is determined by colorimetry. *Analytica Chimica Acta* **429**, 117-123.

Tarutani, T., 1970. Chromatographic behaviour of silicic acid on sephadex columns. *Journal of Chromatography A* **50**, 523-526.

Ten Elshof, J.E., Besselink, R., Stawski, T.M., Castricum, H.L., 2015. Time-Resolved Small-Angle X-Ray Scattering. *The Sol-Gel Handbook-Synthesis, Characterization, and Applications: Synthesis, Characterization and Applications, 3-Volume Set*, 673-712.

Tobler, D.J., Shaw, S., Benning, L.G., 2009. Quantification of initial steps of nucleation and growth of silica nanoparticles: An *in-situ* SAXS and DLS study. *Geochimica et Cosmochimica Acta* **73**, 5377-5393.

Weres, O., Yee, A., Tsao, L., 1981. Kinetics of silica polymerization. Journal of *Colloid and Interface Science* **84**, 379-402.

Appendix C

Supplementary Information for Chapter 7

Structure of a lysozyme molecule

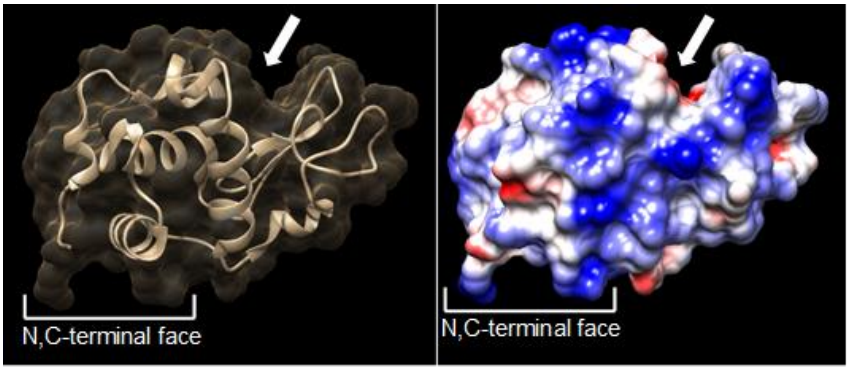

Figure C.1: *Structure of the lysozyme molecule with the protein secondary structure shown by the ribbon and the molecular surface as a ghost surface (left) and the Coulomb surface indicating the distribution of surface charge across the molecule surface (blue – positive, red – negative, white – neutral) (right). The N,C-terminal face and active site location (arrow) are indicated. Both structures were drawn in Chimera 1.10 (Pettersen et al., 2004) using entry 2VB1 (Wang et al., 2007) in the Protein Database PDB.*

XRD of composites

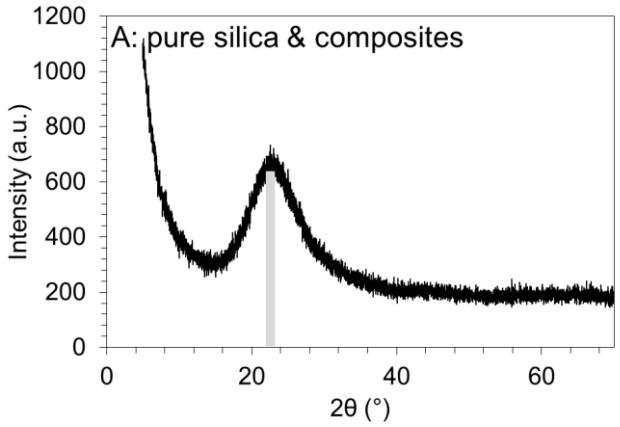

Figure C.2: *XRD of dried pure silica and dried composites (they are perfectly overlapping). All patterns only show the broad peak at ~24° 2θ characteristic of amorphous silica and no peaks indicating crystalline SiO_2 phases are present.*

Frequencies and band assignments in FTIR spectra

Table C-1 *Frequencies and band assignments in FTIR spectra of silica, lysozyme and silica-lysozyme composites in Figure 7.2 (Benning et al., 2004).*

Band no.	Approx. waveno. [cm^{-1}]	Assignments	Main group
1	3300–3400	O–H stretching	Water
2	2930–2960	C–H_3 stretching C–H_2 stretching	Methyl and methylene groups in lipids (impurities in crystallized lysozyme)
3	1630	O–H stretching	Water in hydrogen bonded silanols
4	1650	C=O stretching	Amide I, mostly from β-sheets in protein
5	1540	N–H bending, C–N stretching	Amide II, protein
6	950–1200	C–O stretching, P=O stretching	Polysaccharides (impurities in crystal-lized lysozyme)
7	1060	Si–O stretching	Siloxane, often exhibits a shoulder at 1200 cm^{-1} corresponding to the Si–O stretching of SiO_4 tetrahedra
8	950	Si–OH stretching	Silanol in hydrated silica
9	800	Si–O stretching	Multiple siloxane (Si–O–Si) in solid amorphous silica

Carbon and lysozyme content of composites

Table C-2 *Results from total carbon analyses of silica, lysozyme and silica-lysozyme composites*

	Lysozyme added [ppm]	Carbon content [wt.%]	Lysoz. in composite[2)] [wt.%]
Silica	0	0	0.0
Lysozyme	–	51.4[1)]	–
Silica-lysozyme composites formed by co-precipitation			
CoP_25	25	0.4	0.7
CoP_63	63	1.2	2.3
CoP_100	100	3.7	7.3
CoP_250	250	4.8	9.4
CoP_500	500	8.9	17.3
CoP_750	750	12.2	23.7
CoP_1000	1000	13.9	27.1
Silica-lysozyme composites formed by adsorption			
Ads_100	100	0.5	1.0
Ads_250	250	9.0	17.5
Ads_500	500	16.3	31.8
Ads_1000	1000	16.8	32.7

[1)] Calculated based on a lysozyme molecule with the formula $C_{613}H_{959}N_{193}O_{185}S_{10}$ and a molecular weight of 14'313 g/mol (Gasteiger et al., 2005)

[2)] Calculated based on carbon content in lysozyme (51.4 wt.%)

Calculation of monolayer coverage

Table C-3 *Calculation of jamming limits Θ_∞ for RSA monolayers and surface coverages Θ for pure end-on and side-on orientation of lysozyme associated with the silica in the composites.*

sample ID	Lys in composite [wt.%]	Lysozyme molec.[1] [#]	Silica particles[2] [#]	Molec./particle ratio [-]	$\Theta_{end\text{-}on}$ [-]	$\Theta_{side\text{-}on}$ [-]	Θ/Θ_∞ (end-on) [%]	Θ/Θ_∞ (side-on) [%]
Θ_∞ (CoP)	–	–	–	–	2.263[3]	3.304[4]	–	–
CoP_25	0.7	2.95E+17	1.10E+19	0.03	0.014	0.031	1%	1%
CoP_63	2.3	9.68E+17	1.08E+19	0.09	0.046	0.103	2%	3%
CoP_100	7.3	3.07E+18	1.02E+19	0.30	0.153	0.344	7%	10%
CoP_250	9.4	3.96E+18	1.00E+19	0.40	0.201	0.453	9%	14%
CoP_500	17.3	7.28E+18	9.14E+18	0.80	0.406	0.914	18%	28%
CoP_750	23.7	9.98E+18	8.43E+18	1.18	0.603	1.357	27%	41%
CoP_1000	27.1	1.14E+19	8.06E+18	1.42	0.722	1.624	32%	49%
Θ_∞ (Ads)	–	–	–	–	1.915[3]	2.679[4]	–	–
Ads_100	1.0	4.21E+17	5.82E+18	0.07	0.024	0.054	1%	2%
Ads_250	17.5	7.37E+18	4.85E+18	1.52	0.505	1.136	26%	42%
Ads_500	31.8	1.34E+19	4.01E+18	3.34	1.110	2.498	58%	93%
Ads_1000	32.7	1.38E+19	3.96E+18	3.48	1.157	2.603	60%	97%

[1] Calculated based on 1 g of composite and a molecular weight of 14'313 g/mol for lysozyme (Gasteiger et al., 2005).

[2] Calculated based on 1 g of composite and a molecular weight of 142'373 g/mol for the silica particles in the adsorption experiments (∅ = 5.2 nm) and 54'476 g/mol for the silica particles in the precipitation experiments (∅ = 4.2 nm). The molecular weights for silica were calculated according to Iler (1979).

[3] Calculated according to Equation 7.2

[4] Calculated according to Equation 7.3

EELS spectra at C edge for support foil and lysozyme

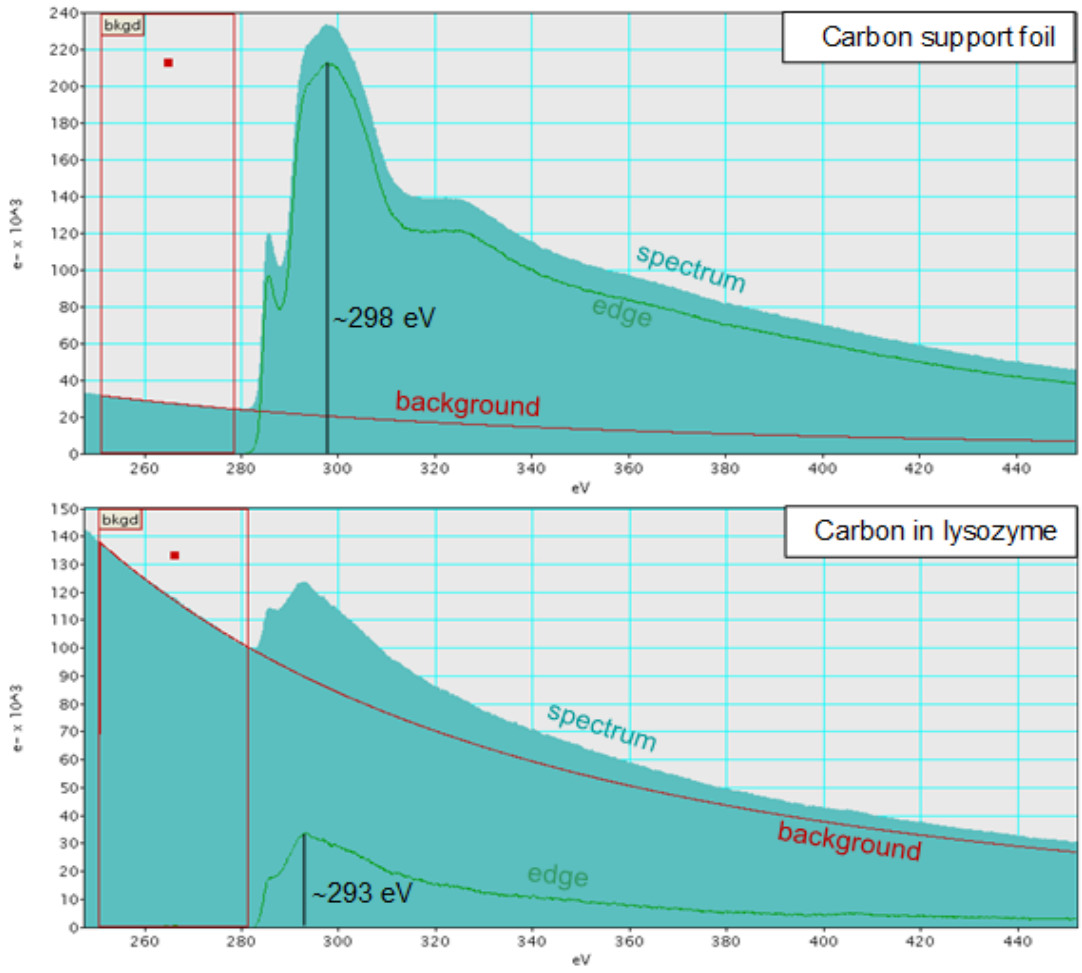

Figure C.3: *EELS spectra of the carbon support foil and the carbon in lysozyme (measured above a hole in the support foil). The K-edge position is different enough that, for collection of the EELS maps, the energy window could be chosen as to not include contributions from the support film. Thus the carbon maps used to construct Figure 7.5 in the main text only show carbon signals related to lysozyme*

Particle size distribution of pure silica

The particle size distribution of silica nanoparticles in the absence of lysozyme was determined by fitting of the scattering curve (Figure C.4). At low-q part of the data ($q < 0.1$ nm^{-1}) the curve starts to reach a plateau where $I(q)$ scales as q^0. This indicates that the particles have a finite size and are not aggregated in solution. The fitting was done under the assumption that silica nanoparticles are spherical in shape (Tobler et al., 2009).

Scattering intensity, $I(q)$ from the collection of monodisperse spherical particles is given by Equation C.1 and C.2 and is a function of a number density of particles, N, the scattering contrast, $(\Delta\rho)^2$, particle volume, V, and a sphere form factor $P(q)$ (Guinier and Fournet, 1955):

$$I(q) = N(\Delta\rho)^2 V^2 P(q) \tag{C.1}$$

$$P(q,R) = \left(2\frac{\sin(qR) - qR\sin(qR)}{q^3R^3}\right)^2 \tag{C.2}$$

Equation C.2 is normalized so that $P(q\rightarrow 0)=1$, therefore intensity at a zero angle $I(q=0)$ is equal to $N(\Delta\rho)V^2$.

For polydisperse spherical particles Equation C.1 and C.2 are no longer valid and the size distribution function $D(r)$ has to be included in the expression for the form factor. The averaged form factor of spheres is then given by Equation C.3:

$$P(q,\bar{R},\sigma) \geq \frac{\int_0^\infty D(r,\bar{R},\sigma)P(q,r)r^{3d}dr}{\int_0^\infty D(r,\bar{R},\sigma)r^{3d}dr} \tag{C.3}$$

where $\bar{R}$ denotes the averaged radius, and σ is a variance of the distribution. Parameter d takes values of 0, 1, and 2 and depending on d the averaging yields accordingly intensity, volume (mass) or number weighted value of $\bar{R}$ (Svergun et al., 2000). In such a case $I(q=0) = N(\Delta\rho)^2 < V^2 >$, where $< V^2 >$ denotes the distribution-averaged squared volume of a spherical particle, because $<P(q=0)>$ = 1. The choice of a $D(r)$ function is usually not trivial for real-life particulate systems (Kril and Birringer, 1998), and in highly polydisperse systems one has to consider asymmetric and/or multimodal distributions. From the shape of the scattering curve in Figure C.4 one can expect that this indeed the case e.g., from two bending points at q = ~0.2 nm^{-1} and q=~0.9 nm^{-1}, in between which pseudo-mass-fractal scaling could be observed. We emphasize that it does not originate from a genuine mass-fractal aggregate (Texeira, 1988). Therefore, instead of guessing the size distribution function, we can find a histogram of contributions from different sizes of spherical particles using structure interference methods and their Monte Carlo derivatives (Martelli and Di Nunzio, 2002). Pauw et al. (2013) and Bressler et al. (2014) released the software package MCSAS v.1.0.1, which we used the find such form-free size distribution histogram for the curve in Figure C.4. The fit to the data is plotted with the original curve is Figure C.4 (left), whereas the corresponding histogram is presented in Figure C.4 (right).

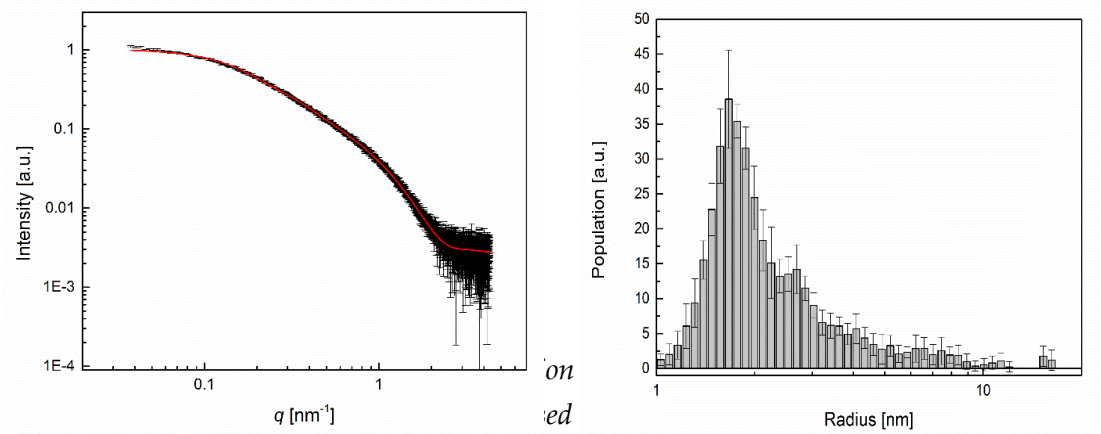

software (left) and histogram showing the particle size distribution obtained from the best fit (right).

Correlation peak position: particle size vs. volume fraction

The scattering curve corresponding to pure silica in Figure 7.6 B (grey curve) originated from the relatively weakly polydisperse silica nanoparticles (Figure C.4). In this pattern for q < 0.06 nm^{-1}, $I(q) \propto q^0$, which indicates a Guinier region and suggests that particles do not interact with each other and have not aggregated. We express the scattering intensity from such pattern simply as:

$$I(q) \propto < P(q) > \quad \text{(C.4)}$$

where, $<P(q)>$ is the generalized function for a form factor of particles, which takes into account their shape, size, polydispersity, volume fraction, and scattering length density difference between the particles and the solvent/buffer.

In the presence of lysozyme, the scattering patterns changed, although the actual contribution of lysozyme to the scattering pattern was negligible (see Figure 6 A and discussion in the main text). Importantly, for q > ~1.5 nm^{-1} there was no difference between the two scattering patterns (Figure 7.6 B, grey and dashed-orange curves). Therefore, under the assumption that the scattering length density (proportional to electron density) of particles remained constant and they were no longer changing in solution, we can state that the volume fraction of particles was constant as well. However, for q < ~1.5 nm^{-1} a broad correlation peak developed and the intensity gradually increased by two orders of magnitude in comparison with the sample without lysozyme. This change in intensity can be rationalized by the

formation of aggregates of silica in the presence of lysozyme (thus, the overall increase in intensity due to the formation of larger structures), as well as the development of inter-particle interferences caused by the fact that particles are located closely together within the aggregates (thus, the correlation peak; ten Elshof et al., 2015). This overall effect of particle aggregation on scattering intensity is expressed as:

$$I(q) \propto < P(q) > S_{eff}(q) \tag{C.5}$$

Here, $S_{eff}(q)$ is an effective structure factor function, which describes the particle-particles interferences in solution. Overall such a function should contain contributions representing both the observed increase in intensity at low-q as well as the correlation peak (Beaucage and Schaefer, 1994; Sztucki et al., 2006; Stawski et al., 2011). Let us discuss only the correlation peak contributions. The peak's maximum position at q_{max} corresponds to the interparticle distance d:

$$d = \frac{2\pi}{q_{max}} \tag{C.6}$$

This is a very useful relationship in SAXS analysis, due to its simplicity. However, Equation C.6 is an approximation, because although the position of the peak depends primarily on d, the exact position is also dependent on the physical model applied to express the correlation, as we show below.

In the most common case, the contribution of the correlation peak to $S_{eff}(q)$ is modeled in terms of the non-sticky hard sphere potential U. For spherical species, the interparticle distance can be associated with the particles' effective hard-sphere radii $d = 2R_{eHS}$. U for the radial distance between particles r follows:

$$U = 0 \ \ for\ r > 2R_{eHS} \tag{C.7b}$$

and

$$U = \infty \ \ for\ r < 2R_{eHS} \tag{C.7b}$$

The straight forward form of the structure factor $S(q)$ describing the interparticle correlation in Born-Green approximation is expressed as following (Guinier and Fournet, 1955; Beaucage and Schaefer, 1994; Stawski et al., 2011):

$$S(q) = \frac{1}{1 + 8\phi\left(3\dfrac{\sin(2qR_{eHS}) - 2qR_{eHS}\cos(2qR_{eHS})}{(2qR_{eHS})^3}\right)} \tag{C.8}$$

Here, φ denotes a volume fraction of particles building the correlated system (aggregate). In Figure C.5, we plot Equation C.8 for several values of φ and $R_{eHS} = const$. Characteristically, the intensity of the first peak in the oscillation also increases as a

function of increasing φ. The curves were simulated for R_{eHS} = 2.5 nm. Therefore according to Equation C.6 the q_{max} should be at ~1.26 nm^{-1}, whereas in fact it is at ~1.16 nm^{-1}, which would suggest the radius of ~2.7 nm (+8%).

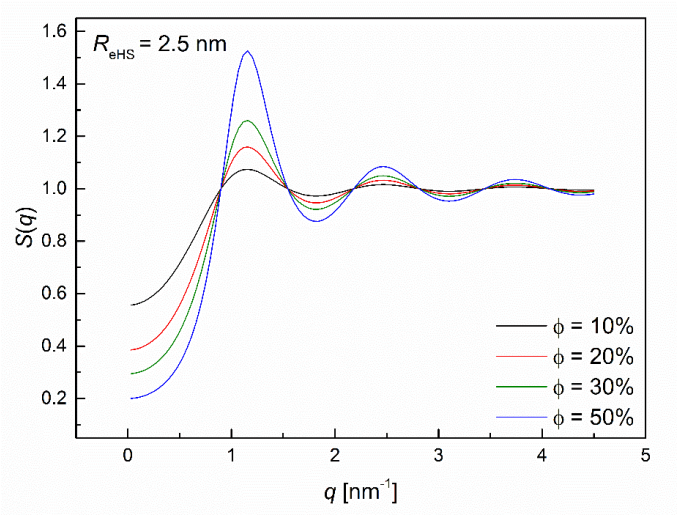

Figure C.5: *Structure factor S(q) as a function of q at different volume fractions calculated according to the Born-Green approximation (Equation C.8; Guinier and Fournet, 1955; Beaucage and Schaefer, 1994; Stawski et al., 2011).*

Equation C.8 does not take into account the multi-body interactions in between the particles. Equation C.9 represents the solution of the structure factor in Percus-Yevick approximation, which takes into account such higher-order interferences (Kinning and Thomas, 1984).

$$S(q) = \frac{1}{1 + 24\phi\dfrac{G(q, \phi, R_{eHS})}{2R_{eHS}}} \tag{C.9a}$$

where $S(q)$ depends on volume fraction of interacting neighboring scatterers, φ. The function $G(q,v,R_{eHS})$ has the following form:

$$\begin{aligned} &SG(q, \phi, R_{eHS}) \\ &= A\frac{\sin(2qR_{eHS}) - (2qR_{eHS})\cos(2qR_{eHS})}{(2qR_{eHS})^2} + B\frac{2(2qR_{eHS})\sin(2qR_{eHS}) + [2 - (2qR_{eHS})^2]\cos(2qR_{eHS}) - 2}{(2qR_{eHS})^3} \\ &+ C\frac{-(2qR_{eHS})^4\cos(2qR_{eHS}) + 4[3(2qR_{eHS})^2 - 6]\cos(2qR_{eHS}) + 4[(2qR_{eHS})^3 - 6(2qR_{eHS})]\sin(2qR_{eHS}) + 24}{(2qR_{eHS})^5} \end{aligned} \tag{C.9b}$$

In Equation C.6b the parameters A, B and C are dependent on φ, through the following expressions:

$$A = \frac{(1 + 2\phi)^2}{(1 - \phi)^4}, B = \frac{-6\phi\left(\dfrac{1 + \phi}{2}\right)^2}{(1 - \phi)^4}, C = \frac{\phi A}{2} \tag{C.9c}$$

In Figure C.6 we plot Equation C.9 for several values of φ and R_{eHS} = *const.* Not only does the Equation C.9 yield sharper peaks than Equation C.8, for the same φ values, but the apparent position of the first peak shifts towards higher q-values with increasing φ. Like in the previous case the curves were simulated for R_{eHS} = 2.5 nm. For φ = 10%, q_{max}= ~1.21 nm^{-1}, which corresponds to the apparent radius of ~2.6 nm (+4%). For φ = 50%, q_{max}= ~1.39 nm^{-1}, and the apparent radius is ~2.3 nm (-10%).

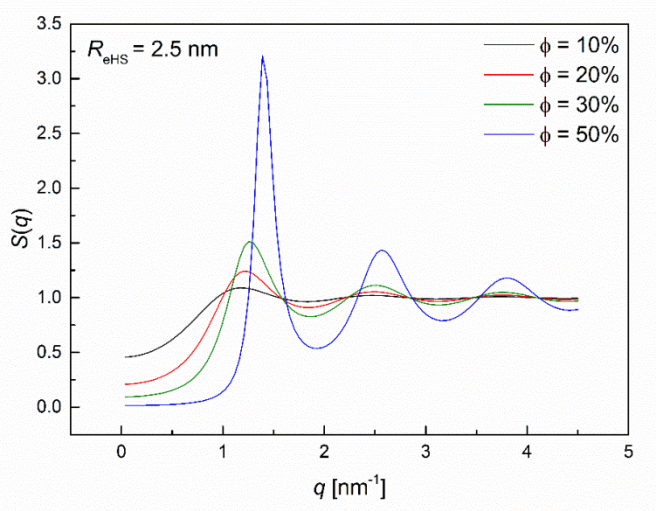

Figure C.6: *Structure factor S(q) as a function of q at different volume fractions calculated according to the Percus-Yevick approximation (Equation C.9; Kinning and Thomas, 1984).*

References Supporting Information

Benning, L.G., Phoenix, V.R., Yee, N., Tobin, M.J., 2004. Molecular characterization of cyanobacterial silicification using synchrotron infrared micro-spectroscopy. *Geochimica et Cosmochimica Acta* **68**, 729-741.

Beaucage, G., Schaefer, D.W., 1994. Structural studies of complex systems using small-angle scattering: a unified Guinier/power-law approach. *Journal of Non-Crystalline Solids* **172**, 797-805.

Breßler, I., Pauw, B.R., Thünemann, A., 2014. *McSAS: A package for extracting quantitative form-free distributions*. arXiv preprint arXiv:1412.1900.

Gasteiger, E., Hoogland, C., Gattiker, A., Wilkins, M. R., Appel, R. D., Bairoch, A., 2005. Protein identification and analysis tools on the ExPASy server. *The Proteomics Protocols Handbook*, 571-607.

Guinier, A, Fournet, G., 1955. *Small angle scattering of X-rays*. Wiley & Sons, New York.

Iler, R.K. , 1979. *The chemistry of silica: solubility, polymerization, colloid and surface properties, and biochemistry*. Wiley, London.

Kinning, D.J., Thomas, E.L., 1984. Hard-sphere interactions between spherical domains in diblock copolymers. *Macromolecules* **17**, 1712-1718.

Kril, C.E., Birringer, R., 1998. Estimating grain-size distributions in nanocrystalline materials from X-ray diffraction profile analysis. *Philosophical Magazine A* **77**, 621-640.

Martelli, S., Di Nunzio, P. E., 2002. Particle size distribution of nanospheres by Monte Carlo fitting of small angle x-ray scattering curves. *Particle and Particle Systems Characterization* **19**, 247-255.

Pauw, B.R., Pedersen, J.S., Tardif, S., Takata, M., Iversen, B.B., 2013. Improvements and considerations for size distribution retrieval from small-angle scattering data by Monte Carlo methods. *Journal of Applied Crystallography* **46**, 365-371.

Pettersen, E. F., Goddard, T. D., Huang, C. C., Couch, G. S., Greenblatt, D. M., Meng, E. C., Ferrin, T. E., 2004. UCSF Chimera—a visualization system for exploratory research and analysis. *Journal of Computational Chemistry* **25**, 1605-1612.

Stawski, T.M., Veldhuis, S.A., Besselink, R., Castricum, H.L., Portale, G., Blank, D.H., ten Elshof, J.E, 2011. Nanostructure development in alkoxide-carboxylate-derived precursor films of barium titanate. *Journal Physical Chemistry C* **116**, 425-434.

Svergun, D.I., Konarev, P.V., Volkov, V.V., Koch, M.H.J., Sager, W.F.C., Smeets, J., Blokhuis, E.M., 2000. A small angle x-ray scattering study of the droplet–cylinder transition in oil-rich sodium bis (2-ethylhexyl) sulfosuccinate microemulsions. *Journal of Chemical Physics* **113**, 1651-1665.

Sztucki, M., Narayanan, T., Belina, G., Moussaid, A., Pignon, F., Hoekstra, H., 2006. Kinetic arrest and glass-glass transition in short-ranged attractive colloids. *Physical Review E* **74**, 051504.

Teixeira, J., 1988. Small-angle scattering by fractal systems. *Journal of Applied Crystallography* **21**, 781-785.

ten Elshof, J.E., Besselink, R., Stawski, T.M., Castricum, H.L., 2015. Time-Resolved Small-Angle X-Ray Scattering. *The Sol-Gel Handbook-Synthesis, Characterization, and Applications: Synthesis, Characterization and Applications, 3-Volume Set*, 673-712.

Tobler, D.J., Shaw, S., Benning, L.G., 2009. Quantification of initial steps of nucleation and growth of silica nanoparticles: An *in-situ* SAXS and DLS study. *Geochimica et Cosmochimica Acta* **73**, 5377-5393.

Wang, J., Dauter, M., Alkire, R., Joachimiak, A., Dauter, Z., 2007. Triclinic lysozyme at 0.65 Å resolution. *Acta Crystallographica, Section D: Biological Crystallography* **63**, 1254-1268.